

# Compression and Buckling of Composite Panels with Curvilinear Fibers

by

Reynaldo A. Olmedo

Thesis submitted to the Faculty of the

Virginia Polytechnic Institute and State University

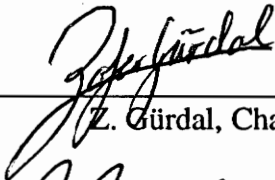
in partial fulfillment of the requirements for the degree of

MASTER OF SCIENCE

in

Engineering Mechanics

APPROVED:

  
\_\_\_\_\_  
Z. Gürdal, Chairman

  
\_\_\_\_\_  
O. H. Griffin

  
\_\_\_\_\_  
M. W. Hyer

  
\_\_\_\_\_  
E. R. Johnson

August 1992

Blacksburg, Virginia

c.2

LD  
5655  
V855  
1992  
0464  
c.2

# Compression and Buckling of Composite

## Panels with Curvilinear Fibers

by

Reynaldo A. Olmedo

Z. Gürdal, Committee Chairman

Engineering Mechanics

(ABSTRACT)

The plane in-plane compression response for a symmetrically laminated composite panel with a spatially varying fiber orientation has been analyzed for four different boundary conditions. Variation of the fiber angle along the length of a composite laminate results in stiffness properties that change as a function of location. The laminates are therefore termed variable stiffness panels. This work presents an analysis of the stiffness variation and its effect on the in-plane and buckling response of the panel. The fiber orientation is assumed to vary only in one spatial direction, although the analysis can be extended to fibers that vary in two spatial directions. A system of coupled elliptic partial differential equations that govern the in-plane behavior of these panels has been derived. Solving these equations yields the displacement fields, from which the strains, stresses, and stress resultants can be subsequently calculated. A numerical solution has been obtained using an iterative collocation technique. Corresponding closed form solutions are presented for the in-plane problem for four different sets of boundary conditions. Three of the cases presented have exact solutions, and therefore serve to validate the numerical model. The Ritz Method has been used to find the buckling loads and buckling modes for the variable stiffness panels. Improvements in the buckling load of up to 80% over straight fiber configurations were found. Results for three different panel aspect ratios are presented.

**Abstract**

## ACKNOWLEDGEMENTS

The funding for this work was provided by the Aircraft Structures Branch at NASA Langley Research Center through grant NAG 1-643. I gratefully acknowledge NASA's financial support. I thank my committee members for their review of my work and for their suggestions and comments. I also acknowledge the help of Dr. Calvin Ribbens of the Computer Science department at Virginia Tech for installing the ELLPACK software and providing technical assistance with the development of the computer code. I am indebted to my advisor, Prof. Zafer Gürdal, for his help and guidance, and for the valuable knowledge that I gained while working with him. A mi Papá, mi Mamá, 'Abuelita' Marcos, Juan G., Claudia y Marvín, les agradezco por todo su apoyo, aliento y, sobre todo, su cariño.

# TABLE OF CONTENTS

<b>Chapter 1. The Variable Stiffness Design Concept</b>	<b>1</b>
1.1 Introduction	1
1.2 Overview of Variable Stiffness Structures	3
1.2.1 Early Research	3
1.2.2 Recent Research	5
1.3 Variable Stiffness in This Investigation	7
1.4 Approach	8
<b>Chapter 2. Laminate Theory for Variable Stiffness Panels</b>	<b>11</b>
2.1 Lamina Constitutive Relations	11
2.1.1 Straight Fiber Lamina	11
2.1.2 Curvilinear Fiber Lamina	12
2.2 Classical Lamination Theory	13
2.2.1 Kinematics	13
2.2.2 Stress and Moment Resultants	13
2.2.3 The Material Invariants	16
2.2.4 Effective Material Properties	17
<b>Chapter 3. In-Plane Analysis</b>	<b>24</b>
3.1 Introduction	24
3.2 Governing Equations	24
3.2.1 Equilibrium Approach	24
3.2.2 Stress Function Approach	25
3.2.3 Selected Approach	27
3.3 Boundary Conditions	27
3.3.1 Case I: Free Transverse Edges	28
3.3.2 Case II: Fixed Transverse Edges	28
3.3.3 Case III: Transverse Loading	30
3.3.4 Case IV: Straight-but-Free Transverse Edges	30
3.4 Numerical Solution	32
3.4.1 Solution to a General Elliptic PDE	32
3.4.2 Application to Variable Stiffness Panels	34
3.4.3 Convergence and Grid Refinement	34
3.5 Closed Form Solutions	43
3.5.1 Closed Form Solution, Case I	43
3.5.2 Closed Form Solution, Case II	47
3.5.3 Closed Form Solution, Case III	50
3.5.4 Closed Form Solution, Case IV	52
3.6 Overall Panel Stiffness	54
3.7 Failure Analysis	54
<b>Chapter 4. In-Plane Results and Discussion</b>	<b>57</b>
4.1 Introduction	57

4.2	Case I Boundary Conditions . . . . .	57
4.2.1	Deformations and Strains . . . . .	58
4.2.1.1	The $u$ displacement field . . . . .	58
4.2.1.2	The $v$ displacement field . . . . .	61
4.2.1.3	Effects of the Displacement Gradients . . . . .	65
4.2.2	Stress Resultants . . . . .	67
4.2.3	The Closed Form Solution . . . . .	74
4.2.4	Equivalent Stiffness . . . . .	78
4.2.5	Rectangular Panels . . . . .	80
4.3	Case II Boundary Conditions . . . . .	85
4.3.1	Deformations and Strains . . . . .	85
4.3.2	Stress Resultants . . . . .	87
4.3.3	Equivalent Stiffness . . . . .	87
4.4	Case III Boundary Conditions . . . . .	89
4.4.1	Deformations . . . . .	89
4.4.2	Stress Resultants . . . . .	91
4.4.3	Equivalent Stiffness . . . . .	91
4.4.4	Rectangular Panels . . . . .	94
4.5	Case IV Boundary Conditions . . . . .	94
4.5.1	Deformations . . . . .	96
4.5.2	Stress Resultants . . . . .	100
4.5.3	Equivalent Stiffness . . . . .	103
4.6	Validity of the Numerical Model . . . . .	103
<b>Chapter 5.</b>	<b>Buckling Analysis . . . . .</b>	<b>107</b>
5.1	Introduction . . . . .	107
5.1.1	Coordinate System . . . . .	107
5.2	Stability Analysis by The Ritz Method . . . . .	109
5.2.1	Strain Energy . . . . .	109
5.2.2	Potential Energy of the In-Plane Loads . . . . .	110
5.2.3	Second Variation of the Total Potential Energy . . . . .	110
5.3	The Eigenvalue Problem . . . . .	111
5.3.1	The Effects of Anisotropy . . . . .	111
5.3.2	The $w$ Displacement Function . . . . .	113
5.3.3	The Stiffness Matrix . . . . .	114
5.3.4	The Geometric Stiffness Matrix . . . . .	115
5.3.4.1	Case I boundary conditions . . . . .	116
5.3.4.2	Case II and Case IV boundary conditions . . . . .	116
5.3.4.3	Case III boundary conditions . . . . .	116
5.3.5	The Problem and Its Solution . . . . .	117
<b>Chapter 6.</b>	<b>Buckling Results and Discussion . . . . .</b>	<b>118</b>
6.1	Introduction . . . . .	118
6.2	Convergence of the Ritz Method . . . . .	119
6.3	Buckling for Case I . . . . .	121

6.3.1	The Square Panel . . . . .	121
6.3.2	The Long Panel . . . . .	124
6.4	Buckling for Case II . . . . .	124
6.4.1	The Square Panel . . . . .	127
6.4.2	The Long Panel . . . . .	130
6.4.3	The Short Panel . . . . .	133
6.5	Buckling for Case III . . . . .	136
6.5.1	The Square Panel . . . . .	136
6.5.2	The Long Panel . . . . .	139
6.5.3	The Short Panel . . . . .	142
6.6	Buckling for Case IV . . . . .	142
6.6.1	The Square Panel . . . . .	142
6.6.2	The Long Panel . . . . .	145
6.6.3	The Short Panel . . . . .	149
6.7	Buckling Modes . . . . .	149
6.8	Failure . . . . .	157
<b>Chapter 7.</b>	<b>Concluding Remarks . . . . .</b>	<b>159</b>
7.1	Conclusions . . . . .	159
7.1.1	In-Plane Response . . . . .	159
7.1.2	Buckling . . . . .	159
7.2	Suggestions for Future Work . . . . .	160
<b>Appendix 1.</b>	<b>The Stiffness Matrix . . . . .</b>	<b>162</b>
<b>References</b>	<b>. . . . .</b>	<b>167</b>
<b>Vita</b>	<b>. . . . .</b>	<b>169</b>

## LIST OF TABLES

Table 3.1	Convergence of the Displacements at $y = b/2$ for $a/b = 1.0$ . . . . .	40
Table 3.2	Convergence of the Displacements at $y = b/2$ for $a/b = 0.5$ . . . . .	42
Table 3.3	Convergence of the Displacements at $y = b/2$ for $a/b = 2.0$ . . . . .	45
Table 3.4	Strain Allowables for the T300-N5208 Material System. . . . .	56
Table 4.1	Numerically Calculated and Exact Values of $u$ and $N_y$ for Cases II and IV. . .	105
Table 4.2	Numerically Calculated and Exact Values of $u$ and $N_y$ for Case III. . . . .	106
Table 6.1	Convergence of The Ritz Method for Case I. . . . .	120
Table 6.2	Buckling vs. Failure Load for Various Variable Stiffness Configurations. . . .	158

## LIST OF FIGURES

Figure 1.1	Exploded View of a Conventional $[\theta / -\theta / \theta]$ Laminate Lay-Up. . . . .	2
Figure 1.2	Fiber Orientation, Fiber Paths, and $[\pm\theta]_{ns}$ Laminate Configuration for (i) $T_0 = 45^\circ$ , $T_1 = -45^\circ$ and (ii) $T_0 = 45^\circ$ , $T_1 = 0^\circ$ . . . . .	9
Figure 2.1	Stress Resultants, Moment Resultants and Laminate Configuration (Ref.[12]). . . . .	15
Figure 2.2	Effective Axial Modulus $E_x$ . . . . .	20
Figure 2.3	Effective Transverse Modulus, $E_y$ . . . . .	21
Figure 2.4	Effective Shear Modulus, $G_{xy}$ . . . . .	22
Figure 2.5	Effective Major and Minor Poisson's Ratios, $\nu_{xy}$ and $\nu_{yx}$ . . . . .	23
Figure 3.1	Panel and Quarter Panel Boundary Conditions for (i) Free and (ii) Fixed Transverse Edges. . . . .	29
Figure 3.2	Panel and Quarter Panel Boundary Conditions for (i) Transverse Loading and (ii) Free-but-Straight Transverse Edges. . . . .	31
Figure 3.3	Domain Discretization and Collocation Points with $5 \times 5$ Gridlines. . . . .	33
Figure 3.4	Algorithm for Calculating the $u$ and $v$ Displacement Fields (Case I). . . . .	35
Figure 3.5	Sixty Five Point Convergence Grid . . . . .	37
Figure 3.6	Convergence of $N_y$ at $y=b/2$ for $a/b=1.0$ . . . . .	39
Figure 3.7	Convergence of $N_y$ at $y=b/2$ for $a/b=0.5$ . . . . .	41
Figure 3.8	Convergence of $N_y$ at $y=b/2$ for $a/b=2.0$ . . . . .	44
Figure 4.1	The $u$ Displacement for Case I Panels as a Function of $x/a$ for Various Values of $T_1$ . . . . .	59
Figure 4.2	Normalized Axial Strain, $\epsilon_x$ , for (i) $T_0 = 45^\circ$ , $T_1 = 0^\circ$ and (ii) $T_0 = 45^\circ$ , $T_1 = 90^\circ$ Panels with $a/b = 1$ , as a Function of $x$ and $y$ . . . . .	60
Figure 4.3	The $u$ Displacement for Case I as a Function of $y/b$ for Various Values of $T_1$ . . . . .	62
Figure 4.4	The $v$ Displacement for Case I as a Function of $x/a$ for Various Values of $T_1$ . . . . .	63
Figure 4.5	The $v$ Displacement for Case I as a Function of $y/b$ for Various Values of $T_1$ . . . . .	64

Figure 4.6	Normalized Transverse Strain, $\epsilon_y$ , for (i) $T_o = 45^\circ, T_1 = 0^\circ$ and (ii) $T_o = 45^\circ, T_1 = 90^\circ$ Panels with $a/b = 1$ , as a Function of $x$ and $y$ . . . . .	66
Figure 4.7	Shear Strain, $\gamma_{xy}$ , for (i) $T_o = 45^\circ, T_1 = 0^\circ$ and (ii) $T_o = 45^\circ, T_1 = 90^\circ$ Panels with $a/b = 1$ , as a Function of $x$ and $y$ . . . . .	68
Figure 4.8	Shear Stress Resultant for (i) $T_o = 45^\circ, T_1 = 0^\circ$ and (ii) $T_o = 45^\circ, T_1 = 90^\circ$ Panels with $a/b = 1$ , as a Function of $x$ and $y$ . . . . .	69
Figure 4.9	Maximum Shear Stress Resultant for Case I as a Function of $T_1$ for Panels with $T_o = 45^\circ$ . . . . .	70
Figure 4.10	Axial Stress Resultant for (i) $T_o = 45^\circ, T_1 = 0^\circ$ and (ii) $T_o = 45^\circ, T_1 = 90^\circ$ Panels with $a/b = 1$ , as a Function of $x$ and $y$ . . . . .	72
Figure 4.11	Axial Stress Resultant as a Function of $x/a$ for (i) $T_1 \leq 45^\circ$ and (ii) $T_1 \geq 45^\circ$ . . . . .	73
Figure 4.12	Transverse Stress Resultant for (i) $T_o = 45^\circ, T_1 = 0^\circ$ and (ii) $T_o = 45^\circ, T_1 = 90^\circ$ Panels with $a/b = 1$ , as a Function of $x$ and $y$ . . . . .	75
Figure 4.13	Transverse Stress Resultant for Case I as a Function of $x/a$ for (i) $T_1 \leq 45^\circ$ and (ii) $T_1 \geq 45^\circ$ . . . . .	76
Figure 4.14	Comparison of $N_x$ for the Numerical and Closed Form Solutions for Panels with (i) $T_1 = 0^\circ$ and (ii) $T_1 = 90^\circ$ . . . . .	77
Figure 4.15	Equivalent Panel Stiffnesses for Case I for Straight and Curvilinear Fiber Panels. . . . .	79
Figure 4.16	Shear Stress Resultant Distribution for Different Aspect Ratios with (i) $T_1 = 0^\circ$ (at $x/a = 0.36$ ) and (ii) $T_1 = 90^\circ$ (at $x/a = 0.32$ ). . . . .	81
Figure 4.17	Axial Stress Resultant Distribution for Different Aspect Ratios with (i) $T_1 = 0^\circ$ and (ii) $T_1 = 90^\circ$ . . . . .	83
Figure 4.18	Transverse Stress Resultant Distribution for Different Aspect Ratios with (i) $T_1 = 0^\circ$ and (ii) $T_1 = 90^\circ$ . . . . .	84
Figure 4.19	Axial Displacement (i) and Axial Strain (ii) as a Function of $x/a$ for Case II Panels. . . . .	86
Figure 4.20	Transverse Stress Resultant as a Function of $x/a$ For Case II Panels with (i) $T_1 < 45^\circ$ and (ii) $T_1 > 45^\circ$ . . . . .	88
Figure 4.21	Equivalent Axial Stiffness for Variable and Straight Fiber Panels for Case II. . . . .	90
Figure 4.22	Normalized Axial Displacement as a Function of $x/a$ for Case III Panels. . . . .	92

Figure 4.23	Transverse Stress Resultant as a Function of $x/a$ For Case III Panels. . . . .	93
Figure 4.24	Equivalent Axial Stiffness for Variable and Straight Fiber Panels for Case III. . . . .	95
Figure 4.25	Normalized Axial Displacement as a Function of $x/a$ for Case IV Panels. . . . .	97
Figure 4.26	Comparison of the Axial Displacement Distributions for Case I and Case IV Panels with $T_1 = 0^\circ$ and $T_1 = 90^\circ$ . . . . .	98
Figure 4.27	Normalized Transverse Strain, $\epsilon_o$ , for Case IV Panels as a Function of $T_1$ . . . . .	99
Figure 4.28	Transverse Stress Resultant as a Function of $x/a$ For Case IV Panels with (i) $T_1 < 45^\circ$ and (ii) $T_1 > 45^\circ$ . . . . .	101
Figure 4.29	Comparison of the Transverse Stress Resultant Distributions for Case I and Case IV Panels with $T_1 = 0^\circ$ and $T_1 = 90^\circ$ . . . . .	102
Figure 4.30	Equivalent Axial Stiffness for Variable and Straight Fiber Panels for Case IV. . . . .	104
Figure 5.1	Panel $\bar{x}-\bar{y}$ and $x-y$ Coordinate Systems. . . . .	108
Figure 6.1	Critical Buckling Load as a Function of $T_o$ and $T_1$ for Case I ( $a/b = 1$ ). . . . .	122
Figure 6.2	Critical Load as a Function of Stiffness for Case I ( $a/b = 1$ ). . . . .	123
Figure 6.3	Critical Buckling Load as a Function of $T_o$ and $T_1$ for Case I ( $a/b = 2$ ). . . . .	125
Figure 6.4	Critical Load as a Function of Stiffness for Case I ( $a/b = 2$ ). . . . .	126
Figure 6.5	Critical Buckling Load as a Function of $T_o$ and $T_1$ for Case II ( $a/b = 1$ ). . . . .	128
Figure 6.6	Critical Load as a Function of Stiffness for Case II ( $a/b = 1$ ). . . . .	129
Figure 6.7	Critical Buckling Load as a Function of $T_o$ and $T_1$ for Case II ( $a/b = 2$ ). . . . .	131
Figure 6.8	Critical Load as a Function of Stiffness for Case II ( $a/b = 2$ ). . . . .	132
Figure 6.9	Critical Buckling Load as a Function of $T_o$ and $T_1$ for Case II ( $a/b = 0.5$ ). . . . .	134
Figure 6.10	Critical Load as a Function of Stiffness for Case II ( $a/b = 0.5$ ). . . . .	135

Figure 6.11	Critical Buckling Load as a Function of $T_0$ and $T_1$ for Case III ( $a/b = 1$ ).	137
Figure 6.12	Critical Load as a Function of Stiffness for Case III ( $a/b = 1$ ).	138
Figure 6.13	Critical Buckling Load as a Function of $T_0$ and $T_1$ for Case III ( $a/b = 2$ ).	140
Figure 6.14	Critical Load as a Function of Stiffness for Case III ( $a/b = 2$ ).	141
Figure 6.15	Critical Buckling Load as a Function of $T_0$ and $T_1$ for Case III ( $a/b = 0.5$ ).	143
Figure 6.16	Critical Load as a Function of Stiffness for Case III ( $a/b = 0.5$ ).	144
Figure 6.17	Critical Buckling Load as a Function of $T_0$ and $T_1$ for Case IV ( $a/b = 1$ ).	146
Figure 6.18	Critical Load as a Function of Stiffness for Case IV ( $a/b = 1$ ).	147
Figure 6.19	Critical Buckling Load as a Function of $T_0$ and $T_1$ for Case IV ( $a/b = 2$ ).	148
Figure 6.20	Critical Load as a Function of Stiffness for Case IV ( $a/b = 2$ ).	150
Figure 6.21	Critical Buckling Load as a Function of $T_0$ and $T_1$ for Case IV ( $a/b = 0.5$ ).	151
Figure 6.22	Critical Load as a Function of Stiffness for Case IV ( $a/b = 0.5$ ).	152
Figure 6.23	One Half-Wave Buckling Mode for Variable Stiffness Panels.	154
Figure 6.24	Two Half-Waves Buckling Mode for Variable Stiffness Panels.	155
Figure 6.25	Four Half-Waves Buckling Mode for Variable Stiffness Panels.	156

# CHAPTER 1

## The Variable Stiffness Design Concept

### 1.1 Introduction

During the last fifteen years, the use of fiber reinforced composites has begun to shift from strictly military applications to civil aerospace and automotive applications. The Office of Technology Assessment [1] and the Suppliers of Advanced Composite Materials Association [2] have cited innovative design techniques as one of the critical factors guiding the expanded use of composite materials. Under present market conditions, the structural gains from using composites must outweigh the added material and manufacturing costs involved. Therefore, designers must exploit every possible advantage inherent in the use of these materials. The design of composite structures involves more design variables than the design of metallic structures, and therefore provides more room for tailorability. With a traditional isotropic material design, aerospace structures often require the assembly of tens or even hundreds of metal parts. Design of aerospace structures with composite materials often results in lighter structures that need little, if any, assembly. However, the design of composite structures has traditionally been conservative, and the full potential of these materials has yet to be exploited.

A traditional composite lamina or sheet is made up of a thermosetting or thermoplastic polymer resin, in which very stiff straight fibers are embedded. The orientation of the high stiffness fibers determines the elastic behavior of the laminae. A laminate is simply a group of laminae bonded together. A laminate made up of three laminae is shown in Figure 1.1. The response for any of the layers shown in Figure 1.1 can be expressed in two different coordinate systems. In the first coordinate system, the 1 direction is defined as the direction parallel to the fibers; the 2 direction is perpendicular to the 1 direction in the plane of the lamina. The strength parameters of composite laminae always refer to the 1-2 coordinate system, so this system is important when predicting failure. The  $x$ - $y$  system runs parallel to the sides of the rectangular plate and is the reference frame for the loads that are to be applied. Therefore,  $\theta$  is the angle between the 1 direction and the  $x$  direction.

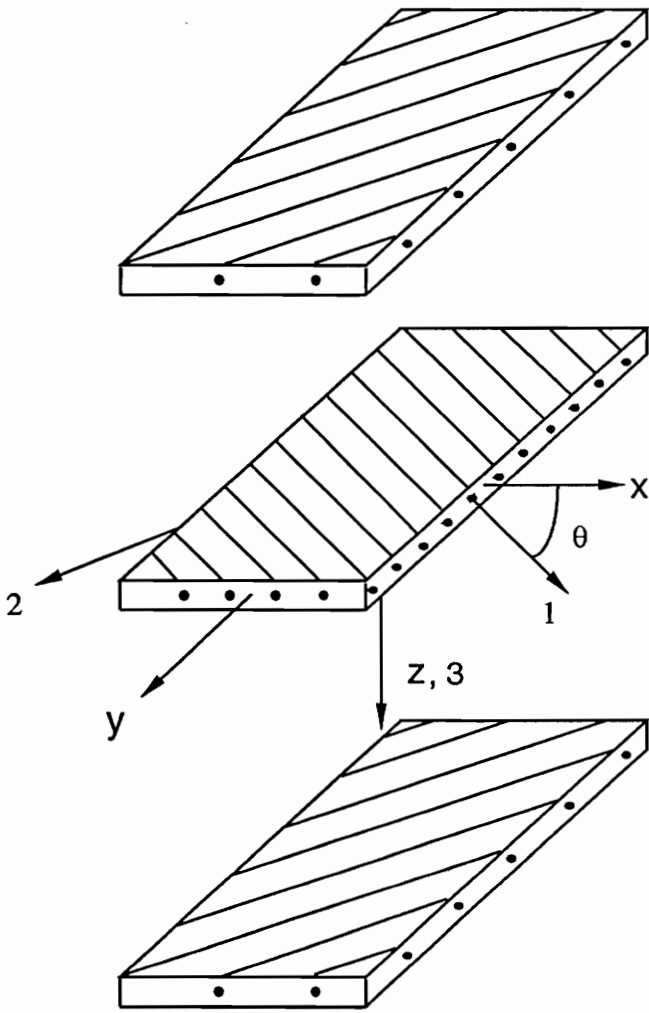


**Figure 1.1 Exploded View of a Conventional  $[\theta / -\theta / \theta]$  Laminate Lay-Up.**

In the design of composite panels, the traditional design variables have been ply thickness, ply orientation, stacking sequence, and even ply material. These parameters may be varied to obtain a desired strength or stiffness. Once cured, the laminate in Figure 1.1 will exhibit properties that are constant with respect to the coordinates  $x$  and  $y$ ; in the plane, the elastic behavior is governed by constants defined for the entire laminate.

The variable stiffness concept, which will be introduced in this chapter, yields elastic constants or plate stiffnesses are functions of the panel coordinates,  $x$  and  $y$ . By using this concept a designer may create a more efficient structure. There are several ways to obtain a variable stiffness configuration using composite materials. They are described in the next section. This work investigates the in-plane behavior of one type of variable stiffness panels, and presents methods of analysis for various boundary conditions and demonstrates gains that can be obtained by using this configuration, especially for buckling critical applications.

## 1.2 Overview of Variable Stiffness Structures

Works suggesting the use of variable stiffnesses in order to tailor a structure to a particular application began appearing about thirty years ago. This early research mainly focused on the formulation of theoretical models in which the elastic properties are non-homogeneous. Since most of these investigations were carried out before great advances in digital computing, they often lack analytical results or illustrative examples. Works published in the last ten years make extensive use of digital computers, and are therefore better able to illustrate some of the advantages of the variable stiffness concept.

### 1.2.1 Early Research

One of the earliest works addressing the variable stiffness concept is by Mishiku and Teodosiu [3], in which the general solution for a static plane elastic problem assuming non-homogeneous elastic properties is derived. A technique of successive approximations is employed using the theory of complex variables and the theory of elasticity. The inhomogeneity within an isotropic material is designed to model damage, imperfections, or variations in the modulus due to temperature changes. It is shown that for an axisymmetrically loaded cylindrical vessel, large variations in the stresses

arise when the modulus changes around the circumference. Although the loading is axisymmetric, the shear stress  $\tau_{r,\theta}$  develops due to the changes in stiffness.

As composites became more widely used in military applications, researchers began to see their potential for stiffness tailorability. The concept that the stiffness of a fiber reinforced composite structure should be tailored to satisfy a set of constraints is articulated in a 1969 study by Pao [4]. The concept proposed in Ref. 4 is well suited for application to shell problems. Pressure vessels often take the form of cylinders, since this shape is ideal for pressure loads and is easy to manufacture. However, the ends, or bulkheads, of the vessel are difficult to design. Since there is a mismatch in the deformations of the cylindrical part of the vessel and the bulkhead, and the pressure load is redistributed due to the change in geometry, bulkheads are subject to large bending moments. Pao has derived the governing equation which, when solved for the moduli and Poisson's ratio, results in a bulkhead design with no bending moments. The resulting moduli and Poisson's ratio are functions of the shell coordinates. The possible variations in the elastic properties are analyzed as functions of the vessel geometry. Pao suggested using a variable fiber volume fraction laminates in order to obtain the variable stiffnesses.

Many aerospace applications require structures that vary in thickness. These structures also exhibit variable stiffness. Ashton [5] published a study detailing the stability analysis of tapered anisotropic plates. A series approximation is used to describe the bending stiffnesses as functions of the plate coordinates. The Ritz method is used to find the critical load, and closed form solutions are presented for the integrals that define the bending potential energy. The main objective of the study was the application of the Ritz method to a non-conventional problem; therefore, the local stress analysis of the tapered geometry is ignored.

The use of the variable stiffness concept in shell structures has also been investigated by Leissa and Vagins [6]. Their work proposes varying the stiffness of a structure in order to obtain a homogeneous stress field. For example, hoop stresses arise when a pressure vessel is loaded hydrostatically or a disk is spun about its polar axis. Generally, these stresses vary as functions of the radial direction. For example, in a thick isotropic cylinder loaded under internal pressure, the hoop stresses are high near the inner radius and very low close to the outer radius. The same is true for the rotating disk,

where the stresses are due to the centrifugal body forces. Leissa and Vagins argue that this stress distribution does not utilize the material efficiently because the material close to the inner radius carries most of the load. A constant hoop stresses through the vessel cross section is a better design. The governing equations that must be satisfied to achieve a homogeneous stress state are presented, along with their solution for different cylinder and disk geometries. The issue of how to actually manufacture cylinders and disks with variable moduli is not addressed.

## 1.2.2 Recent Research

When stiffness or strength tailoring of composite panels has been necessary, engineers have resorted to what is known as the dropped ply. A dropped ply is a ply that does not run continuously throughout the panel, but instead is terminated within the panel to achieve a reduction in stiffness and thickness. For example, an aircraft wing is thicker at the root than at the tip; if laminated composites are being used, the best way to achieve this is to terminate plies internally within the structure. The dropped ply, however, complicates the analysis. A dropped ply causes the formation of resin rich areas around the ply drop. In addition, dropped plies give rise to large interlaminar stresses due to the stiffness gradient and the changes in geometry. Kemp and Johnson [7] have shown this to be the cause of a low strain to failure for panels with dropped plies. However, DiNardo and Lagace [8] have shown that stress concentration due to the ply drop-off plays an insignificant role in the buckling load of these panels. Instead, the main parameter affecting the buckling mode and critical load is the change in stiffness that results from the dropped plies. The effect of the change in stiffness has been isolated by analyzing laminates in which some of the internal layers are divided into two parts with different stiffnesses. Instead of having a continuous ply, their analysis considered a layer which is made up of two plies with different fiber angles, joined together so that there is no change in thickness, only a change in stiffness. These angle-change plates exhibited a buckling response similar to that of the plates with ply drop-offs. DiNardo has shown that for the angle-change plates and the ply drop-off plates, the Ritz method accurately predicts the buckling load, but for extreme changes in stiffness it fails to predict the buckling mode.

There are few alternatives to stiffness tailoring via ply drop-offs. For composite laminae Leissa and Martin [9] have introduced the concept of using a variable fiber volume fraction for stiffness

tailoring. The fibers in any of the layers in Figure 1.1 are parallel and equally spaced. Therefore, the ratio of the volume occupied by fibers to that occupied by the polymer resin remains constant for any cross section. Varying the spacing of the fibers within a layer so that there are areas where the fibers are closely packed and areas where they are sparsely packed, results in a variable fiber volume fraction. If the fiber volume fraction is varied, the stiffnesses of the composite sheet also vary. Leissa and Martin present a study of how variations in the fiber volume fraction affect the elastic constants. The fiber volume fraction is allowed to vary as a polynomial function of one coordinate only. The in-plane behavior is analyzed by applying the Ritz method. As expected, by varying the fiber volume fraction, large gradients in the stresses arise. Although the loading condition is uniaxial compression, a large shear stress also develops. Estimates of the natural frequencies and critical buckling load are also obtained by using the Ritz method. By choosing a configuration in which most of the fibers are embedded near the center of the plate, an increase of 20% in the critical buckling load and natural frequencies are obtained.

An alternative to the tapered geometry and the variable fiber volume fraction is the curvilinear fiber format. As the name suggests, the fibers in the composite are not straight, but follow curved paths instead. As mentioned before, the stiffnesses of the panel in Figure 1.1 are determined by the angle  $\theta$ . If the angle  $\theta$  is allowed to vary as a function of the coordinates  $x$  and  $y$ , the stiffnesses will also vary as functions of  $x$  and  $y$ . An interesting application of this concept has been proposed by Kuo, et. al. [10]. If Kevlar fibers that follow a sinusoidal path are embedded in an elastomeric polymer matrix, large deformations are possible due to the fiber configuration and the material properties of the matrix. When loaded in tension, the fibers will tend to align themselves with the loading direction, and the composite sheet will exhibit enhanced stiffness as it is stretched. The analysis is inherently non-linear, and a step-wise technique is used to determine the changes in the fiber geometry as the load is increased. Different wave geometries and matrix/fiber properties are considered. The numerical model indeed predicts a stiffening of the composite as the applied strain increases. Furthermore, there is a high energy associated with deformation. The author proposes optimizing the fiber arrangement to obtain a tailored elastic response.

One of the most recent studies using the curvilinear fiber format has been undertaken by Hyer and Charette [11]. They have studied location-dependent stiffnesses to obtain improvements in the

strength of laminates with central holes analyzed with a finite element technique. The direction of the fibers varied as a function of the spatial position in the panel. The fiber orientation in each of the finite elements is constant, but varies from one element to another to match the location of the principal stress direction at one of the gauss points. The fiber angles are determined using an iterative technique and are piecewise functions of the  $x$  and  $y$  coordinates. By combining variable stiffness layers with straight fiber layers, the location of failure is moved away from the hole edge, and the ultimate load is increased by 60% over a quasi-isotropic straight-fiber baseline design. However, there is a decrease of 13% in the critical buckling load.

### 1.3 Variable Stiffness in This Investigation

Recent developments in manufacturing techniques, such as computer controlled three-axes filament winding, tape-laying machines, and fiber and tow placement technology, make it possible to fabricate composite panels that utilize the curvilinear fiber concept. In this work the linear elastic response of panels made from curvilinear plies is examined. However, as a consequence of practical limitations on processing techniques that result in fiber patterns that are parallel to one another, the fiber orientation is made to vary only along the one of the coordinates. In this work, a linear variation of  $\theta$  with respect to  $x$  has been chosen. The reason behind this choice is that with a linear function closed form solutions may be obtained for the elastic response. In addition, it greatly simplifies the buckling analysis. This work presents the analysis of variable stiffness panels having a  $[\pm\theta]_{ns}$  stacking sequence. This stacking sequence is symmetric and balanced so that the analysis can be further simplified.

The angle variation is therefore described by the equation,

$$\theta(x) = \begin{cases} \frac{2(T_1 - T_0)}{a}x + T_0 & 0 \leq x \leq \frac{a}{2} \\ \frac{2(T_0 - T_1)}{a}x + T_0 & -\frac{a}{2} \leq x < 0 \end{cases}, \quad (1.1)$$

where  $a$  is the total length of the panel in the  $x$  direction (its width is given by  $b$ ),  $T_0$  is the angle at  $x = 0$ , and  $T_1$  the angle at  $x = a/2$ . The fiber orientation is symmetric with respect to the midlength of the panel ( $x = 0$ ). The fiber paths are therefore smooth antisymmetric functions of

the  $x$  coordinate and are defined by,

$$y = \begin{cases} \frac{-a \log \left[ \cos \left[ T_0 + \frac{2(T_1 - T_0)x}{a} \right] \right]}{2(T_1 - T_0)} + C & 0 \leq x \leq \frac{a}{2} \\ \frac{a \log \left[ \cos \left[ T_0 + \frac{2(T_0 - T_1)x}{a} \right] \right]}{2(T_0 - T_1)} + C & -\frac{a}{2} \leq x < 0 \end{cases} \quad (1.2)$$

Although at the outset the limitations on the fiber orientations may seem too restrictive, it is possible to generate panels with a wide range of properties. For example, two of the angle variations and panel laminations are presented in Figure 1.2 for different values of  $T_1$ , with  $T_0 = 45^\circ$ . With this configuration, the stiffnesses of each layer are functions of  $x$  due to the curvilinear paths followed by the high stiffness fibers. There is no variation of the stiffnesses in the  $y$  direction. The laminate configurations shown in the figure correspond to a  $[\pm\theta(x)]_{ns}$  lay-up. Under uniaxial compression in the  $x$  direction, panel (i) exhibits an area of high stiffness around  $x = \pm a/4$  because the fibers are aligned with the load; for panel (ii) the high stiffness area is located around  $x = \pm a/2$ . A panel with  $T_0 = T_1$  would have straight fibers and would exhibit constant stiffnesses with respect to  $x$  and  $y$ .

## 1.4 Approach

The purpose of this work is to address the in-plane and buckling response of panels that have a variable stiffness configuration. Four sets of boundary conditions and three panel aspect ratios are considered. The solution of the in-plane problem is obtained through two different techniques. The first technique involves applying collocation to solve the equilibrium equations for the displacements; the strains and stress resultants are subsequently calculated. The second technique utilizes symbolic manipulation in order to find closed form expressions for the displacements, strains and stress resultants. Three of the four closed-form solutions are exact. With the in-plane problem solved, the buckling analysis is undertaken by using the Ritz method. Symbolic manipulation is used to find the stiffness matrix, while a numerical technique is used to calculate the geometric stiffness matrix for each set of boundary conditions.

Three chapters and an appendix in this work are devoted to describing the analysis of the variable stiffness panels, while two chapters present the results obtained using these analysis techniques. A review of the Classical Lamination Theory for layered orthotropic materials is given in Chapter 2. The theory is extended to the variable stiffness configuration and four effective material properties

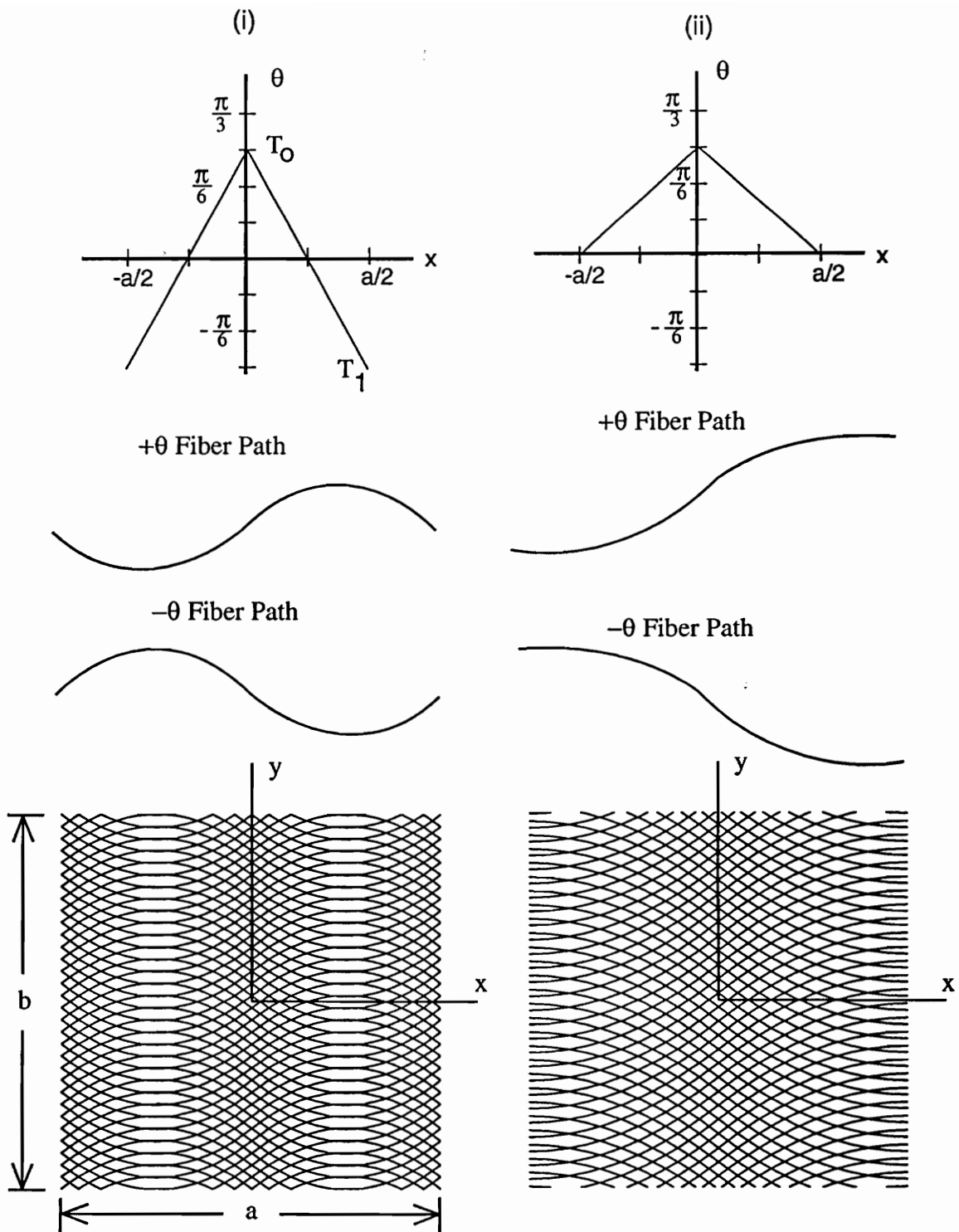


**Figure 1.2** Fiber Orientation, Fiber Paths, and  $[\pm\theta]_{ns}$  Laminate Configuration for (i)  $T_0 = 45^\circ$ ,  $T_1 = -45^\circ$  and (ii)  $T_0 = 45^\circ$ ,  $T_1 = 0^\circ$

are introduced. In Chapter 3, the governing equations for variable stiffness panels are derived and the four boundary conditions that are to be analyzed are defined. The numerical solution, which utilizes Hermite Collocation to solve the governing equations, is described in detail. Closed form solutions are developed for all four sets of boundary conditions.

The results section of this work begins with Chapter 4, where the in-plane response of the variable stiffness panels is analyzed using the techniques presented in Chapter 3. Six variable stiffness configurations are discussed, and results for three different panel aspect ratios are presented. In Chapter 5 the theory that governs the buckling behavior of the variable stiffness panels is introduced. The Ritz Method is used here to find the buckling load, and most of the chapter is dedicated to adapting this method to the variable stiffness problem. Tedious derivations necessary for the analysis have been placed in Appendix 1. In Chapter 6, the buckling response of the variable stiffness panels is analyzed for the four sets of boundary conditions. Emphasis is placed on finding variable stiffness configurations that have high buckling loads. Finally, major conclusions are reviewed in Chapter 7, along with suggestions for future work with this concept.

# CHAPTER 2

## Laminate Theory for Variable Stiffness Panels

### 2.1 Lamina Constitutive Relations

The elastic behavior of orthotropic materials is governed by nine elastic constants. For plane elastic problems only six elastic constants are relevant. For composite materials this number reduces to four because the material is orthotropic and there is no extension-shear coupling. The material constants for a composite material are modulus in the 1 direction,  $E_1$ , the modulus in the 2 direction,  $E_2$ , Poisson's ratio,  $\nu_{12}$ , and the shear modulus,  $G_{12}$ . When a lamina is loaded in a direction other than either the 1 or 2 directions, its response can be obtained by the use of strain and stress transformations. When many laminae are bonded together to form a laminate, their collective response is obtained by using lamination theory.

The results presented herein are based on a four layer  $[\pm\theta]_s$  graphite-epoxy laminate having  $E_1 = 26.25$  Msi,  $E_2 = 1.49$  Msi,  $G_{12} = 1.04$  Msi, and  $\nu_{12} = 0.28$ , with a layer thickness of 0.005 in. (hence  $h = 0.02$  in.).

#### 2.1.1 Straight Fiber Lamina

For a lamina assumed to be in a plane stress state (e.g.,  $\sigma_3 = \sigma_z = 0$ ), the strain-stress relation for the 1-2 coordinate system is given by

$$\begin{Bmatrix} \epsilon_1 \\ \epsilon_2 \\ \gamma_{12} \end{Bmatrix} = \begin{bmatrix} \frac{1}{E_1} & -\frac{\nu_{12}}{E_1} & 0 \\ -\frac{\nu_{12}}{E_1} & \frac{1}{E_2} & 0 \\ 0 & 0 & \frac{1}{G_{12}} \end{bmatrix} \begin{Bmatrix} \sigma_1 \\ \sigma_2 \\ \tau_{12} \end{Bmatrix}. \quad (2.1)$$

However, often the strains are the known quantities, and the above expression is more useful in its inverted form,

$$\begin{Bmatrix} \sigma_1 \\ \sigma_2 \\ \tau_{12} \end{Bmatrix} = \begin{bmatrix} Q_{11} & Q_{12} & 0 \\ Q_{12} & Q_{22} & 0 \\ 0 & 0 & Q_{66} \end{bmatrix} \begin{Bmatrix} \epsilon_1 \\ \epsilon_2 \\ \gamma_{12} \end{Bmatrix}, \quad (2.2)$$

where the reduced stiffnesses  $Q_{ij}$  are defined in terms of the material properties as,

$$Q_{11} = \frac{E_1}{1 - \nu_{12}\nu_{21}}, \quad (2.3)$$

$$Q_{12} = \frac{\nu_{12}E_2}{1 - \nu_{12}\nu_{21}}, \quad (2.4)$$

$$Q_{22} = \frac{E_2}{1 - \nu_{12}\nu_{21}}, \quad (2.5)$$

$$Q_{66} = G_{12}. \quad (2.6)$$

If all the layers in a laminate are made of the same material, the stress-strain relations in the 1-2 system will be the same for all layers, regardless of their individual orientation. The constitutive relation in the  $x$ - $y$  system can be obtained by applying coordinate transformations to equation 2.2. It is given by,

$$\begin{Bmatrix} \sigma_x \\ \sigma_y \\ \tau_{xy} \end{Bmatrix} = \begin{bmatrix} \bar{Q}_{11} & \bar{Q}_{12} & \bar{Q}_{16} \\ \bar{Q}_{12} & \bar{Q}_{22} & \bar{Q}_{26} \\ \bar{Q}_{16} & \bar{Q}_{26} & \bar{Q}_{66} \end{bmatrix} \begin{Bmatrix} \epsilon_x \\ \epsilon_y \\ \gamma_{xy} \end{Bmatrix}, \quad (2.7)$$

where the matrix  $[\bar{Q}]$  is obtained by a transformation of  $[Q]$  as,

$$[\bar{Q}] = [T]^{-1}[Q][T]^{-T}. \quad (2.8)$$

The elements of the transformation matrix  $[T]$  are trigonometric functions of  $\theta$ , such that  $[T] = [T(\theta)]$ ; the elements of the matrix are given in Ref. [12]. Each layer will therefore have a different matrix  $[\bar{Q}]$ , depending on the angle  $\theta$ . Finally, the strains in equation 2.7 are given by the linear strain-displacement relationship,

$$\begin{Bmatrix} \epsilon_x \\ \epsilon_y \\ \gamma_{xy} \end{Bmatrix} = \begin{Bmatrix} \frac{\partial u}{\partial x} \\ \frac{\partial v}{\partial y} \\ \frac{\partial u}{\partial y} + \frac{\partial v}{\partial x} \end{Bmatrix}. \quad (2.9)$$

The shear strain  $\gamma_{xy}$  is the engineering shear strain and not the tensorial strain.

## 2.1.2 Curvilinear Fiber Lamina

The constitutive relations described above can be applied to lamina with curvilinear fibers by making very simple modifications. Recall that the fiber angle for a curvilinear lamina is defined as a function of  $x$ , as given in equation 1.1. The 1-2 system constitutive relations remain the same, but the  $x$ - $y$  constitutive relations change because the fiber angle,  $\theta$ , is a function of the  $x$  coordinate. Therefore, the reduced stiffness matrix is also a function of  $x$ ,  $[\bar{Q}] = [\bar{Q}(\theta)] = [\bar{Q}(x)]$ , or

$$\begin{Bmatrix} \sigma_x \\ \sigma_y \\ \tau_{xy} \end{Bmatrix} = \begin{bmatrix} \bar{Q}_{11}(x) & \bar{Q}_{12}(x) & \bar{Q}_{16}(x) \\ \bar{Q}_{12}(x) & \bar{Q}_{22}(x) & \bar{Q}_{26}(x) \\ \bar{Q}_{16}(x) & \bar{Q}_{26}(x) & \bar{Q}_{66}(x) \end{bmatrix} \begin{Bmatrix} \epsilon_x \\ \epsilon_y \\ \gamma_{xy} \end{Bmatrix}. \quad (2.10)$$

The strain-displacement relations remain as given by equation 2.9.

## 2.2 Classical Lamination Theory

The response of conventional (constant stiffness) thin composite plates can be accurately obtained by using Classical Lamination Theory (CLT) [12,13]. CLT will be used to analyze the variable stiffness panels.

### 2.2.1 Kinematics

The kinematic assumptions of CLT are that the bonds between layers are perfect and infinitesimally thin and that straight lines normal to the laminate midplane remain straight and normal after deformation. In addition, there is no stretching or shrinking in the  $z$  direction, or  $\epsilon_z = 0$ . The displacements at any point in the laminate are therefore given by,

$$u = u^\circ - z \frac{\partial w}{\partial x}, \quad (2.11)$$

$$v = v^\circ - z \frac{\partial w}{\partial y}, \quad (2.12)$$

$$w = w^\circ, \quad (2.13)$$

where the terms  $u^\circ$ ,  $v^\circ$ , and  $w^\circ$  indicate the axial, transverse, and out-of-plane midplane displacements, respectively. The partial derivatives with respect to  $w$  denote the rotations of the midplane. Substituting equations 2.11-2.13 into equation 2.7 results in the following constitutive relation for the  $k^{th}$  layer,

$$\begin{Bmatrix} \sigma_x \\ \sigma_y \\ \tau_{xy} \end{Bmatrix}_k = \begin{bmatrix} \bar{Q}_{11}(x) & \bar{Q}_{12}(x) & \bar{Q}_{16}(x) \\ \bar{Q}_{12}(x) & \bar{Q}_{22}(x) & \bar{Q}_{26}(x) \\ \bar{Q}_{16}(x) & \bar{Q}_{26}(x) & \bar{Q}_{66}(x) \end{bmatrix}_k \begin{Bmatrix} \epsilon_x^\circ + z\kappa_x \\ \epsilon_y^\circ + z\kappa_y \\ \gamma_{xy}^\circ + z\kappa_{xy} \end{Bmatrix}. \quad (2.14)$$

The  $\kappa$ 's are the curvatures of the midplane and are defined by,

$$\begin{Bmatrix} \kappa_x \\ \kappa_y \\ \kappa_{xy} \end{Bmatrix} = \begin{Bmatrix} -\frac{\partial^2 w}{\partial x^2} \\ -\frac{\partial^2 w}{\partial y^2} \\ -2\frac{\partial^2 w}{\partial y \partial x} \end{Bmatrix}. \quad (2.15)$$

### 2.2.2 Stress and Moment Resultants

Instead of dealing with the stresses in the individual layers, one advantage of CLT is that stress and moment resultants are used to define the stress state for the laminate. The stress resultants

reflect the average stress per unit length at different points in the laminate, and are given by,

$$\begin{Bmatrix} N_x \\ N_y \\ N_{xy} \end{Bmatrix} = \int_{-h/2}^{h/2} \begin{Bmatrix} \sigma_x \\ \sigma_y \\ \tau_{xy} \end{Bmatrix} dz = \sum_{k=1}^N \int_{z_{k-1}}^{z_k} \begin{Bmatrix} \sigma_x \\ \sigma_y \\ \tau_{xy} \end{Bmatrix} dz. \quad (2.16)$$

Similarly, for loads that cause bending, the moment resultants are defined as the local bending moment per unit length. The positive direction for the stress and moment resultants acting on a plate element are shown in Figure 2.1. Also shown is the laminate stacking sequence configuration, where  $h$  is the total thickness of the laminate, and the coordinate of the bottom and top edges of the  $k^{\text{th}}$  layer are denoted by  $z_k$  and  $z_{k-1}$ , respectively.

By substituting equation 2.14 into equation 2.16, the following expression is obtained,

$$\begin{Bmatrix} N_x \\ N_y \\ N_{xy} \end{Bmatrix} = \sum_{k=1}^N \int_{z_{k-1}}^{z_k} \begin{bmatrix} \bar{Q}_{11} & \bar{Q}_{12} & \bar{Q}_{16} \\ \bar{Q}_{12} & \bar{Q}_{22} & \bar{Q}_{26} \\ \bar{Q}_{16} & \bar{Q}_{26} & \bar{Q}_{66} \end{bmatrix}_k \left\{ \int_{z_{k-1}}^{z_k} \begin{Bmatrix} \epsilon_x^o \\ \epsilon_y^o \\ \gamma_{xy}^o \end{Bmatrix} dz + \int_{z_{k-1}}^{z_k} \begin{Bmatrix} \kappa_x \\ \kappa_y \\ \kappa_{xy} \end{Bmatrix} z dz \right\}. \quad (2.17)$$

In the above equation, matrix  $[\bar{Q}]$  is a function of  $x$ , but the notation of equation 2.10 has been dropped for the sake of simplicity. Since the midplane strains and curvatures are constant with respect to  $z$ , they can be moved outside of the integral. After rearranging, the expression for the vector  $\{N\}$  is given by

$$\begin{Bmatrix} N_x \\ N_y \\ N_{xy} \end{Bmatrix} = \begin{bmatrix} A_{11} & A_{12} & A_{16} \\ A_{12} & A_{22} & A_{26} \\ A_{16} & A_{26} & A_{66} \end{bmatrix} \begin{Bmatrix} \epsilon_x^o \\ \epsilon_y^o \\ \gamma_{xy}^o \end{Bmatrix} + \begin{bmatrix} B_{11} & B_{12} & B_{16} \\ B_{12} & B_{22} & B_{26} \\ B_{16} & B_{26} & B_{66} \end{bmatrix} \begin{Bmatrix} \kappa_x \\ \kappa_y \\ \kappa_{xy} \end{Bmatrix}, \quad (2.18)$$

where

$$A_{ij} = \sum_{k=1}^N (\bar{Q}_{ij})_k (z_k - z_{k-1}) \quad \begin{matrix} i = 1, 2, 6 \\ j = 1, 2, 6 \end{matrix} \quad (2.19)$$

and

$$B_{ij} = \frac{1}{2} \sum_{k=1}^N (\bar{Q}_{ij})_k (z_k^2 - z_{k-1}^2) \quad \begin{matrix} i = 1, 2, 6 \\ j = 1, 2, 6 \end{matrix} \quad (2.20)$$

The definition of the moment resultants is similar to the definition for stress resultants and is expressed as,

$$\{M\} = \int_{-h/2}^{h/2} \{\sigma\} z dz, \quad (2.21)$$

which is analogous to equation 2.16. By a similar procedure the moment resultants can be expressed as

$$\begin{Bmatrix} M_x \\ M_y \\ M_{xy} \end{Bmatrix} = \begin{bmatrix} D_{11} & D_{12} & D_{16} \\ D_{12} & D_{22} & D_{26} \\ D_{16} & D_{26} & D_{66} \end{bmatrix} \begin{Bmatrix} \epsilon_x^o \\ \epsilon_y^o \\ \gamma_{xy}^o \end{Bmatrix} + \begin{bmatrix} D_{11} & D_{12} & D_{16} \\ D_{12} & D_{22} & D_{26} \\ D_{16} & D_{26} & D_{66} \end{bmatrix} \begin{Bmatrix} \kappa_x \\ \kappa_y \\ \kappa_{xy} \end{Bmatrix}, \quad (2.22)$$

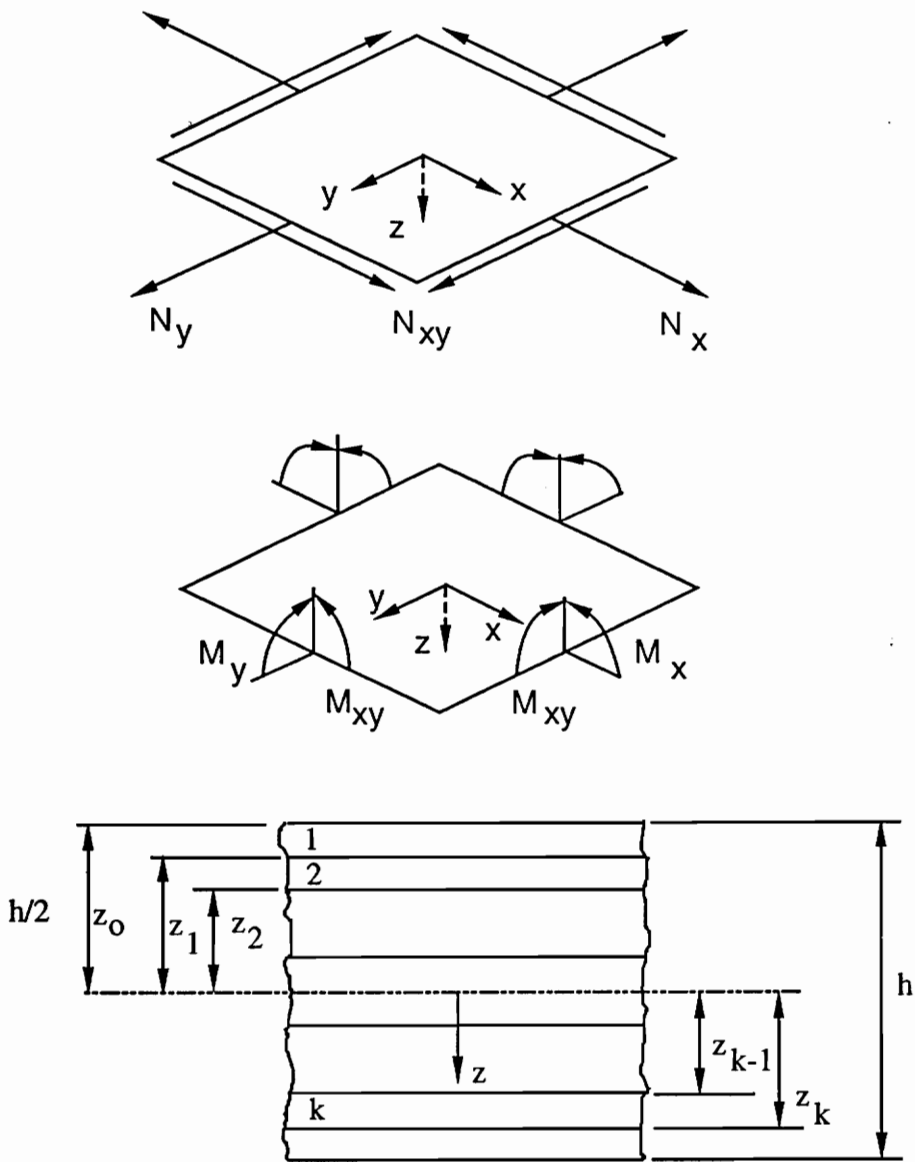


**Figure 2.1** Stress Resultants, Moment Resultants and Laminate Configuration (Ref.[12]).

where

$$D_{ij} = \frac{1}{3} \sum_{k=1}^N (\bar{Q}_{ij})_k (z_k^3 - z_{k-1}^3) \quad \begin{matrix} i = 1, 2, 6 \\ j = 1, 2, 6 \end{matrix} \quad (2.23)$$

The elements of the [A], [B], and [D] matrices are called the extensional, coupling, and bending stiffnesses, because they govern the response due to in-plane strain, coupling between extension and twisting, and bending, respectively. The response of the panel is obtained in terms of the midplane strains and curvatures, and equation 2.14 is used to obtain the the response of the individual plies. The stresses or strains can then be transformed to the 1-2 coordinate system in order to evaluate the strength.

### 2.2.3 The Material Invariants

Tsai and Pagano[14] have proposed a simple method for calculating the matrices [A], [B] and [D]. A set of material invariants is defined as,

$$U_1 = \frac{3Q_{11} + 3Q_{22} + 2Q_{12} + 4Q_{66}}{8}, \quad (2.24)$$

$$U_2 = \frac{Q_{11} - Q_{22}}{2}, \quad (2.25)$$

$$U_3 = \frac{Q_{11} + Q_{22} - 2Q_{12} - 4Q_{66}}{8}, \quad (2.26)$$

$$U_4 = \frac{Q_{11} + Q_{22} + 6Q_{12} - 4Q_{66}}{8}, \quad (2.27)$$

$$U_5 = \frac{Q_{11} + Q_{22} - 2Q_{12} + 4Q_{66}}{8}. \quad (2.28)$$

The CLT matrices can then be expressed as,

$$[\mathbf{A}, \mathbf{B}, \mathbf{D}] = \begin{bmatrix} U_1 V_0 + U_2 V_1 + U_3 V_3 & U_4 V_0 - U_3 V_3 & -(1/2)U_2 V_2 - U_3 V_4 \\ (Symmetric) & U_1 V_0 - U_2 V_1 + U_3 V_3 & -(1/2)U_2 V_2 + U_3 V_4 \\ & & U_5 V_0 - U_3 V_3 \end{bmatrix}, \quad (2.29)$$

where,

$$V_0\{A,B,D\} = \{h, 0, \frac{h^3}{12}\}, \quad (2.30)$$

$$V_1\{A,B,D\} = \int_{-\frac{h}{2}}^{\frac{h}{2}} \cos(2\theta) \{1, z, z^2\} dz, \quad (2.31)$$

$$V_2\{A,B,D\} = \int_{-\frac{h}{2}}^{\frac{h}{2}} \sin(2\theta) \{1, z, z^2\} dz, \quad (2.32)$$

$$V_{3\{A,B,D\}} = \int_{-\frac{h}{2}}^{\frac{h}{2}} \cos(4\theta) \{1, z, z^2\} dz, \quad (2.33)$$

$$V_{4\{A,B,D\}} = \int_{-\frac{h}{2}}^{\frac{h}{2}} \sin(4\theta) \{1, z, z^2\} dz. \quad (2.34)$$

In this work, only symmetric angle-ply laminates ( $[\pm\theta]_{ns}$ ) are being considered. Due to the symmetry of the stacking sequence,  $[\mathbf{B}] = \mathbf{0}$ . In addition, since the stacking sequence is balanced,  $A_{16} = A_{26} = 0$ . Therefore,  $[\mathbf{A}]$  reduces to

$$[\mathbf{A}] = h \begin{bmatrix} U_1 & U_4 & 0 \\ U_4 & U_1 & 0 \\ 0 & 0 & U_5 \end{bmatrix} + h \begin{bmatrix} U_2 & 0 & 0 \\ 0 & -U_2 & 0 \\ 0 & 0 & 0 \end{bmatrix} \cos(2\theta) + h \begin{bmatrix} U_3 & -U_3 & 0 \\ -U_3 & U_3 & 0 \\ 0 & 0 & -U_3 \end{bmatrix} \cos(4\theta), \quad (2.35)$$

where  $\theta = \theta(x)$ .

For the in-plane response of the laminate, the constitutive relation simplifies to

$$\begin{Bmatrix} N_x \\ N_y \\ N_{xy} \end{Bmatrix} = \begin{bmatrix} A_{11} & A_{12} & 0 \\ A_{12} & A_{22} & 0 \\ 0 & 0 & A_{66} \end{bmatrix} \begin{Bmatrix} \epsilon_x^0 \\ \epsilon_y^0 \\ \gamma_{xy}^0 \end{Bmatrix}, \quad (2.36)$$

where the elements of the matrix  $[\mathbf{A}]$  are functions of  $x$ . The bending response is uncoupled from the in-plane response and is given by

$$\begin{Bmatrix} M_x \\ M_y \\ M_{xy} \end{Bmatrix} = \begin{bmatrix} D_{11} & D_{12} & D_{16} \\ D_{12} & D_{22} & D_{26} \\ D_{16} & D_{26} & D_{66} \end{bmatrix} \begin{Bmatrix} \kappa_x \\ \kappa_y \\ \kappa_{xy} \end{Bmatrix}. \quad (2.37)$$

The application of the Classical Lamination Theory to variable stiffness panels involves first obtaining the displacement fields for the given configuration and boundary conditions. The stresses and stress resultants can then be obtained. For the buckling analysis, the configuration, boundary conditions and bending stiffnesses determine the critical load and mode shapes.

## 2.2.4 Effective Material Properties

If the in-plane response of a laminate is being considered, it is useful to analyze the stiffness of the panel by using effective material properties that are analogous to  $E_1$ ,  $E_2$ ,  $\nu_{12}$ , and  $G_{12}$ . The in-plane constitutive relation can be inverted and expressed as,

$$\begin{Bmatrix} \epsilon_x^0 \\ \epsilon_y^0 \\ \gamma_{xy}^0 \end{Bmatrix} = \frac{1}{A_{11}A_{22} - A_{12}^2} \begin{bmatrix} A_{22} & -A_{12} & 0 \\ -A_{12} & A_{11} & 0 \\ 0 & 0 & \frac{A_{11}A_{22} - A_{12}^2}{A_{66}} \end{bmatrix} \begin{Bmatrix} N_x \\ N_y \\ N_{xy} \end{Bmatrix}. \quad (2.38)$$

The stress resultant vector  $\{N\}$  has units of force per unit length; if it is divided by the panel thickness  $h$ , the units of the resulting vector are force per unit length squared, which are the units of stress. A pseudo-stress vector  $\{\sigma^*\}$ , may therefore be defined as,

$$\begin{Bmatrix} \sigma_x^* \\ \sigma_y^* \\ \tau_{xy}^* \end{Bmatrix} = \frac{1}{h} \begin{Bmatrix} N_x \\ N_y \\ N_{xy} \end{Bmatrix}. \quad (2.39)$$

By substituting the pseudo-stress vector into equation 2.38, the inverted constitutive equation becomes,

$$\begin{Bmatrix} \epsilon_x^o \\ \epsilon_y^o \\ \gamma_{xy}^o \end{Bmatrix} = \frac{1}{h(A_{11}A_{22} - A_{12}^2)} \begin{bmatrix} A_{22} & -A_{12} & 0 \\ -A_{12} & A_{11} & 0 \\ 0 & 0 & \frac{A_{11}A_{22} - A_{12}^2}{A_{66}} \end{bmatrix} \begin{Bmatrix} \sigma_x^* \\ \sigma_y^* \\ \tau_{xy}^* \end{Bmatrix}. \quad (2.40)$$

An analogy may now be drawn between equation 2.40 and equation 2.1 by looking at the elements of equation 2.40 as the compliances of the entire panel. Therefore, the effective  $x$  direction modulus is defined as,

$$E_x(x) = \frac{A_{11}A_{22} - A_{12}^2}{hA_{22}}. \quad (2.41)$$

For variable stiffness panels, it is defined as a function of  $x$  and reflects the effective local modulus of the panel in the  $x$  direction. Similarly, a  $y$  direction effective modulus is defined by,

$$E_y(x) = \frac{A_{11}A_{22} - A_{12}^2}{hA_{11}}. \quad (2.42)$$

An effective Poisson's ratio is defined by

$$\nu_{xy}(x) = \frac{A_{12}}{A_{22}}. \quad (2.43)$$

This quantity reflects the amount of free strain in the  $y$  direction obtained from either tension or compression in the  $x$  direction. For variable stiffness panels, it is also a function of  $x$ . Similarly the minor Poisson's ratio,  $\nu_{yx}$ , which is given by

$$\nu_{yx}(x) = \frac{A_{12}}{A_{11}} = \nu_{xy} \frac{E_y}{E_x}, \quad (2.44)$$

determines the amount of strain induced in the  $x$  direction due to tension or compression in the  $y$  direction. Finally, the effective shear modulus is defined as,

$$G_{xy} = \frac{1}{hA_{66}} \quad (2.45)$$

Since there is a linear relationship between  $\theta$  and  $x$ , it is possible to demonstrate the tailoring possibilities using a few figures. The normalized axial effective stiffness  $E_x$  is shown in Figure 2.2 as a function of  $\theta$ . As expected, the value of  $E_x$  is highest when the fiber angle is  $0^\circ$ . Also shown in Figure 2.2 is an example of how this plot can be used to determine the stiffness distribution for a given set of angles  $T_0$  and  $T_1$ . The axial stiffness distribution for a panel having  $T_0 = 0^\circ$  and  $T_1 = 30^\circ$  is given by the segment of the curve in Figure 2.2 (i) that lies between  $\theta = 0^\circ$  and  $\theta = 30^\circ$ , indicated by the shaded region. The curve has been amplified and plotted as a function of  $x/a$  in (ii). The  $\theta$  scale and the  $x$  scale can be interchanged because there exists a linear relationship between them. For any angle combination it is therefore possible to use Figure 2.2 (i) to determine the stiffness distribution. If  $T_0 > T_1$ , then the scale is simply read from right to left. For straight fiber laminates,  $T_0 = T_1$ , and the effective stiffness has a single value that is constant with respect to  $x$ . The stiffness gradient is high for values of  $T_0$  and  $T_1$  that are between  $5^\circ$  and  $60^\circ$ , so within this range, small differences between  $T_0$  and  $T_1$  will result in large changes in stiffness with respect to  $x$ . For values of  $T_0$  and  $T_1$  greater than  $60^\circ$  there is very little change in  $E_x$ , since the curve for those angles is nearly flat. The same is true when the angles are close to  $0^\circ$ .

The other effective material properties may be analyzed using curves ranging from  $0^\circ$  to  $90^\circ$ . Shown in Figures 2.3-2.5 are the curves for  $E_y$ ,  $G_{xy}$ ,  $\nu_{xy}$  and  $\nu_{yx}$ , respectively. The gains and trade-offs of stiffness tailoring become apparent by looking at the figures collectively. For a panel with  $T_0 = 0^\circ$  and  $T_1 = 30^\circ$ , the axial modulus  $E_x$  decreases by 64% between the middle of the panel,  $x/a = 0$ , and the panel ends,  $x/a = \pm 0.5$ . The transverse modulus  $E_y$  increases by 36% for the same configuration. There is a drastic change in  $G_{xy}$  and  $\nu_{xy}$ , since at  $x/a = \pm 0.5$  their value is five times greater than at  $x/a = 0$ .

In general, if the angles  $T_0$  and  $T_1$  are chosen so that there is an decrease in  $E_x$  along the panel length, a significant increase in  $E_y$  will result. The effects on  $G_{xy}$  and  $\nu_{xy}$  depend on the actual values of  $T_0$  and  $T_1$  because there are peaks in the curves at  $45^\circ$  and  $25^\circ$ , respectively. However, even for small changes in fiber angle, there will be significant changes in these two properties.

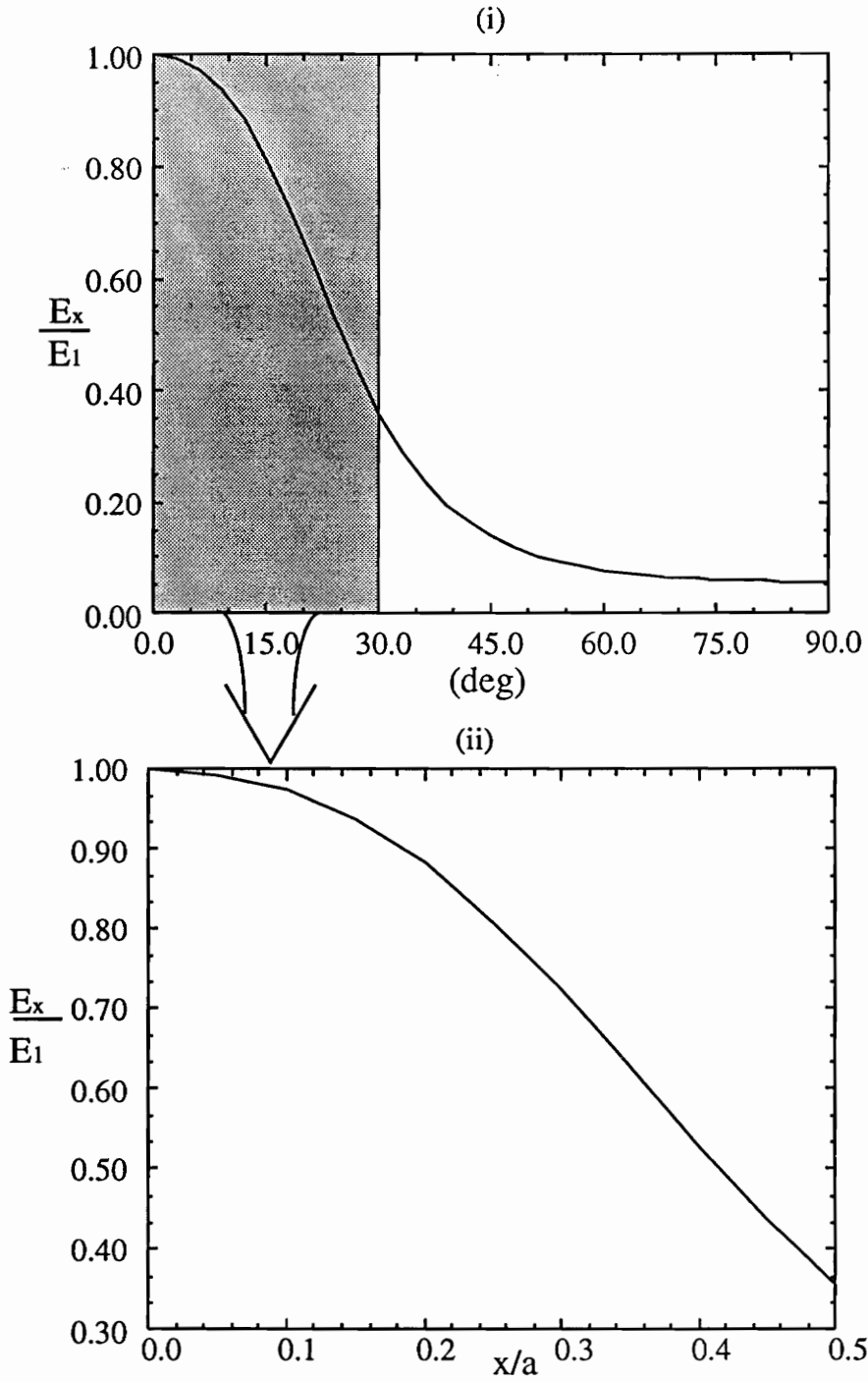


Figure 2.2 Effective Axial Modulus  $E_x$ .

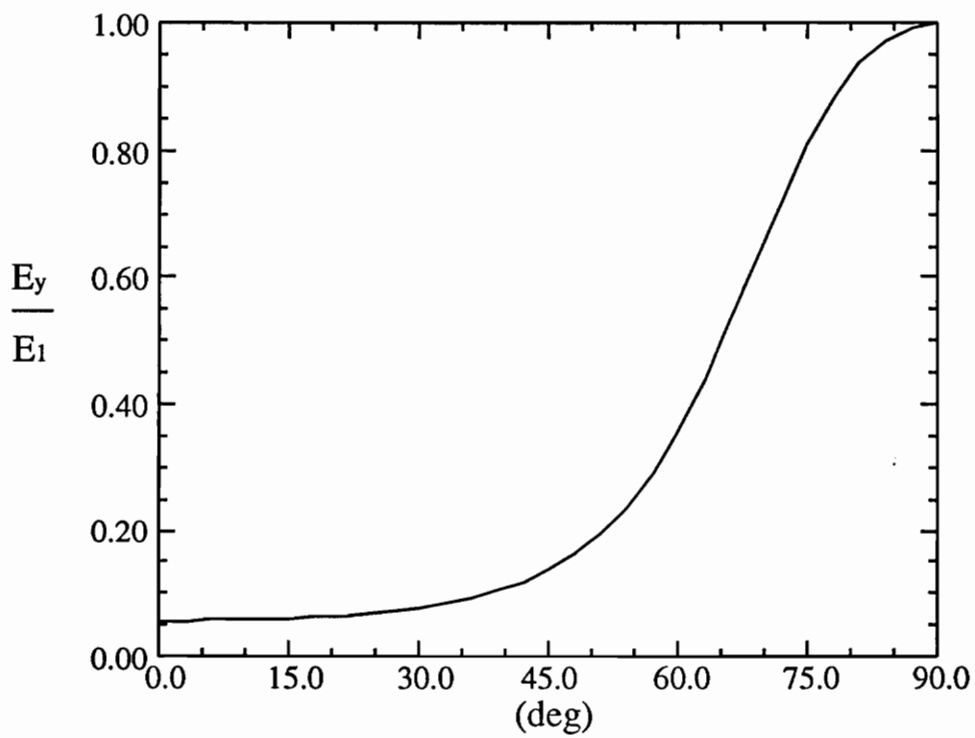


Figure 2.3 Effective Transverse Modulus,  $E_y$ .

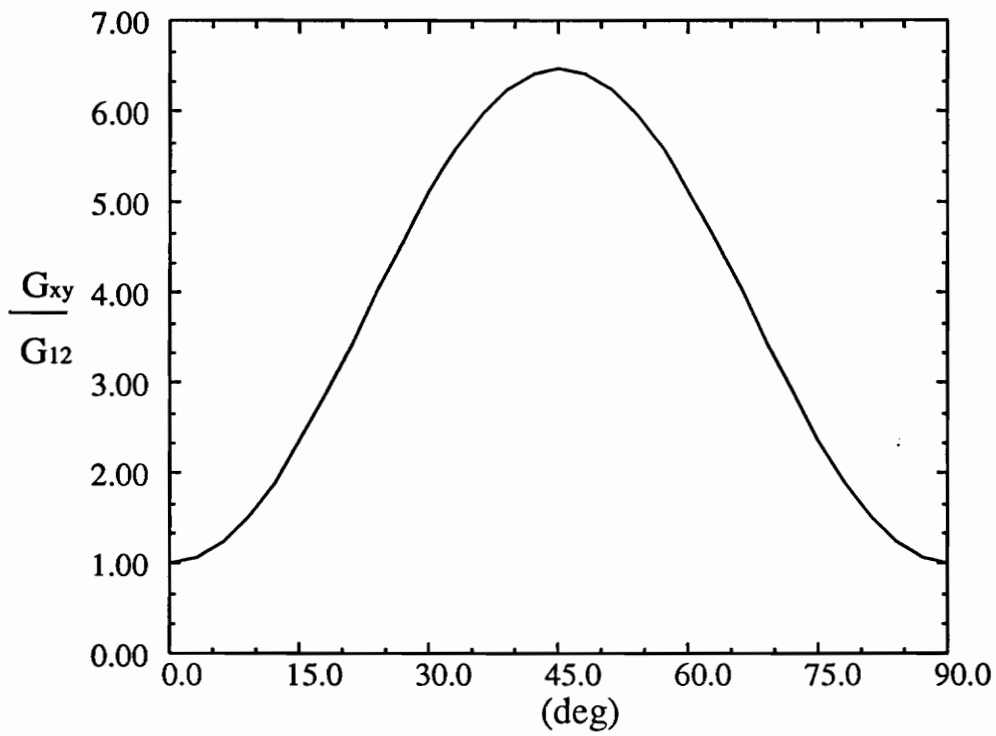
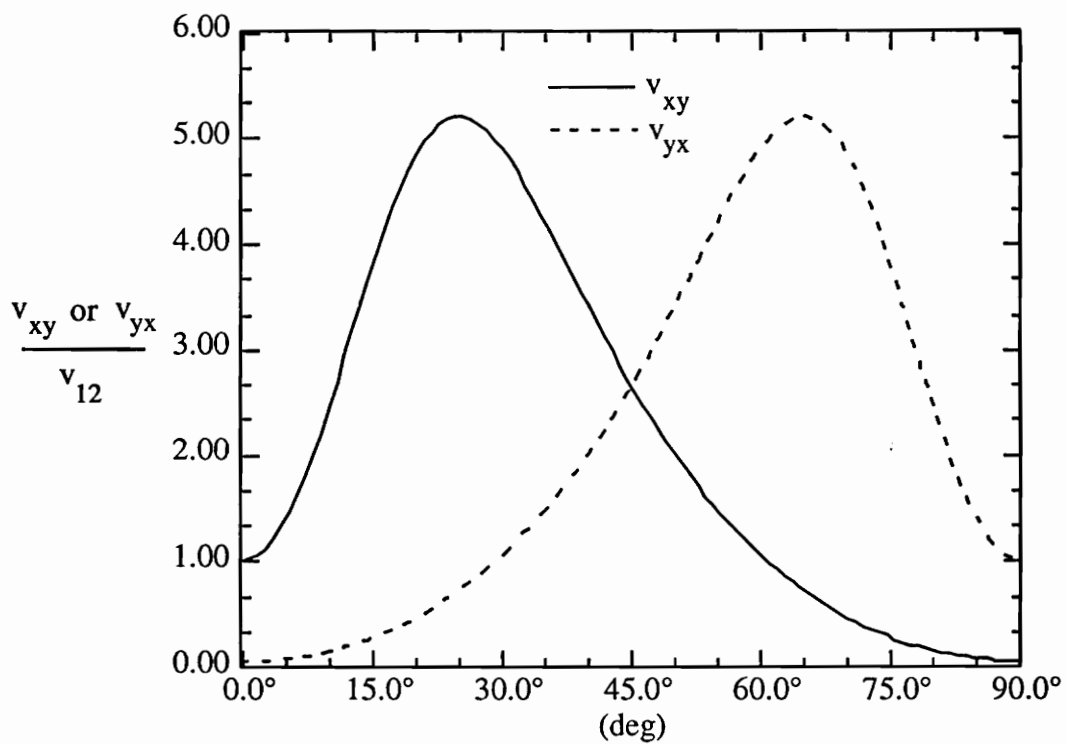


Figure 2.4 Effective Shear Modulus,  $G_{xy}$ .



**Figure 2.5** Effective Major and Minor Poisson's Ratios,  $\nu_{xy}$  and  $\nu_{yx}$ .

# CHAPTER 3

## In-Plane Analysis

### 3.1 Introduction

The in-plane analysis of the variable stiffness panels is described in this chapter. First, the equations that govern the in-plane response are derived using two different approaches. The four different sets of boundary conditions that have been studied in this work are then presented. A general numerical solution to a set of these governing equations is then introduced, along with a study of how this solution converges for this particular problem. Since the buckling analysis itself will be complex and computationally intensive, it is necessary to arrive at closed form solutions whenever possible. Closed form solutions are presented for each of the four sets of boundary conditions. Finally, the concept of overall panel stiffness and the issue of failure are presented.

### 3.2 Governing Equations

The changes in stiffness presented in the previous chapter pose a major hurdle in the analysis of the in-plane response of the variable stiffness panels. In this section, the equations governing the elastic response are derived. It is through the solution of these equations that the displacements, strains, and stress resultants can be obtained. Two approaches are presented here. In the first approach, the solution of a system of differential equations yields the displacement fields, from which the strain and stress resultants are subsequently calculated. An alternate approach is also presented. By using a stress function, a governing differential equation is obtained. This differential equation yields the stress resultants, and the constitutive relation is used to solve for the strains.

#### 3.2.1 Equilibrium Approach

The equilibrium equations of CLT are derived in detail by Whitney [13]. They are obtained by applying Hamilton's principle using the first variation of the total potential energy of the panel. Since the types of laminates presented in this study lack extension-twist coupling, only two of those equations are relevant for the in-plane response. They are given by,

$$\frac{\partial N_x}{\partial x} + \frac{\partial N_{xy}}{\partial y} = 0, \quad (3.1)$$

and

$$\frac{\partial N_y}{\partial y} + \frac{\partial N_{xy}}{\partial x} = 0. \quad (3.2)$$

Recall that the in-plane constitutive relation for a symmetric angle-ply laminate is given by

$$\begin{Bmatrix} N_x \\ N_y \\ N_{xy} \end{Bmatrix} = \begin{bmatrix} A_{11} & A_{12} & 0 \\ A_{12} & A_{22} & 0 \\ 0 & 0 & A_{66} \end{bmatrix} \begin{Bmatrix} \epsilon_x^o \\ \epsilon_y^o \\ \gamma_{xy}^o \end{Bmatrix}. \quad (3.3)$$

Substituting equation 3.3 and the linear strain-displacement relations into equations 3.1 and 3.2 yields,

$$A_{11}(x) \frac{\partial^2 u}{\partial x^2} + A_{66}(x) \frac{\partial^2 u}{\partial y^2} + \{A_{12}(x) + A_{66}(x)\} \frac{\partial^2 v}{\partial x \partial y} + \frac{\partial A_{11}(x)}{\partial x} \frac{\partial u}{\partial x} + \frac{\partial A_{12}(x)}{\partial x} \frac{\partial v}{\partial y} = 0, \quad (3.4)$$

and

$$A_{66}(x) \frac{\partial^2 v}{\partial x^2} + A_{22}(x) \frac{\partial^2 v}{\partial y^2} + \{A_{12}(x) + A_{66}(x)\} \frac{\partial^2 u}{\partial x \partial y} + \frac{\partial A_{66}(x)}{\partial x} \left( \frac{\partial u}{\partial y} + \frac{\partial v}{\partial x} \right) = 0, \quad (3.5)$$

where the  $A_{ij}$  are functions of  $x$ . Equation 3.4 is an elliptic partial differential equation in terms of the axial displacement  $u$ , with terms that couple it with the transverse displacement,  $v$ . Likewise, equation 3.5 is an elliptic partial differential equation in  $v$ , with terms that couple it with  $u$ . The simultaneous solution of these equations yields the  $u$  and  $v$  displacement fields, from which the strains can be calculated. The constitutive equations can then be applied to obtain the stress resultants.

### 3.2.2 Stress Function Approach

An alternative approach to the in-plane problem is to formulate the response in terms of a stress function,  $\Phi$ , such that,

$$N_x = \frac{\partial^2 \Phi}{\partial y^2}, \quad (3.6)$$

$$N_y = \frac{\partial^2 \Phi}{\partial x^2}, \quad (3.7)$$

and

$$N_{xy} = -\frac{\partial^2 \Phi}{\partial x \partial y}. \quad (3.8)$$

The above definition of the stress resultants automatically satisfies the equilibrium equations. Substituting equations 3.6-3.8 into the inverted form of equation 3.3, the constitutive relation may be expressed as,

$$\begin{Bmatrix} \epsilon_x^o \\ \epsilon_y^o \\ \gamma_{xy}^o \end{Bmatrix} = \frac{1}{A_{11}A_{22} - A_{12}^2} \begin{bmatrix} A_{22} & -A_{12} & 0 \\ -A_{12} & A_{11} & 0 \\ 0 & 0 & \frac{A_{11}A_{22} - A_{12}^2}{A_{66}} \end{bmatrix} \begin{Bmatrix} \frac{\partial^2 \Phi}{\partial y^2} \\ \frac{\partial^2 \Phi}{\partial x^2} \\ -\frac{\partial^2 \Phi}{\partial x \partial y} \end{Bmatrix}. \quad (3.9)$$

As a result of the CLT assumptions, all but one of the compatibility equations of the linear theory of elasticity are satisfied. The strains are therefore subject to the equation,

$$\frac{\partial^2 \epsilon_x^o}{\partial y^2} + \frac{\partial^2 \epsilon_y^o}{\partial x^2} - \frac{\partial^2 \epsilon_{xy}^o}{\partial x \partial y} = 0, \quad (3.10)$$

where  $\epsilon_{xy}^o$  is the tensorial shear strain,  $\epsilon_{xy}^o = \gamma_{xy}^o/2$ . The governing equation is obtained by substituting the strains from equation 3.9 into equation 3.10 and differentiating. A symbolic manipulator, Mathematica [15], has been used to differentiate the terms in equation 3.10, since the extensional stiffnesses,  $A_{ij}$ , are functions of  $x$ . The resulting governing equation is given by,

$$\begin{aligned} & \frac{A_{11}\Phi_{,xxxx} + A_{22}\Phi_{,yyyy}}{A_{11}A_{22} - A_{12}^2} \\ & + \left\{ \frac{-2A_{12}}{A_{11}A_{22} - A_{12}^2} + \frac{1}{2A_{66}} \right\} \Phi_{,xxyy} \\ & + \left\{ \frac{-2A_{11}A_{22}A'_{11} + 4A_{11}A_{12}A'_{12} - 2A_{11}^2A'_{22}}{(A_{11}A_{22} - A_{12}^2)^2} + \frac{2A'_{11}}{A_{11}A_{22} - A_{12}^2} \right\} \Phi_{,xxx} \\ & + \left\{ \frac{2A_{12}A_{22}A'_{11} - 4A_{12}^2A'_{12} + 2A_{11}A_{12}A'_{22}}{(A_{11}A_{22} - A_{12}^2)^2} - \frac{2A'_{12}}{A_{11}A_{12} - A_{12}^2} - \frac{A'_{66}}{2A_{66}^2} \right\} \Phi_{,xyy} \\ & + \left\{ \frac{2A_{22}^2A'_{11} - 8A_{12}A_{22}A'_{11}A'_{12} + 8A_{12}^2A'_{12}^2}{(A_{11}A_{22} - A_{12}^2)^3} \right. \\ & \left. + \frac{4A_{11}A_{22}A'_{11}A'_{22} - 8A_{11}A_{12}A'_{12}A'_{22} + 2A_{11}^2A'_{22}^2}{(A_{11}A_{22} - A_{12}^2)^3} \right\} (A_{11}\Phi_{,xx} - A_{12}\Phi_{,yy}) \\ & + \left\{ \frac{-2A_{22}A'_{11}^2 + 4A_{12}A'_{11}A'_{12} + 2A_{11}A'_{12}^2 - 4A_{11}A'_{11}A'_{22}}{(A_{11}A_{22} - A_{12}^2)^2} \right. \\ & \left. + \frac{-A_{11}A_{22}A''_{11} + 2A_{11}A_{12}A''_{12} - A_{11}^2A''_{22}}{(A_{11}A_{22} - A_{12}^2)^2} + \frac{A''_{11}}{A_{11}A_{22} - A_{12}^2} \right\} \Phi_{,xx} \\ & + \left\{ \frac{2A_{22}A'_{11}A'_{12} - 6A_{12}A'_{12}^2 + 2A_{12}A'_{11}A'_{22} + 2A_{11}A'_{12}A'_{22}}{(A_{11}A_{22} - A_{12}^2)^2} \right. \\ & \left. + \frac{A_{12}A_{22}A''_{11} - 2A_{12}^2A''_{12} + A_{11}A_{12}A''_{22}}{(A_{11}A_{22} - A_{12}^2)^2} - \frac{A''_{12}}{A_{11}A_{22} - A_{12}^2} \right\} \Phi_{,yy} = 0, \quad (3.11) \end{aligned}$$

where the subscripts on  $\Phi$  indicate partial differentiation with respect to the variables that follow the comma; one and two primes on the  $A_{ij}$  indicate the first and second partial derivatives with respect to  $x$ , respectively. Equation 3.11 is a fourth order homogeneous partial differential equation with variable coefficients. Its solution yields the stress function  $\Phi$ ; differentiation of  $\Phi$  with respect to  $x$  and  $y$  yields the stress resultants. Once the stress resultants are known, the strains can be obtained by applying equation 3.9.

### 3.2.3 Selected Approach

In this work, the solution of equations 3.4 and 3.5 is used to determine the in-plane response. The equilibrium approach has been chosen because it is flexible and straightforward. The solution of elliptic equations with variable coefficients has been studied extensively [16]; therefore, the solution of this system poses a computational challenge rather than a mathematical one. By solving for the displacement fields, the strains and stress resultants are easily obtainable for different combinations of displacement (Dirichlet) and stress resultant (Neumann) boundary conditions.

The stress function approach is inferior by comparison. Although the solution of equation 3.11 may be obtained using a finite difference technique, it is likely to be computationally intensive, since it involves two space variables, has variable coefficients, and requires mixed boundary conditions [17]. Furthermore, displacement boundary conditions cannot be applied using this method. Although the solution yields the stress resultants directly, the displacements are difficult to obtain, since they involve the calculation of numerical integrals.

## 3.3 Boundary Conditions

Variable stiffness panels subjected to four different boundary conditions have been analyzed. The boundary conditions have been chosen to reflect the most common panel loading conditions; a schematic for each set of conditions is shown in Figures 3.1 and 3.2. Each condition is described below. There are planes of symmetry at  $x = 0$  and  $y = 0$ , so a quarter of the panel may be modeled in order to reduce the size of the problem. The quarter panel boundary conditions are also shown in Figures 3.1 and 3.2. The boundary conditions at  $x = 0$  and  $y = 0$  enforce symmetry of the displacement fields and are given by,

$$\text{along } y = 0, \quad v = 0 \quad \text{and} \quad \frac{\partial u}{\partial y} = 0, \quad (3.12)$$

and

$$\text{along } x = 0, \quad u = 0 \quad \text{and} \quad \frac{\partial v}{\partial x} = 0. \quad (3.13)$$

The boundary conditions for the other two edges determine the loading conditions and are defined individually for each case.

### 3.3.1 Case I: Free Transverse Edges

Case I is a set of boundary conditions commonly found in the analysis of plates. It consists of an applied uniform end shortening,  $u_0$ , at  $x = \pm a/2$ . A uniform end shortening has been chosen because under testing conditions a uniform end displacement is applied, while the equivalent load is measured. The transverse edges,  $y = \pm b/2$  have no applied transverse loads, and free to deform; since no transverse load is applied,  $N_y(x, \pm b/2) = 0$ . There is no applied shear stress resultant, therefore  $N_{xy}$  is identically zero along the perimeter of the panel. These boundary conditions are shown in Figure 3.1 (i). In terms of the displacements, the quarter panel loading conditions are given by,

$$\text{along } x = \frac{a}{2}, \quad u = u_0 \quad \text{and} \quad \frac{\partial v}{\partial x} = -\frac{\partial u}{\partial y} = 0, \quad (3.14)$$

and

$$\text{along } y = \frac{b}{2}, \quad \frac{\partial u}{\partial y} = -\frac{\partial v}{\partial x} \quad \text{and} \quad \frac{\partial v}{\partial y} = -\frac{A_{12}(x)}{A_{22}(x)} \frac{\partial u}{\partial x}. \quad (3.15)$$

### 3.3.2 Case II: Fixed Transverse Edges

As in case I, a uniform end shortening is applied at  $x = \pm a/2$ . The transverse edges, however, remain fixed, so  $v(x, \pm b/2) = 0$ . By restraining the transverse expansion of the panel, the panel is subjected to biaxial compression due to the Poisson effect when the end shortening is applied. There is no shear stress applied on any of the edges. A schematic for this case is shown in Figure 3.1(ii). The displacement boundary conditions are,

$$\text{along } x = \frac{a}{2}, \quad u = u_0 \quad \text{and} \quad \frac{\partial v}{\partial x} = -\frac{\partial u}{\partial y} = 0, \quad (3.16)$$

and

$$\text{along } y = \frac{b}{2}, \quad \frac{\partial u}{\partial y} = -\frac{\partial v}{\partial x} = 0 \quad \text{and} \quad v = 0. \quad (3.17)$$

Panel Boundary Conditions

Quarter Panel Boundary Conditions

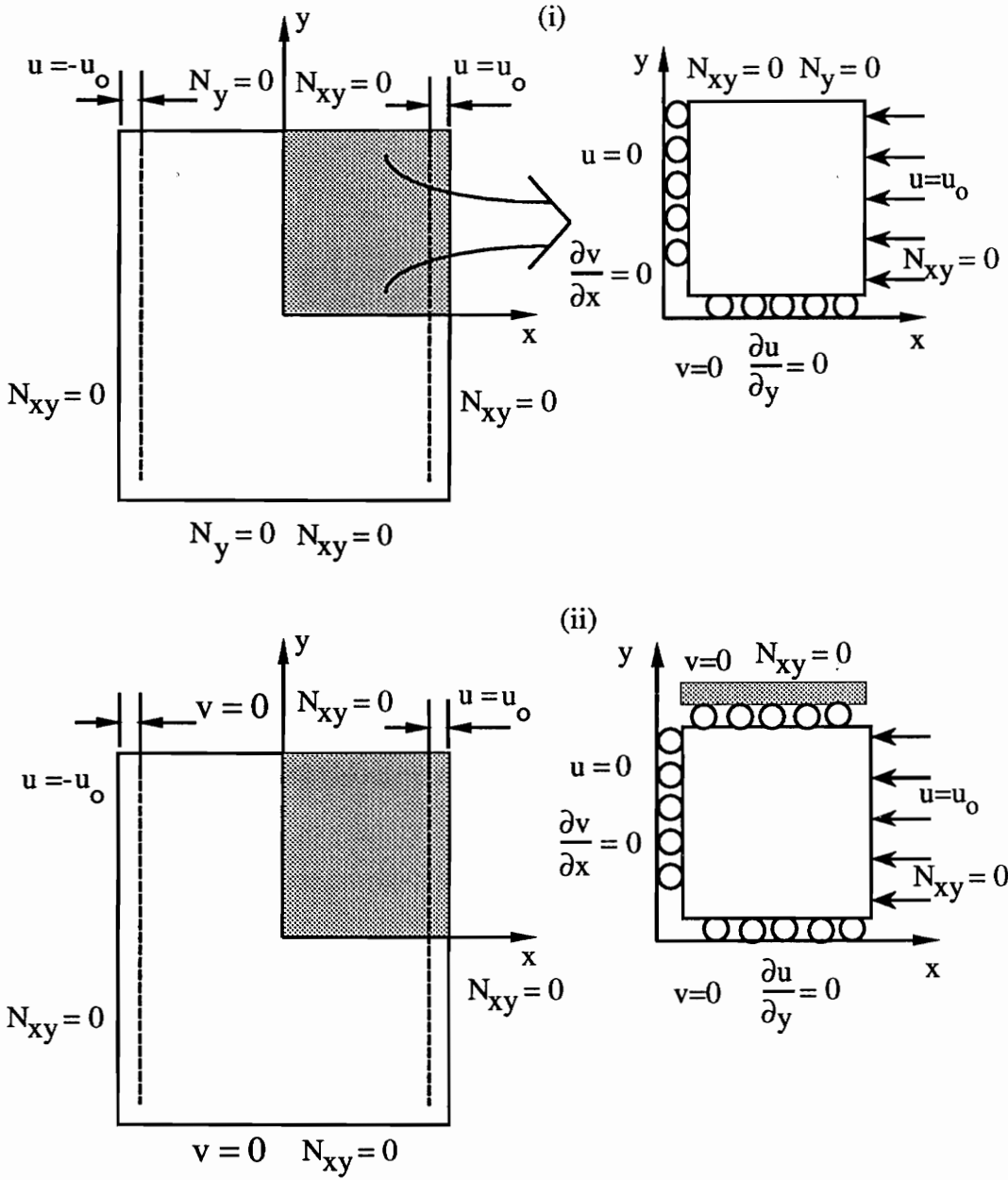


Figure 3.1 Panel and Quarter Panel Boundary Conditions for (i) Free and (ii) Fixed Transverse Edges.

### 3.3.3 Case III: Transverse Loading

Case III represents transverse loading of the panel. A uniform transverse displacement,  $v_o$ , is applied at  $y = \pm b/2$ . Again, a displacement has been prescribed because it is the loading condition during testing. There is no applied axial load, so  $N_x(\pm a/2, y) = 0$ . Again, the shear stress resultant is identically zero along the perimeter of the panel. These boundary conditions are shown in Figure 3.2(i). For the quarter panel, the displacement boundary conditions are:

$$\text{along } x = \frac{a}{2}, \quad \frac{\partial u}{\partial x} = -\frac{A_{12}(x)}{A_{11}(x)} \frac{\partial v}{\partial y} \quad \text{and} \quad \frac{\partial v}{\partial x} = -\frac{\partial u}{\partial y}, \quad (3.18)$$

and

$$\text{along } y = \frac{b}{2}, \quad \frac{\partial u}{\partial y} = -\frac{\partial v}{\partial x} = 0 \quad \text{and} \quad v = v_o. \quad (3.19)$$

### 3.3.4 Case IV: Straight-but-Free Transverse Edges

When a variable stiffness panel is loaded under the boundary conditions for case I, the transverse edges do not remain straight. Instead, as will be shown in the next chapter, at  $y = \pm b/2$  the  $v$  displacement is a function of  $x$ . It is conceivable that, by using stiffeners that have large in-plane bending stiffnesses, the transverse edges of a variable stiffness panel may be allowed to move freely but be required to remain straight. The boundary conditions for this case are shown as case IV in Figure 3.2(ii). The requirement that the integral of  $N_y$  along the transverse edges be identically zero ensures that the net transverse load acting on the panel is zero. The integral expression for  $N_y$  at  $y = \pm b/2$  is therefore given by

$$P_y = \int_{-\frac{a}{2}}^{\frac{a}{2}} N_y \left( x, \pm \frac{b}{2} \right) dx = 0, \quad (3.20)$$

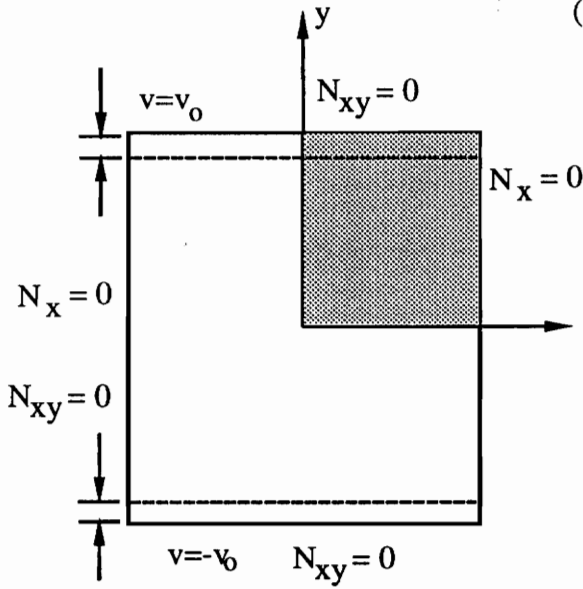
where  $P_y$  denotes the net load at the transverse edges. The transverse strain, denoted by  $\epsilon_o$ , is calculated so that this condition is satisfied. Also,  $N_{xy}$  is identically zero along the perimeter of the panel. The displacement boundary conditions are:

$$\text{along } x = \frac{a}{2}, \quad u = u_o \quad \text{and} \quad \frac{\partial v}{\partial x} = -\frac{\partial u}{\partial y} = 0, \quad (3.21)$$

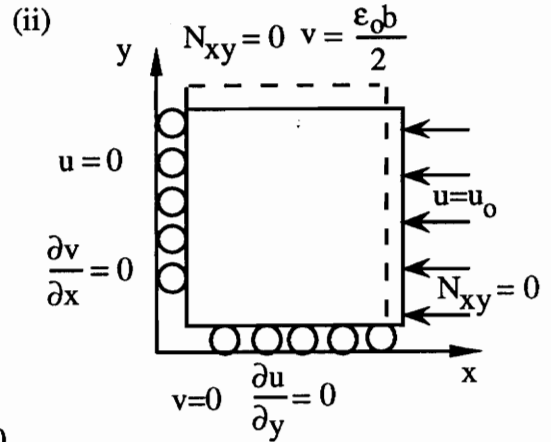
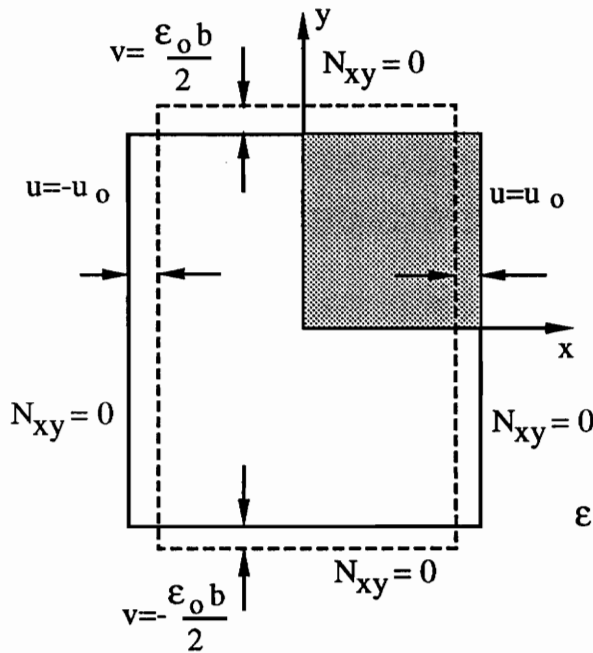
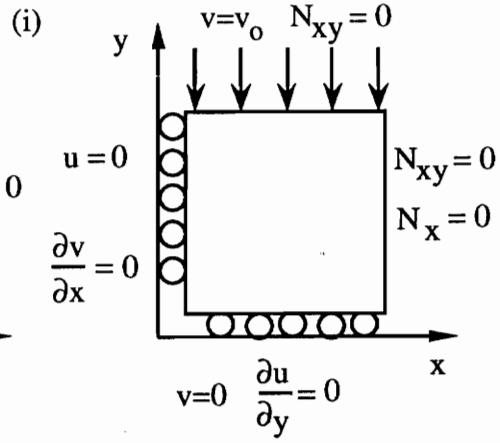
and

$$\text{along } y = \frac{b}{2}, \quad \frac{\partial u}{\partial y} = -\frac{\partial v}{\partial x} = 0 \quad \text{and} \quad v = \frac{b}{2} \epsilon_o. \quad (3.22)$$

Panel Boundary Conditions



Quarter Panel Boundary Conditions



$\epsilon_0$  is such that  $\int_{-a/2}^{a/2} N_y(x, \pm b/2) dx = 0$

Figure 3.2 Panel and Quarter Panel Boundary Conditions for (i) Transverse Loading and (ii) Free-but-Straight Transverse Edges.

## 3.4 Numerical Solution

### 3.4.1 Solution to a General Elliptic PDE

A generalized elliptic equation with variable coefficients is given by,

$$c\alpha_{,xx} + 2d\alpha_{,xy} + e\alpha_{,yy} + f\alpha_{,x} + g\alpha_{,y} + h\alpha = k, \quad (3.23)$$

where  $c, d, e, f, g, h$  and  $k$  are functions of  $x$  and  $y$ . The ellipticity condition requires that  $d^2 - ce < 0$  for all  $x$  and  $y$ . A numerical solution to the above equation may be obtained for problems with linear boundary conditions by using Hermite collocation. With this technique, the domain is first discretized into  $(NGRX-1) \times (NGRY-1)$  rectangles, where  $NGRX$  and  $NGRY$  are the number of grid lines in the  $x$  and  $y$  directions, respectively. The solution for  $\alpha$  is obtained using a Hermite bicubic piecewise polynomial approximation, given by

$$\alpha(x, y) = \sum_{k=1}^{NGRX} \sum_{j=1}^{NGRY} a_{k,j} h_k(x) h_j(y) + b_{k,j} h_k(x) g_j(y) + c_{k,j} g_k(x) h_j(y) + d_{k,j} g_k(x) g_j(y), \quad (3.24)$$

where

$$h_k(x) = \begin{cases} 0 & x \leq x_{k-1}, x_{k+1} \leq x \\ -2 \left( \frac{x-x_{k-1}}{x_k-x_{k-1}} \right)^3 + 3 \left( \frac{x-x_{k-1}}{x_k-x_{k-1}} \right)^2 & x_{k-1} \leq x \leq x_k \\ -2 \left( \frac{x_{k+1}-x}{x_{k+1}-x_k} \right)^3 + 3 \left( \frac{x_{k+1}-x}{x_{k+1}-x_k} \right)^2 & x_k \leq x \leq x_{k+1} \end{cases} \quad (3.25)$$

and

$$g_k(x) = \begin{cases} 0 & x \leq x_{k-1}, x_{k+1} \leq x \\ \left( \frac{x-x_{k-1}}{x_k-x_{k-1}} \right)^2 (x-x_k) & x_{k-1} \leq x \leq x_k \\ \left( \frac{x_{k+1}-x}{x_{k+1}-x_k} \right)^2 (x-x_k) & x_k \leq x \leq x_{k+1} \end{cases}, \quad (3.26)$$

and where  $x_k$  is the  $k^{\text{th}}$  grid point. The coefficients  $a_{k,j}, b_{k,j}, c_{k,j}$ , and  $d_{k,j}$  are determined so that  $\alpha(x, y)$  satisfies equation 3.23 exactly at the collocation (Gauss) points of each rectangle and also satisfies the boundary conditions at a set of boundary collocation points. The grid and collocation points are shown in Figure 3.3 for a discretization of the domain in which  $NGRX = NGRY = 5$ . For a  $NGRX$  by  $NGRY$  grid there will be  $4 \times NGRX \times NGRY$  collocation points. Therefore,  $4 \times NGRX \times NGRY$  equations are generated for the coefficients. Once the coefficients are obtained, the function  $\alpha(x, y)$  and its derivatives may be approximated anywhere in the domain. A general code for applying this technique has been developed by Rice, et.al [18], as part of a software package called ELLPACK, which has been used in this work to implement the numerical solution.

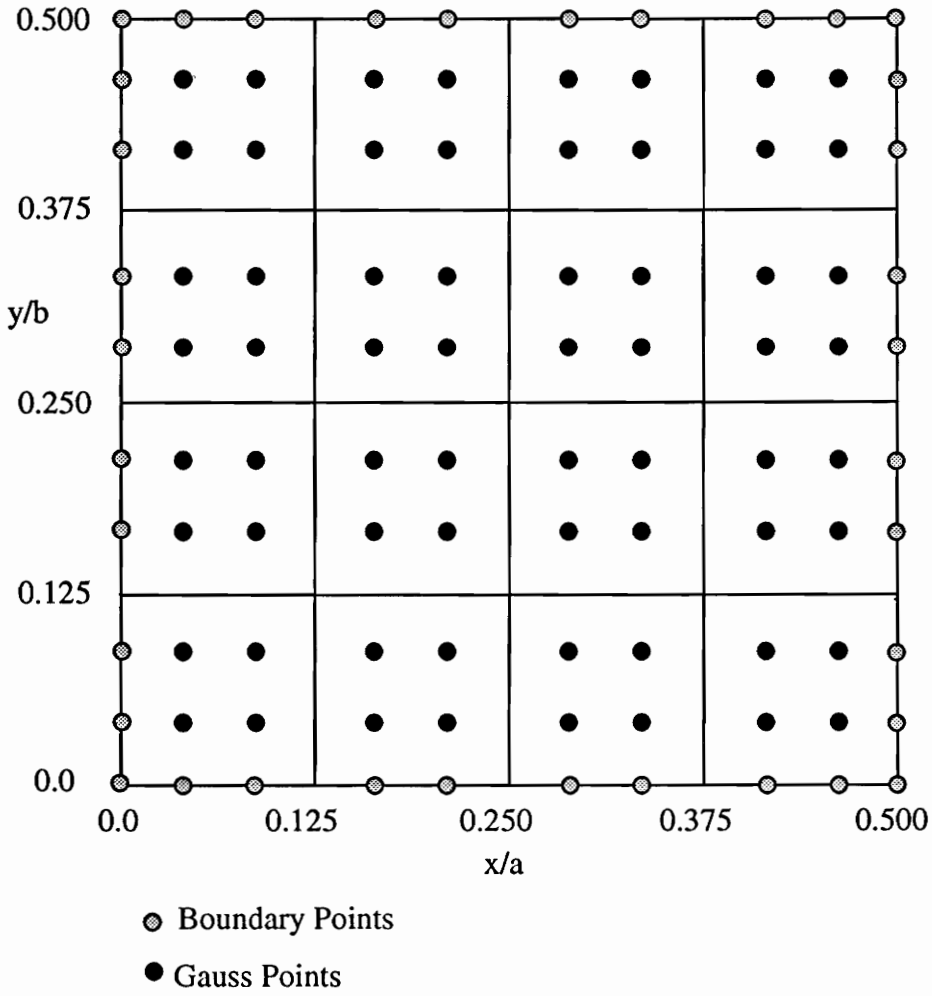


**Figure 3.3 Domain Discretization and Collocation Points with  $5 \times 5$  Gridlines.**

### 3.4.2 Application to Variable Stiffness Panels

Application of the Hermite collocation technique to the elastic response of the variable stiffness panels simply requires a formulation of the problem in such a way that it can be adapted to the ELLPACK code. Equations 3.4 and 3.5, which govern the elastic response, can be re-written in the following form,

$$A_{11}(x) \frac{\partial^2 u}{\partial x^2} + A_{66}(x) \frac{\partial^2 u}{\partial y^2} + \frac{\partial A_{11}(x)}{\partial x} \frac{\partial u}{\partial x} = p(x, y), \quad (3.27)$$

$$A_{66}(x) \frac{\partial^2 v}{\partial x^2} + A_{22}(x) \frac{\partial^2 v}{\partial y^2} + \frac{\partial A_{66}(x)}{\partial x} \frac{\partial v}{\partial x} = q(x, y), \quad (3.28)$$

where

$$p(x, y) = - \{A_{12}(x)A_{66}(x)\} \frac{\partial^2 v}{\partial x \partial y} - \frac{\partial A_{12}(x)}{\partial x} \frac{\partial v}{\partial y}, \quad (3.29)$$

and

$$q(x, y) = - \{A_{12}(x) + A_{66}(x)\} \frac{\partial^2 u}{\partial x \partial y} - \frac{\partial A_{66}(x)}{\partial x} \frac{\partial u}{\partial y}. \quad (3.30)$$

Equations 3.27 and 3.28 constitute a system of non-homogeneous partial differential equations with variable coefficients. Since  $d = d(x, y) = 0$  for both equations, and the  $A_{ij}$  are positive-definite, the ellipticity condition is satisfied for all  $x$  and  $y$ . Equation 3.27 contains the non-homogeneous term  $p(x, y)$ , which depends on partial derivatives of  $v$ . Likewise, equation 3.28 contains the non-homogeneous term  $q(x, y)$ , which depends on partial derivatives of  $u$ . The equations cannot be decoupled; therefore, in order to obtain a numerical solution using ELLPACK, an iterative technique is necessary. The algorithm for calculating the displacements for a panel with case I boundary conditions is shown in Figure 3.4. The iterative solution of the system begins with an assumed solution for the  $v$  displacement field. The  $v$  field is then used to obtain  $p(x, y)$ , and Hermite collocation is used to solve equation 3.27 for  $u(x, y)$ . The solution for  $u$  then becomes the input for  $q(x, y)$ , and a new solution for  $v$  is obtained by applying Hermite collocation to equation 3.28. The control program iterates, alternating between the two equations until the solutions converge.

### 3.4.3 Convergence and Grid Refinement

The solution of the numerical algorithm is considered to have converged when both displacement fields change by less than one part per million from one iteration to the next. This convergence

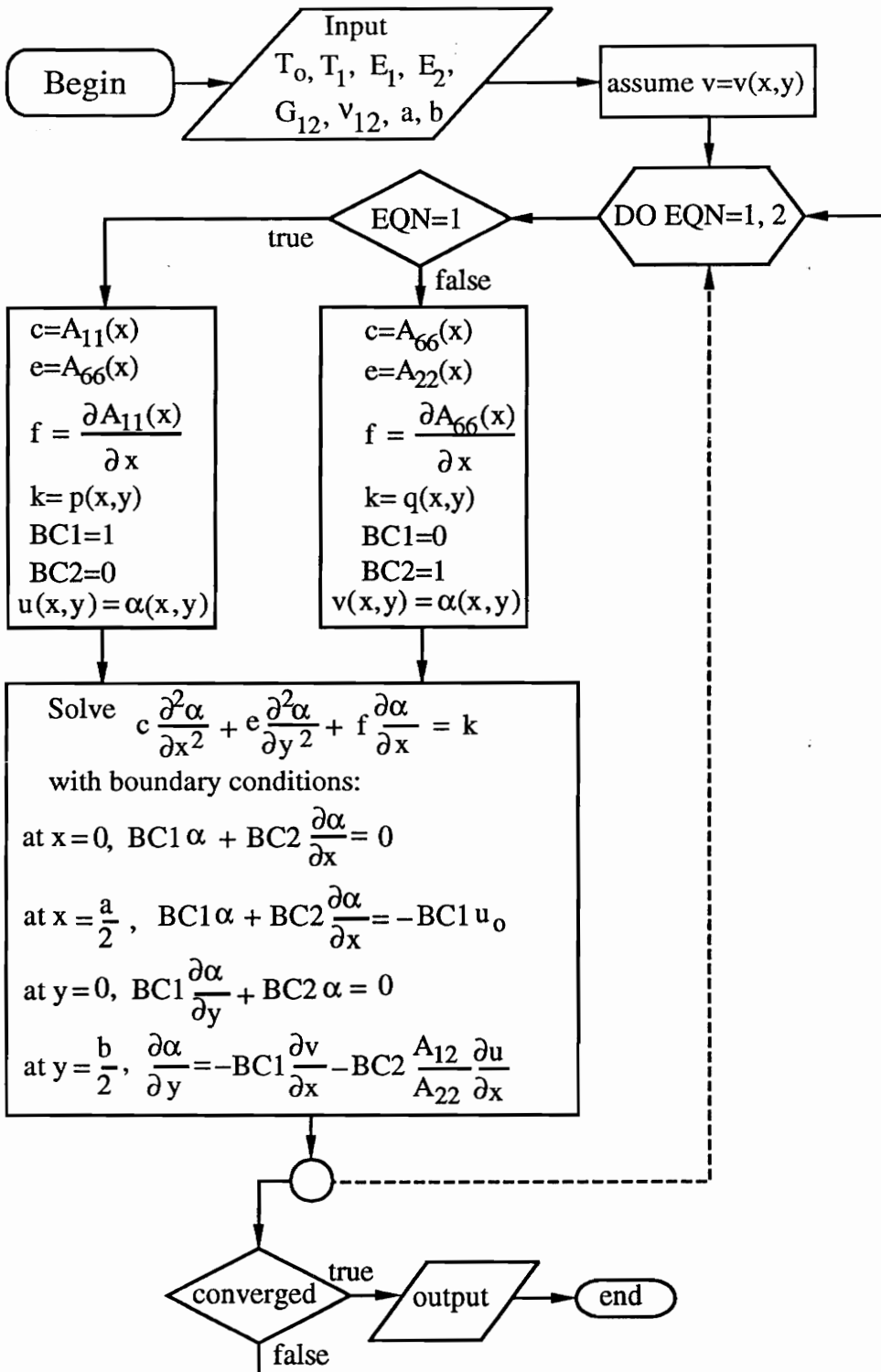


Figure 3.3 Algorithm for Calculating the  $u$  and  $v$  Displacement Fields (Case I).

criterion terminates the iteration loop in Figure 3.4 and is given by,

$$\left| \frac{u_k(x_i, y_j)}{u_{k-1}(x_i, y_j)} - 1 \right| < 10^{-6}, \quad \text{and} \quad \left| \frac{v_k(x_i, y_j)}{v_{k-1}(x_i, y_j)} - 1 \right| < 10^{-6}, \quad (3.31)$$

where the  $k^{\text{th}}$  iteration is denoted by  $k$ . With this criterion, at least two iterations are necessary. The points  $(x_i, y_j)$  are shown in Figure 3.5. This is the set of 65 arbitrary points where convergence is checked using equation 3.31. In order to capture the convergence of the method away from the collocation points, the convergence grid is different from the discretization grid. In addition, the number of convergence points remains constant regardless of the size of the discretization grid. The convergence points are spread out over the quarter panel to ensure convergence throughout. The program continues to iterate until the condition is satisfied at every point. The arrows in the figure denote the direction in which convergence is checked, starting with the upper right corner, where convergence is believed to be slow. Note that the origin of the convergence grid itself starts at  $(a/20, b/20)$ . The grid does not start at the origin because  $u$  and  $v$  are identically zero at  $x = 0$  and  $y = 0$ , respectively, and therefore result in division by zero if the convergence criterion is applied along those lines. In order to avoid an infinite loop when using this convergence criterion, a variable is also set to the maximum allowable number of iterations.

An adequate grid for the numerical model was obtained through a grid refinement study. As will be shown, the case which is most difficult to model is case I, mainly because the boundary conditions at  $y = b/2$  are of the Neumann type and the displacement fields exhibit large gradients. For a coarse grid, the condition that  $N_y = 0$  at  $y = b/2$  is satisfied only at the collocation points; at other points along the boundary, the transverse force resultant often has large non-zero values. Therefore, the important issues in choosing a grid become making sure that the boundary conditions are satisfied along the entire boundary and checking that the displacement fields converge to a single value as the grid is refined. For this study, the fiber angles have been chosen such that  $T_0 = 0^\circ$  and  $T_1 = 90^\circ$ , under the assumption that the grid obtained from this study may be used for any values of  $T_0$  and  $T_1$  that lie between  $0^\circ$  and  $90^\circ$ .

For each grid, the grid spacing,  $d$ , is defined as,

$$d = \frac{a}{2(NGRX - 1)}. \quad (3.32)$$

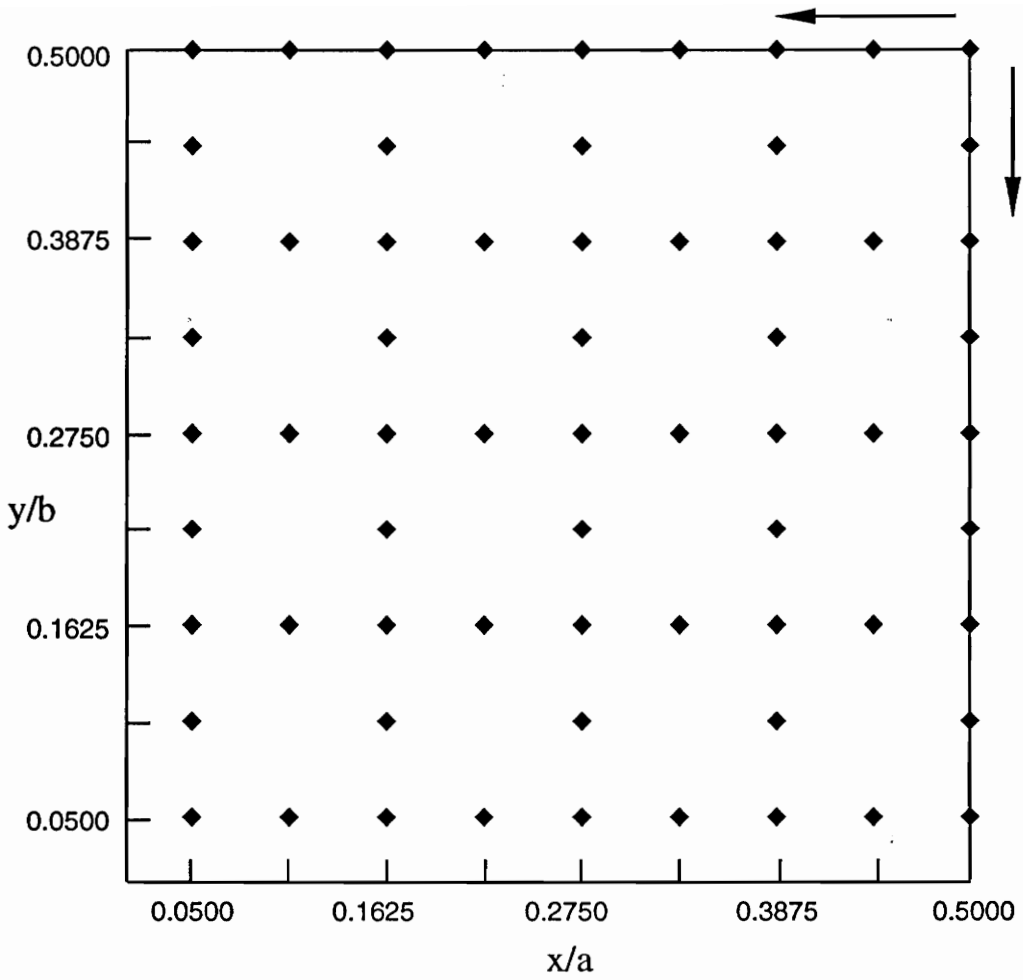


**Figure 3.5 Sixty Five Point Convergence Grid .**

For the results presented here a square grid has been used, therefore  $NGRX = NGRY$ . The convergence of the transverse stress resultant,  $N_y$ , at the free edge is shown in Figure 3.6 for a square panel ( $a/b = 1$ ) having  $T_0 = 0^\circ$  and  $T_1 = 90^\circ$ . The values for each curve have been normalized with respect to the value obtained using a  $3 \times 3$  grid, which is the coarsest grid possible. The data points correspond to grids with 3, 5, 7, 9, 11, 13, 15, 17 and 19 grid lines in the  $x$  and  $y$  directions, and have been taken at three test points at the upper boundary. There is a large change in the values of  $N_y$  when the grid is refined from  $3 \times 3$  to  $5 \times 5$ . The improvements for the subsequent grids are marginally smaller. Note that the point  $(3a/8, b/2)$ , which is closest to the upper right corner, is the last to converge. For the  $d/a$  value that corresponds to a  $15 \times 15$  grid, all the values have converged to zero, and the boundary condition is truly satisfied. The normalized displacements are shown in Table 3.1 along with the grid size and the normalized grid spacing,  $d/a$ . The displacements have been normalized with respect to  $a$ , the panel length. Again, a large improvement is seen for both displacement fields when the grid is changed from  $3 \times 3$  to  $5 \times 5$ . For a  $15 \times 15$  grid, the displacements at each point have converged to within five significant figures. The difference between the displacements obtained using the  $13 \times 13$  grid and the  $15 \times 15$  grid is less than 0.05%. For the  $17 \times 17$  and  $19 \times 19$  grids the improvements in the displacements are even smaller and do not justify the resulting increase in computing time. Therefore, a  $15 \times 15$  grid size has been used for the numerical analysis of square panels in this investigation.

The effect of the panel aspect ratio on the convergence of the numerical solution has been studied by testing a short and a long panel, with aspect ratios of 0.5 and 2.0, respectively, having  $T_0 = 0^\circ$  and  $T_1 = 90^\circ$ . The convergence of the transverse stress resultant of the short panel is shown in Figure 3.7. The transverse stress resultant at the three test points converges uniformly to zero as  $d/a$  decreases; it is zero for the discretization with  $13 \times 13$  gridlines. The convergence of the displacements is shown in Table 3.2. As shown, the displacements converge to a constant value as  $d$  decreases. For this aspect ratio, it was necessary to include a test with a  $21 \times 21$  grid, since the displacements at  $(a/8, b/2)$  do not sufficiently converge for the first 9 grids. However, the solution converges when  $NGRX$  and  $NGRY$  are both nineteen. The difference between the  $21 \times 21$  discretization and the  $19 \times 19$  discretization is less than 0.05%. The boundary condition is also

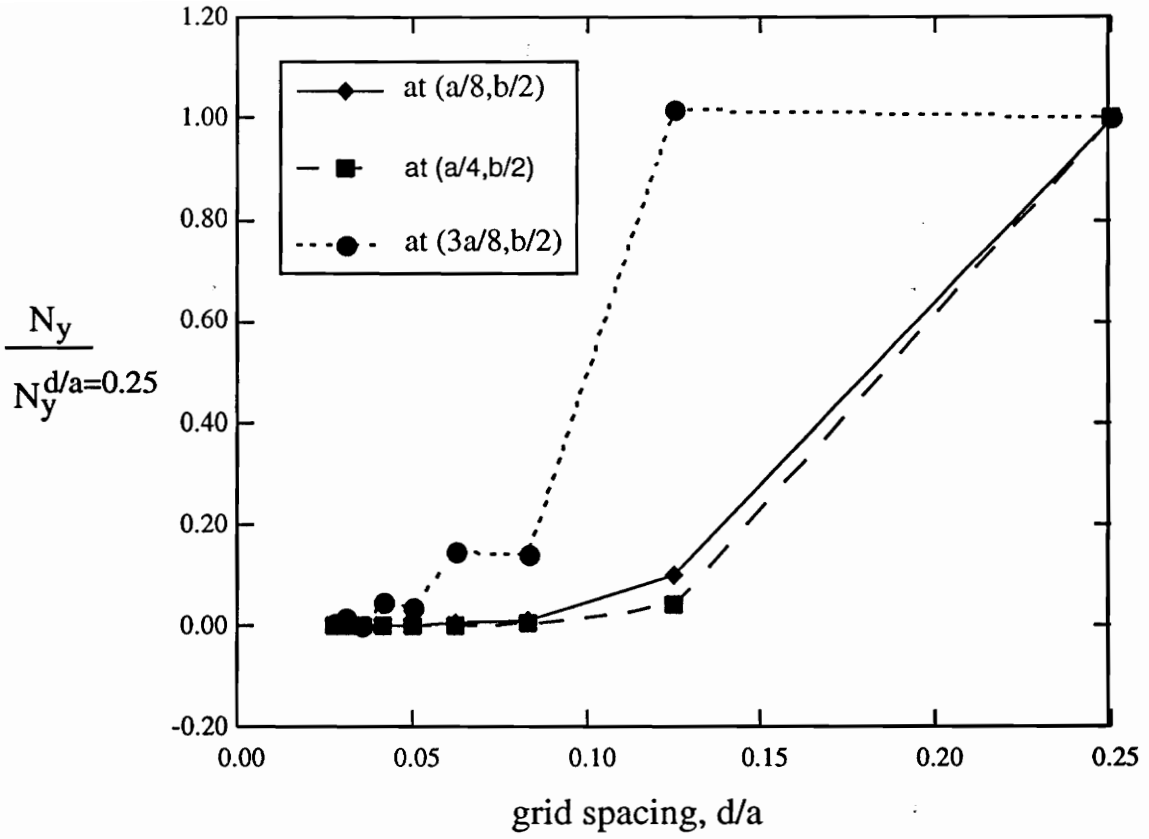


Figure 3.6 Convergence of  $N_y$  at  $y=b/2$  for  $a/b=1.0$ .

**Table 3.1** Convergence of the Displacements at  $y = b/2$  for  $a/b = 1.0$ .

Grid	Spacing, $d/a$	$\frac{u(a/8,b/2)}{a}$	$\frac{u(a/4,b/2)}{a}$	$\frac{u(3a/8,b/2)}{a}$
3 × 3	0.25000	0.037031	0.071271	0.34732
5 × 5	0.12500	0.046860	0.11634	0.34855
7 × 7	0.08333	0.045046	0.11930	0.35710
9 × 9	0.06250	0.044708	0.11974	0.35741
11 × 11	0.05000	0.044566	0.11986	0.35768
13 × 13	0.04167	0.044525	0.11990	0.35769
15 × 15	0.03571	0.044506	0.11991	0.35774
17 × 17	0.03125	0.044501	0.11992	0.35774
19 × 19	0.02778	0.044499	0.11992	0.35776
Grid	Spacing, $d/a$	$\frac{v(a/8,b/2)}{a}$	$\frac{v(a/4,b/2)}{a}$	$\frac{v(3a/8,b/2)}{a}$
3 × 3	0.25000	-0.34366	-0.39320	-0.26282
5 × 5	0.12500	-0.35506	-0.38788	-0.28912
7 × 7	0.08333	-0.35127	-0.38461	-0.28889
9 × 9	0.06250	-0.35045	-0.38407	-0.28892
11 × 11	0.05000	-0.35019	-0.38398	-0.28877
13 × 13	0.04167	-0.35007	-0.38396	-0.28883
15 × 15	0.03571	-0.35001	-0.38395	-0.28880
17 × 17	0.03125	-0.34997	-0.38395	-0.28882
19 × 19	0.02778	-0.34995	-0.38395	-0.28881

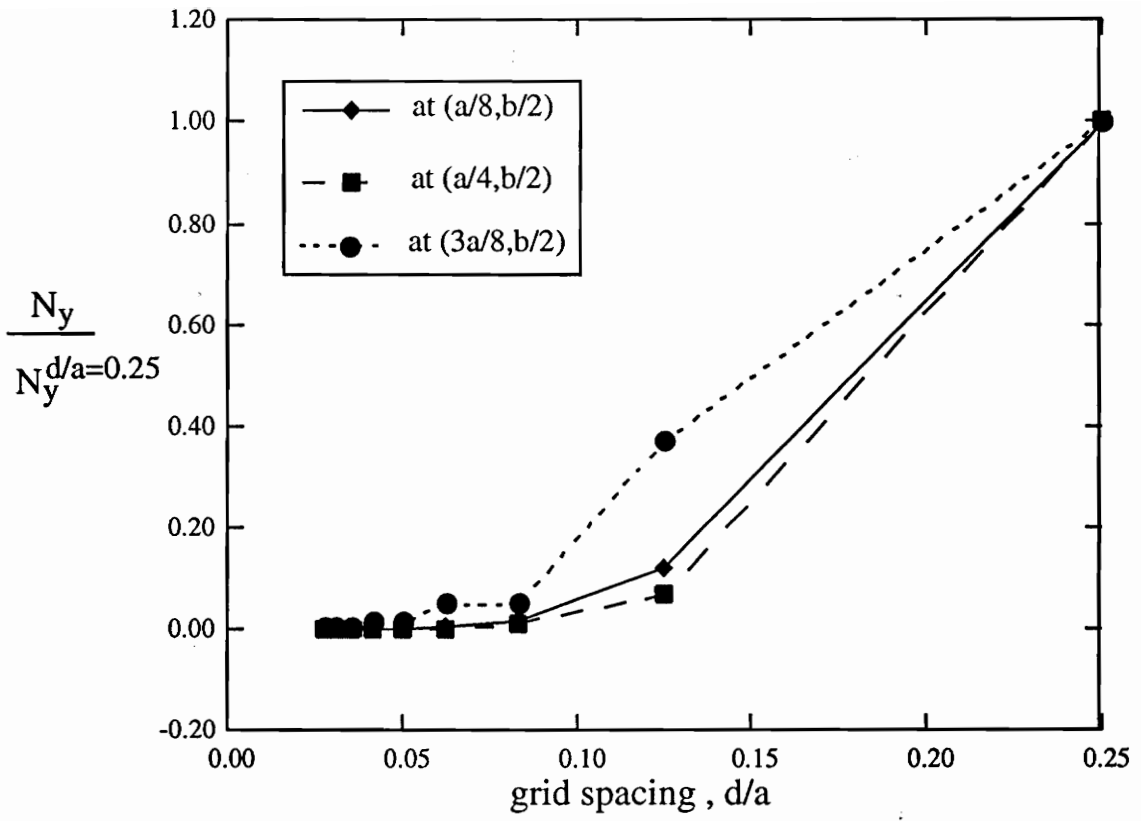


Figure 3.7 Convergence of  $N_y$  at  $y=b/2$  for  $a/b=0.5$ .

**Table 3.2 Convergence of the Displacements at  $y = b/2$  for  $a/b = 0.5$ .**

Grid	Spacing, $d/a$	$\frac{u(a/8, b/2)}{a}$	$\frac{u(a/4, b/2)}{a}$	$\frac{u(3a/8, b/2)}{a}$
3 × 3	0.25000	0.047312	0.074921	0.30770
5 × 5	0.12500	0.054007	0.11730	0.34126
7 × 7	0.08333	0.048447	0.11919	0.35644
9 × 9	0.06250	0.046620	0.11987	0.35798
11 × 11	0.05000	0.045752	0.12026	0.35853
13 × 13	0.04167	0.045332	0.12048	0.35860
15 × 15	0.03571	0.045101	0.12060	0.35867
17 × 17	0.03125	0.044974	0.12066	0.35868
19 × 19	0.02778	0.044899	0.12069	0.35869
21 × 21	0.02500	0.044886	0.12071	0.35869
Grid	Spacing, $d/a$	$\frac{v(a/8, b/2)}{a}$	$\frac{v(a/4, b/2)}{a}$	$\frac{v(3a/8, b/2)}{a}$
3 × 3	0.25000	-0.56765	-0.60959	-0.48762
5 × 5	0.12500	-0.60008	-0.63489	-0.53959
7 × 7	0.08333	-0.60029	-0.63441	-0.54051
9 × 9	0.06250	-0.59982	-0.63376	-0.54019
11 × 11	0.05000	-0.59957	-0.63361	-0.53993
13 × 13	0.04167	-0.59940	-0.63357	-0.53992
15 × 15	0.03571	-0.59918	-0.63357	-0.53987
17 × 17	0.03125	-0.59916	-0.63357	-0.53987
19 × 19	0.02778	-0.59916	-0.63358	-0.53985
21 × 21	0.02500	-0.59902	-0.63359	-0.53985

satisfied for that grid size. The convergence of  $N_y$  for the long panel is shown in Figure 3.8. The values also converge to zero, although the value of  $N_y(3a/8, b/2)$  is zero only for the  $19 \times 19$  grid. The convergence of the displacements for the long panel is shown in Table 3.3. The displacements seem to converge at the value of  $d$  corresponding to a  $13 \times 13$  grid; however, the value of  $N_y$  has not converged to zero for this grid. The reason for this discrepancy is most likely that the Hermite polynomial series does not converge as well for the derivatives of the displacements as it does for the displacements themselves. This phenomenon would explain why no large improvements in  $N_y$  are seen between the  $3 \times 3$  grid and the  $5 \times 5$  grid, and also between the  $7 \times 7$  grid and the  $9 \times 9$  grid. With this in mind, a  $19 \times 19$  grid has been used for long panels.

In summary, for square panels, a model with an angle difference of  $90^\circ$  converges adequately with a  $15 \times 15$  grid. While the convergence of short and long panels requires the use of a  $19 \times 19$  grid, it was subsequently found that it is possible to achieve convergence using a  $15 \times 15$  grid if the difference between  $T_0$  and  $T_1$  is less than  $60^\circ$ .

## 3.5 Closed Form Solutions

Simple solutions to the in-plane problem are desired in order to make the code for the buckling analysis as efficient and inexpensive as possible. In this section, closed form solutions to the in-plane response of variable stiffness panels under the four different types of boundary conditions are derived. The solutions for cases II-IV are exact.

### 3.5.1 Closed Form Solution, Case I

For a panel with free transverse edges, loaded by uniform uniaxial end shortening,  $u_0$ , along the  $x$  direction, the  $u$  displacement can be assumed to be a function of the  $x$  coordinate only, independent of the transverse coordinate  $y$ . As shown in Figure 3.1, for the free transverse edges, the transverse stress resultant is zero along  $y = \pm b/2$ . Assuming that the transverse stress resultant,  $N_y$ , is identically zero for all  $x$  and  $y$ , the expression

$$N_y = A_{12} \frac{\partial u}{\partial x} + A_{22} \frac{\partial v}{\partial x} = 0, \quad (3.33)$$

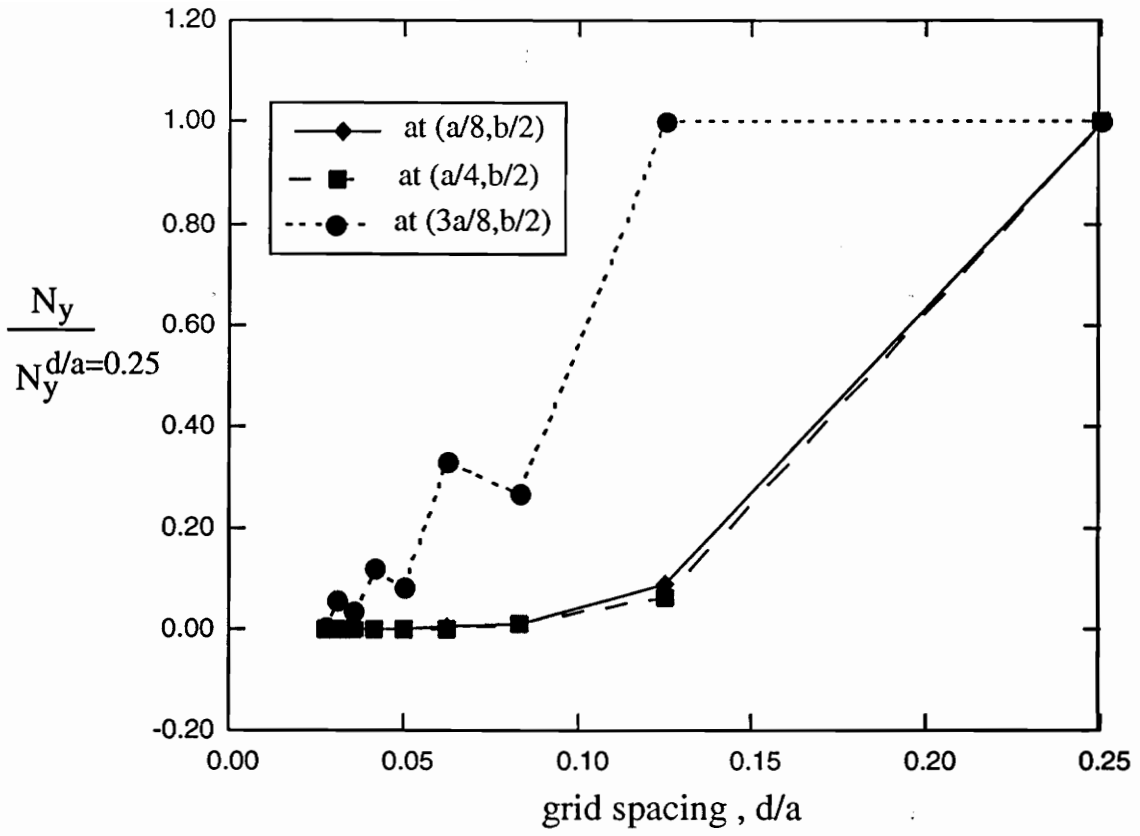


Figure 3.8 Convergence of  $N_y$  at  $y=b/2$  for  $a/b=2.0$ .

**Table 3.3 Convergence of the Displacements at  $y = b/2$  for  $a/b = 2.0$ .**

Grid	Spacing, $d/a$	$\frac{u(a/8, b/2)}{a}$	$\frac{u(a/4, b/2)}{a}$	$\frac{u(3a/8, b/2)}{a}$
3 × 3	0.25000	0.042757	0.10215	0.39785
5 × 5	0.12500	0.053782	0.13693	0.39518
7 × 7	0.08333	0.052548	0.13852	0.39583
9 × 9	0.06250	0.052500	0.13878	0.39561
11 × 11	0.05000	0.052468	0.13886	0.39573
13 × 13	0.04167	0.052467	0.13888	0.39569
15 × 15	0.03571	0.052464	0.13889	0.39572
17 × 17	0.03125	0.052464	0.13890	0.39571
19 × 19	0.02778	0.052463	0.13890	0.39572
Grid	Spacing, $d/a$	$\frac{v(a/8, b/2)}{a}$	$\frac{v(a/4, b/2)}{a}$	$\frac{v(3a/8, b/2)}{a}$
3 × 3	0.25000	-0.19685	-0.25736	-0.14581
5 × 5	0.12500	-0.20611	-0.24863	-0.15329
7 × 7	0.08333	-0.20369	-0.24588	-0.15421
9 × 9	0.06250	-0.20341	-0.24574	-0.15456
11 × 11	0.05000	-0.20328	-0.24568	-0.15453
13 × 13	0.04167	-0.20324	-0.24566	-0.15461
15 × 15	0.03571	-0.20321	-0.24566	-0.15459
17 × 17	0.03125	-0.20320	-0.24565	-0.15461
19 × 19	0.02778	-0.20320	-0.24565	-0.15461

can be used to solve for the transverse strain as,

$$\frac{\partial v}{\partial y} = -\frac{A_{12}(x)}{A_{22}(x)} \frac{\partial u}{\partial x}. \quad (3.34)$$

Next, it is assumed that the axial stress resultant,  $N_x$ , has a constant value,  $N_o$ , everywhere in the panel. By substituting equation 3.34, the expression

$$N_x = A_{11} \frac{\partial u}{\partial x} + A_{12} \frac{\partial v}{\partial x} = N_o, \quad (3.35)$$

can be solved for the axial strain as,

$$\frac{\partial u}{\partial x} = \frac{N_o A_{22}}{A_{11} A_{22} - A_{12}^2}. \quad (3.36)$$

When the expressions for the  $A_{ij}$  from equation 2.35 are substituted into equation 3.36, and the resulting expression is simplified using trigonometric identities, the axial strain becomes,

$$\frac{\partial u}{\partial x} = \frac{2N_x [U_1 - U_2 \cos(2\theta) + U_3 \cos(4\theta)]}{h [2U_1^2 - U_2^2 - 2U_4^2 - U_2^2 \cos(4\theta) + 4U_1 U_3 \cos(4\theta) + 4U_3 U_4 \cos(4\theta)]}, \quad (3.37)$$

where the orientation angle  $\theta$  is a function of the  $x$  coordinate, as given by equation 1.1. Integration of equation 3.37 with respect to  $x$  results in the closed form expression for the  $u$  displacement. The integration has been carried out using the Mathematica symbolic manipulator. Each term in equation 3.37 has been integrated individually. By using trigonometric identities and other substitutions, for a linear angle variation, the  $u$  displacement field is given in three parts plus a constant of integration as,

$$u(x) = u_1(x) + u_2(x) + u_3(x) + u_r, \quad (3.38)$$

where

$$u_1(x) = \frac{-aN_o U_1 \tan^{-1} \left[ \frac{(C_2 - C_1) \tan(2\theta)}{\sqrt{C_1^2 - C_2^2}} \right]}{2\sqrt{C_1^2 - C_2^2} (T_o - T_1) h}, \quad (3.39)$$

$$u_2(x) = \frac{aN_o U_2 \tan^{-1} \left[ \frac{2C_2 \sin(2\theta)}{\sqrt{-2(C_1 C_2 + C_2^2)}} \right]}{2\sqrt{-2(C_1 C_2 + C_2^2)} (T_o - T_1) h}, \quad (3.40)$$

$$u_3(x) = \frac{aN_o U_2 \theta}{C_2 (T_o - T_1) h} + \frac{aN_o U_3 C_1 \tan^{-1} \left[ \frac{(C_2 - C_1) \tan(2\theta)}{\sqrt{C_1^2 - C_2^2}} \right]}{2C_2 \sqrt{C_1^2 - C_2^2} (T_o - T_1) h}, \quad (3.41)$$

and where

$$C_1 = 2U_1^2 - U_2^2 - 2U_4^2, \quad (3.42)$$

and

$$C_2 = 4U_1U_3 + 4U_3U_4 - U_2^2. \quad (3.43)$$

The constant of integration  $u_r$  can be evaluated by suppressing the rigid body motion of the panel, requiring that  $u = 0$  at  $x/a = 0$ .

In order to obtain the  $v$  displacement field, equations 3.36 and 2.35 are substituted into equation 3.34 and the resulting expression is integrated with respect to  $y$ . The  $v$  displacement field is given by

$$v(x, y) = \frac{-2N_o [U_4 - U_3 \cos(4\theta)] y}{h [C_1 + C_2 \cos(4\theta)]}. \quad (3.44)$$

Equation 3.38 can be used to estimate the resulting stress resultant due to an applied end displacement, or vice-versa. Once the value of  $N_o$  is known, the transverse displacements for the panel,  $v(x, y)$ , may be obtained using equation 3.44. The inputs for both equations are  $T_o$ ,  $T_1$ ,  $a$ ,  $b$ ,  $h$ , the material properties, and the applied end displacement  $u(a/2, y) = u_o$ . Note that the  $u$  displacement field is independent of  $b$ , as is the case for straight fiber panels.

### 3.5.2 Closed Form Solution, Case II

When the transverse edges,  $y = \pm b/2$ , are fixed, it is possible to obtain an exact closed form solution for the displacement fields and stress resultants. The boundary conditions for this case are illustrated in Figure 3.1. Since  $v = 0$  along  $y = b/2$ ,  $y = 0$  (plane of symmetry), and  $y = -b/2$ , it is concluded that  $v(x, y) = 0$  for all  $x$  and  $y$ . In addition, since all four edges of the panel remain straight, and the panel is assumed to remain flat, the shear strain and shear stress resultant are zero for all  $x$  and  $y$ . Since the partial derivative of  $u$  with respect to  $y$  must be zero for all  $x$  and  $y$ , the  $u$  displacement field is only a function of  $x$ .

The first equilibrium equation simplifies to,

$$\frac{\partial N_x}{\partial x} = A_{11} \frac{\partial^2 u}{\partial x^2} + \frac{\partial A_{11}}{\partial x} \frac{\partial u}{\partial x} = 0 \quad (3.45)$$

Due to the boundary conditions, the elliptic equations are decoupled, and the  $u$  displacement field can be obtained in closed form. The previous expression implies that

$$N_x = A_{11} \frac{\partial u}{\partial x} = N_o + f(y), \quad (3.46)$$

where  $N_o$  is a constant. However, since  $u$  is independent of  $y$ , the function  $f(y)$  must be identically zero. Solving the above equation for the axial strain yields:

$$\frac{\partial u}{\partial x} = \frac{N_o}{A_{11}}. \quad (3.47)$$

By integrating equation 3.47 such that,

$$u = \int \frac{N_o}{A_{11}} dx, \quad (3.48)$$

the  $u$  displacement field is obtained. The integral for  $u$  can be evaluated by substituting for  $A_{11}$  from equation 2.35, to obtain

$$u(x) = \int \frac{N_o}{h[U_1 + U_2 \cos(2\theta) + U_3 \cos(4\theta)]} dx, \quad (3.49)$$

where  $\theta = \theta(x)$ . The above integration can be carried out by first changing the integration variable to  $\theta$  using the linear relationship between  $\theta$  and  $x$ , such that

$$dx = \frac{a d\theta}{2(T_1 - T_o)}. \quad (3.50)$$

The cosine terms are rewritten in their complex exponential form using the relationship,

$$\cos \theta = \frac{e^{i\theta} + e^{-i\theta}}{2}. \quad (3.51)$$

Through these substitutions the integral becomes

$$u(\theta) = \frac{N_o a}{2(T_1 - T_o) h} \int \frac{d\theta}{U_1 + \frac{U_2}{2} (e^{2i\theta} + e^{-2i\theta}) + \frac{U_3}{2} (e^{4i\theta} + e^{-4i\theta})}. \quad (3.52)$$

The variable transformation,  $e^{2i\theta} = t$ , is applied to equation 3.52, and the  $u$  displacement is now given by

$$u(t) = \frac{N_o a}{2ihU_3(T_1 - T_o)} \int \frac{t dt}{t^4 + \frac{2U_1}{U_3} t^2 + \frac{U_2}{U_3} (t^3 + t) + 1}. \quad (3.53)$$

This integral may now be evaluated using a partial fraction expansion. The roots of the polynomial in the denominator are given by

$$t_1 = \frac{1}{2}(\sqrt{-4 + (-\omega + \phi)^2} + \omega - \phi), \quad (3.54)$$

$$t_2 = \frac{1}{2}(-\sqrt{-4 + (-\omega + \phi)^2} + \omega - \phi), \quad (3.55)$$

$$t_3 = \frac{1}{2}(\sqrt{-4 + (\omega + \phi)^2} - \omega - \phi), \quad (3.56)$$

$$t_4 = \frac{1}{2}(-\sqrt{-4 + (\omega + \phi)^2} - \omega - \phi), \quad (3.57)$$

where

$$\omega = \sqrt{2 + \frac{U_2^2}{4U_3^2} - \frac{2U_1}{U_3}}, \quad (3.58)$$

and

$$\phi = \frac{U_2}{2U_3}. \quad (3.59)$$

If the partial fraction expansion is now implemented, the integral

$$u(t) = \frac{N_o a}{2ihU_3(T_1 - T_o)} \int \frac{q_1}{t - t_1} + \frac{q_2}{t - t_2} + \frac{q_3}{t - t_3} + \frac{q_4}{t - t_4} dt, \quad (3.60)$$

must equal equation 3.53. The values of the  $q_j$  are obtained by solving the resulting linear system of equations:

$$\begin{bmatrix} 1 & 1 & 1 & 1 \\ -t_2 - t_3 - t_4 & -t_1 - t_3 - t_4 & -t_1 - t_2 - t_4 & -t_1 - t_2 - t_3 \\ t_2 t_3 + t_2 t_4 + t_3 t_4 & t_1 t_3 + t_1 t_4 + t_3 t_4 & t_1 t_2 + t_1 t_4 + t_2 t_4 & t_1 t_2 + t_1 t_3 + t_2 t_3 \\ -t_2 t_3 t_4 & -t_1 t_3 t_4 & -t_1 t_2 t_4 & -t_1 t_2 t_3 \end{bmatrix} \begin{Bmatrix} q_1 \\ q_2 \\ q_3 \\ q_4 \end{Bmatrix} = \begin{Bmatrix} 0 \\ 0 \\ 1 \\ 0 \end{Bmatrix}. \quad (3.61)$$

Finally, the integral is obtained as

$$u(x) = \frac{-iN_o a}{2hU_3(T_1 - T_o)} \sum_{j=1}^4 q_j \log(e^{2i\theta} - t_j) + C, \quad (3.62)$$

where  $\theta = \theta(x)$  and the constant  $C$  is a complex number found by suppressing the rigid body motion of the panel.

The second equilibrium equation simplifies to

$$\frac{\partial N_y}{\partial y} = 0, \quad (3.63)$$

where

$$N_y = A_{12} \frac{\partial u}{\partial x}. \quad (3.64)$$

The equilibrium equation implies that  $N_y$  is a function of  $x$  only. By substituting for the axial strain from equation 3.47 into equation 3.64, the expression for the transverse stress resultant becomes,

$$N_y(x) = \frac{A_{12}}{A_{11}} N_o. \quad (3.65)$$

The closed form solution for this case provides exact values of the displacements and stress resultants for any panel. This solution may be used instead of the computationally intensive numerical technique to analyze the elastic response of the variable stiffness panels when the transverse edges are fixed.

### 3.5.3 Closed Form Solution, Case III

For this case, there is an applied transverse displacement  $v_o$  at  $y/b = 0.5$ . This loading condition is such that the edges remain straight during deformation. There is no shear deformation, so the  $v$  displacement field is independent of  $x$ , and the  $u$  displacement field is independent of  $y$ . Due to the lack of shear, the equilibrium equations simplify, since terms containing partial derivatives of  $u$  with respect to  $y$  and partial derivatives of  $v$  with respect to  $x$  vanish. For this case they are given by,

$$A_{11}(x) \frac{\partial^2 u}{\partial x^2} + \frac{\partial A_{11}(x)}{\partial x} \frac{\partial u}{\partial x} + \frac{\partial A_{12}(x)}{\partial x} \frac{\partial v}{\partial y} = 0, \quad (3.66)$$

and

$$A_{22}(x) \frac{\partial^2 v}{\partial y^2} = 0. \quad (3.67)$$

From the second equation it is concluded that  $v$  displacement is a linear function of  $y$ . Since the applied transverse displacement at  $y = b/2$  is  $v_o$ , and the symmetry condition requires that  $v = 0$  at  $y = 0$ , the  $v$  displacement field is described by

$$v(x, y) = \frac{2v_o}{b} y. \quad (3.68)$$

Equation 3.66 may be written in the form,

$$\frac{\partial N_x}{\partial x} = 0. \quad (3.69)$$

By integrating this equation, the following expression for the axial stress resultant is obtained,

$$N_x = N_o + f(y). \quad (3.70)$$

However, due to the boundary conditions,  $N_x$  is zero at  $x = a/2$ , so it must be zero for all  $x$  and  $y$ . Therefore, for this loading condition, the only load is in the form of a transverse stress resultant,  $N_y$ .

Solving for the transverse stress resultant is fairly simple. Since the axial stress resultant is zero, the equation,

$$N_x = A_{11} \frac{\partial u}{\partial x} + A_{12} \frac{\partial v}{\partial y} = 0, \quad (3.71)$$

may be solved for the axial strain and combined with equation 3.68 to yield,

$$\frac{\partial u}{\partial x} = -2 \frac{A_{12} v_o}{A_{11} b}. \quad (3.72)$$

The axial strain is then substituted into the stress-strain relation for  $N_y$ . The result is

$$N_y = \frac{2v_o}{b} \left( A_{22} - \frac{A_{12}^2}{A_{11}} \right), \quad (3.73)$$

which is a function of  $x$  only.

The  $u$  displacement field is also a function of  $x$  only, and it is obtained by integrating equation 3.72 using the techniques from the previous section. The integral needed to obtain  $u = u(x)$  is given by

$$u(x) = -\frac{2v_o}{b} \int \frac{U_4 - U_3 \cos 4\theta}{[U_1 + U_2 \cos(2\theta) + U_3 \cos(4\theta)]} dx, \quad (3.74)$$

where  $\theta = \theta(x)$ . As has been shown previously, the integration variable is changed to  $\theta$  by using the linear relationship between  $\theta$  and  $x$ . The exponential form of the cosine terms is then substituted, as given by equation 3.51. After making the variable transformation to  $t$ , the integral becomes

$$u(t) = -\frac{v_o ia}{2b(T_1 - T_o)} \int \frac{t^4 - 2\frac{U_4}{U_3}t^2 + 1}{t \left( t^4 + \frac{U_2}{U_3}(t^3 + t) + 2\frac{U_1}{U_3}t^2 + 1 \right)} dt. \quad (3.75)$$

By using a partial fraction expansion, the integral can be expressed as,

$$u(t) = -\frac{v_o ia}{2b(T_1 - T_o)} \int \frac{q'_1}{t - t'_1} + \frac{q'_2}{t - t'_2} + \frac{q'_3}{t - t'_3} + \frac{q'_4}{t - t'_4} + \frac{q'_5}{t - t'_5} dt, \quad (3.76)$$

where the first four roots,  $t'_1, \dots, t'_4$ , are equal to the  $t_j$  described for case II, and the fifth root  $t'_5$  is zero. The constants  $q'_j$  are found by solving the resulting system of 5 equations and 5 unknowns. Finally, the axial displacement is given by,

$$u(x) = \frac{-v_o i a}{2b(T_1 - T_o)} \sum_{j=1}^5 q'_j \log(e^{2i\theta} - t'_j) + C. \quad (3.77)$$

Note that the axial displacement depends on the fiber configuration ( $T_o$  and  $T_1$ ), and on the applied transverse displacement,  $v_o$ . The axial displacement is due to the Poisson expansion in the axial direction when the panel is loaded in the transverse direction.

### 3.5.4 Closed Form Solution, Case IV

For case IV the transverse edges of a variable stiffness panel are allowed to move freely but required to remain straight. The requirement that the integral of  $N_y$  be identically zero ensures that the net load being applied is zero. As in previous cases, since the edges remain straight, the shear strain and stress resultant are zero for all  $x$  and  $y$ . The  $u$  displacement field is only a function of  $x$ ; similarly, the  $v$  displacement field is only a function of  $y$ . The equilibrium equations also simplify to

$$A_{11}(x) \frac{\partial^2 u}{\partial x^2} + \frac{\partial A_{11}(x)}{\partial x} \frac{\partial u}{\partial x} + \frac{\partial A_{12}(x)}{\partial x} \frac{\partial v}{\partial y} = 0, \quad (3.78)$$

and

$$A_{22}(x) \frac{\partial^2 v}{\partial y^2} = 0. \quad (3.79)$$

The solution for the  $v$  displacement, from equation 3.79, is given by  $v(x, y) = \epsilon_o y$ , where  $\epsilon_o$  is an unknown constant such that  $\epsilon_o b/2$  is the displacement at  $y = b/2$  necessary to satisfy the integral condition,

$$P_y = \int_{-\frac{a}{2}}^{\frac{a}{2}} N_y \left( x, \frac{b}{2} \right) dx = 0. \quad (3.80)$$

The  $u$  displacement could be obtained by solving 3.79, but an alternative method is used below.

Solving for  $\epsilon_o$  and the  $u$  displacement field involves manipulating the governing equations. Equation 3.78 is equivalent to

$$\frac{\partial N_x}{\partial x} = 0. \quad (3.81)$$

The axial stress resultant is therefore given by

$$N_x = N_o + f(y) = A_{11} \frac{\partial u}{\partial x} + A_{12} \epsilon_o, \quad (3.82)$$

where  $N_o$  is a constant. Since the right side of the above equation is independent of  $y$ ,  $f(y)$  is zero.

From equation 3.82, the axial strain may be expressed as

$$\frac{\partial u}{\partial x} = \frac{N_o}{A_{11}} - \frac{A_{12}}{A_{11}} \epsilon_o. \quad (3.83)$$

By substitution, the transverse stress resultant is given by:

$$N_y = \frac{A_{12} N_o}{A_{11}} + \frac{A_{22} A_{11} - A_{12}^2}{A_{11}} \epsilon_o. \quad (3.84)$$

Recall that the  $A_{ij}$  are functions of  $x$ . The integral of  $N_y$  at  $y = b/2$  along the  $x$  direction becomes

$$P_y = \int_{-\frac{a}{2}}^{\frac{a}{2}} \frac{A_{12} N_o}{A_{11}} + \frac{A_{22} A_{11} - A_{12}^2}{A_{11}} \epsilon_o \, dx = 0. \quad (3.85)$$

By using the transformation and partial fraction expansion described for case II, the definite integral simplifies to

$$\int_{-\frac{a}{2}}^{\frac{a}{2}} N_y(x, \frac{b}{2}) \, dx = c N_o + d \epsilon_o = 0, \quad (3.86)$$

where the constants  $c$  and  $d$ , which depend on the  $A_{ij}$ , are given by,

$$c = \int_{-\frac{a}{2}}^{\frac{a}{2}} \frac{A_{12}}{A_{11}} \, dx, \quad (3.87)$$

and

$$d = \int_{-\frac{a}{2}}^{\frac{a}{2}} \frac{A_{22} A_{11} - A_{12}^2}{A_{11}} \, dx. \quad (3.88)$$

The transverse strain that satisfies the integral condition for a given load  $N_o$  is therefore given by

$$\epsilon_o = -\frac{c}{d} N_o. \quad (3.89)$$

The  $u$  displacement field is obtained by integrating equation 3.83. The integral of this expression is

$$u(x) = \frac{-i N_o a}{2(T_1 - T_o)} \left\{ \frac{1}{U_3 h} \sum_{j=1}^4 q_j \log(e^{2i\theta} - t_j) - \frac{c}{2d} \sum_{j=1}^5 q'_j \log(e^{2i\theta} - t'_j) \right\} + C, \quad (3.90)$$

where, the  $q_j$  and  $t_j$ , and the  $q'_j$  and  $t'_j$  are equal to those obtained for cases II and III, respectively. Again, the constant  $C$  is evaluated by suppressing the rigid body motion of the panel.

The algorithm for using this closed form solution is rather simple. First the value of  $N_o$  is obtained for the given value of  $u_o$  at  $x = a/2$ . Next, the value of  $\epsilon_o$  is obtained using equations 3.87, 3.88 and 3.89. The displacements, strains and stress resultants are then easily calculated using the remaining formulae.

### 3.6 Overall Panel Stiffness

Engineering applications often require an estimate of the overall stiffness of a structural component. An equivalent panel stiffness  $E_x^{eq}$  can be defined as a global quantity for a variable stiffness panel by

$$E_x^{eq} = \frac{F_x a}{h b u_o} \quad \text{where} \quad F_x = \int_0^{b/2} N_x(a/2, y) dy, \quad (3.91)$$

and where  $u_o$  is the end shortening, or  $u(a/2, y)$ . The value of  $E_x^{eq}$  is a measure of the stiffness encountered when prescribing the displacement  $u_o$  at the panel end. For panels under case III boundary conditions, a similar quantity,  $E_y^{eq}$ , is defined by,

$$E_y^{eq} = \frac{F_y b}{h a v_o} \quad \text{where} \quad F_y = \int_0^{a/2} N_y(x, b/2) dx, \quad (3.92)$$

The equivalent stiffnesses of the variable stiffness panels serve as parameters by which comparisons to straight fiber configurations can be made.

### 3.7 Failure Analysis

Since the strains and stresses in the variable stiffness panels will vary as functions of  $x$ , and sometimes also as functions of  $y$ , it is necessary to check for failure at different points in the panel. In this investigation, the failure characteristics of each panel have been assessed using the maximum strain criterion [12]. The maximum strain criterion describes a rectangular envelope within which the strains must lie. If the strains are greater (in the case of tensile strains) or smaller (in the case of compressive strains) than a set of prescribed limits, failure has occurred. The criterion is defined in terms of the strains in the 1-2 coordinate system (see section 1.1) and is given by

$$\begin{aligned}
 X_{\epsilon_c} < \epsilon_1 < X_{\epsilon_t} \\
 Y_{\epsilon_c} < \epsilon_2 < Y_{\epsilon_t} \\
 |\gamma_{12}| < S_{\epsilon},
 \end{aligned}
 \tag{3.93}$$

where  $X_{\epsilon_c}$  and  $Y_{\epsilon_c}$  are the limits for the compressive strains in the 1 and 2 directions, respectively, and  $X_{\epsilon_t}$  and  $Y_{\epsilon_t}$  are the limits for the tensile strains in the 1 and 2 directions, respectively; the absolute limit for the shear strain is  $\gamma_{12}$  is given by  $S_{\epsilon}$ . For the material system defined in section 2.1, the maximum and minimum allowable values for the strains are given in Table 3.4. Note that while the 1 direction compressive strength is the same in tension as in compression, for the 2 direction the compressive strength is six times larger than the tensile strength.

The algorithm for the variable stiffness panels depends on which boundary condition is being analyzed. For case I, the strains are functions of  $x$  and  $y$ , so the algorithm checks for failure in two dimensions. Equation 3.93 is applied along 50 different values of  $x/a$  for 20 different values of  $y/b$ . This results in a failure grid that consists of 1000 points spread out over the quarter panel area. The subroutine that has been developed compares the 1-2 direction strains to the allowable values and returns the location of failure, the layer ( $+\theta$  or  $-\theta$ ) in which the failure occurred, the allowable that was exceeded, and the ratio of the strain to the allowable value. With this information, the location and mode of the first failure can be obtained. For cases II-IV, the strains are functions of the  $x$  direction only. The algorithm that has been employed is similar to the one for case I, except that 100 check points are used in the  $x$  direction only.

**Table 3.4 Strain Allowables for the T300-N5208 Material System.**

$X_{\epsilon_t}$	$8.29 \times 10^{-3}$
$X_{\epsilon_c}$	$-8.29 \times 10^{-3}$
$Y_{\epsilon_t}$	$3.88 \times 10^{-3}$
$Y_{\epsilon_c}$	$-23.88 \times 10^{-3}$
$S_{\epsilon}$	$9.48 \times 10^{-3}$

# CHAPTER 4

## In-Plane Results and Discussion

### 4.1 Introduction

The results obtained by applying the numerical and closed form solutions developed in Chapter 3 are presented and discussed in this chapter. The results presented here, although normalized, are based on a four layer graphite epoxy  $[\pm\theta]_s$  laminate. Due to symmetry, the results presented are for one quarter of the panel only. A description of the response for each case is presented for square plates. Finally, the overall stiffness of the variable stiffness panels are described, and significant trends that depend on the aspect ratio,  $a/b$ , are highlighted.

Since every possible combination of  $T_0$  and  $T_1$  cannot be studied, it is useful to limit the values of these angles to be used in this study. The values to be studied are first limited to lie between  $0^\circ$  and  $90^\circ$ . This criterion eliminates configurations such as those in which the fiber angle may become both positive and negative within a single layer. An angle of  $T_0 = 45^\circ$  has been chosen, and  $T_1$  is allowed to vary. In this study the in-plane response of panels having  $T_0 = 45^\circ$  and values of  $T_1$  ranging from  $0^\circ$  to  $90^\circ$  in increments of  $15^\circ$  have been modeled. Important trends are investigated using two configurations with large angle changes, one with  $T_1 = 0^\circ$  and the other with  $T_1 = 90^\circ$ .

### 4.2 Case I Boundary Conditions

The form of the governing equations for a variable stiffness panel under Case I boundary conditions cannot be solved via an exact closed form solution. The approximate closed form solution derived in Chapter 3 involves two important assumptions: the transverse stress resultant,  $N_y$ , is assumed to be zero, and axial stress resultant,  $N_x$ , is assumed to be constant throughout the panel area. The numerical solution is, therefore, the only reliable manner in which variable stiffness panels under these boundary conditions may be analyzed. In addition to a discussion on the deformation and stress distribution of these panels, the validity of these assumptions be analyzed in this section in light of results obtained numerically using Hermite collocation.

## 4.2.1 Deformations and Strains

### 4.2.1.1 The $u$ displacement field

For panels with straight fibers loaded in uniaxial compression, the deformation pattern is simple. The  $u$  and  $v$  displacements vary as linear functions of  $x$  and  $y$ , respectively. If the panels have variable stiffnesses, the deformation patterns are not so simple. The numerically calculated  $u$  displacements at  $y/b = 0.3$  are shown in Figure 4.1 as a function of the normalized  $x$  coordinate for various values of  $T_1$ . The values for  $u$  have been normalized with respect to the applied end displacement,  $u_o$ . The panel with  $T_1 = 45^\circ$  is actually a straight fiber panel and exhibits a linear relation between  $u$  and  $x$ . For any variable stiffness panel the  $u$  displacement a non-linear function of  $x$ . As the difference between  $T_o$  and  $T_1$  increases, so does the deviation away from linearity. Hence, the the curves for  $T_1 = 0^\circ$  and  $T_1 = 90^\circ$  bound all the other curves.

The reason for the non-linear relation between  $u$  and  $x$  is best understood in terms of the changes in the axial strain,  $\epsilon_x$ , that result from change in the axial stiffness (see Figure 2.2). The axial strain is shown in Figure 4.2 as a function of the  $x$  and  $y$  coordinates for panels having  $T_1 = 0^\circ$  and  $T_1 = 90^\circ$ . The darker areas represent areas of high axial strain. Note that for both cases the axial strain is a function of  $x$  and  $y$ . For the panel with  $T_1 = 0^\circ$ , the axial strain is highest at  $x/a = 0$ , where the panel is most compliant, and lowest at  $x/a = 0.5$  where the panel is least compliant. Similarly, for the panel having  $T_1 = 90^\circ$  the most compliant part of the panel and the area of highest axial strain are located at  $x = a/2$ ; the least compliant part and the area of lowest axial strain are located at  $x/a = 0$ . From the definition of  $\epsilon_x$  it follows that a  $u$  vs.  $x$  curve for a panel with  $T_1 = 0^\circ$  must have a lower slope at  $x/a = 0.5$  than it does at  $x/a = 0$ , and hence the curve must be convex. The opposite is true for the panel with  $T_1 = 90^\circ$  and the  $u$  vs.  $x$  curve must be concave. The shape of the curves in Figure 4.1 is therefore determined by the change in the axial stiffness. Concave curves result when the angle  $T_1$  is smaller than  $T_o$ , and convex curves result when  $T_1$  is larger than  $T_o$ . The curves for  $T_1 = 75^\circ$  and  $T_1 = 90^\circ$  in Figure 4.1 are almost identical because, as was observed in Chapter 2, the axial stiffness distributions for both configurations are nearly identical.

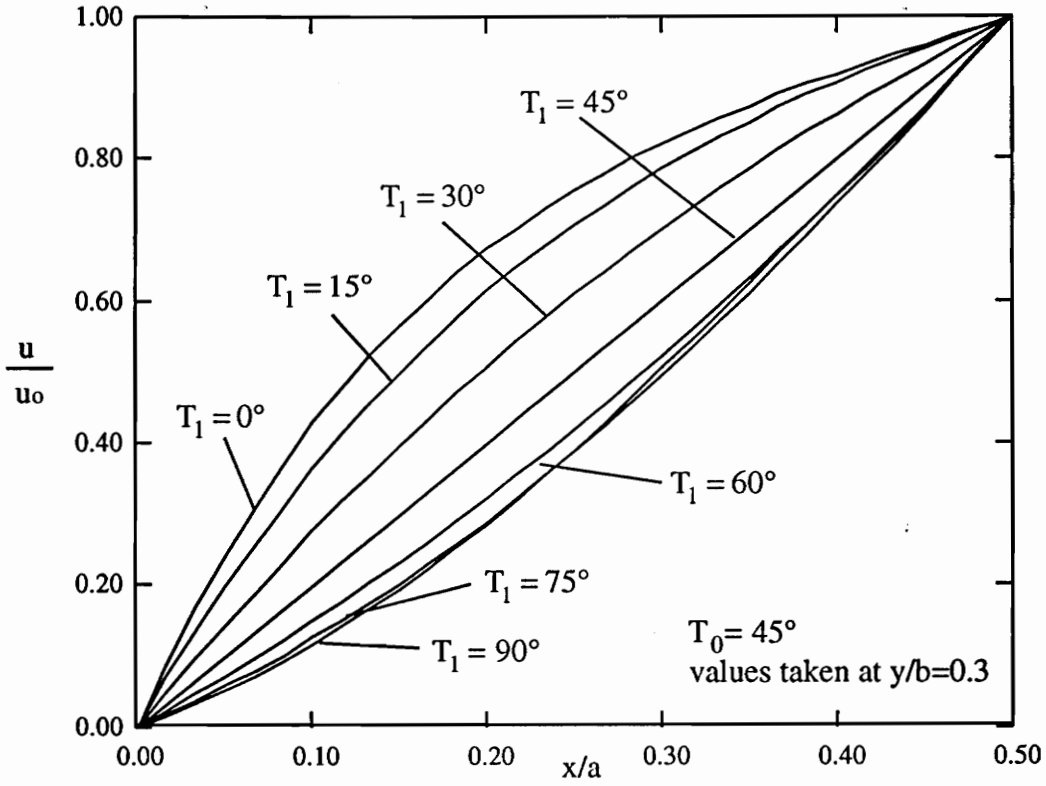


**Figure 4.1** The  $u$  Displacement for Case I Panels as a Function of  $x/a$  for Various Values of  $T_1$ .

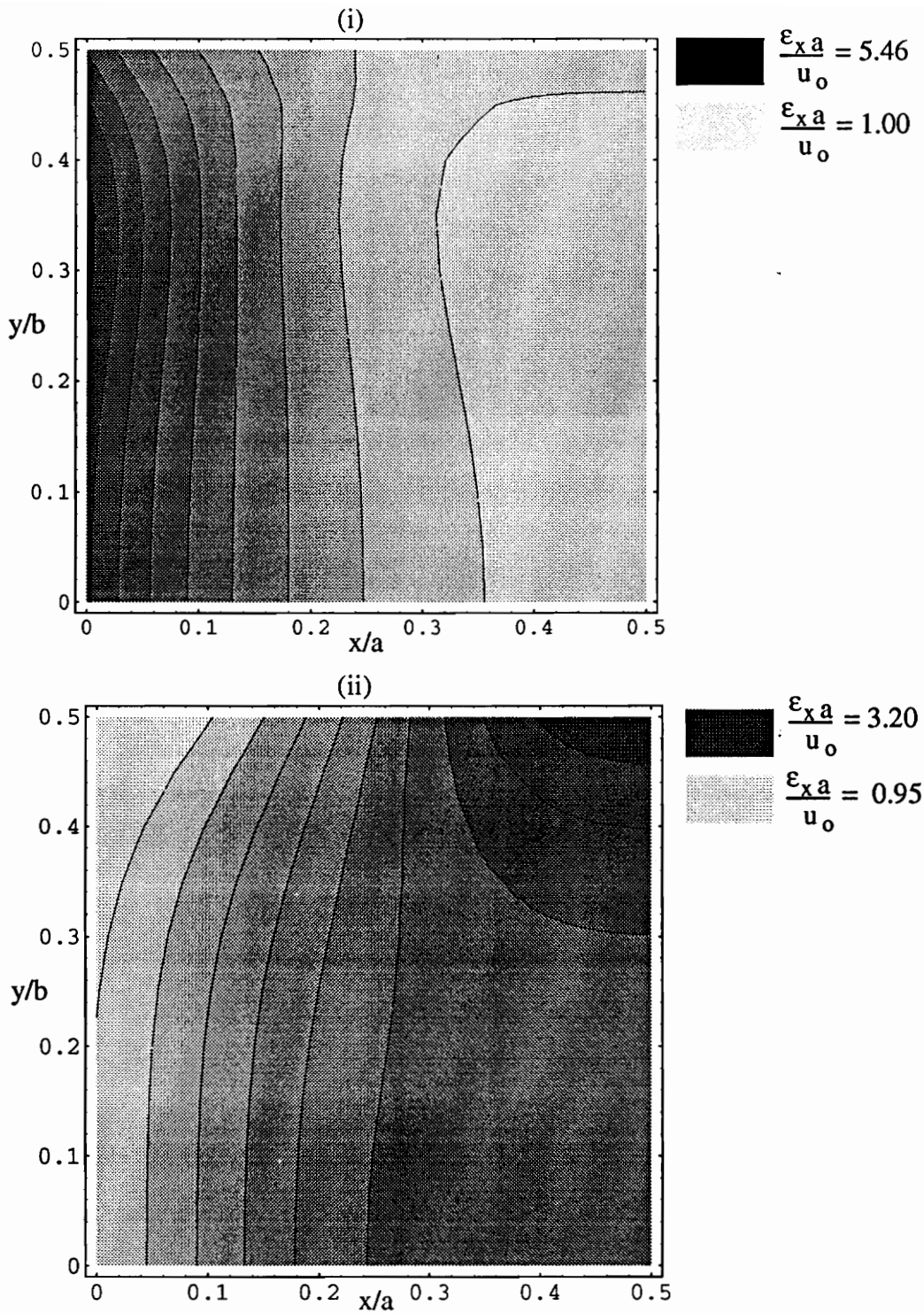


**Figure 4.2** Normalized Axial Strain,  $\epsilon_x$ , for (i)  $T_0 = 45^\circ$ ,  $T_1 = 0^\circ$  and (ii)  $T_0 = 45^\circ$ ,  $T_1 = 90^\circ$  Panels with  $a/b = 1$ , as a Function of  $x$  and  $y$ .

The normalized  $u$  displacement at  $x/a = 0.3$  is shown in Figure 4.3 as a function of  $y/b$ . For the panel with  $T_1 = 45^\circ$  the line is flat. Since for straight fiber panels  $u$  is independent of  $y$ . The curves for the variable stiffness panels are almost flat for values of  $y/b$  less than 0.20. However, for values of  $y/b$  greater than 0.20 there are significant changes in  $u$ . For example, for the panel with  $T_1 = 0^\circ$  the value of  $u$  at  $y/b = 0.5$  is 10% less than at  $y/b = 0$ ; for  $T_1 = 90^\circ$  the change is 26%. Note that the curves for  $T_1 = 30^\circ$  and  $T_1 = 60^\circ$  are nearly flat, since these values are close to  $45^\circ$ . Finally, the reasons for the changes in  $u$  with respect to  $y$ , and for the small areas of high strain seen in Figure 4.2 will be explained in more detail after the discussion on the  $v$  displacement field.

#### 4.2.1.2 The $v$ displacement field

It was shown in Chapter 2 that the equivalent Poisson's ratio,  $\nu_{xy}$ , changes as a function of  $x$  for the variable stiffness panels (see Figure 2.5). The transverse expansion of the panel due to the compressive load depends on  $\nu_{xy}$  and the axial strain,  $\epsilon_x$ . Therefore, since both  $\nu_{xy}$  and  $\epsilon_x$  are functions of  $x$ , the transverse deformation also depends on  $x$ . Since the edge at  $y/b = 0.5$  is free and initially straight, when a compressive load is applied, it deforms in a non-uniform fashion along the  $x$  direction. A plot of the transverse displacement  $v$  at  $y/b = 0.5$  is shown as a function of  $x$  in Figure 4.4. The curves have been normalized with respect to the applied end displacement,  $u_0$ . The curve for the panel with  $T_1 = 45^\circ$  is flat because panels with straight fibers expand uniformly. However, the curves for any variable stiffness panel are not flat; instead, the panels deform more at  $x/a = 0$  than they do at  $x/a = 0.5$ . The panel with  $T_1 = 0^\circ$  has the largest transverse deformation because as  $x/a$  approaches zero the area of high axial strain coincides with a large value for  $\nu_{xy}$ . Although the panel with  $T_1 = 90^\circ$  has the highest axial strain at  $x/a = 0.5$ , the largest transverse deflection occurs at  $x/a = 0$  because there the effective Poisson's ratio is 47 times larger than at  $x/a = 0.5$ . The non-uniformity of the transverse expansion increases as the difference between  $T_0$  and  $T_1$  increases, and the edges of the panels with  $T_1 = 30^\circ$  and  $T_1 = 60^\circ$  exhibit only small changes in the  $v$  displacement along  $y/b = 0.5$ .

The variation of  $v$  as a function of  $y/b$  and  $T_1$  is shown in Figure 4.5 at the panel end,  $x/a = 0.5$ . The relationship between  $v$  and  $y/b$  is linear for most values of  $T_1$ , except for  $T_1 = 0^\circ$  and  $T_1 = 15^\circ$ .

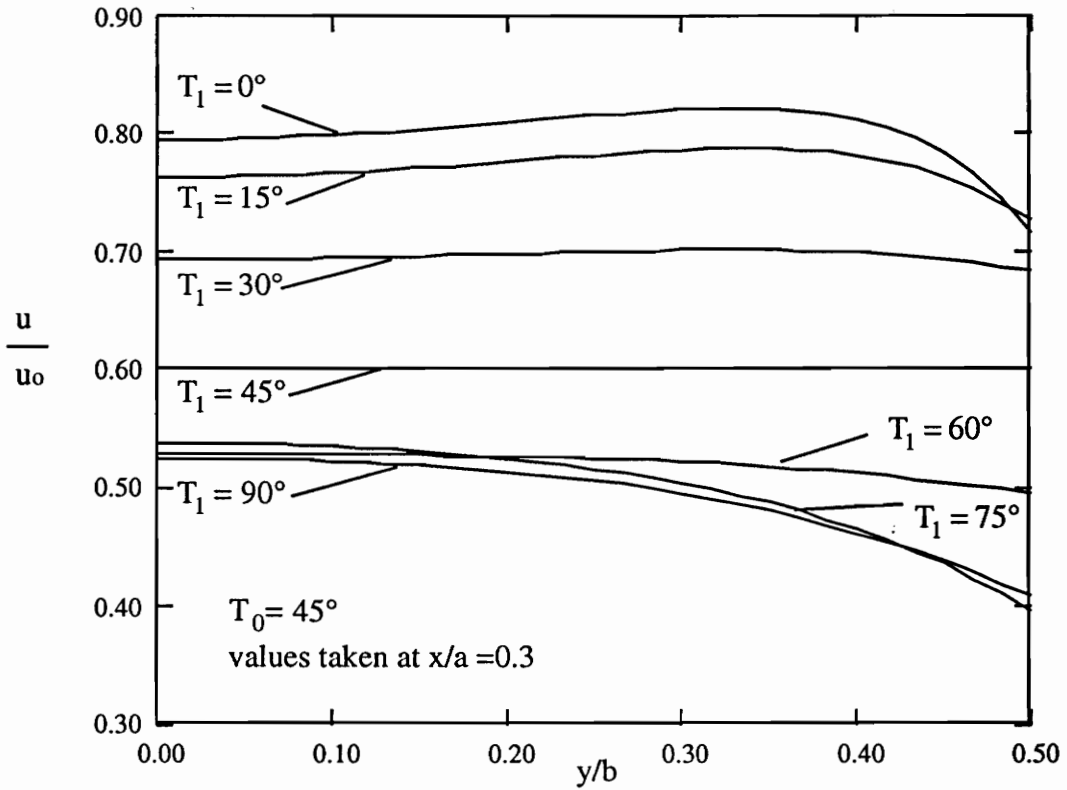


**Figure 4.3** The  $u$  Displacement for Case I as a Function of  $y/b$  for Various Values of  $T_1$ .

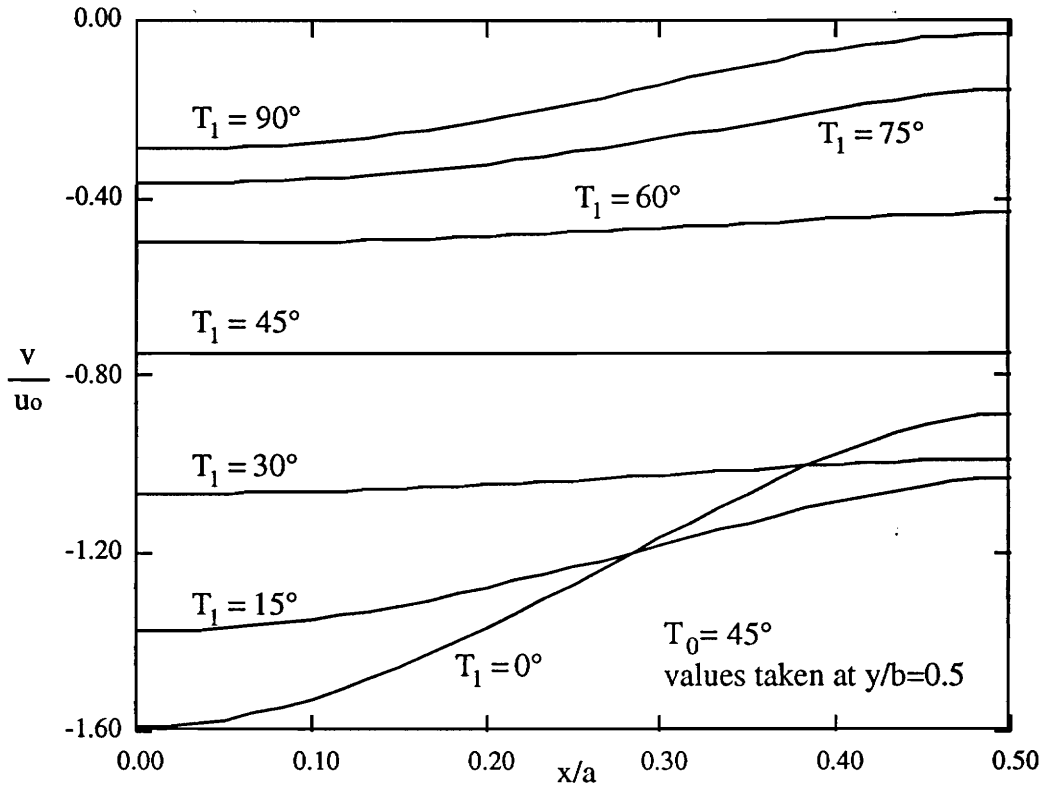


**Figure 4.4** The  $v$  Displacement for Case I as a Function of  $x/a$  for Various Values of  $T_1$ .

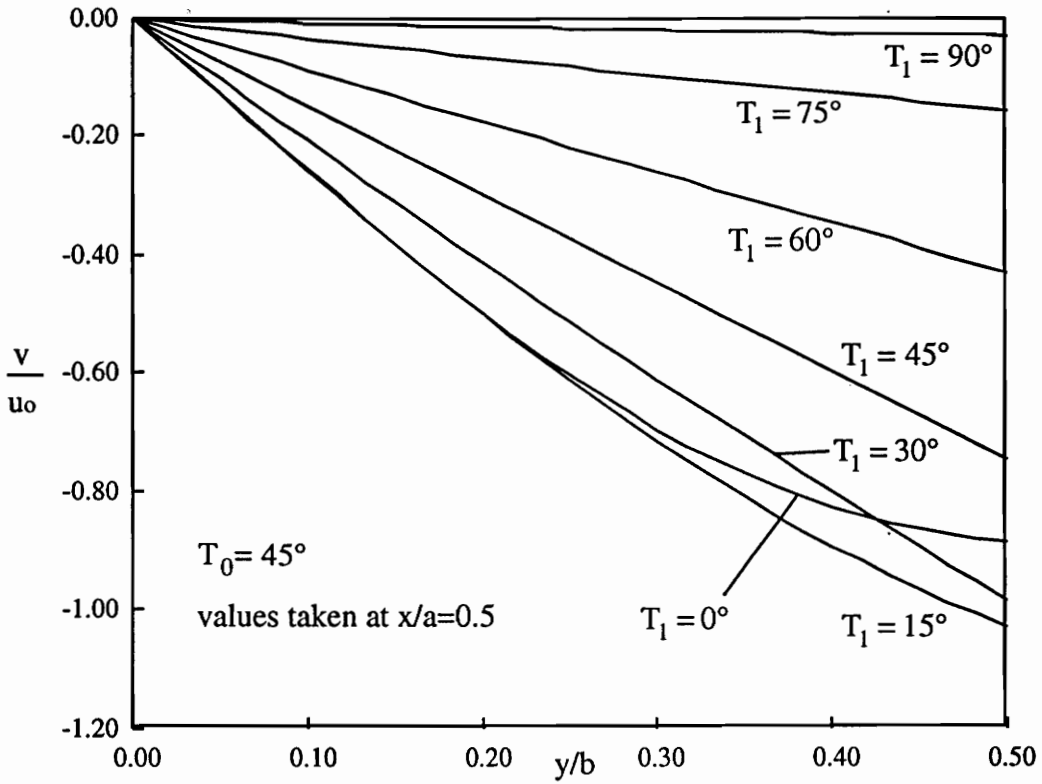


**Figure 4.5** The  $v$  Displacement for Case I as a Function of  $y/b$  for Various Values of  $T_1$ .

Recall from the formulation of the boundary conditions that along  $y/b = 0.5$  the transverse stress resultant must be zero, or

$$\frac{\partial v}{\partial y} = -\frac{A_{12}}{A_{22}} \frac{\partial u}{\partial x} = -\frac{A_{12}}{A_{22}} \epsilon_x. \quad (4.1)$$

Hence, the slope of the curves in Figure 4.5 must be such that at  $y/b = 0.5$  the boundary condition is satisfied. It has been shown in Figure 4.2 that the lowest value of  $\epsilon_x$  occurs at  $(x/a, y/b) = (0.5, 0.5)$ , and this is the reason why Figure 4.5 the curves for  $T_1 = 0^\circ$  and  $T_1 = 15^\circ$  do not have a constant slope and bend upward close to the boundary.

A map of the transverse strain is shown in Figure 4.6 for panels having  $T_1 = 0^\circ$  and  $T_1 = 90^\circ$ . The areas of high strain are identified by the dark colors. The transverse strain is a function of  $x$  and  $y$ . Both panels have areas of high transverse strain at  $x/a = 0$ , which, as was shown in Figure 4.4, is the location of the largest amount of transverse deformation for both panels. Close to the upper boundary,  $y/b = 0.5$ , there is a steady decrease in  $\epsilon_y$  along the  $x$  direction for the  $T_1 = 0^\circ$  configuration. This may be attributed to the large changes in  $\nu_{xy}$  that take place along the  $x$  direction for that configuration. By contrast,  $\epsilon_y$  is uniform for all  $x/a$  values greater than 0.35 for the  $T_1 = 90^\circ$  configuration, which is due to the very small change in  $\nu_{xy}$  between  $75^\circ$  and  $90^\circ$ .

### 4.2.1.3 Effects of the Displacement Gradients

It has been shown that the  $u$  and  $v$  displacement fields are functions of both coordinates  $x$  and  $y$ . Since the panel expands non-uniformly in the transverse direction, the shear strain component  $\frac{\partial v}{\partial x}$  is non-zero. According to Figure 4.4 that quantity is negative under compression for the panels being considered in this study. However, at the upper boundary,  $y/b = 0.5$ , the shear boundary condition requires the shear strain to be zero. Therefore, the value of  $\frac{\partial u}{\partial y}$  must be equal and opposite to  $\frac{\partial v}{\partial x}$ . As shown in Figure 4.3 the value of  $\frac{\partial u}{\partial y}$  is indeed positive close to  $y/b = 0.5$ . The boundary condition is satisfied, but the shear strain is non-zero away from the planes of symmetry and the panel edges. Changes in  $u$  with respect to  $y$ , however, must disappear close to  $x/a = 0$  and  $x/a = 0.5$ , since those edges have the prescribed values of 0 and  $u_0$ . It follows that gradients in the  $u$  field that develop close to these boundaries give rise to the small areas of high strain,  $\epsilon_x$ , seen in Figure 4.2.

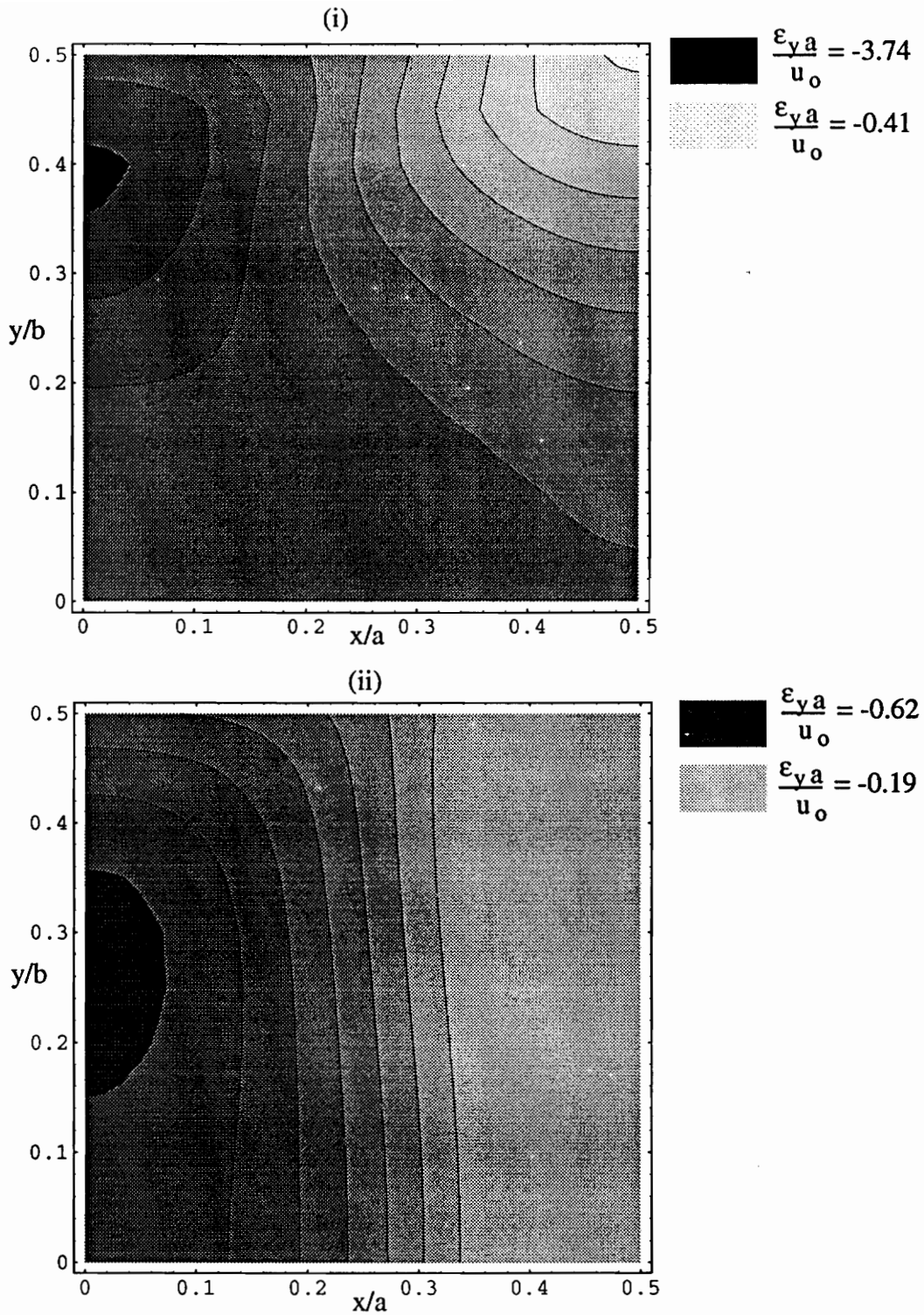


**Figure 4.6** Normalized Transverse Strain,  $\epsilon_y$ , for (i)  $T_0 = 45^\circ, T_1 = 0^\circ$  and (ii)  $T_0 = 45^\circ, T_1 = 90^\circ$  Panels with  $a/b = 1$ , as a Function of  $x$  and  $y$ .

The boundary and symmetry conditions require the shear strain to be equal to zero along all four boundaries of the quarter plate area. Therefore, one can expect to encounter shear only in the interior of the quarter panel area, although the panels are loaded uniaxially and there is no shear-extension coupling in the constitutive equation. A map of the shear strain,  $\gamma_{xy}$  is shown in Figure 4.7 for panels with  $T_1 = 0^\circ$  and  $T_1 = 90^\circ$ . The dark areas represent places where the shear strain is high. For the panel with  $T_1 = 0^\circ$ , the peak in the shear strain occurs at  $(x/a, y/b) = (0.36, 0.40)$ . There is a large shear gradient close to  $x/a = 0.5$  and  $y/b = 0.5$  because the shear strain must be zero along those lines in order to satisfy the boundary conditions. For the panel with  $T_1 = 90^\circ$  the maximum strain is located close to the center of the quarter panel  $(x/a, y/b) = (0.32, 0.30)$ , and the gradients are not as high.

## 4.2.2 Stress Resultants

The strains in a variable stiffness panel have been shown to be functions of  $x$  and  $y$ . It is, therefore, expected that the stress resultants will also be functions of  $x$  and  $y$ . The changes in the stress resultants must be such that the plate equilibrium equations are satisfied at every point. The equilibrium equations therefore provide the framework within which these results are interpreted. The discussion of the stress resultants begins by analyzing the shear stress resultant,  $N_{xy}$ .

As discussed above, the non-uniform deformation of the panel gives rise to a shear strain,  $\gamma_{xy}$ . This shear strain, by definition, causes the presence of the shear stress resultant,  $N_{xy}$ , the distribution of which is shown in Figure 4.8 for panels with  $T_1 = 0^\circ$  and  $T_1 = 90^\circ$ . Note the similarity between the contour plot of the shear strain and the distribution of the stress resultant. For the panel with  $T_1 = 0^\circ$ , there is a sharp peak along  $y/b = 0.4$ , where the normalized  $N_{xy}$  is 0.36, followed by a steep decline to zero along  $y/b = 0.5$  and  $x/a = 0.5$ . The peak for the panel with  $T_1 = 90^\circ$  is not as sharp, and the maximum value of 0.11 is reached along  $y/b = 0.3$ . The peak for the  $T_1 = 0^\circ$  panel is higher since this panel undergoes a larger shear deformation due to the large variation in  $\nu_{xy}$  along the  $x$  direction. The values of the maximum normalized stress resultants is shown in Figure 4.9 as a function of the angle  $T_1$ . As the difference between  $T_0$  and  $T_1$  increases, so does the amount of shear. The angle configuration with the highest shear stress resultant has

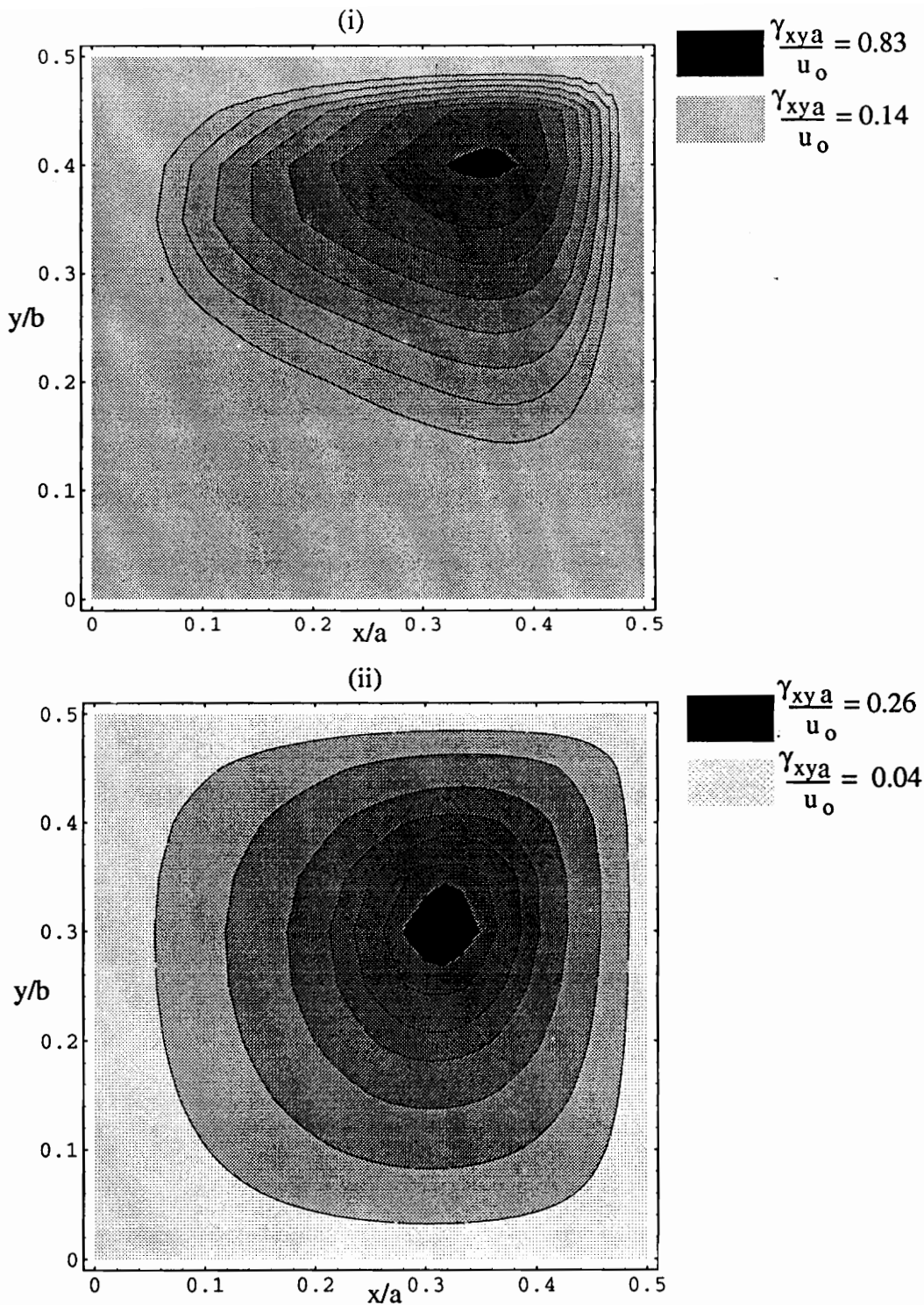


**Figure 4.7** Shear Strain,  $\gamma_{xy}$ , for (i)  $T_o = 45^\circ, T_1 = 0^\circ$  and (ii)  $T_o = 45^\circ, T_1 = 90^\circ$  Panels with  $a/b = 1$ , as a Function of  $x$  and  $y$ .

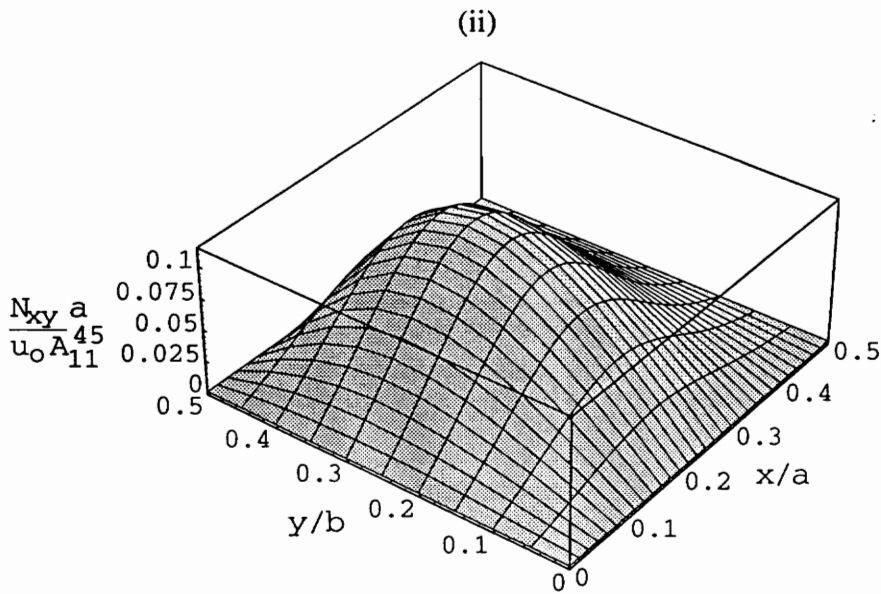
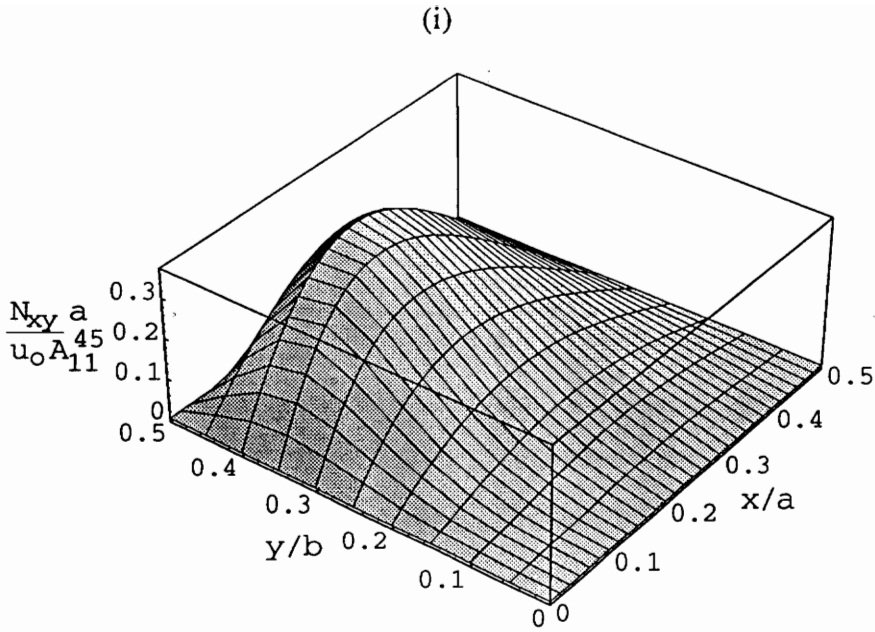


**Figure 4.8** Shear Stress Resultant for (i)  $T_0 = 45^\circ, T_1 = 0^\circ$  and (ii)  $T_0 = 45^\circ, T_1 = 90^\circ$  Panels with  $a/b = 1$ , as a Function of  $x$  and  $y$ .

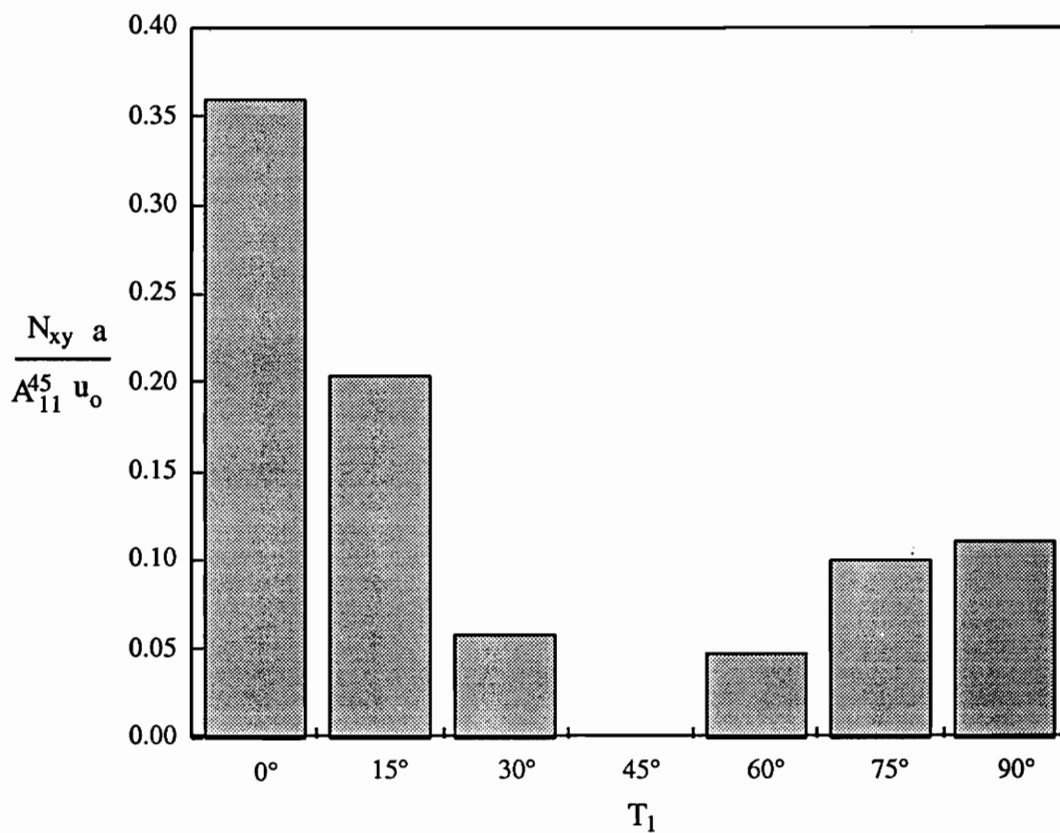


**Figure 4.9** Maximum Shear Stress Resultant for Case I as a Function of  $T_1$  for Panels with  $T_0 = 45^\circ$ .

$T_1 = 0^\circ$ . In addition, there is very little difference between the maximum values for  $T_1 = 75^\circ$  and  $T_1 = 90^\circ$  because, as explained earlier, the equivalent stiffnesses are nearly equal for these two configurations.

Equation 3.1 requires that changes in  $N_{xy}$  with respect to  $y$  be accompanied by changes in the axial stress resultant,  $N_x$ , with respect to  $x$ . Since the shear stress resultant exhibits a large negative gradient with respect to  $y$  close to  $y/b = 0.5$ , an equal and opposite gradient (in the  $x$  direction) is found in the axial stress resultant close to the upper boundary ( $y/b = 0.5$ ). A surface plot of the normalized axial stress resultant over the quarter panel area is shown in Figure 4.10 for  $T_1 = 0^\circ$  and  $T_1 = 90^\circ$ . The axial stress resultant for the panel with  $T_1 = 0^\circ$  remains constant at 2.70 for values of  $y/b$  less than 0.25. However, at the upper boundary,  $y/b = 0.5$ , there is a large peak at  $x/a = 0.5$  and a large through at  $x/a = 0$ . At a normalized value of 4.70, the value of  $N_x$  at the peak is 74% higher than the constant value of 2.70 for small values of  $y/b$ . The value at the through is only 1.85, which is a 31% decrease from 2.70. The shear effects therefore seem most prevalent in the upper half of the quarter panel. The panel with  $T_1 = 90^\circ$  exhibits a similar gradient in the axial stress resultant, except that the changes in  $N_x$  are not confined to the area close to the upper boundary. There is a small peak at  $(x/a, y/b) = (0, 0)$ , and the value of  $N_x$  is not constant for any part of the domain. The normalized value of  $N_x$  at  $(x/a, y/b) = (0.5, 0.5)$  is 0.60, while at  $(0, 0.5)$  it is only 0.25; at  $(0, 0)$  it is 0.57.

The changes in  $N_x$  for the second panel are not confined to the area close to the upper boundary because for this panel the peak in the shear stress resultant is close to the center of the quarter panel, and there is a significant gradient in  $N_{xy}$  even for small values of  $y/b$ . The axial stress resultant distribution is shown as a function of  $x/a$  at  $y/b = 0.5$  for various values of  $T_1$  is shown in Figure 4.11. As the difference between  $T_0$  and  $T_1$  increases, so does the magnitude of the change in  $N_x$  along the  $x$  direction. The difference between the value of  $N_x$  at  $x/a = 0$  and  $x/a = 0.5$  for the panel with  $T_1 = 30^\circ$  is 27%, while for  $T_1 = 15^\circ$  it is 103%. Similarly, for  $T_1 = 60^\circ$ , the difference is 30%, and for  $T_1 = 75^\circ$  it is 109%. The curves are staggered because each configuration exhibits a different amount of stiffness; low values of  $T_1$  cause the panel to have more stiffness than higher values, as will be shown later.

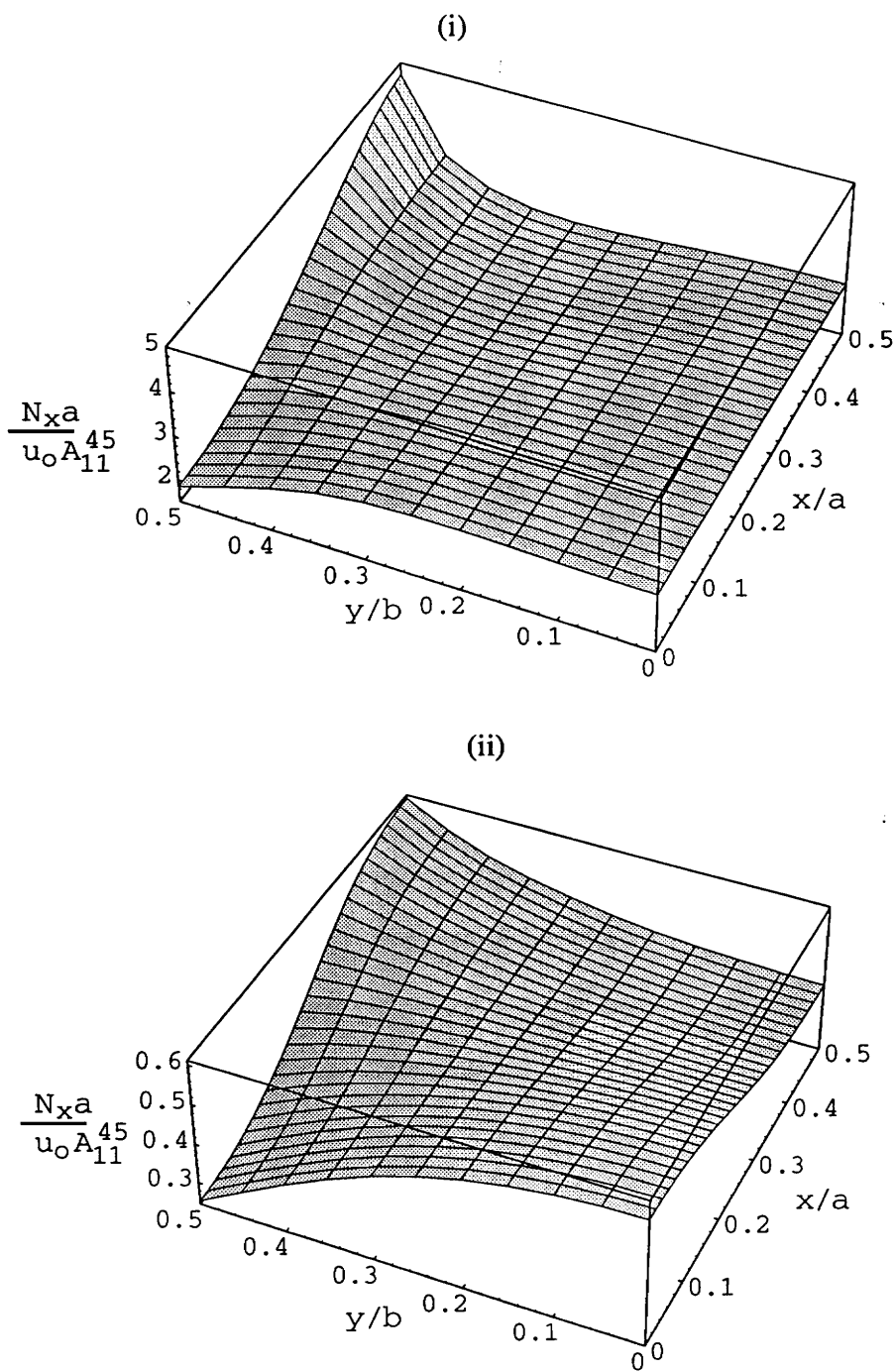


**Figure 4.10** Axial Stress Resultant for (i)  $T_0 = 45^\circ$ ,  $T_1 = 0^\circ$  and (ii)  $T_0 = 45^\circ$ ,  $T_1 = 90^\circ$  Panels with  $a/b = 1$ , as a Function of  $x$  and  $y$ .

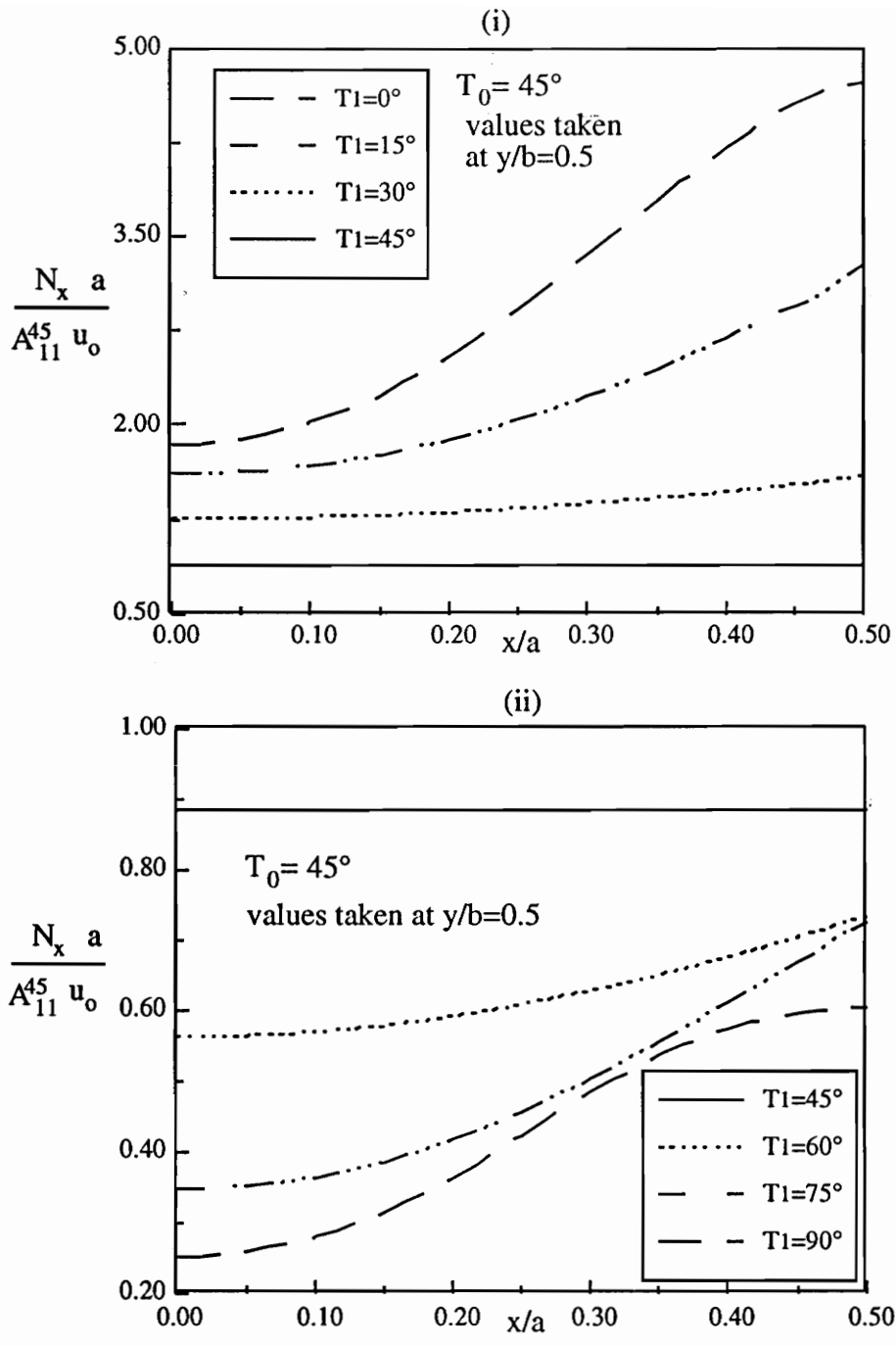
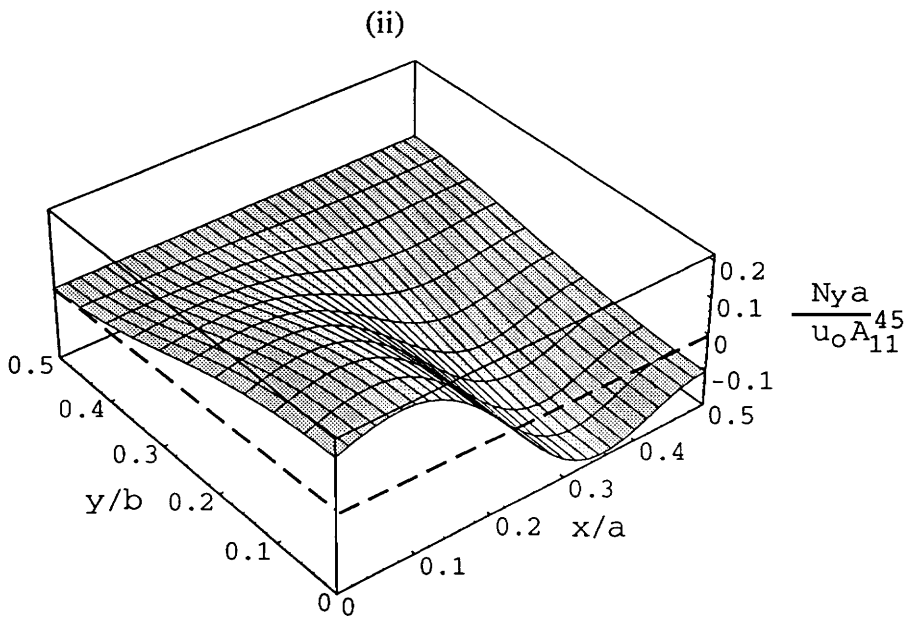
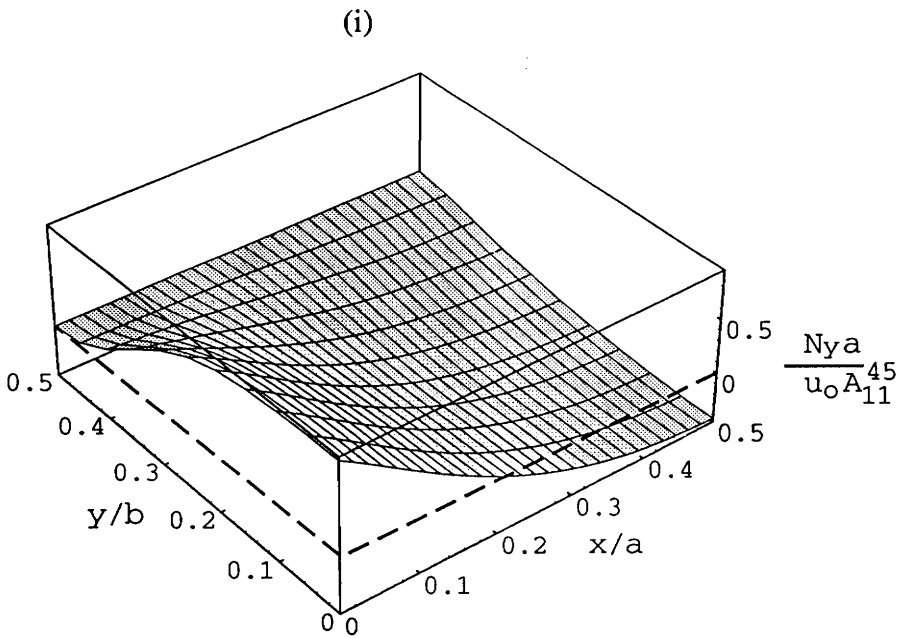


Figure 4.11 Axial Stress Resultant as a Function of  $x/a$  for (i)  $T_1 \leq 45^\circ$  and (ii)  $T_1 \geq 45^\circ$ .

The behavior of the transverse stress resultant with respect to the  $y$  coordinate is governed by equation 3.2. Since there is a gradient in the shear stress resultant with respect to  $x$ , there must be an equal but opposite gradient in the transverse stress resultant in the  $y$  direction. Hence, a transverse load is present, although the loading is applied in the  $x$  direction only. A surface plot of the normalized  $N_y$  is shown in Figure 4.12 for panels having  $T_1 = 0^\circ$  and  $T_1 = 90^\circ$ . The transverse stress resultant for both panel configurations is zero at  $y/b = 0.5$ , which is the required boundary condition for this case. In addition, the magnitude of  $N_y$  reaches a maximum at  $y/b = 0$ . Under compression, the value of  $u_o$  is negative, so that for the panel with  $T_1 = 0^\circ$  the transverse load is compressive for values of  $x/a$  less than 0.22 and tensile for values of  $x/a$  greater than 0.22. For the other panel configuration, the transverse load is compressive for values of  $x/a$  less than 0.24, and tensile for greater values of  $x/a$ . The magnitude of the transverse stress resultant depends on the shear stress resultant distribution. Recall that when the difference between  $T_o$  and  $T_1$  is large, large shear deformations occur, and the gradient of  $N_{xy}$  in the  $x$  direction is high. The distribution of  $N_y$  at  $y/b = 0$  is shown in Figure 4.13 along the  $x$  coordinate for various values of  $T_1$ . As the angle difference decreases so does the magnitude of  $N_y$ . When values for  $T_1$  are less than  $45^\circ$ , there is a significant increase in the maximum value of  $N_y$  as the angle  $T_1$  is decreased. For example, the maximum value for the  $T_1 = 0^\circ$  configuration is 1.98 times larger than it is for  $T_1 = 15^\circ$ . By contrast, the maximum value of  $N_y$  for the  $T_1 = 90^\circ$  configuration is only 1.38 times larger than the value for the  $T_1 = 75^\circ$  configuration.

### 4.2.3 The Closed Form Solution

So far all the results that have been presented are obtained numerically. Now that an understanding of the deformation patterns and stress distributions has been established, the closed form solution developed for this case may be evaluated. The assumptions that were made when the solution was developed have been proven wrong. The axial stress resultant is not constant for all values of  $x$  and  $y$  if the panel has a variable stiffness configuration. The distribution of  $N_x$  over the panel area is compared to the closed form solution for two values of  $T_1$ ,  $0^\circ$  and  $90^\circ$ , in Figure 4.14. For the panel with  $T_1 = 0^\circ$  there is a large amount of error at  $y/b = 0.5$ , since the closed form solution overestimates the stress resultant by 34% at  $x/a = 0$  and underestimates it by 47% at  $x/a = 0.5$ .



**Figure 4.12** Transverse Stress Resultant for (i)  $T_0 = 45^\circ$ ,  $T_1 = 0^\circ$  and (ii)  $T_0 = 45^\circ$ ,  $T_1 = 90^\circ$  Panels with  $a/b = 1$ , as a Function of  $x$  and  $y$ .

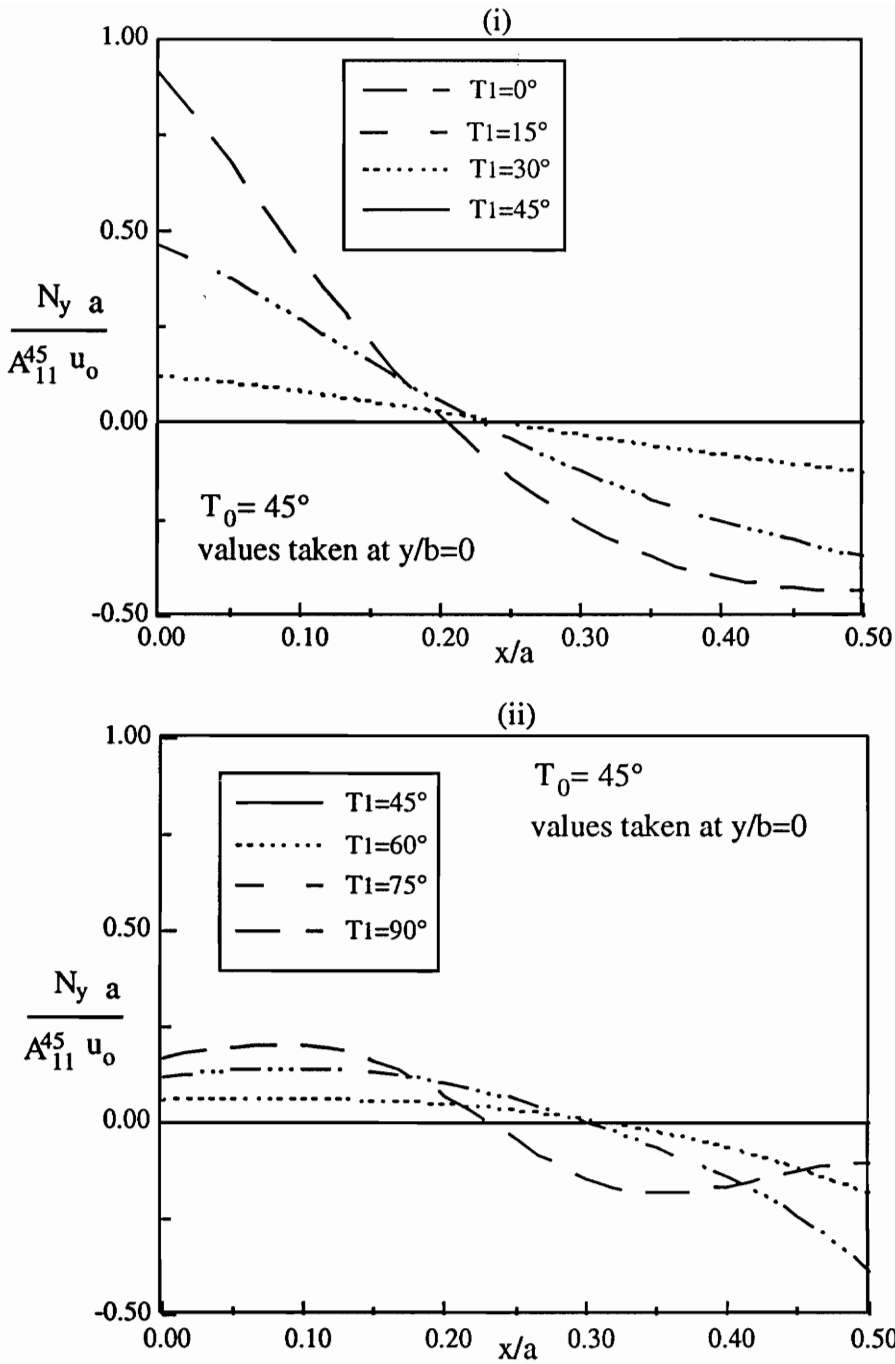


**Figure 4.13** Transverse Stress Resultant for Case I as a Function of  $x/a$  for  
 (i)  $T_1 \leq 45^\circ$  and (ii)  $T_1 \geq 45^\circ$ .

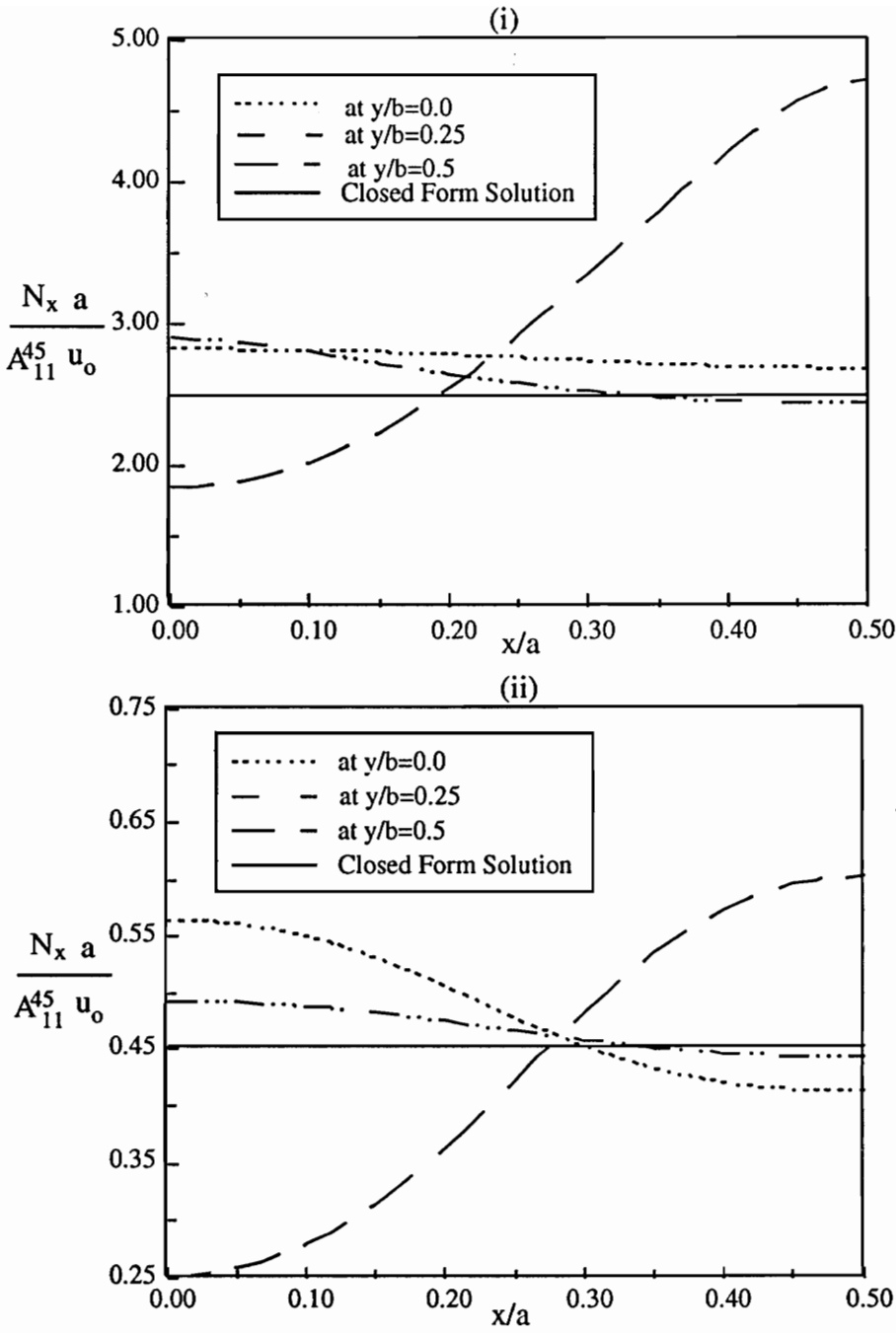


**Figure 4.14** Comparison of  $N_x$  for the Numerical and Closed Form Solutions for Panels with (i)  $T_1 = 0^\circ$  and (ii)  $T_1 = 90^\circ$ .

When  $T_1 = 90^\circ$  the error is greater, since the value of  $N_x$  is overestimated by 80% at  $x/a = 0$  and underestimated by 25% at  $x/a = 0.5$ . However, as the value of  $y/b$  decreases, so does the difference between the closed form solution and the numerical solution.

As the difference between the angles  $T_0$  and  $T_1$  is decreased, however, the shear effects in the panel are not as significant and the closed form solution may yield useful results. For example, when  $T_1 = 30^\circ$  the maximum error in the value of  $N_x$  is 19%, and when  $T_1 = 60^\circ$  the maximum error is 16%. These errors are localized at the upper boundary, and the stress resultant is reasonably well predicted for small values of  $y/b$ .

The closed form solution also fails to account for the transverse stress resultant,  $N_y$ , which is not zero for all  $x$  and  $y$ . In fact, for the configuration with  $T_1 = 90^\circ$  for part of the domain it is of the same order of magnitude as  $N_x$ . Finally, the shear stress resultant given by the closed form is not identically zero at  $x/a = 0$  and  $x/a = 0.5$ , and therefore the solution does not satisfy the boundary conditions.

Due to these large discrepancies in the numerical solution and the closed form solution, values for the displacements or strains calculated using the closed form solution will be erroneous. In fact, the  $v$  displacements for a panel with  $T_1 = 0^\circ$  can be underestimated by as much as 400%. If the difference between  $T_0$  and  $T_1$  is small, the closed form solution proves useful when it is necessary to get raw 'ballpark' figures on the axial stress resultant, and as will be shown, in estimating the overall panel stiffness.

#### 4.2.4 Equivalent Stiffness

As described in the previous chapter, the overall equivalent stiffness of a component is often useful in structural analysis. The overall equivalent stiffness,  $E_x^{eq}$  is shown in Figure 4.15 for a panel with  $T_0 = 45^\circ$  and different values of  $T_1$ . Also shown is the value of  $E_x^{eq}$  obtained by using the closed form solution and the curve for the straight fiber configuration. A panel having  $T_1 = 0^\circ$  is almost three times more stiff than the panel with  $45^\circ$  straight fibers. Similarly, by having the variable stiffness configuration with  $T_1 = 90^\circ$ , the stiffness is reduced to half of what it is for the  $45^\circ$  straight fiber panel. A variable stiffness panel with  $T_1 = 0^\circ$  has the same equivalent stiffness as

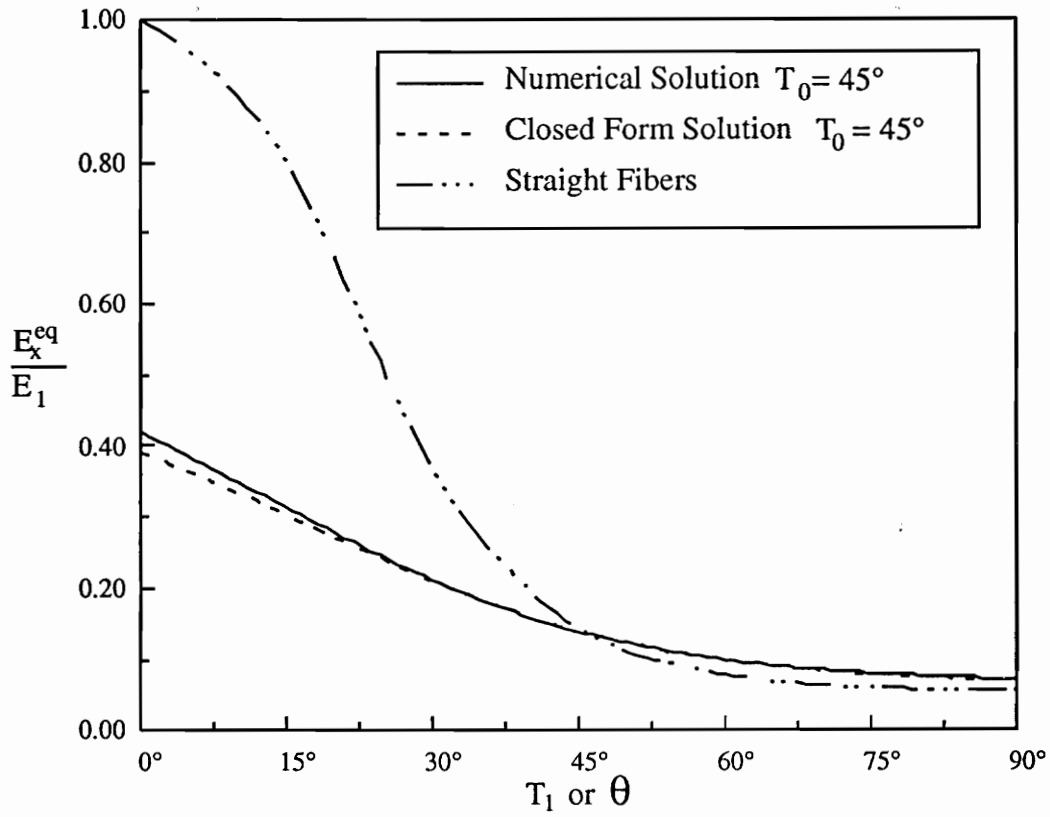


**Figure 4.15** Equivalent Panel Stiffnesses for Case I for Straight and Curvilinear Fiber Panels.

a straight fiber panel with  $\theta = 28^\circ$ . Similarly, a variable stiffness configuration with  $T_1 = 75^\circ$  has the same equivalent stiffness as a straight fiber panel with  $\theta = 60^\circ$ . Although with  $T_0 = 45^\circ$  the maximum value of the normalized equivalent stiffness is 0.42, panels with other values of  $T_0$  could be used to obtain higher equivalent stiffnesses.

A comparison of the numerical and closed form solutions show that the overall stiffness is underestimated by 7.4% by using the closed form solution instead of the numerical solution, although there are substantial savings in the computing time. As the value of  $T_1$  approaches  $45^\circ$ , both curves converge, but begin to diverge once more as the value of  $T_1$  increases past  $45^\circ$ . The error when  $T_1 = 90^\circ$  is only 2.2%. The closed form solution may sometimes yield results that are highly erroneous for the local strains and stress resultants. However, the closed form solution is able to capture the global response in the  $x$  direction.

## 4.2.5 Rectangular Panels

So far the discussion on the in-plane response of the variable stiffness panels has focused on square panels. If the aspect ratio,  $a/b$ , of the panel is varied, the gradients in the panel change so that the stress resultants behave differently. For example, the shear stress resultant,  $N_{xy}$  is shown in Figure 4.16 at  $x/a = 0.32$  as a function of  $y/b$  for three different aspect ratios, (0.5, 1.0 and 2.0), and for two values of  $T_1$ , ( $0^\circ$  and  $90^\circ$ ). When  $T_1 = 0^\circ$ , the changes in  $N_{xy}$  are such that the location of the maximum value of  $N_{xy}$  is shifted towards the center of the panel, although the maximum value is nearly the same for all three aspect ratios. The maximum  $N_{xy}$  when  $a/b = 0.5$  occurs at  $y/b = 0.46$ , close to the upper edge, and the gradient to zero at  $y/b = 0.5$  is very high. Note that the value of  $N_{xy}$  for this aspect ratio is small for all values of  $y/b$  less than 0.25. This indicates that the shear effects are isolated in the area close to the unloaded edge. When  $a/b = 1$  the maximum value occurs at  $y/b = 0.38$ , and there is a significant gradient with respect to all values of  $y/b$ , even for  $y/b$  values close to 0.0. For the panel with  $a/b = 2$  the maximum shear stress resultant is located at  $y/b = 0.30$ , and the stress resultant is nearly symmetric about this location.

The configuration with  $T_1 = 90^\circ$  responds very differently to the changes in the aspect ratio. Changes in the aspect ratio do not significantly alter the location of the maximum value, but instead

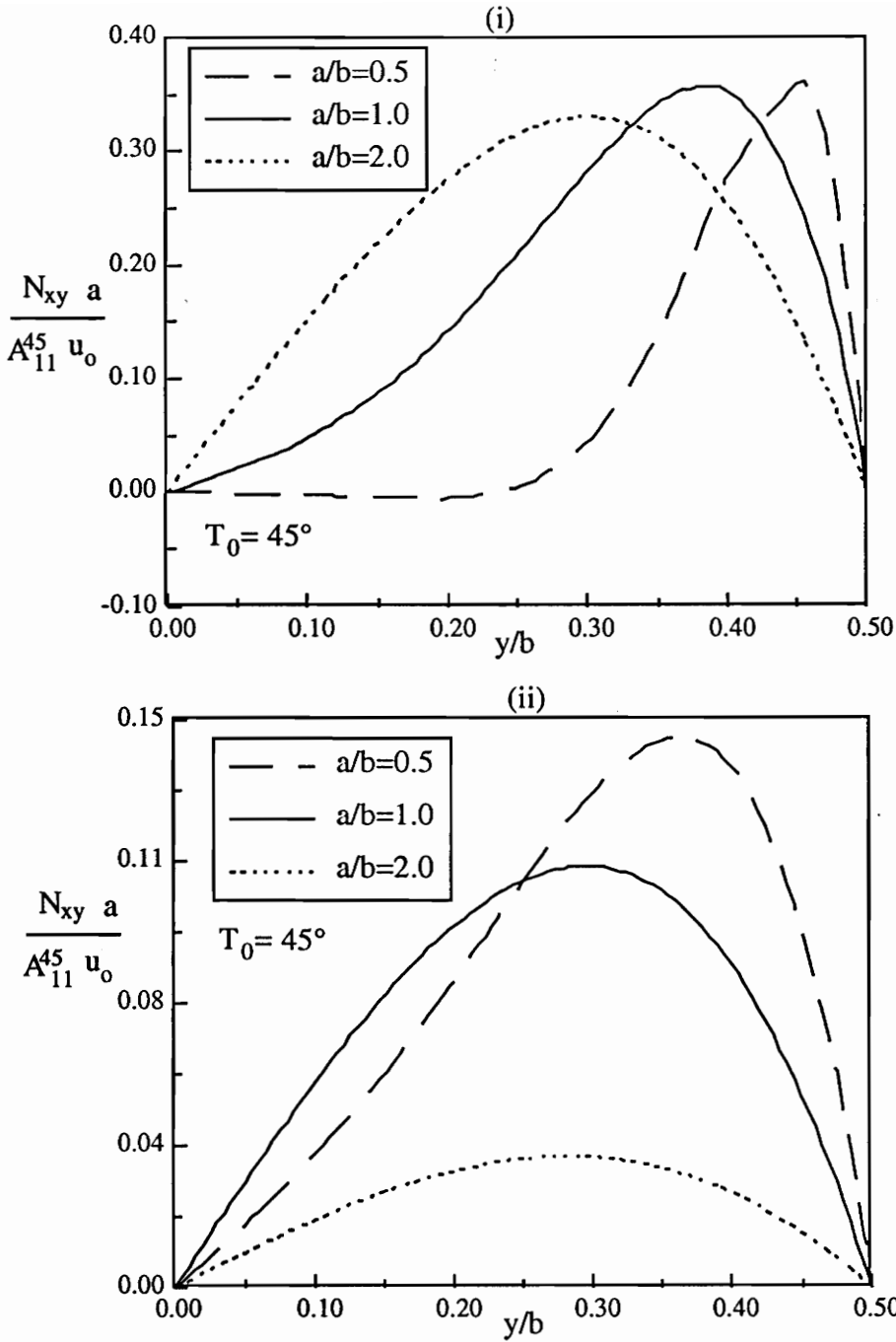


**Figure 4.16** Shear Stress Resultant Distribution for Different Aspect Ratios with (i)  $T_1 = 0^\circ$  (at  $x/a = 0.36$ ) and (ii)  $T_1 = 90^\circ$  (at  $x/a = 0.32$ ).

affect the magnitude of this maximum. The maximum value when  $a/b = 1$  is 3.2 times larger than for the value for the panel with  $a/b = 2$ ; for  $a/b = 0.5$  the value is 4.2 times larger. Independent of whether  $T_1 = 0^\circ$  or  $90^\circ$ , the result of a reduction in aspect ratio is to increase the gradient of  $N_y$  with respect to  $y$ ; the shear stress resultant for long plates is more evenly distributed than it is for square or short plates, and hence the gradients are not as large.

The axial stress resultant at  $x/a = 0.5$  is shown in Figure 4.17 as a function of  $y/b$  for both angle configurations and all three aspect ratios. When  $T_1 = 0^\circ$ , the effect of changes in aspect ratio are similar to those found in  $N_{xy}$ . The maximum value of the axial stress resultant remains independent of the aspect ratio. However, the range of values for which large changes in  $N_x$  are present is affected. The panel with  $a/b = 0.5$  has a constant value of  $N_x$  for values of  $y/b$  less than 0.20, and the large variations are isolated at the upper part of the panel. As the aspect ratio is increased, the changes in  $N_x$  reach well into the smaller values of  $y/b$ . For the other configuration, a reduction in the maximum value of  $N_x$  is seen when the aspect ratio is increased. The maximum value of  $N_x$  when  $a/b = 1$  is 1.2 times larger than when  $a/b = 2$ ; when  $a/b = 0.5$  the value is 1.3 times larger.

The same effects that are seen in  $N_{xy}$  and  $N_x$  are found in the transverse stress resultant  $N_y$ . A plot of  $N_y$  at  $x/a = 0$  as a function of  $y/b$  is shown in Figure 4.18 for the two values of  $T_1$  and the three values of  $a/b$ . For the  $T_1 = 0^\circ$  configuration there is no difference in the maximum value of  $N_y$  between a panel with  $a/b = 0.5$  and one with  $a/b = 1$ , instead the change is in the location of this maximum. When  $a/b = 2$  the maximum value is 1.45 times smaller for than the other two aspect ratios. There are significant reductions in the maximum value of  $N_y$  when a  $T_1 = 90^\circ$  configuration is used. The normalized value of  $N_y$  decreases from 0.26 to 0.17 and 0.045 as the aspect ratio is increased from 0.5 to 1.0 and 2.0, respectively.

The two configurations presented respond differently to the changes in  $a/b$  because for  $T_1 = 0^\circ$  the changes in  $\nu_{xy}$  will always be large, regardless of the aspect ratio, and the gradients are not reduced but are shifted instead. By comparison, the  $T_1 = 90^\circ$  configuration has a mild variation in  $\nu_{xy}$  and having a plate with a high aspect ratio contributes to a significant reduction in the shear strain, since the panel expands transversely in a more uniform fashion. It follows that the closed

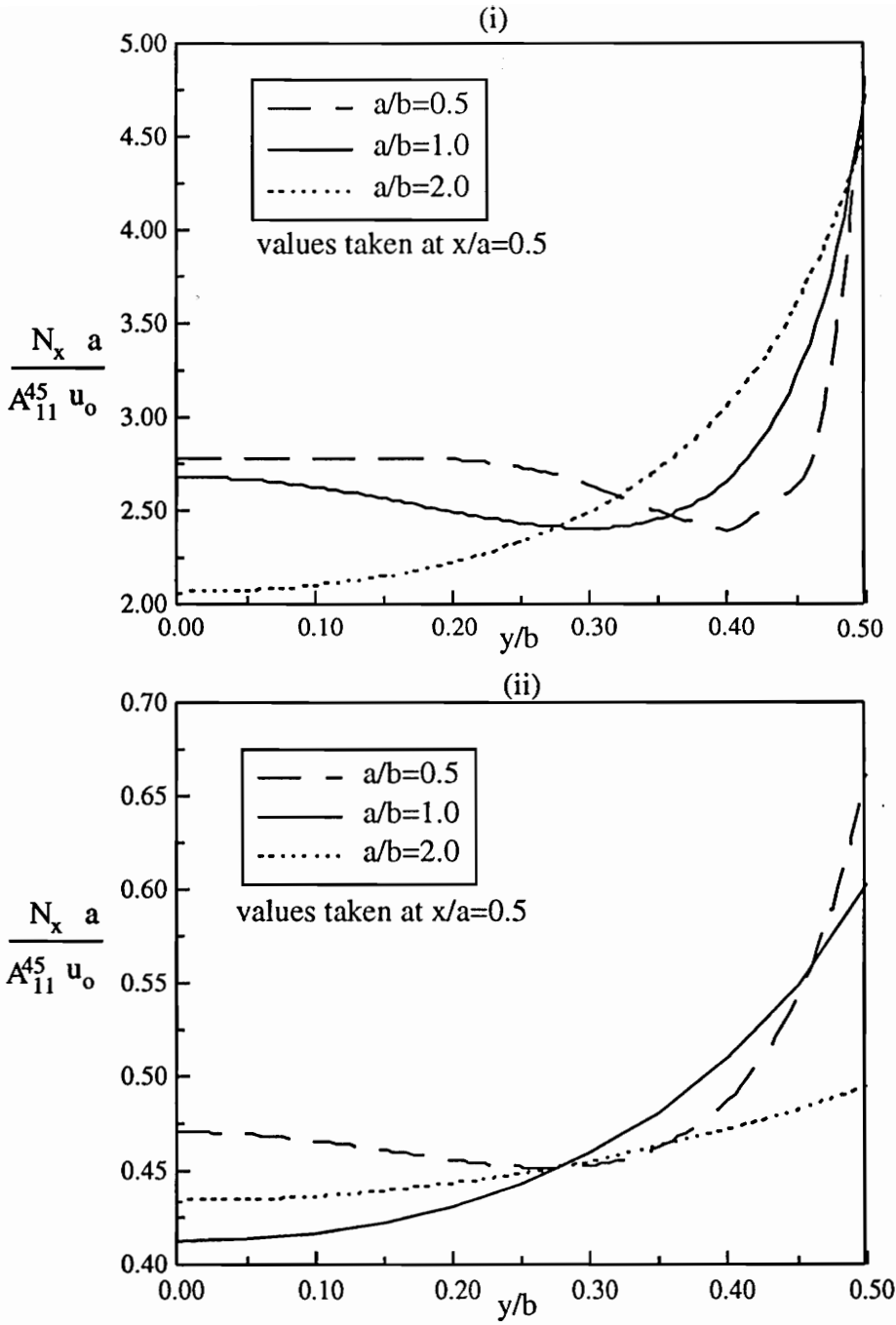


**Figure 4.17** Axial Stress Resultant Distribution for Different Aspect Ratios with (i)  $T_1 = 0^\circ$  and (ii)  $T_1 = 90^\circ$ .

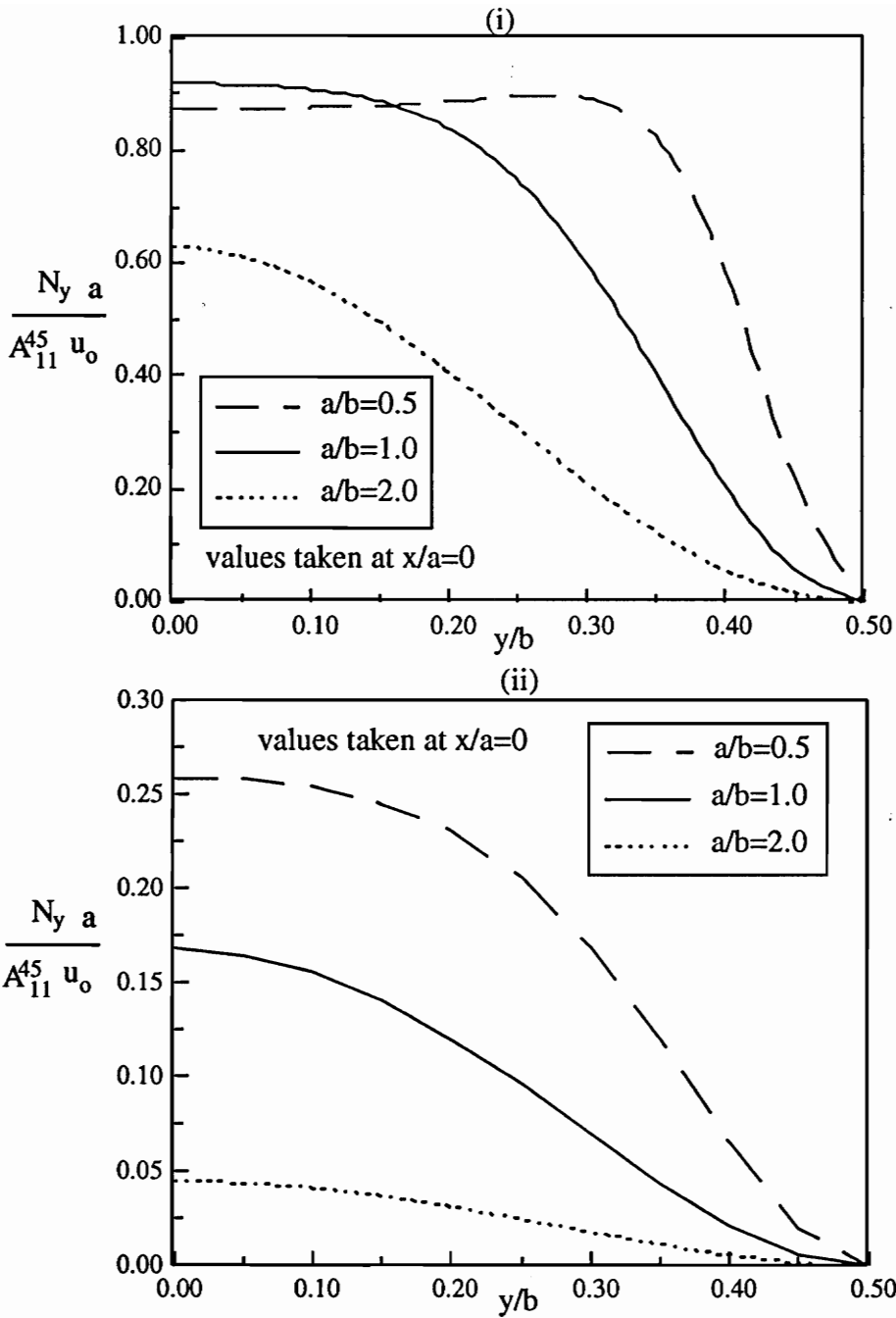


**Figure 4.18** Transverse Stress Resultant Distribution for Different Aspect Ratios with (i)  $T_1 = 0^\circ$  and (ii)  $T_1 = 90^\circ$ .

form solution should perform well for long panels with values of  $T_1$  that range between  $45^\circ$  and  $90^\circ$ , since the transverse and shear stress resultants will be small for such configurations.

### 4.3 Case II Boundary Conditions

The analysis of variable stiffness panels with fixed transverse edges subjected to uniform end shortening is straight forward, since their elastic response may be modeled using the closed form solution developed in Chapter 3. As in the previous section, for the results presented here the angle  $T_0$  is  $45^\circ$ . The shear effects that greatly complicate the analysis of panels under Case I boundary conditions are not seen for this case, and the analysis is greatly simplified. From the closed form solution, equations 3.62 and 3.65, it is concluded that the response is independent of  $a/b$ .

#### 4.3.1 Deformations and Strains

When compressed in the  $x$  direction, a panel would ordinarily expand in the transverse direction; however, due to the boundary conditions, no such expansion takes place, and the transverse displacement,  $v$ , is identically zero for all  $x$  and  $y$ . Since an axial load is applied, the only deformation is in the form of the axial displacement,  $u$ . Furthermore, the closed form solution for this case is such that the  $u$  displacement depends only on the  $x$  coordinate. Therefore, the shear strain is zero for all  $x$  and  $y$ .

The normalized  $u$  displacement and axial strain,  $\epsilon_x$ , are shown in Figure 4.19 as a function of the normalized coordinate  $x/a$  and the angle  $T_1$ . The  $u$  displacement for this case is similar to the  $u$  displacement for Case I (see Figure 4.1), except that  $u$  is a function of  $x$  only. The  $u$  vs.  $x$  curves are not linear for the variable stiffness panels, and the degree of convexity or concavity is large when the difference between  $T_1$  and  $T_0$  is large. There is great similarity between the displacement curves for  $T_1 = 75^\circ$  and  $T_1 = 90^\circ$ , which, as noted earlier, is due to the similarity in the stiffness distribution for these two cases. The strain distribution depends on whether  $T_1$  is greater or less than  $45^\circ$ . As shown in the figure, if  $T_1 = 0^\circ$ , the strain is highest at  $x/a = 0$ ; if  $T_1 = 90^\circ$ , the strain is highest at  $x/a = 0.5$ . At  $x/a = 0$  the fiber angle for all three configurations shown is  $45^\circ$ , yet the strain for the  $T_1 = 0^\circ$  configuration is two times larger than the straight fiber configuration and seven times larger than the  $T_1 = 90^\circ$  configuration.

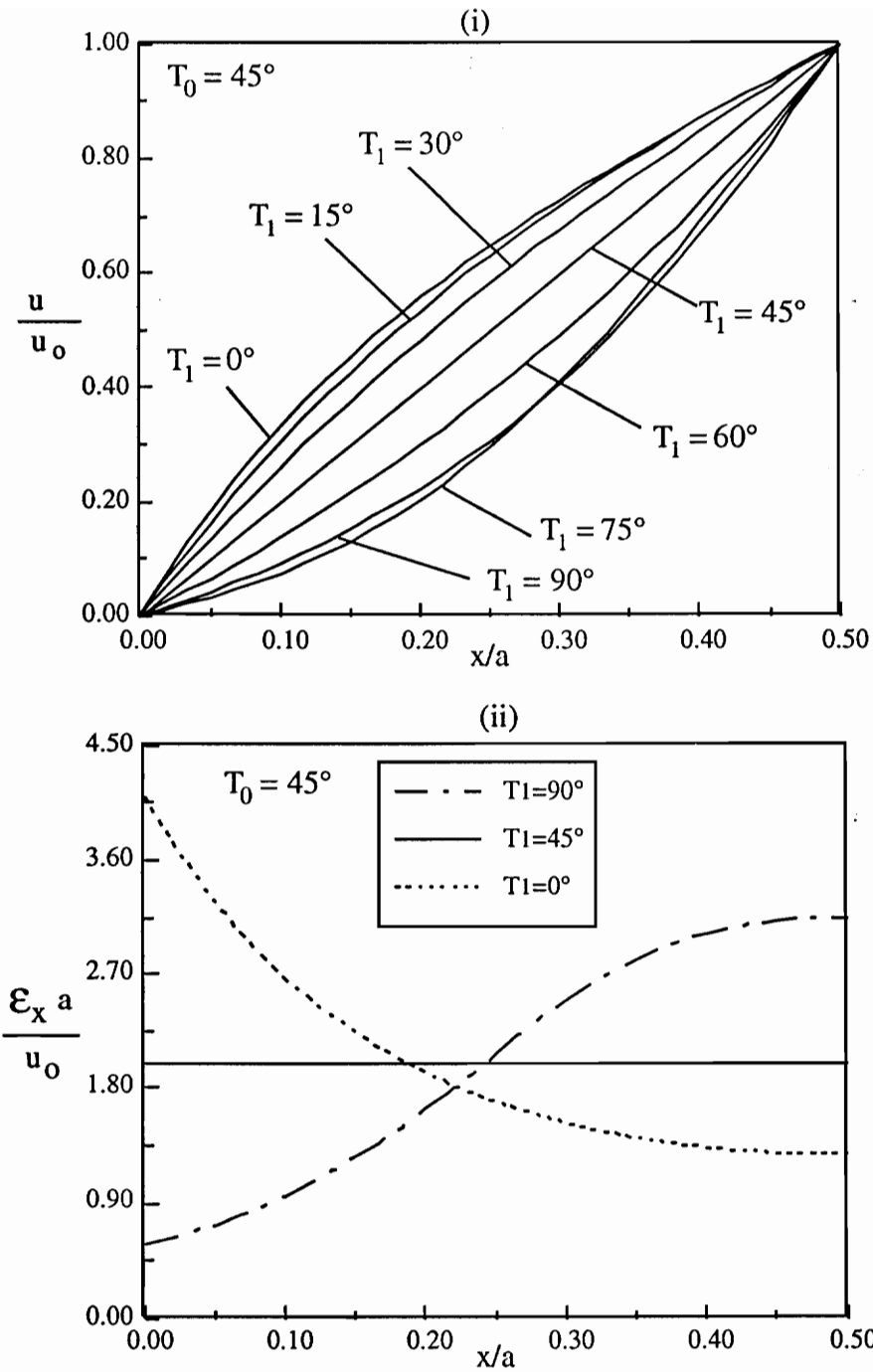


**Figure 4.19** Axial Displacement (i) and Axial Strain (ii) as a Function of  $x/a$  for Case II Panels.

### 4.3.2 Stress Resultants

Since the shear strain is zero for this set of boundary conditions, the shear stress resultant is also zero for all  $x$  and  $y$ . The axial strain is distributed so that, although the stiffness changes, the axial stress stress resultant,  $N_x$  remains constant for all  $x$  and  $y$ . This satisfies the equilibrium equations, since there is no change in  $N_{xy}$  with respect to  $y$ .

When the transverse edges are free (Case I), all the variable stiffness configurations tend to expand more in the transverse direction at  $x/a = 0$  than at  $x/a = 0.5$  for a panel with  $T_0 = 45^\circ$ . Under Case II boundary conditions this transverse expansion is restrained, and a transverse load,  $N_y$ , is induced. The transverse stress resultant,  $N_y$  is a function of  $x$ , as denoted by equation 3.65. By substitution of equation 2.44 into equation 3.65, the following expression is obtained,

$$N_y(x) = \frac{A_{12}}{A_{11}} N_o = \nu_{yx}(x) N_o, \quad (4.2)$$

which is now expressed in terms of the minor Poisson's ratio,  $\nu_{yx}$ . The transverse stress resultant is therefore proportional to the  $\nu_{yx}(x)$ . The normalized  $N_y$  is shown in Figure 4.20 as a function of  $x/a$ . The normalized value of  $N_y$  for all configurations is always positive, which means that under axial compression, when  $u_o$  is negative, the transverse load is also compressive. When  $T_1 = 45^\circ$ , the value of  $N_y$  remains constant with respect to  $x$ , since the panel has a straight fiber configuration. For the configurations where  $T_1$  is less than  $45^\circ$  (Figure 4.20(i)), the value of  $N_y$  is highest at  $x/a = 0$ , and a lowest at  $x/a = 0.5$ . All three curves slope down, reflecting the decrease in  $\nu_{yx}$  along the length of the panel. When  $T_1$  is greater than  $45^\circ$  (Figure 4.20(ii)), the transverse load reflects an initial increase in  $\nu_{yx}$ , as is shown by the  $T_1 = 60^\circ$  curve. However, the value of  $\nu_{yx}$  reaches a peak when the fiber angle is  $65^\circ$  (see Figure 2.5). Therefore, the  $N_y$  curves for  $T_1 = 75^\circ$  and  $T_1 = 90^\circ$  reach a maximum, and begin to decrease for values of  $x/a$  greater than 0.34 and 0.23, respectively.

### 4.3.3 Equivalent Stiffness

The equivalent overall stiffness,  $E_x^{eq}$ , for panels subjected to these boundary conditions is slightly higher than for panels under case I boundary conditions because the transverse expansion due to the Poisson effect is restrained. The equivalent stiffness for panels under case II boundary

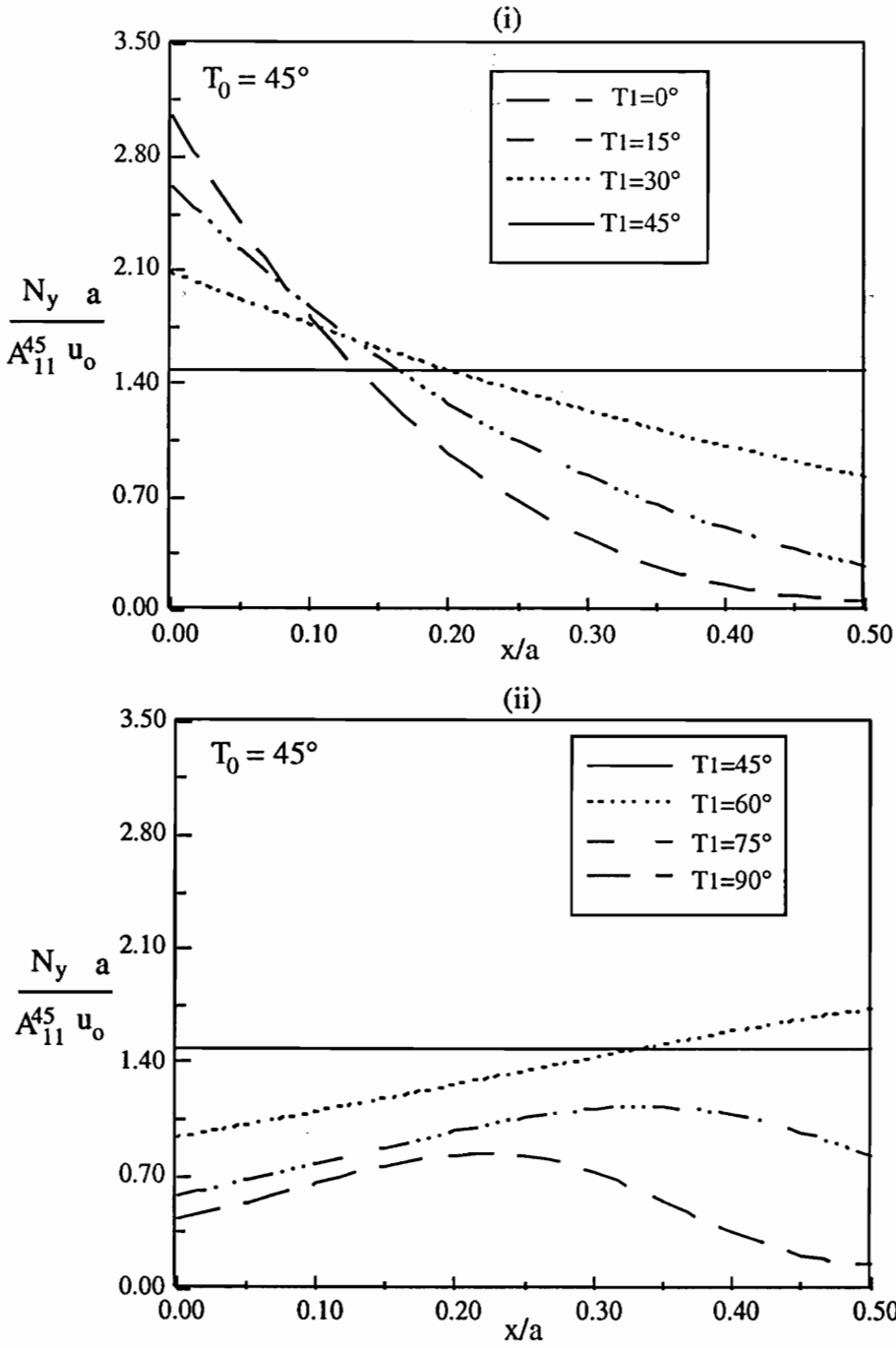


**Figure 4.20** Transverse Stress Resultant as a Function of  $x/a$  For Case II  
 Panels with (i)  $T_1 < 45^\circ$  and (ii)  $T_1 > 45^\circ$ .

conditions is shown in Figure 4.21 as a function of the angle  $T_1$ . The effective stiffness for panels with a straight fiber configuration are also shown as a function of  $\theta$ . The range of values for the variable stiffness panels is from 0.64 when  $T_1 = 0^\circ$  to 0.10 when  $T_1 = 90^\circ$ , whereas under case I boundary conditions they ranged from 0.42 to 0.07. A variable stiffness panel with  $T_1 = 15^\circ$  has the same stiffness as a straight fiber panel with  $\theta = 33^\circ$ . Similarly, a variable stiffness panel with  $T_1 = 60^\circ$  has the same equivalent stiffness as a straight fiber panel with  $\theta = 72^\circ$ . By using other values of  $T_0$ , other equivalent stiffnesses may be obtained.

## 4.4 Case III Boundary Conditions

The boundary conditions for case III are different from all other boundary conditions in that the applied displacement is in the  $y$  direction only. The deformations in the  $x$  direction are induced, and occur as a result of the Poisson's effect. In addition, there is no shear deformation anywhere in the panel and the analysis may be carried out through the closed form solution.

### 4.4.1 Deformations

For this set of boundary conditions the applied displacement at  $y/b = 0.5$  is a constant value  $v_0$ . As described in Chapter 3, the  $v$  displacement field is a linear function of  $y$ , as given by equation 3.68. Due to the Poisson effect, the panel contracts or expands in the  $x$  direction, depending on whether  $v_0$  is positive or negative, respectively. The resulting  $u$  displacement field is a function of  $x$ . Since the  $u$  displacement is induced instead of applied, its distribution is determined by the minor Poisson's ratio,  $\nu_{yx}$ , not by  $E_x$ , as in previous cases. From equation 3.72, the axial strain,  $\epsilon_x$ , may be expressed as

$$\epsilon_x = -2 \frac{v_0}{b} \nu_{yx}(x). \quad (4.3)$$

Hence, the axial strain at each  $x$  location is proportional to the value of  $\nu_{yx}$  at that location. The normalized  $u$  displacement is shown in Figure 4.22 as a function of  $x/a$  for various values of  $T_1$ . The panel with the smallest end deflection (at  $x/a = 0.5$ ) is the one with the  $T_1 = 0^\circ$  configuration. This panel deflects the least because the value of  $\nu_{yx}$  decreases along the length of panel, and is less than unity for most values of  $x$ . The panel with the largest deflection has  $T_1 = 90^\circ$ . Note that the slope of the curve for this configuration curve changes considerably for values of  $x/a$  greater than

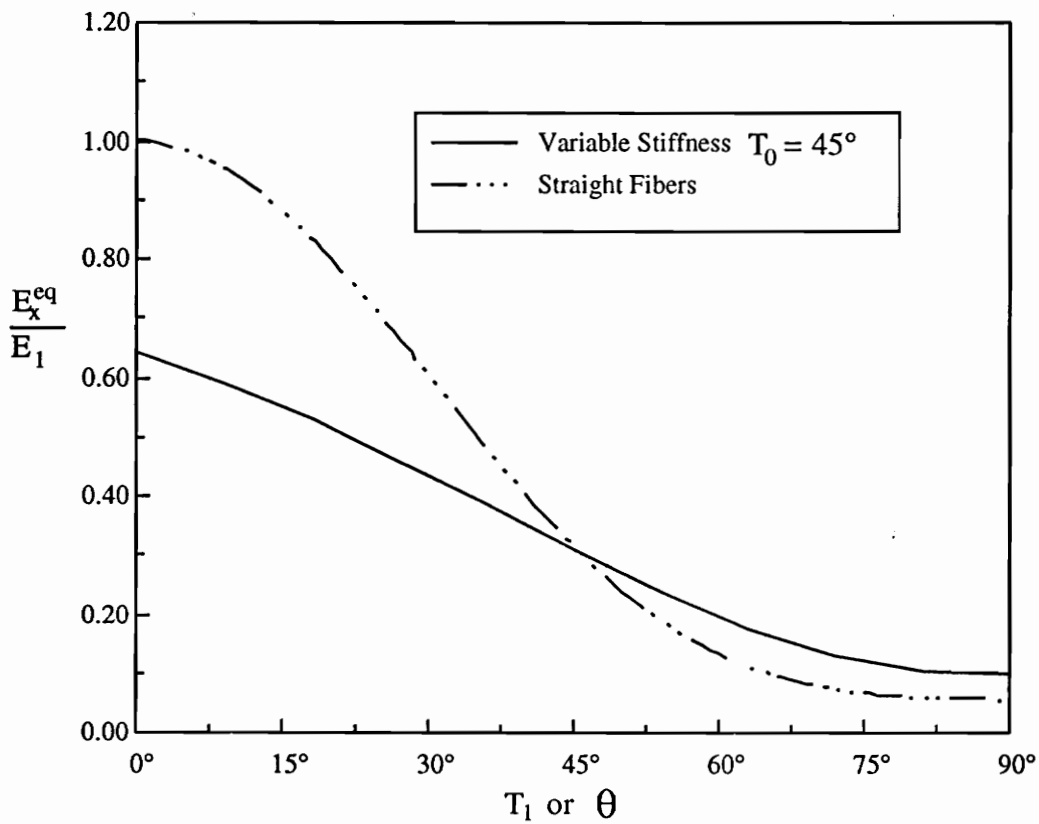


**Figure 4.21** Equivalent Axial Stiffness for Variable and Straight Fiber Panels for Case II.

0.30. The reason for the change in slope is that  $\nu_{yx}$  reaches a maximum when the fiber angle is  $65^\circ$ , and then decreases significantly as the fiber angle increases beyond this value. This decrease in  $\nu_{yx}$  causes the change in slope in the  $u$  vs.  $x$  curve. Therefore, for configurations with  $T_1$  greater than  $65^\circ$  the highest axial strain will not occur at  $x/a = 0$  or  $x/a = 0.5$ , but within the quarter panel area.

#### 4.4.2 Stress Resultants

There is only one non-zero stress resultant for this case; it is the transverse stress resultant,  $N_y$ . The value of  $N_y$  depends on the applied transverse displacement,  $v_o$ , and the material properties. From equation 3.73, the transverse stress resultant may be expressed as

$$N_y = 2 \frac{v_o}{b} \frac{A_{11}A_{22} - A_{12}^2}{A_{11}} = 2 \frac{v_o h}{b} E_y. \quad (4.4)$$

The  $\frac{2v_o}{b}$  term in the above equation is equal to the amount of strain  $\epsilon_y$  that has been applied to the panel. The transverse stress resultant is proportional to the effective transverse stiffness, which is a function of  $x$ . The normalized transverse stress resultant is shown in Figure 4.23 as a function of the normalized coordinate  $x/a$ . For the panel configuration with  $T_1 = 90^\circ$ , most of the load is concentrated close to the edge, at  $x/a = 0.5$ . The value of  $N_y$  at  $x/a = 0.5$  is 7.22 times larger than at  $x/a = 0$ . The steep increase in the value of  $N_y$  for this configuration is caused by the gradual alignment of the fibers with the loading direction as  $x/a$  increases; at  $x/a = 0.5$  the fiber angle coincides with the loading direction and the effective transverse stiffness,  $E_y$ , reaches its maximum value. As  $T_1$  approaches  $45^\circ$ , the transverse load decreases to the point where it has a constant value when the fibers are straight ( $T_1 = 45^\circ$ ). For values of  $T_1$  smaller than  $45^\circ$ , there is a slight decrease in the transverse stress resultant as  $x/a$  increases. However, the transverse effective stiffness does not exhibit large changes between  $30^\circ$  and  $0^\circ$ , and therefore the decrease in  $N_y$  is not drastic. The value of  $N_y$  at  $x/a = 0.5$  is 0.41 times smaller than at  $x/a = 0$  for the  $T_1 = 0^\circ$  configuration.

#### 4.4.3 Equivalent Stiffness

The transverse overall equivalent stiffness,  $E_y^{eq}$ , for the variable stiffness panels is a smeared quantity. The load at the upper boundary,  $y/b = 0.5$ , integrated and an equivalent load is found. The

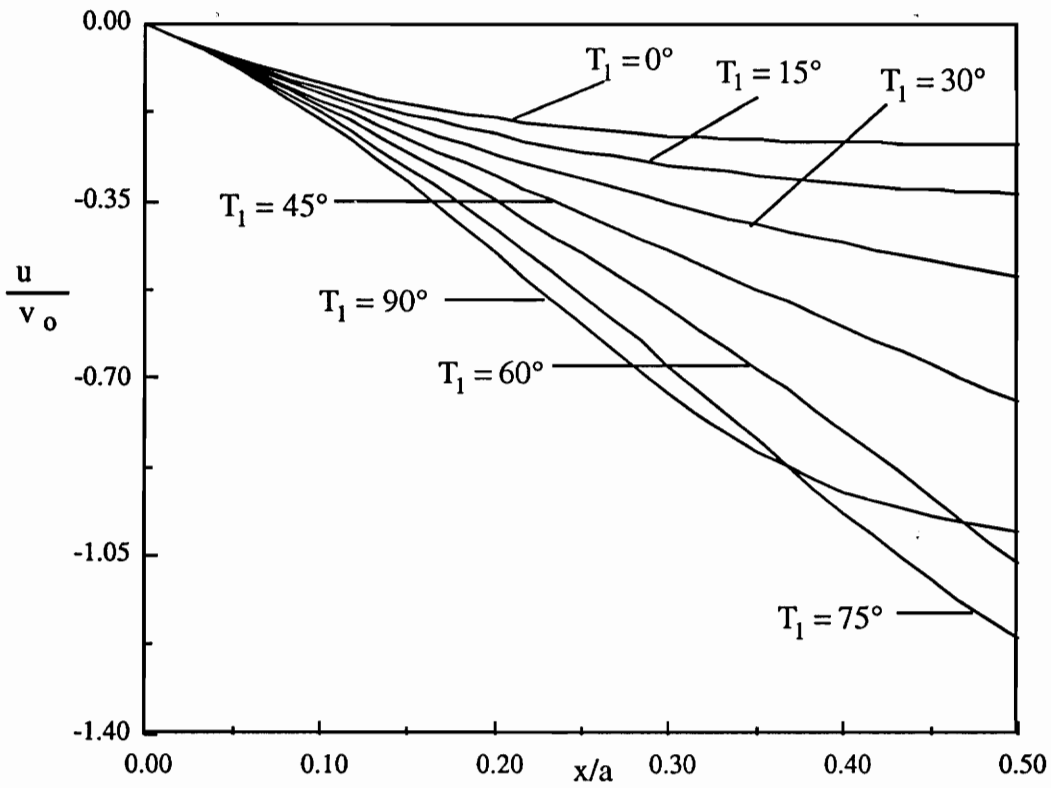


**Figure 4.22 Normalized Axial Displacement as a Function of  $x/a$  for Case III Panels.**

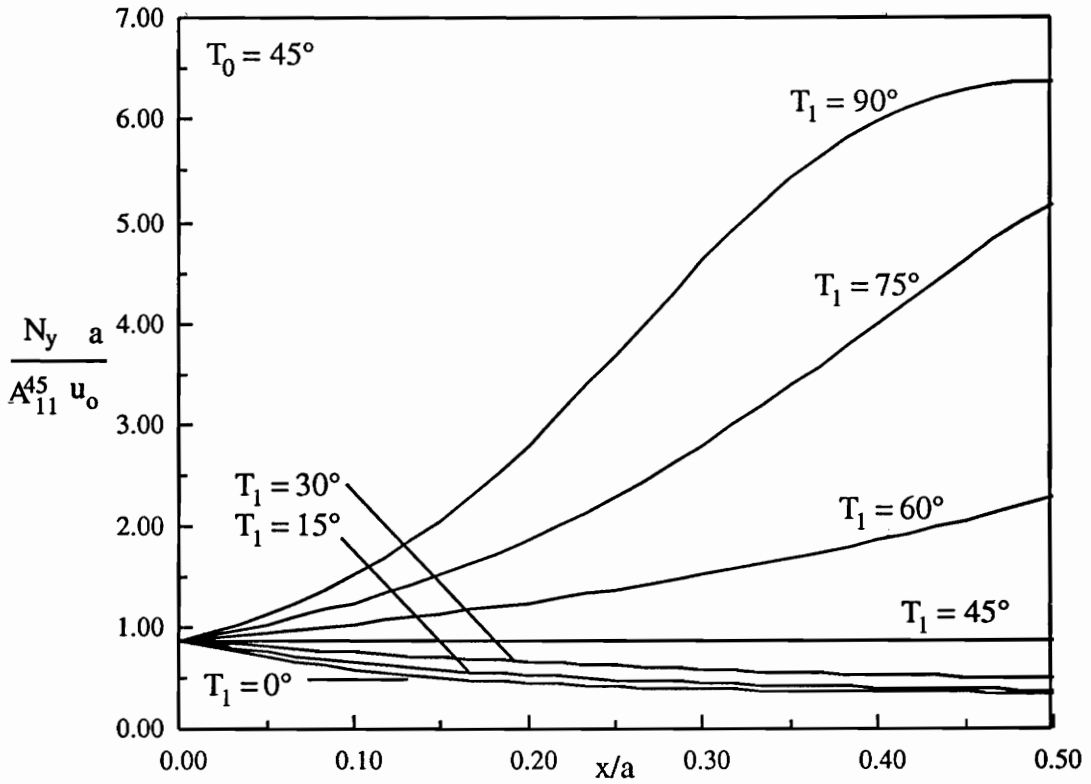


**Figure 4.23** Transverse Stress Resultant as a Function of  $x/a$  For Case III Panels.

equivalent transverse stiffness for transversely loaded variable stiffness panels is shown in Figure 4.24 as a function of  $T_1$ . The value of  $E_y^{eq}$  changes by only 13% as  $T_1$  changes from  $0^\circ$  to  $45^\circ$ . This is because for these configurations the fibers are not aligned with the load, and most of the load is carried by the compliant matrix, not the stiff fibers. As the value of  $T_1$  increases past  $45^\circ$ , however, the equivalent stiffness increases substantially, and at  $T_1 = 90^\circ$  it is 7.70 times larger than it is at  $T_1 = 0^\circ$ . The configuration with  $T_1 = 0^\circ$  has the same transverse stiffness as a straight fiber panel with  $\theta = 28^\circ$ . Likewise, a variable stiffness panel with  $T_1 = 75^\circ$  has an  $E_y^{eq}$  value equal to that of a straight fiber panel with  $\theta = 62^\circ$ . Larger equivalent stiffnesses than the one presented here are possible if a value greater than  $45^\circ$  is chosen for  $T_0$ .

#### 4.4.4 Rectangular Panels

The results presented above are for square panels ( $a/b = 1$ ). The  $a/b$  term in the expression for axial displacement, equation 3.77, will alter the solution by a certain factor. For example, a panel with  $a/b = 2$  has twice the axial displacement for every value of  $x$ , when compared to a square panel. However, if when comparing the response of long and short panels, the value of  $\frac{v_0}{b}$  is kept constant, the normalized solution remains the same, regardless of the aspect ratio. Therefore, if the applied transverse strain remains constant when making comparisons, the response is independent of  $a/b$ . This is, then, simply a matter of notation. Although the applied *displacement* was chosen as the boundary condition, it should be kept in mind that the *transverse strain* must be constant, so when the results are normalized their values turn out the same, regardless of the value of  $a/b$ .

### 4.5 Case IV Boundary Conditions

The boundary conditions for case IV require that the upper boundary of the quarter panel remain straight. This boundary condition eliminates the presence of a shear strain or shear stress resultant in the panel. The panel can be analyzed using a closed form solution. Since the integral of the transverse stress resultant along the upper edge,  $P_y$ , is identically zero, but the edge itself is free to move, the response for this set of boundary conditions is similar to the response of panels under Case I boundary conditions, for which the stress resultant itself is required to be zero at  $y/b = 0.5$ . In addition to the in-plane response for various variable stiffness configurations, a few

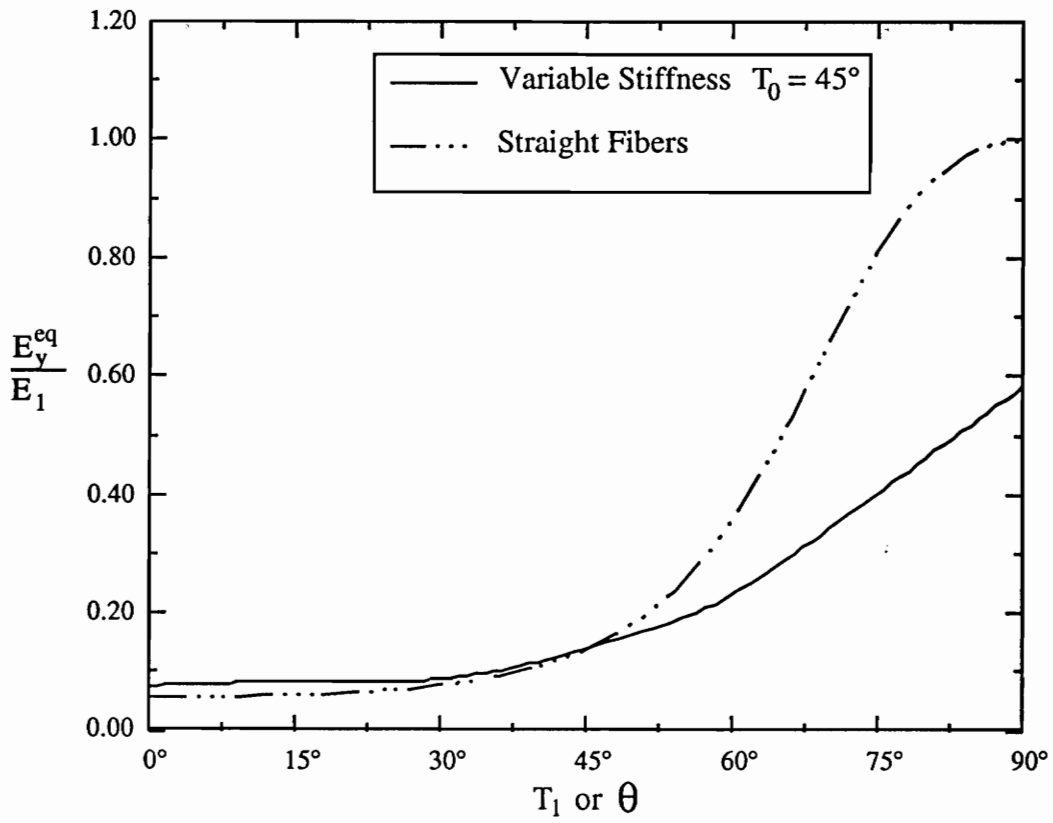


**Figure 4.24** Equivalent Axial Stiffness for Variable and Straight Fiber Panels for Case III.

comparisons are made to panels under Case I boundary conditions. The response of panels under Case IV boundary conditions is independent of the panel aspect ratio  $a/b$ . For straight fiber panels there is no difference between Case I and Case IV boundary conditions.

### 4.5.1 Deformations

The deformations for panels under these boundary conditions is similar to the response found for Cases I. The  $u$  displacement varies as a function of  $x$  in such a way that the strain is highest at  $x/a = 0$  for panels with  $T_0 > T_1$ . This is shown in Figure 4.25, where the normalized  $u$  displacement is shown as a function of  $x/a$ . Conversely, when  $T_1$  is larger than  $T_0$ , an area of high strain is found at  $x/a = 0.5$ .

The axial displacement along the panel length for two variable stiffness configurations under Case I and Case IV boundary conditions is compared in Figure 4.26. When  $T_1 = 0^\circ$  the response between the Case I panel (at  $y/b = 0$ ) and the Case IV panel are indistinguishable for all values of  $x/a$ . The response is almost identical because when  $T_1 = 0^\circ$ , the distortions in the displacement fields for Case I caused by the presence of shear are isolated away from  $y/b = 0$ . When  $T_1 = 90^\circ$  the shear strain is more evenly distributed throughout the quarter panel. Therefore, the axial response for this configuration under Case I boundary conditions is quite different from the response for Case IV. The panel under Case I boundary conditions exhibits a higher axial displacement for every value of  $x/a$ .

As explained in Chapter 3, the governing equations for this case simplify in such a way that the transverse displacement,  $v$ , is a linear function of the  $y$  coordinate. However, the value of the transverse displacement depends on  $\epsilon_0$ , which is obtained from the integral condition at  $y/b = 0.5$ . The value of the strain  $\epsilon_0$  that is necessary to satisfy the integral condition for this case depends on the values of  $T_0$  and  $T_1$  (which determine the values of the  $A_{ij}$  in equations 3.85-3.88). The normalized value of  $\epsilon_0$  is shown in Figure 4.27 as a function of  $T_1$ . The normalized value is negative for all values of  $T_1$ , indicating that under end shortening the transverse strain is always positive. When the value of  $T_1$  is  $45^\circ$ , and the fibers are straight, the normalized value of  $\epsilon_0$  is  $-0.75$ . When  $T_1 = 0^\circ$ , since the panel tends to expand more in the transverse direction, the value is  $-1.36$ . A much smaller value is needed when the panel-end angle  $T_1$  is  $90^\circ$ ; it is only  $-0.13$ .

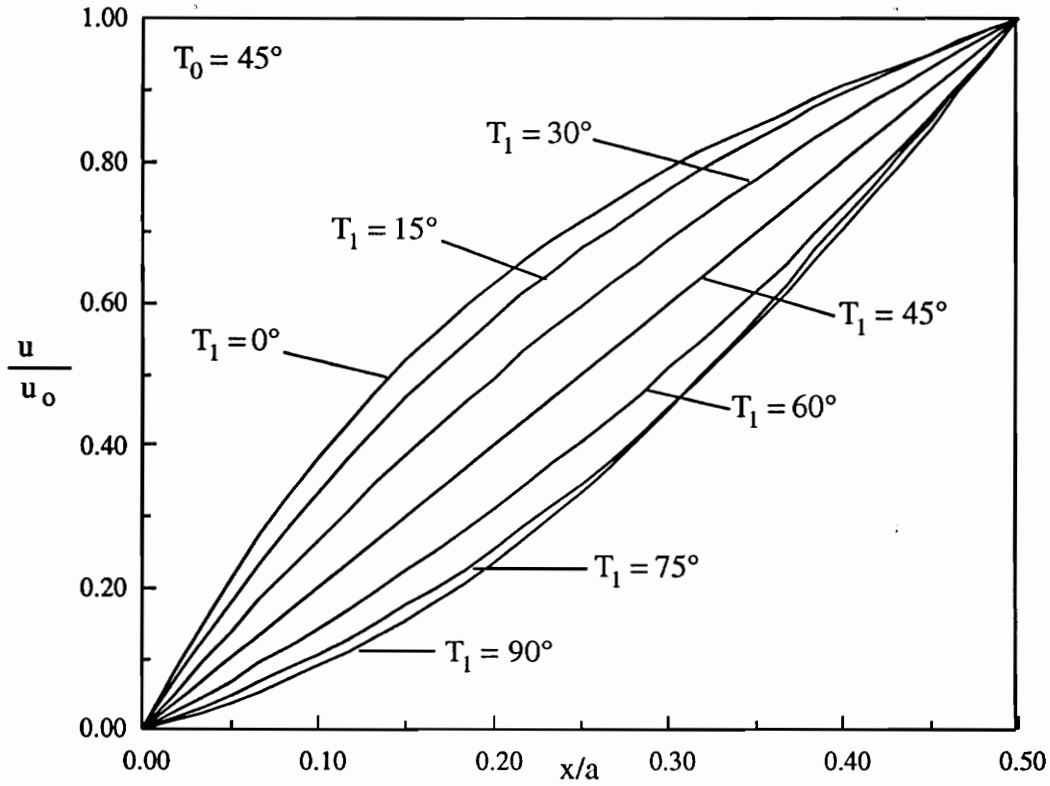


**Figure 4.25 Normalized Axial Displacement as a Function of  $x/a$  for Case IV Panels.**

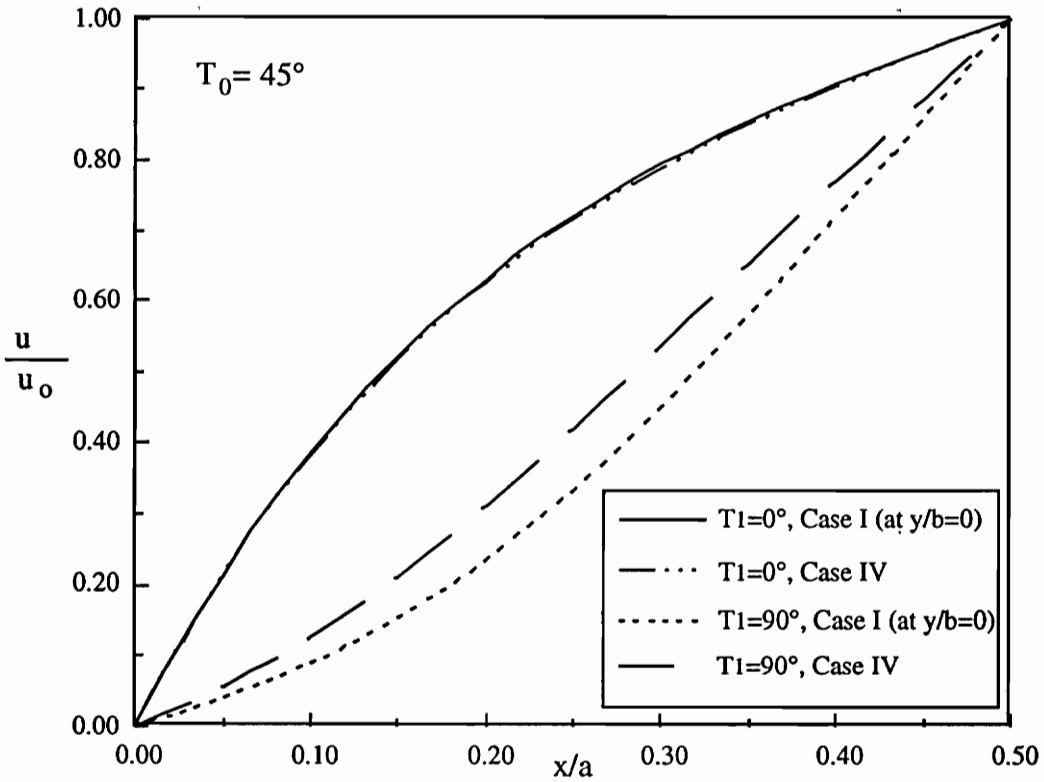


**Figure 4.26** Comparison of the Axial Displacement Distributions for Case I and Case IV Panels with  $T_1 = 0^\circ$  and  $T_1 = 90^\circ$ .

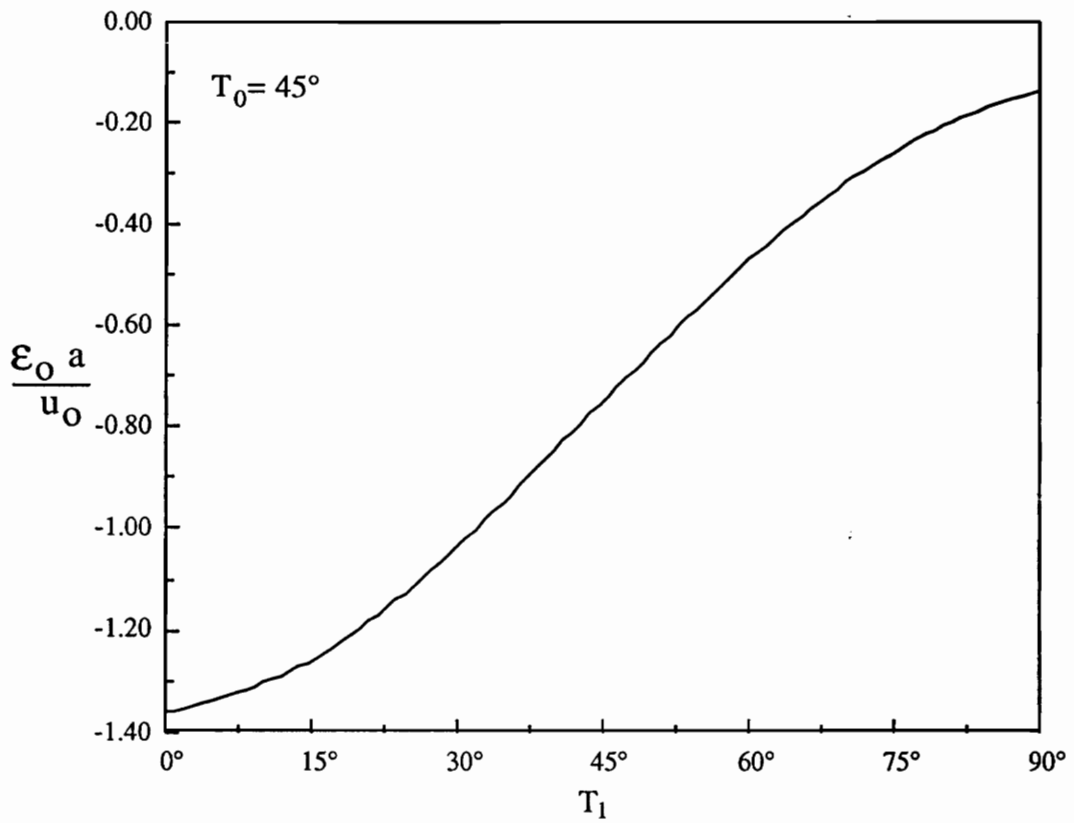


**Figure 4.27** Normalized Transverse Strain,  $\epsilon_0$ , for Case IV Panels as a Function of  $T_1$ .

## 4.5.2 Stress Resultants

Although the axial strain,  $\epsilon_x$ , and the stiffnesses are functions of  $x$ , the axial stress resultant for this case is a constant,  $N_o$ . However, the transverse stress resultant is a function of  $x$ . The expression for  $N_y$  given in equation 3.84 may be expressed as

$$N_y = \frac{A_{12}N_o}{A_{11}} + \frac{A_{22}A_{11} - A_{12}^2}{A_{11}}\epsilon_o = \nu_{yx}N_o + hE_y\epsilon_o. \quad (4.5)$$

The first term in the expression for  $N_y$  is the part of the transverse stress resultant due to the Poisson expansion of the panel, while the other term is the response to the transverse strain,  $\epsilon_o$ . The normalized transverse stress resultant is shown in Figure 4.28 as a function of  $x/a$ . Note that as in case I, parts of the panel are subjected to transverse tension while others to transverse compression, depending on  $u_o$ . The value of  $N_y$  for a straight fiber configuration is zero for all  $x$  and  $y$ . As the angle  $T_1$  increases or decreases away from  $45^\circ$ , the panel is subjected to tensile and compressive loads, depending on the value of  $x/a$ . The largest loads for panels with  $T_1$  values less than  $45^\circ$  develop at  $x/a = 0$ , while for panels with  $T_1$  values greater than  $45^\circ$ , the maximum occurs at  $x/a = 0.5$ .

The transverse load for two variable stiffness configurations ( $T_1 = 0^\circ$  and  $90^\circ$ ) is shown in Figure 4.29 as a function of  $x/a$  for Case I and Case IV boundary conditions. When  $T_1 = 0^\circ$  the values of  $N_y$  for Case I differ from those for Case IV by less than 4.8% over the entire range of  $x/a$ . This leads to the conclusion that if the shear is concentrated in the upper portion of the panel, then for values of  $y/b$  close to zero, the Case I panel expands in a uniform fashion. Although for one set of boundary conditions the panel deforms freely at  $y/b = 0.5$ , and for the other there is a uniform transverse expansion, the response for small values of  $y/b$  is the same. This may be explained by St. Venant's principle. The boundary conditions are similar enough, and the area of large gradients is sufficiently removed from the lower part of the quarter panel, that only the upper part of the panel is affected by the shear deformation. However, this is not true of panels with a  $T_1 = 90^\circ$  configuration. For this configuration the transverse load for the panel under Case IV boundary conditions is always higher than for the panel with Case I boundary conditions. At  $x/a = 0.5$  the value of  $N_y$  for the Case IV panel is seven times larger than for the panel under Case I boundary conditions.

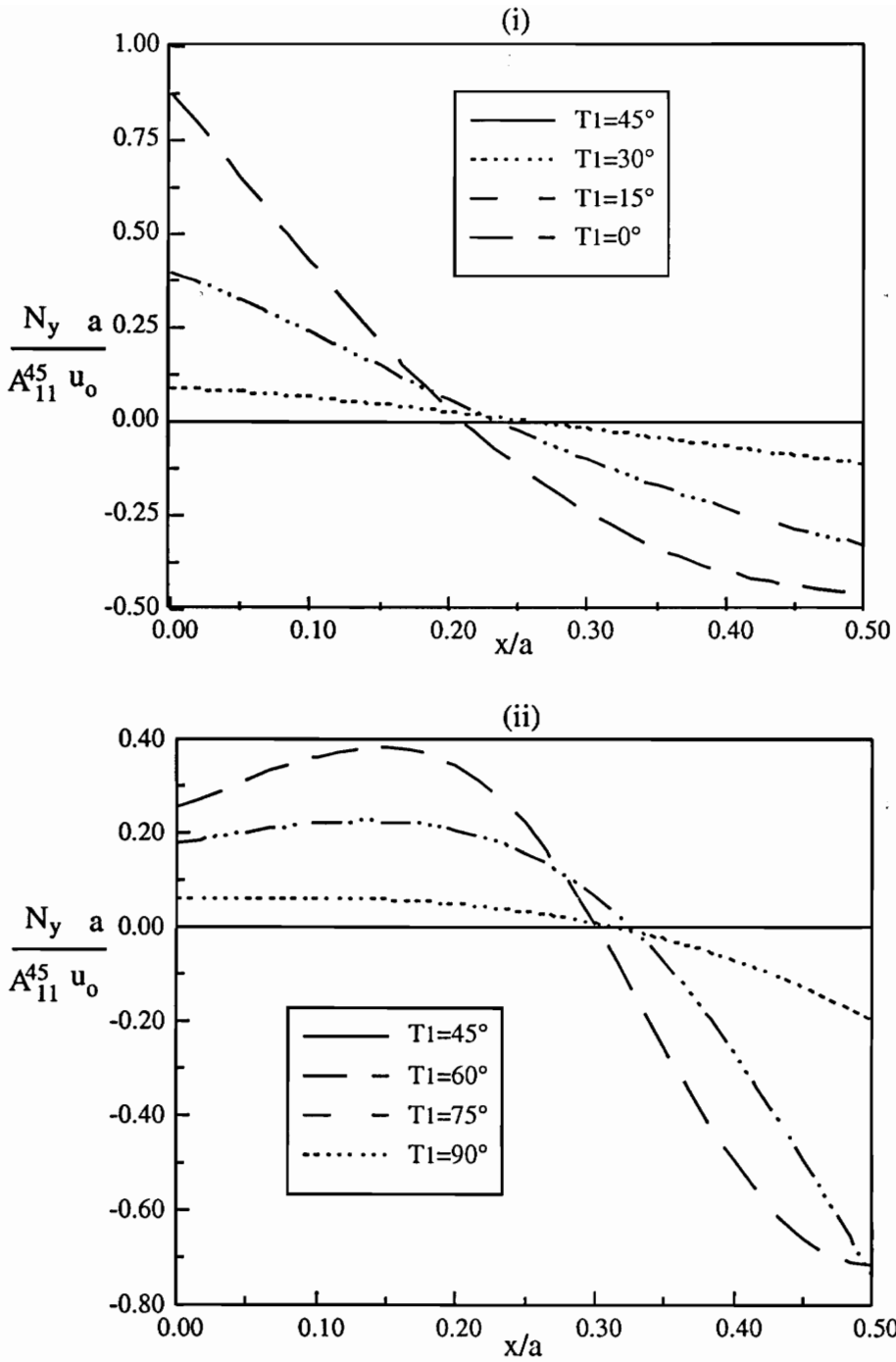


**Figure 4.28** Transverse Stress Resultant as a Function of  $x/a$  For Case IV  
Panels with (i)  $T_1 < 45^\circ$  and (ii)  $T_1 > 45^\circ$ .

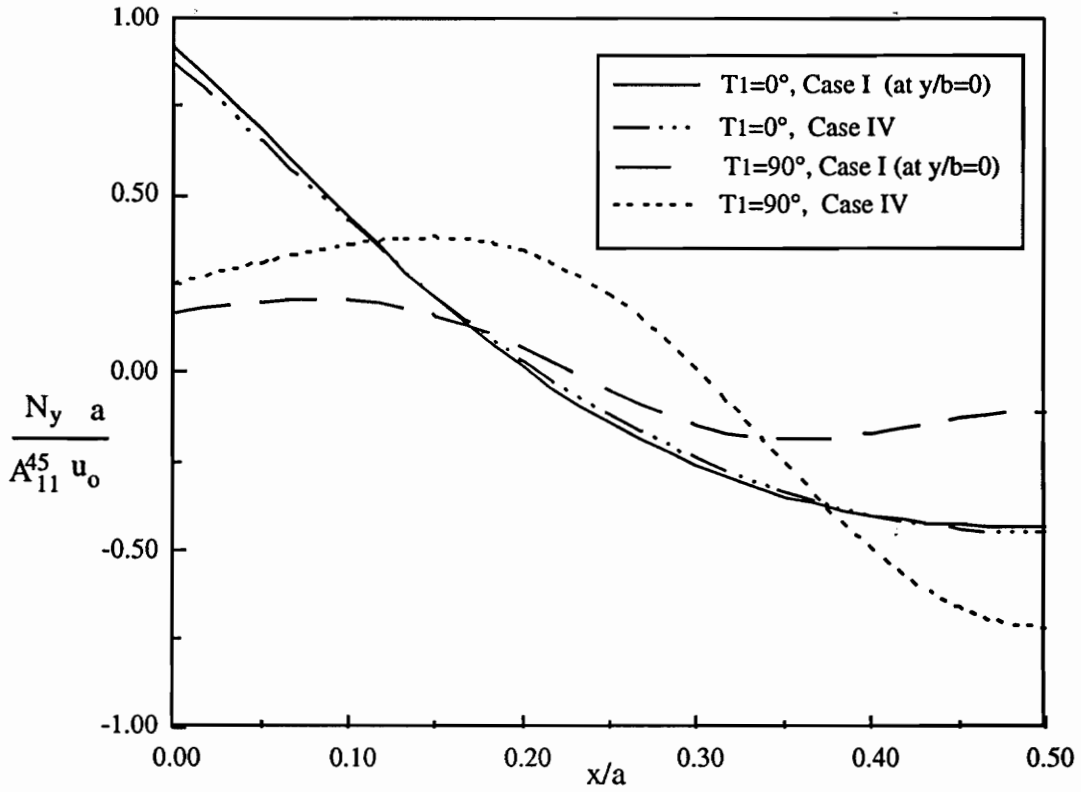


**Figure 4.29** Comparison of the Transverse Stress Resultant Distributions for Case I and Case IV Panels with  $T_1 = 0^\circ$  and  $T_1 = 90^\circ$ .

### 4.5.3 Equivalent Stiffness

Further proof of the similarity between the response of Case I and Case IV panels is given by the similarities in the overall equivalent panel stiffness,  $E_x^{eq}$ . The normalized axial stiffness is shown in Figure 4.30 as a function of the angle  $T_1$ . As expected, the panels with the smaller values of  $T_1$  tend to have a higher equivalent stiffness. The values between the Case I and Case IV panels differ by less than 7%. This indicates that the axial response, in a global sense, is almost identical for both sets of boundary conditions. The shear strain and shear stress resultant that arise for Case I panels therefore have little bearing on the axial response of the panels, although locally they distort the displacement fields and stress resultants.

## 4.6 Validity of the Numerical Model

Although the response of panel subjected to the boundary conditions for Cases II, III and IV is obtainable through the closed form solutions presented in Chapter 3, developing numerical models for these cases is useful in establishing the accuracy of the numerical model. An exact closed form solution for Case I was not found, so establishing the validity of the first set of results presented in this Chapter is critical. Displacements and stress resultants that have been calculated with the numerical model are compared to the exact values in Table 4.1 for Cases II and IV for a panel with  $T_1 = 45^\circ$ . The error for any of the values that were sampled is less than 0.5%. The error in the values for the stress resultant is slightly higher than for the displacement; this is expected, since the stress resultants involve the derivatives of the displacements, and the discretization error inherent in the numerical technique is augmented. A comparison of the numerical and exact values for Case III is shown in Table 4.2. The correlation between the results from the numerical model and the exact solution is particularly good for this case. The displacements obtained using the numerical solution are exact up to six significant figures, and the error in the stress resultant is less than 0.01%. The numerical solution therefore provides an accurate solution to the in-plane problem for the variable stiffness panels. Although the equations for Case I the governing elliptic equations do not simplify at all, given the results for Cases II-IV, the numerical solution must be accurate.

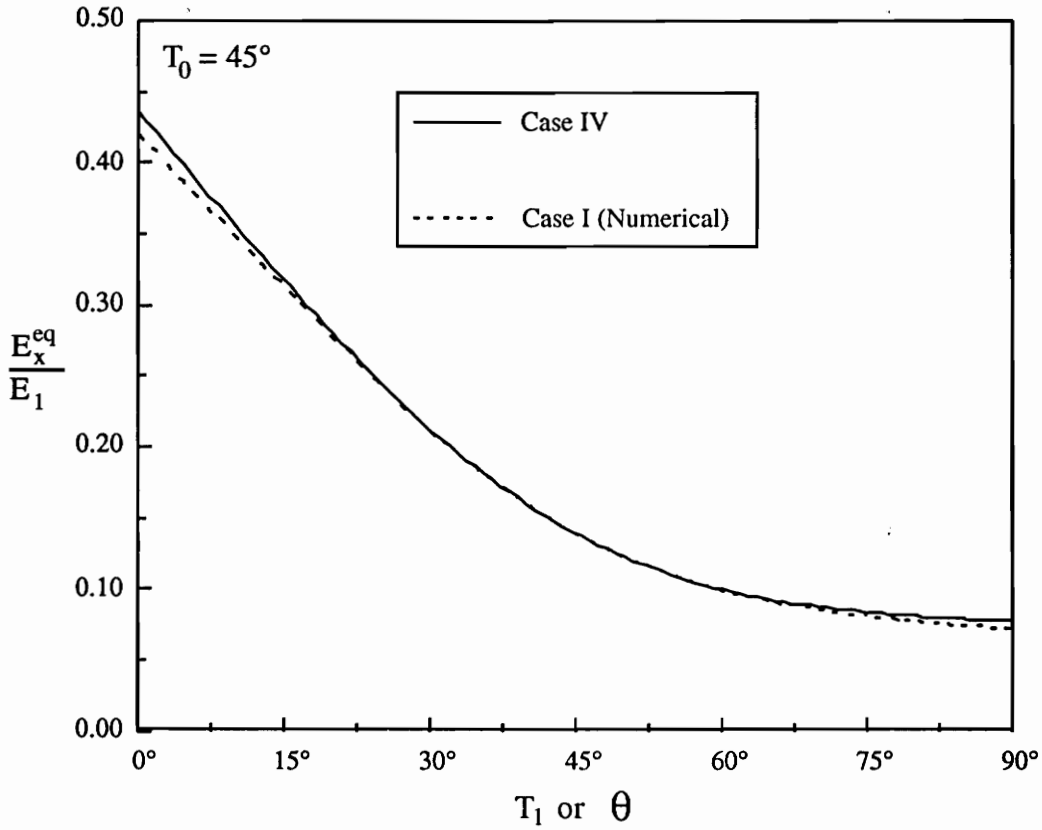


**Figure 4.30** Equivalent Axial Stiffness for Variable and Straight Fiber Panels for Case IV.

**Table 4.1 Numerically Calculated and Exact Values of  $u$  and  $N_y$  for Cases II and IV.**

$u$ or $N_y$	Case II		Case IV	
	Numerical	Exact	Numerical	Exact
$\frac{u(0,b/4)}{u_0}$	$O(-18)^*$	0.000000	$O(-18)^*$	0.000000
$\frac{u(a/10,b/4)}{u_0}$	0.331278	0.331155	0.384438	0.384428
$\frac{u(a/5,b/4)}{u_0}$	0.557417	0.557298	0.628681	0.628665
$\frac{u(3a/10,b/4)}{u_0}$	0.728114	0.728071	0.790251	0.790243
$\frac{u(2a/5,b/4)}{u_0}$	0.870195	0.870192	0.905544	0.905543
$\frac{u(a/2,b/4)}{u_0}$	1.000000	1.000000	1.000000	1.000000
$\frac{N_y(0,b/4) a}{u_0 A_{11}^{45}}$	3.06520	3.06485	0.876454	0.876333
$\frac{N_y(a/10,b/4) a}{u_0 A_{11}^{45}}$	1.81393	1.82018	0.427756	0.426715
$\frac{N_y(a/5,b/4) a}{u_0 A_{11}^{45}}$	0.974927	0.975891	0.0350224	0.0347818
$\frac{N_y(3a/10,b/4) a}{u_0 A_{11}^{45}}$	0.446620	0.446414	-0.240203	-0.240144
$\frac{N_y(2a/5,b/4) a}{u_0 A_{11}^{45}}$	0.157273	0.157225	-0.398918	-0.398899
$\frac{N_y(a/2,b/4) a}{u_0 A_{11}^{45}}$	0.0653786	0.0653810	-0.450526	-0.450534

\*Number is of the order  $10^{-18}$

**Table 4.2 Numerically Calculated and Exact Values of  $u$  and  $N_y$  for Case III.**

Case III		
$u$ or $N_y$	Numerical	Exact
$\frac{u(0,b/4)}{v_0}$	$O(-17)^*$	0.000000
$\frac{u(a/10,b/4)}{v_0}$	-0.117307	-0.117307
$\frac{u(a/5,b/4)}{v_0}$	-0.183982	-0.183982
$\frac{u(3a/10,b/4)}{v_0}$	-0.217539	-0.217539
$\frac{u(2a/5,b/4)}{v_0}$	-0.231384	-0.231384
$\frac{u(a/2,b/4)}{v_0}$	-0.236056	-0.236056
$\frac{N_y(0,b/4) a}{v_0 A_{11}^{45}}$	0.884285	0.884286
$\frac{N_y(a/10,b/4) a}{v_0 A_{11}^{45}}$	0.594033	0.594024
$\frac{N_y(a/5,b/4) a}{v_0 A_{11}^{45}}$	0.461013	0.461008
$\frac{N_y(3a/10,b/4) a}{v_0 A_{11}^{45}}$	0.398990	0.398991
$\frac{N_y(2a/5,b/4) a}{v_0 A_{11}^{45}}$	0.371435	0.371436
$\frac{N_y(a/2,b/4) a}{v_0 A_{11}^{45}}$	0.363577	0.363577

\*Number is of the order  $10^{-17}$

# CHAPTER 5

## Buckling Analysis

### 5.1 Introduction

The in-plane response of the variable stiffness panels presented in the previous chapter reveals that distribution of the in-plane loads throughout the panel area depends on the values of  $T_0$  and  $T_1$ . The loads may be distributed in such a way that the load at which stability is lost, or buckling load, surpasses the maximum value that can be obtained with straight fiber configurations. In this chapter the theory that leads to the eigenvalue problem which is used to find the buckling load is presented. The system of equations is derived using the Ritz method. The issue of anisotropy and how its effects may be neglected is then addressed. Finally, the mass and stiffness matrices for each of the cases introduced in Chapter 3 are discussed.

#### 5.1.1 Coordinate System

In the previous chapters, an  $x$ - $y$  coordinate system, the origin of which is located in the center of the panel, was used in the study of the variable stiffness panels. However, since the stability analysis involves integrals of even and odd functions that multiply the stiffnesses and stress resultants, it is convenient to change to a different coordinate system. The  $\bar{x}$ - $\bar{y}$  coordinate system shown in Figure 5.1 is used in the buckling analysis. The transformation between one coordinate system and the other is given by

$$\bar{x} = x + \frac{a}{2} \quad \text{and} \quad \bar{y} = y + \frac{b}{2} \quad (5.1),$$

which is simply a translation from the center of the panel to the lower left corner. The definition of the fiber angle for the variable stiffness panels in the  $\bar{x}$ - $\bar{y}$  coordinate system is given by,

$$\theta(\bar{x}) = \begin{cases} 2\frac{(T_0-T_1)\bar{x}}{a} + T_1 & 0 \leq \bar{x} \leq \frac{a}{2} \\ 2\frac{(T_1-T_0)\bar{x}}{a} + 2T_0 - T_1 & \frac{a}{2} < \bar{x} \leq a \end{cases} \quad (5.2)$$

The  $z$  coordinate is not affected by this translation and remains the same as before.

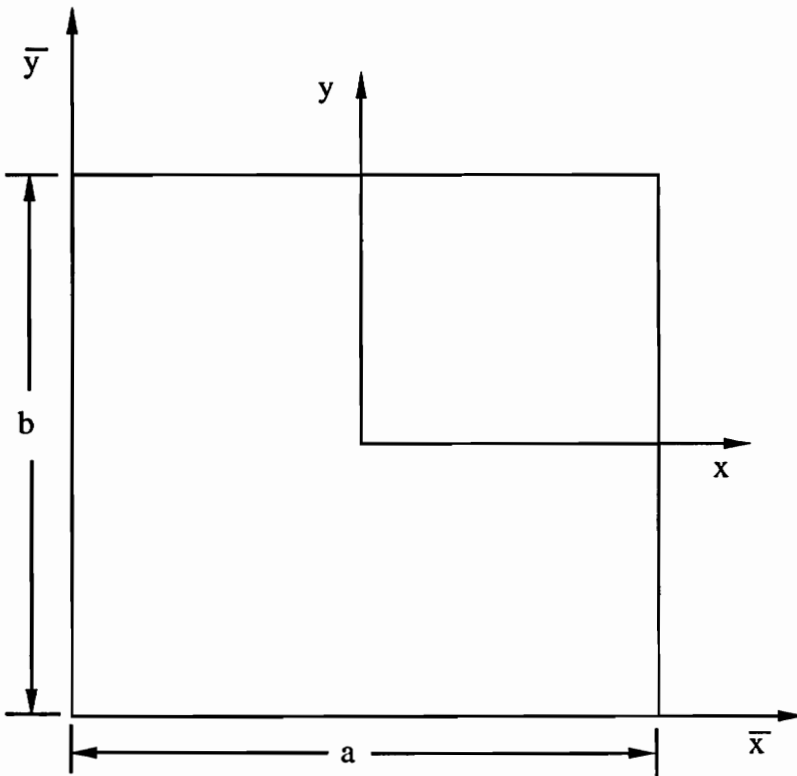


**Figure 5.1** Panel  $\bar{x}$ - $\bar{y}$  and  $x$ - $y$  Coordinate Systems.

## 5.2 Stability Analysis by The Ritz Method

The Ritz method has been used to solve vibration and stability problems for over one hundred years [19]. Therefore, the method itself will not be developed here. Instead, only its application to orthotropic laminated panels will be presented.

The Ritz method is used to find the lowest load that will cause buckling. For the loading conditions being discussed in this work, buckling means the occurrence of an outward displacement,  $w$ , when the in-plane loads on the panel reach a critical limit. An approximation to the out-of-plane displacement function must be provided to carry out the analysis. A series approximation for  $w$  is given by

$$w(\bar{x}, \bar{y}) = \sum_{m=1}^M \sum_{n=1}^N A_{mn} \Phi_m(\bar{x}) \Psi_n(\bar{y}). \quad (5.3)$$

The coefficients  $A_{mn}$  are undetermined constants, and the functions  $\Phi_m$  and  $\Psi_n$  are such that they satisfy the boundary conditions imposed on  $w(\bar{x}, \bar{y})$  around the perimeter of the panel.

The eigenvalue problem is formulated by applying the Trefftz criterion, given by,

$$\delta(\delta^2 \Pi) = 0, \quad (5.4)$$

where  $\Pi$  is the total potential energy of the panel. For the panels in this study,  $\Pi$  consists of two terms, given as follows,

$$\Pi = U + V, \quad (5.5)$$

where  $U$  is the strain energy due to bending, and  $V$  denotes the potential energy of the in-plane loads. For composite panels, each of these terms is explained below.

### 5.2.1 Strain Energy

The strain energy of an elastic body is given by

$$U = \frac{1}{2} \int \int \int (\sigma_{\bar{x}} \epsilon_{\bar{x}} + \sigma_{\bar{y}} \epsilon_{\bar{y}} + \sigma_z \epsilon_z + \sigma_{\bar{x}z} \epsilon_{\bar{x}z} + \sigma_{\bar{y}z} \epsilon_{\bar{y}z} + \sigma_{\bar{x}\bar{y}} \epsilon_{\bar{x}\bar{y}}) d\bar{x} d\bar{y} dz \quad (5.6).$$

However, the assumptions of the Classical Lamination Theory are such that  $\epsilon_z = \epsilon_{\bar{x}z} = \epsilon_{\bar{y}z} = 0$ . Therefore, the strain energy is made up only of the terms containing  $\sigma_{\bar{x}}$ ,  $\sigma_{\bar{y}}$  and  $\sigma_{\bar{x}\bar{y}}$ . By integrating with respect to  $z$  and substituting equations 2.14 and 2.15, the strain energy due to bending becomes

$$\begin{aligned}
U = & \frac{1}{2} \int \int \left[ D_{11} \left( \frac{\partial^2 w}{\partial \bar{x}^2} \right)^2 + 2D_{12} \frac{\partial^2 w}{\partial \bar{x}^2} \frac{\partial^2 w}{\partial \bar{y}^2} + D_{22} \left( \frac{\partial^2 w}{\partial \bar{y}^2} \right)^2 \right. \\
& \left. + 4 \left( D_{16} \frac{\partial^2 w}{\partial \bar{x}^2} + D_{26} \frac{\partial^2 w}{\partial \bar{y}^2} \right) \frac{\partial^2 w}{\partial \bar{x} \partial \bar{y}} + 4D_{66} \left( \frac{\partial^2 w}{\partial \bar{x} \partial \bar{y}} \right)^2 \right] d\bar{x} d\bar{y}. \quad (5.7)
\end{aligned}$$

For straight fiber panels the  $D_{ij}$  may be removed from within the integral sign, since they are independent of  $\bar{x}$  and  $\bar{y}$ . However, for variable stiffness panels, the  $D_{ij}$  are functions of  $\bar{x}$  and must remain as part of the integrand.

## 5.2.2 Potential Energy of the In-Plane Loads

The potential energy of the loads is the other term which is necessary to obtain the total potential energy. The potential energy involves the in-plane forces applied in the pre-buckled state and the midplane strains that result from the out-of plane deflections of the panel. The expression for  $V$  is given by

$$\begin{aligned}
V = & \lambda \int \int (N_{\bar{x}} \epsilon'_{\bar{x}} + N_{\bar{y}} \epsilon'_{\bar{y}} + N_{\bar{x}\bar{y}} \epsilon'_{\bar{x}\bar{y}}) d\bar{x} d\bar{y} = \\
& \frac{1}{2} \lambda \int \int \left[ N_{\bar{x}} \left( \frac{\partial w}{\partial \bar{x}} \right)^2 + N_{\bar{y}} \left( \frac{\partial w}{\partial \bar{y}} \right)^2 + 2N_{\bar{x}\bar{y}} \frac{\partial w}{\partial \bar{x}} \frac{\partial w}{\partial \bar{y}} \right] d\bar{x} d\bar{y}, \quad (5.8)
\end{aligned}$$

where  $\lambda$  is an arbitrary multiplier necessary to determine the buckling load, and  $\epsilon'_{\bar{x}}$ ,  $\epsilon'_{\bar{y}}$ , and  $\epsilon'_{\bar{x}\bar{y}}$  are the strains due to the outward deformation.

## 5.2.3 Second Variation of the Total Potential Energy

In order to arrive at the eigenvalue problem for the critical load, the Trefftz criterion is applied. When  $\delta(\delta^2\Pi) = 0$  the equilibrium of the panel is changing from a stable to an unstable configuration, and it therefore determines the bifurcation point.

Since the expression for  $w$  is given in series form, the Trefftz criterion reduces to

$$\begin{aligned}
& \sum_{m=1}^M \sum_{n=1}^N \left\{ \int_0^a D_{11} \frac{d^2 \Phi_p}{d\bar{x}^2} \frac{d^2 \Phi_m}{d\bar{x}^2} d\bar{x} \int_0^b \Psi_n \Psi_q d\bar{y} + \int_0^a D_{12} \Phi_p \frac{d^2 \Phi_p}{d\bar{x}^2} d\bar{x} \int_0^b \Psi_q \frac{d^2 \Psi_n}{d\bar{y}^2} d\bar{y} \right. \\
& + \int_0^a D_{12} \Phi_p \frac{d^2 \Phi_m}{d\bar{x}^2} d\bar{x} \int_0^b \Psi_n \frac{d^2 \Psi_q}{d\bar{y}^2} d\bar{y} + \int_0^a D_{22} \Phi_p \Phi_m d\bar{x} \int_0^b \frac{d^2 \Psi_n}{d\bar{y}^2} \frac{d^2 \Psi_q}{d\bar{y}^2} d\bar{y} \\
& \left. + 4 \int_0^a D_{66} \frac{d\Phi_p}{d\bar{x}} \frac{d\Phi_m}{d\bar{x}} d\bar{x} \int_0^b \frac{d\Psi_n}{d\bar{y}} \frac{d\Psi_q}{d\bar{y}} d\bar{y} + 2 \int_0^a D_{16} \frac{d^2 \Phi_p}{d\bar{x}^2} \frac{d\Phi_m}{d\bar{x}} d\bar{x} \int_0^b \Psi_q \frac{d\Psi_n}{d\bar{y}} d\bar{y} \right\}
\end{aligned}$$

$$\begin{aligned}
& +2 \int_0^a D_{16} \frac{d\Phi_p}{d\bar{x}} \frac{d^2\Phi_m}{d\bar{x}^2} d\bar{x} \int_0^b \Psi_n \frac{d\Psi_q}{d\bar{y}} d\bar{y} + 2 \int_0^a D_{26} \Phi_m \frac{d\Phi_p}{d\bar{x}} d\bar{x} \int_0^b \frac{d\Psi_q}{d\bar{y}} \frac{d^2\Psi_n}{d\bar{y}^2} d\bar{y} \\
& +2 \int_0^a D_{26} \Phi_p \frac{d\Phi_m}{d\bar{x}} d\bar{x} \int_0^b \frac{d^2\Psi_q}{d\bar{y}^2} \frac{d\Psi_n}{d\bar{y}} d\bar{y} + \lambda \left[ \int_0^a \int_0^b N_{\bar{x}} \frac{d\Phi_p}{d\bar{x}} \frac{d\Phi_m}{d\bar{x}} \Psi_n \Psi_q d\bar{x} d\bar{y} \right. \\
& + \int_0^a \int_0^b N_{\bar{y}} \Phi_p \Phi_m \frac{d\Psi_n}{d\bar{y}} \frac{d\Psi_q}{d\bar{y}} d\bar{x} d\bar{y} + \int_0^a \int_0^b N_{\bar{x}\bar{y}} \Phi_m \frac{d\Phi_p}{d\bar{x}} \Psi_q \frac{d\Psi_n}{d\bar{y}} d\bar{x} d\bar{y} \\
& \left. + \int_0^a \int_0^b N_{\bar{x}\bar{y}} \Phi_p \frac{d\Phi_m}{d\bar{x}} \Psi_n \frac{d\Psi_q}{d\bar{y}} d\bar{x} d\bar{y} \right] A_{mn} = 0 \quad \begin{matrix} p = 1, 2, \dots, M \\ q = 1, 2, \dots, N \end{matrix} \quad (5.9)
\end{aligned}$$

When expanded the above expression leads to a system of  $M \times N$  equations in  $M \times N$  unknowns that results in the following eigenvalue problem,

$$[K]\{A\} - \lambda[M]\{A\} = 0. \quad (5.10)$$

The elements of the stiffness matrix,  $[K]$ , are sums of the integrals containing the  $D_{ij}$ , and the elements of the geometric stiffness matrix,  $[M]$ , are sums of the integrals containing the stress resultants. The lowest value of  $\lambda$  from the solution of this eigenvalue problem determines the critical buckling load or displacement.

## 5.3 The Eigenvalue Problem

The eigenvalue problem that results from the application of equation 5.9 is developed here. In order to apply the Ritz method to variable stiffness panels, it is necessary to ignore the effects of anisotropy so that a trigonometric approximation for  $w$  may be used. The conditions for neglecting anisotropy are presented. The integrals that involve the bending stiffnesses have been obtained in closed form. For the sake of brevity, these integrals are not developed at length, but are presented in detail in the appendix.

### 5.3.1 The Effects of Anisotropy

So far the analysis has included the  $D_{16}$  and  $D_{26}$  terms from the bending stiffness matrix. These terms are known as the anisotropic bending stiffnesses, and represent the coupling between pure bending and twisting inherent in the panel. These terms complicate the analysis because simple trigonometric functions in  $\bar{x}$  and  $\bar{y}$  cannot be chosen for  $\Phi_m$  and  $\Psi_n$ . If the anisotropic bending stiffnesses are to be included in the analysis, then  $\Phi_m$  and  $\Psi_n$  must be the ‘beam functions’, which

are functions that define the natural vibration modes of beams. The integration of the energy terms then becomes very tedious and computationally intensive. Since the bending stiffnesses are already in trigonometric forms, having  $\Phi_m$  and  $\Psi_n$  in terms of sines and cosines is an added advantage because trigonometric identities may be used to simplify the integrands. It is therefore necessary to neglect the  $D_{16}$  and  $D_{26}$  terms. However, simply neglecting the anisotropic bending stiffnesses may lead to large errors in the buckling load, as has been proven by Nemeth [20].

There are certain conditions that must be satisfied so that the anisotropic bending stiffnesses may be neglected. These conditions have been established by Nemeth for straight fiber panels. It is assumed that the same criterion may be used for variable stiffness panels, although the  $D_{16}$  and  $D_{26}$  terms are functions of  $\bar{x}$ . Nemeth has compared results from finite element analysis and results from the Ritz method in which the anisotropic bending stiffnesses have been neglected. He has concluded that for symmetric angle ply laminates, a non-dimensional parameter may be used to determine whether anisotropy may be neglected. This parameter,  $\mu$ , is given by

$$\mu = \max \left[ \frac{D_{16}}{(D_{11}^3 D_{22})^{1/4}}, \frac{D_{26}}{(D_{11} D_{22}^3)^{1/4}} \right] \quad (5.11)$$

For the material system being used in this study, this parameter must satisfy the condition,

$$0.2 < \mu < 1.3 \quad (5.12).$$

The upper and lower bounds on  $\mu$  depend on the material properties and reflect the range for which the anisotropic bending stiffnesses are small compared to  $D_{11}$  and  $D_{22}$ . The non-dimensional parameter indicates that the influence of the  $D_{16}$  and  $D_{26}$  terms in the eigenvalue problem is not significant enough to cause a large amount of error if ignored. For symmetric angle ply laminates, the value of  $\mu$  is largest when the fiber angle is  $45^\circ$ . However, the value depends on the lay-up of the panel. In panels with a  $[\pm\theta]_{ns}$  lay-up, the value of  $\mu$  depends on the number of layers,  $4n$ . For the material system used in this study, the necessary number of layers is 12, or  $n = 3$ . The value of  $\mu$  for this configuration is 0.189. Therefore, in order to carry out experimental testing or to compare the results of the following chapter to those obtained using other analysis techniques, a twelve layer laminate must be used in order to be able to neglect the effects of anisotropy. In the development of the eigenvalue problem, the value of  $D_{16}$  and  $D_{26}$  bending stiffnesses is assumed to be zero.

### 5.3.2 The $w$ Displacement Function

It is necessary to assume a form of the displacement function  $w(\bar{x}, \bar{y})$  in order to carry out the analysis. In this work, all four edges of each panel are assumed to have no out-of-plane displacement. In addition, the applied moment at each edge is identically zero. This applies to all four cases being considered. The boundary conditions are such that

$$w = M_{\bar{x}} = -D_{11} \frac{\partial^2 w}{\partial \bar{x}^2} - D_{12} \frac{\partial^2 w}{\partial \bar{y}^2} = 0, \text{ along } \bar{x} = 0 \text{ and } \bar{x} = a \quad (5.13)$$

and

$$w = M_{\bar{y}} = -D_{12} \frac{\partial^2 w}{\partial \bar{x}^2} - D_{22} \frac{\partial^2 w}{\partial \bar{y}^2} = 0, \text{ along } \bar{y} = 0 \text{ and } \bar{y} = b. \quad (5.14)$$

A series approximation that satisfies the boundary conditions and can be easily incorporated into the analysis is a double sine function, given by,

$$w(\bar{x}, \bar{y}) = \sum_{m=1}^M \sum_{n=1}^N A_{mn} \sin\left(\frac{m\pi\bar{x}}{a}\right) \sin\left(\frac{n\pi\bar{y}}{b}\right). \quad (5.15)$$

The relative magnitude of the coefficients,  $A_{mn}$ , determines the buckling mode, or shape of the panel upon bifurcation.

The double sine series may then be substituted into equation 5.9, assuming that the terms containing the anisotropic bending stiffnesses vanish. In addition, some integrals may be simplified by the relationships,

$$\int_0^l \sin\left(\frac{p\pi\bar{x}}{l}\right) \sin\left(\frac{q\pi\bar{x}}{l}\right) d\bar{x} = \begin{cases} \frac{l}{2} & \text{if } p = q \\ 0 & \text{if } p \neq q \end{cases} = \frac{l}{2} \delta_{pq}, \quad (5.16)$$

and

$$\int_0^l \cos\left(\frac{p\pi\bar{x}}{l}\right) \cos\left(\frac{q\pi\bar{x}}{l}\right) d\bar{x} = \begin{cases} \frac{l}{2} & \text{if } p = q \\ 0 & \text{if } p \neq q \end{cases} = \frac{l}{2} \delta_{pq}, \quad (5.17)$$

where  $\delta_{pq}$  is the Kronecker delta. Equation 5.9 therefore simplifies to

$$\begin{aligned}
& \sum_m^M \sum_n^N \left\{ \frac{\pi^4 b}{2a^4} m^2 p^2 \delta_{qn} \int_0^a D_{11} \sin\left(\frac{p\pi\bar{x}}{a}\right) \sin\left(\frac{m\pi\bar{x}}{a}\right) d\bar{x} \right. \\
& + \frac{\pi^4}{2a^2 b} (m^2 q^2 + n^2 p^2) \delta_{qn} \int_0^a D_{12} \sin\left(\frac{p\pi\bar{x}}{a}\right) \sin\left(\frac{m\pi\bar{x}}{a}\right) d\bar{x} \\
& + \frac{\pi^4}{2b^3} n^2 q^2 \delta_{qn} \int_0^a D_{22} \sin\left(\frac{p\pi\bar{x}}{a}\right) \sin\left(\frac{m\pi\bar{x}}{a}\right) d\bar{x} \\
& + \frac{2\pi^4}{a^2 b} mnpq \delta_{qn} \int_0^a D_{66} \cos\left(\frac{p\pi\bar{x}}{a}\right) \cos\left(\frac{m\pi\bar{x}}{a}\right) d\bar{x} \\
& + \lambda \frac{\pi^2}{a^2} pm \int_0^a \int_0^b N_{\bar{x}} \cos\left(\frac{p\pi\bar{x}}{a}\right) \cos\left(\frac{m\pi\bar{x}}{a}\right) \sin\left(\frac{q\pi\bar{y}}{b}\right) \sin\left(\frac{n\pi\bar{y}}{b}\right) d\bar{x} d\bar{y} \\
& + \lambda \frac{\pi^2}{b^2} qn \int_0^a \int_0^b N_{\bar{y}} \sin\left(\frac{p\pi\bar{x}}{a}\right) \sin\left(\frac{m\pi\bar{x}}{a}\right) \cos\left(\frac{q\pi\bar{y}}{b}\right) \cos\left(\frac{n\pi\bar{y}}{b}\right) d\bar{x} d\bar{y} \\
& + \lambda \frac{\pi^2}{ab} \left[ pn \int_0^a \int_0^b N_{\bar{x}\bar{y}} \sin\left(\frac{m\pi\bar{x}}{a}\right) \cos\left(\frac{p\pi\bar{x}}{a}\right) \sin\left(\frac{q\pi\bar{y}}{b}\right) \cos\left(\frac{n\pi\bar{y}}{b}\right) d\bar{x} d\bar{y} \right. \\
& \left. - mq \int_0^a \int_0^b N_{\bar{x}\bar{y}} \cos\left(\frac{m\pi\bar{x}}{a}\right) \sin\left(\frac{p\pi\bar{x}}{a}\right) \cos\left(\frac{q\pi\bar{y}}{b}\right) \sin\left(\frac{n\pi\bar{y}}{b}\right) d\bar{x} d\bar{y} \right] \Big\} A_{mn} = 0 \quad \begin{array}{l} p = 1, 2, \dots, M \\ q = 1, 2, \dots, N \end{array} \quad (5.18)
\end{aligned}$$

The evaluation of the integrals involving the stiffnesses and the stress resultants is outlined below.

### 5.3.3 The Stiffness Matrix

The terms in equation 5.18 that contain the  $D_{ij}$  group together to form the **stiffness matrix**. The integrands are products of trigonometric functions and the bending stiffnesses. However, as was shown in Chapter 2, the bending stiffnesses are themselves trigonometric functions, namely, linear combinations of  $\cos(2\theta)$  and  $\cos(4\theta)$ . Since there is a linear relationship between  $\theta$  and  $\bar{x}$ , the evaluation of the integrals may be carried out in closed form. The details of this integration have been included in Appendix 1. However, a brief overview is given here.

Each of the bending stiffnesses may be expressed as

$$D_{ij} = \frac{h^3}{12} [K_1 + K_2 \cos(2\theta) + K_3 \cos(4\theta)], \quad (5.19)$$

where  $h$  is the thickness of the laminate,  $K_1$ ,  $K_2$ , and  $K_3$  are constants, and the angle  $\theta$  is given by equation 5.1. For each bending stiffness, the constants in the above equation are the material

invariants introduced in Chapter 2. For example for  $D_{12}$ , the constants are:  $K_1 = U_4$ ,  $K_2 = 0$  and  $K_3 = -U_3$ . In general, the integrals involving  $D_{11}$ ,  $D_{12}$ , and  $D_{22}$  have the form,

$$\frac{h^3}{12} \int_0^a [K_1 + K_2 \cos(2\theta) + K_3 \cos(4\theta)] \sin\left(\frac{p\pi\bar{x}}{a}\right) \sin\left(\frac{m\pi\bar{x}}{a}\right) d\bar{x}. \quad (5.20)$$

By using trigonometric identities, the integrand in the above expression has been reduced to the sum of three cosine terms. Since the fiber angle  $\theta$  is a linear function of  $\bar{x}$ , the integral is easily evaluated.

The value of the integral depends on the values of  $K_1$ ,  $K_2$ ,  $K_3$ ,  $m$  and  $p$ . Since the values for  $K_1, K_2$ , and  $K_3$  are different for each bending stiffness, it is convenient to define a function for the value of the integral in equation 5.20, such that

$$\text{int}_1 = \text{int}_1(K_1, K_2, K_3, m, p) = \frac{h^3}{12} \int_0^a [K_1 + K_2 \cos(2\theta) + K_3 \cos(4\theta)] \sin\left(\frac{p\pi\bar{x}}{a}\right) \sin\left(\frac{m\pi\bar{x}}{a}\right) d\bar{x}. \quad (5.21)$$

Similarly, a function  $\text{int}_2$  may be used to define the integral for the bending energy term in equation 5.18 that contains  $D_{66}$  and is a product of sines and cosines. It is given by,

$$\text{int}_2 = \text{int}_2(K_1, K_3, m, p) = \frac{h^3}{12} \int_0^a [K_1 + K_3 \cos(4\theta)] \cos\left(\frac{p\pi\bar{x}}{a}\right) \cos\left(\frac{m\pi\bar{x}}{a}\right) d\bar{x}. \quad (5.22)$$

The elements of the stiffness matrix are therefore given by,

$$\begin{aligned} K[n + N(m - 1), q + N(p - 1)] &= \frac{\pi^4 b}{2a^4} m^2 p^2 \delta_{qn} \text{int}_1(U_1, U_2, U_3, m, p) \\ &+ \frac{\pi^4}{2a^2 b} (m^2 q^2 + n^2 p^2) \delta_{qn} \text{int}_1(U_4, 0, -U_3, m, p) + \frac{\pi^4}{2b^3} n^2 q^2 \delta_{qn} \text{int}_1(U_1, -U_2, U_3, m, p) \\ &+ \frac{2\pi^4}{a^2 b} m n p q \delta_{qn} \text{int}_2(U_5, -U_3, m, p) \quad \begin{matrix} m, p = 1, 2, \dots, M \\ n, q = 1, 2, \dots, N \end{matrix} \end{aligned} \quad (5.23)$$

### 5.3.4 The Geometric Stiffness Matrix

The geometric stiffness matrix,  $[M]$ , is given by the terms that multiply  $\lambda$  in equation 5.18. The stress resultants have been left as part of the integrand because they are often functions of  $\bar{x}$ , or  $\bar{y}$ , or both. In light of the results presented for the in-plane analysis, some simplifications may be made depending on the set of boundary conditions being studied. However, even for the cases for

which expressions are available for the stress resultants, the complexity of the integrands precludes finding the values of these integrals in a closed form. Therefore, Gaussian quadrature has been used to evaluate the integrals. The assembly of the geometric stiffness matrix is similar to the one given by equation 5.23 for the stiffness matrix. Every time a new integral is calculated as a function of  $m$ ,  $n$ ,  $p$  and  $q$ , its value is added to element located in the  $(n + N(m - 1))^{\text{th}}$  row and  $(q + N(p - 1))^{\text{th}}$  column of the geometric stiffness matrix. The procedure followed for evaluating the integrals for each set of boundary conditions is described below.

#### 5.3.4.1 Case I boundary conditions

For this case all three stress resultants are functions of  $\bar{x}$  and  $\bar{y}$ . It is therefore necessary to calculate each of the integrals using two-dimensional Gaussian quadrature. This becomes a very large computational task, since a new integral must be calculated for every value of  $m$ ,  $n$ ,  $p$  and  $q$ . In addition, due to the large variations in the stress resultants and the oscillatory nature of the integrand, the Gaussian quadrature scheme must be carried out with many terms.

#### 5.3.4.2 Case II and Case IV boundary conditions

The shear stress resultant is zero for all  $\bar{x}$  and  $\bar{y}$  when the panel loaded under Case II or Case IV boundary conditions. This stress resultant is therefore eliminated from the analysis. In addition, the axial stress resultant is constant, so the  $N_{\bar{x}}$  may be moved outside of the integral. The integral involving  $N_{\bar{x}}$  can then be simplified using equations 5.16 and 5.17. The transverse stress resultant is only a function of  $\bar{x}$ , so Gaussian quadrature needs to be applied only in one dimension for every value of  $m$  and  $p$ .

#### 5.3.4.3 Case III boundary conditions

For this set of boundary conditions the computational task is many times smaller than for Case I boundary conditions. The axial and shear stress resultant are identically zero, so only one integral must be calculated. The transverse stress resultant is a function of  $\bar{x}$  and Gaussian quadrature must be applied for every value of  $m$  and  $p$ .

### 5.3.5 The Problem and Its Solution

Once both of the matrices have been assembled, the problem described by equation 5.10 must be solved. For this problem there are  $M \times N$  eigenvalues and as many eigenvectors. In this work, a subroutine from the International Mathematics Subroutine Library (IMSL) [21], which finds the eigenvalues through Gaussian elimination, has been used to find the  $\lambda_1, \lambda_2, \dots, \lambda_{M \times N}$ . Since the loading conditions for these panels are given in terms of applied displacements ( $u_o$  or  $v_o$ ), it is necessary to begin the analysis with an arbitrary value for  $u_o$  or  $v_o$ . The procedure for the in-plane analysis of these panels is linear, and by using the lowest eigenvalue as a proportionality constant, the critical displacement may be found by the expression

$$u_{cr} = \lambda_{\min} u_o, \quad (5.24)$$

where  $\lambda_{\min}$  is the lowest eigenvalue,  $u_o$  is the displacement applied in the pre-buckling state, and  $u_{cr}$  is the critical buckling displacement. The same is true for Case III, where a transverse displacement  $v_o$  is initially applied. The actual out-of-plane displacements are indeterminate, but by substituting the eigenvector corresponding to  $\lambda_{\min}$  for  $A_{mn}$  into equation 5.15, the buckled shape is obtained.

# CHAPTER 6

## Buckling Results and Discussion

### 6.1 Introduction

The analysis described in the previous chapter has been applied to obtain the results presented here. A convergence study is first presented to determine the number of terms necessary in the double sine series for  $w(\bar{x}, \bar{y})$ . Since the distribution of the stress resultants in the panel depends on the aspect ratio, three aspect ratios (0.5, 1.0 and 2.0) are considered. The axial stress resultant is a function of  $\bar{x}$  for Case I, so an average critical load has been obtained by taking the integral of the stress resultant along the edge of the panel and dividing by the length. The average critical load is therefore given by

$$N_{\bar{x}cr} = \frac{1}{b} \int_0^b N_x(a, \bar{y}) d\bar{y}. \quad (6.1)$$

The buckling of panels under Case II and Case IV boundary conditions is described in terms of the critical axial stress resultant,  $N_{cr}$ , that causes the panel to buckle. In addition, since the transverse stress resultant is not constant with respect to  $\bar{x}$  for Case III, an average load is also used to describe the buckling for this case. The average critical transverse load,  $N_{\bar{y}cr}$ , is given by,

$$N_{\bar{y}cr} = \frac{1}{a} \int_0^a N_y(\bar{x}, b) d\bar{x} \quad (6.2).$$

These integrals are carried out numerically using a 20 point Gaussian quadrature rule. The buckling loads have been normalized by multiplying them by a factor,  $k$ , so that the result is a non-dimensional value; this constant is defined by

$$k = \frac{a^2}{E_1 h^3}. \quad (6.3)$$

The buckling modes for each panel are determined by the values of the eigenvector,  $A_{mn}$ . For straight fiber panels, only one of the values in the eigenvector is non-zero, and the panel is said to buckle into  $m$  half-waves in the  $\bar{x}$  direction and  $n$  half-waves in the  $\bar{y}$  direction. For variable stiffness panels many of the  $A_{mn}$  are non-zero, which means that the buckling mode is actually given by a series of sine terms, instead of a single term. However, the buckling modes that have been obtained

are always dominated by a particular pair of  $m$  and  $n$  values. The other coefficients in the series are usually at least one order of magnitude smaller than the coefficient for the dominant mode. The buckling mode may therefore be accurately described by the dominant mode, although some slight variations, which will be presented, do occur.

For the results presented in the following sections, emphasis is placed on variable stiffness configurations that have buckling loads that are larger than those obtained with straight fiber angle-ply configurations. The equivalent stiffness of the panel is used as the parameter to make comparisons to straight fiber configurations. For each aspect ratio, every combination of  $T_0$  and  $T_1$  between  $0^\circ$  and  $90^\circ$  in increments of  $5^\circ$  has been modeled. The buckling loads are first discussed in a case by case basis, followed by a general discussion on the buckling mode shapes.

## 6.2 Convergence of the Ritz Method

The convergence of the Ritz method to the critical eigenvalue depends on the values of the maximum number of terms in the  $\bar{x}$  direction,  $M$ , and in the  $\bar{y}$  direction,  $N$ , used in the double sine series that represents the out of plane displacements. It is necessary to establish the maximum number of terms needed in order for the solution to converge. Case I is the case that exhibits the most difficulty converging, since all three stress resultants,  $N_x$ ,  $N_y$ , and  $N_{xy}$  are non-zero and vary with respect to  $\bar{x}$  and  $\bar{y}$ . Therefore, a panel loaded under Case I boundary conditions was used to establish the convergence criterion for the Ritz method. The angles  $T_0$  and  $T_1$  were  $0^\circ$  and  $90^\circ$ , respectively. The numerical scheme calculates the integrals using 20 point Gaussian quadrature.

The convergence of the eigenvalues for three aspect ratios is shown in Table 6.1 as a function of the terms,  $M$  and  $N$ . The critical end displacement is shown instead of the critical load in order to avoid the error introduced by the numerical integration. Initially, a series with  $M = N$  was tested, but beyond  $M = N = 7$ , the terms of the eigenvector,  $A_{mn}$ , that correspond to values of  $n$  larger than seven are of order  $10^{-8}$ . The influence of those terms in the solution of the first eigenvalue is therefore negligible, so a maximum of seven terms were taken in the  $\bar{y}$  direction. The Ritz Method converges to within five significant figures when  $M = 15$ , regardless of the aspect ratio of the panel. For square panels, even  $M = 13$  yields satisfactory results. In the analysis presented here the values of  $M$  and  $N$  are fifteen and seven, respectively.

**Table 6.1 Convergence of The Ritz Method for Case I.**

$a/b = 0.5$	$a/b = 1.0$	$a/b = 2.0$	$M$	$N$	$M \times N$
$\frac{u_{cr}}{a} \times 10^3$	$\frac{u_{cr}}{a} \times 10^3$	$\frac{u_{cr}}{a} \times 10^3$			
0.332170	0.162110	0.170330	3	3	9
0.332170	0.144682	0.159071	5	5	25
0.320018	0.137542	0.146329	7	7	49
0.314136	0.135662	0.137999	9	7	63
0.323950	0.135450	0.133778	11	7	77
0.298916	0.135380	0.132206	13	7	91
0.282266	0.135370	0.131793	15	7	105
0.282266	0.135325	0.131722	17	7	119

## 6.3 Buckling for Case I

For panels under Case I boundary conditions the analysis involves taking the in-plane response from the ELLPACK model and using it to obtain the geometric stiffness matrix for the buckling problem. The process is therefore computationally intensive. Results for two different aspect ratios are discussed below.

### 6.3.1 The Square Panel

The normalized critical load for a square panel is shown in Figure 6.1 as a function of the angles  $T_0$  and  $T_1$ . The maximum value of the buckling load occurs at  $T_0 = T_1 = 45^\circ$ , which is a straight fiber configuration. For that configuration the normalized value is 1.75. There are many variable stiffness configurations that have a buckling load close to the maximum. However, all of them involve values of  $T_0$  and  $T_1$  that are close to  $45^\circ$ .

Some small gains in the critical load may still be obtained by using a variable stiffness configuration. The normalized buckling load is shown in Figure 6.2 as a function of the equivalent axial stiffness and the angle  $T_0$ . Each curve is obtained by varying the value for  $T_1$  from  $0^\circ$  to  $90^\circ$ . The curve for the straight fiber configuration bounds all the curves for  $T_0$  greater than  $40^\circ$ . However, for values of  $T_0$  between  $0^\circ$  and  $40^\circ$ , the buckling load for some variable stiffness configurations exceeds the values obtained by using straight fibers. A configuration with  $T_0 = 0$  has a buckling load that exceeds those obtained with straight fibers for all equivalent stiffnesses values between 0.26 and 1.00. However, the gains are only marginal. At a normalized stiffness value of 0.80, the buckling load obtained with a variable stiffness configuration is 6% higher than the value obtained with straight fibers. One advantage that may be gained from the variable stiffness configuration is that for a particular value of  $kN_{\bar{x}cr}$ , the equivalent stiffness of the panel can be higher than with a straight fiber configuration. For example for a normalized load of 1.60 the equivalent stiffness with a straight fiber configuration is 0.33, while with a  $T_0 = 0^\circ$  and  $T_1 = 45^\circ$  configuration the value is 0.44.

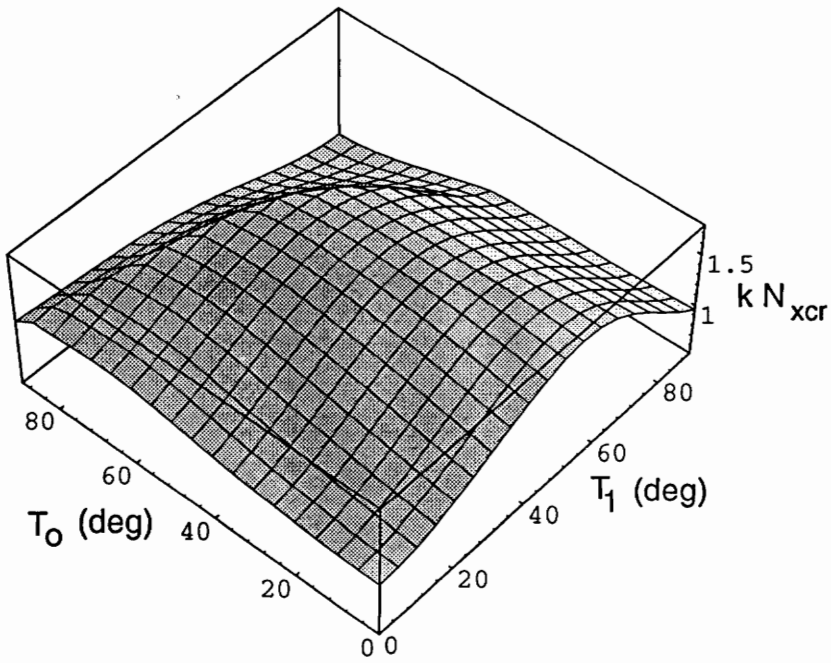


**Figure 6.1** Critical Buckling Load as a Function of  $T_0$  and  $T_1$  for Case I ( $a/b = 1$ ).

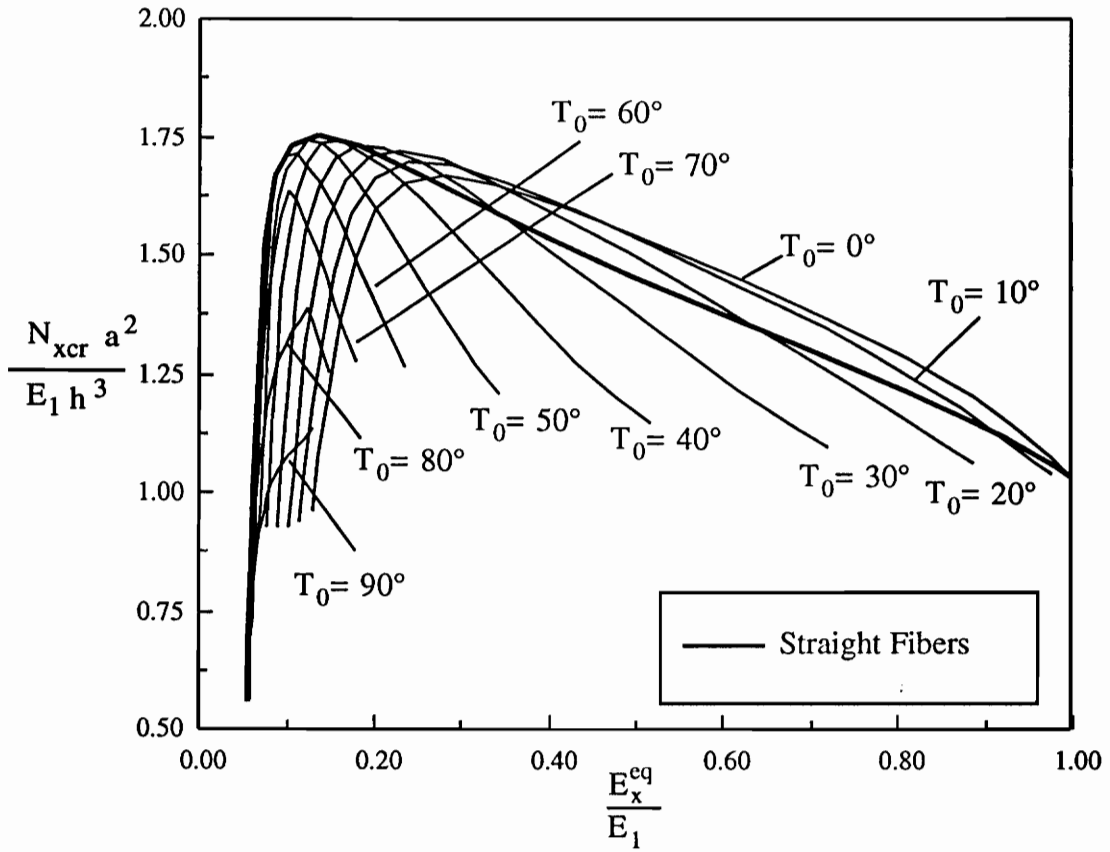


**Figure 6.2** Critical Load as a Function of Stiffness for Case I ( $a/b = 1$ ).

### 6.3.2 The Long Panel

A panel with an aspect ratio of 2.00 was modeled to test the buckling behavior of long panels. The normalized critical load is shown in Figure 6.3 as a function of the angles  $T_0$  and  $T_1$ . The maximum buckling load again occurs again at  $T_0 = T_1 = 45^\circ$ . Most variable stiffness configurations with high buckling loads have values of  $T_0$  and  $T_1$  that range between  $40^\circ$  and  $55^\circ$ , while panels with values of  $T_0$  and  $T_1$  close to zero have very low buckling loads.

The buckling load for this aspect ratio is shown as a function of equivalent stiffness in Figure 6.4. The straight fiber configuration bounds all variable stiffness configurations, regardless of the stiffness. No improvements in the buckling load are obtained, since the straight fiber configurations all have higher buckling loads than the variable stiffness panels. In fact, when  $\theta = 45^\circ$ , the load reaches its maximum at 6.98, and the load for a panel with  $T_0 = 90^\circ$  and  $T_1 = 0^\circ$ , which has the same stiffness, is 48% lower at 3.63.

For straight fiber panels, an applied end shortening only causes an axial stress resultant, while for variable stiffness panels, as shown in Chapter 3, it can give rise to high transverse and shear stresses. This is the reason why no significant increases in the buckling load were found for this set of boundary conditions. By looking at equation 5.18, it is apparent that increasing the length  $a$  reduces the magnitude of the  $N_x$  term in relation to the terms that contain  $N_y$  and  $N_{xy}$ . Uniaxially loaded straight fiber panels lack the shear and transverse loads altogether. Therefore, the marginal gains that were obtained for the square panel are not found in the panel with  $a/b = 2.0$ .

## 6.4 Buckling for Case II

Panels loaded under Case II boundary conditions are subject to biaxial compression. The transverse load is a function of  $\bar{x}$ , but the axial load is constant for all  $\bar{x}$  and  $\bar{y}$ . The buckling of these panels is therefore described in terms of the critical axial stress resultant,  $N_{cr}$ , which corresponds to the value of  $N_x$  that causes buckling. Results for three aspect ratios are presented below.

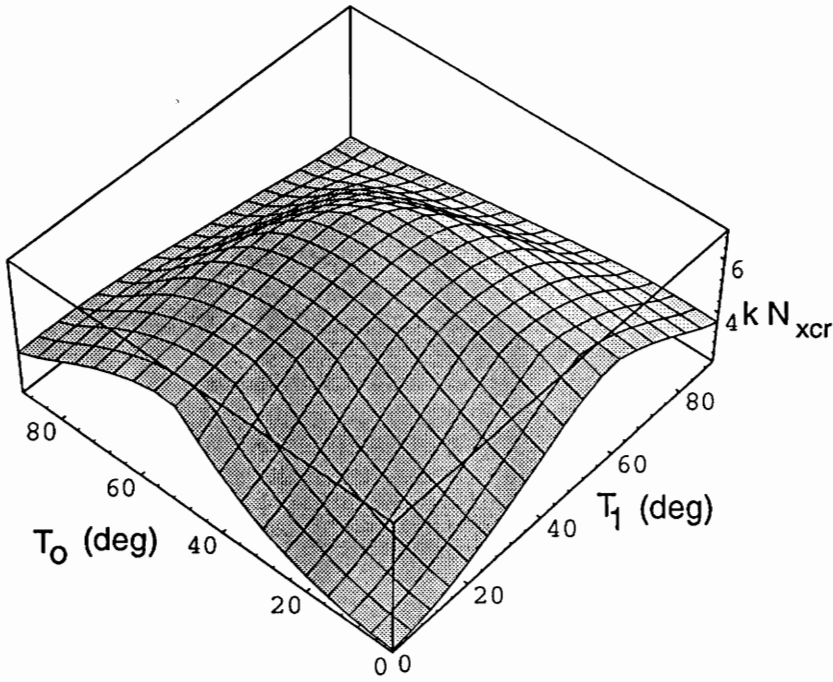


**Figure 6.3** Critical Buckling Load as a Function of  $T_0$  and  $T_1$  for Case I ( $a/b = 2$ ).

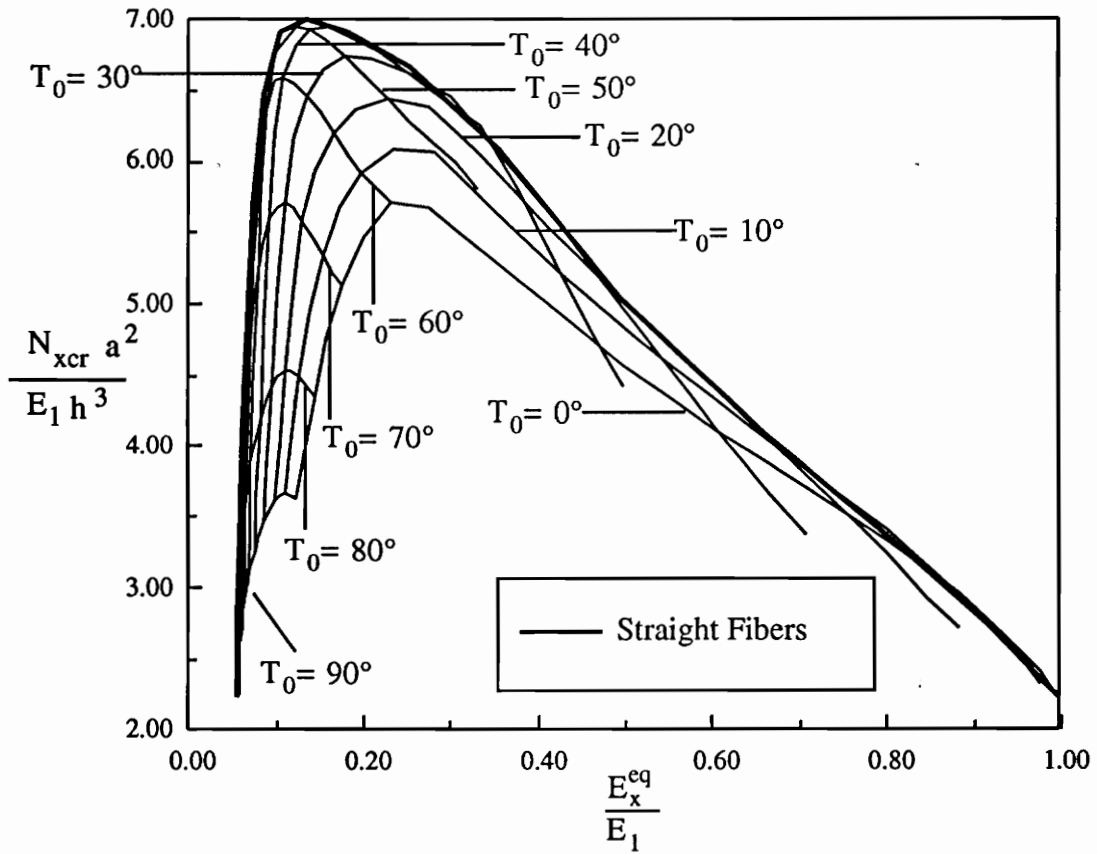


**Figure 6.4** Critical Load as a Function of Stiffness for Case I ( $a/b = 2$ ).

## 6.4.1 The Square Panel

The buckling load as a function of  $T_0$  and  $T_1$  for a square panel is shown in Figure 6.5. The maximum value of  $kN_{cr}$  (1.44) occurs for a variable stiffness configuration, at values of  $T_0 = 0^\circ$  and  $T_1 = 50^\circ$ . This value is 19% higher than the maximum value obtained with a straight fiber configuration (1.21). Most configurations with  $T_0 = 0^\circ$  have a buckling load that is higher than those that can be obtained using straight fibers. The shape of the surface suggests that having a low angle in the middle ( $\bar{x} = a/2$ ) of the panel, and a somewhat higher angle at the ends, are necessary in order to achieve a high buckling load.

This phenomenon is directly related to the transverse load distribution. Recall from Chapter 4 that the transverse load is proportional to  $\nu_{yx}$ . When the angle in the middle of the panel is low and the angle at the panel ends is high, the transverse load is lowest in the middle of the panel and highest at the ends. Such a configuration minimizes the influence of the transverse load by making the integral,

$$\frac{\pi^2}{2b} qn\delta_{qn} \int_0^a N_{\bar{y}} \sin\left(\frac{p\pi\bar{x}}{a}\right) \sin\left(\frac{m\pi\bar{x}}{a}\right) d\bar{x}, \quad (6.4)$$

lower for variable stiffness panels than for straight fiber panels. The integral is lower because the transverse load is high close to the edges  $x = 0$  and  $x = a$ , where the value of the sine terms is close to zero, whereas for straight fiber panels the value of  $N_{\bar{y}}$  is constant.

A better understanding of this effect is gained by Figure 6.6, which shows the buckling load as a function of angle  $T_0$  and equivalent stiffness. Note that the panels with  $T_0 = 0^\circ$  have a higher buckling load than straight fiber panels for all normalized stiffness values that lie between 0.15 and 1.00. As  $T_0$  increases, the maximum buckling load that can be obtained decreases. Most configurations that have buckling loads higher than the straight fiber configurations have values of  $T_0$  between  $0^\circ$  and  $60^\circ$ . This supports the hypothesis that the distribution of the transverse load is what causes the increase in the buckling load. By referring to equation 4.2 and to Figure 2.5 it appears that in order for the transverse load to be higher at the panel ends than at the middle, the angle  $T_0$  must be less than  $65^\circ$  and the angle  $T_1$  must be greater than  $T_0$ . For example, panel with  $T_0 = 30^\circ$  should exhibit gains in the buckling load for those values of  $T_1$  that are greater than  $30^\circ$ .

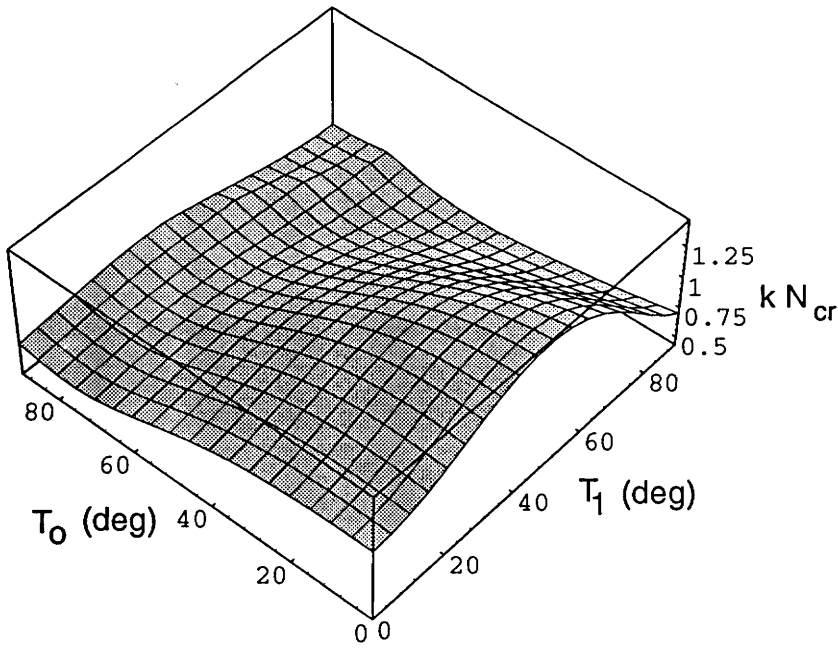


**Figure 6.5** Critical Buckling Load as a Function of  $T_0$  and  $T_1$  for Case II ( $a/b = 1$ ).

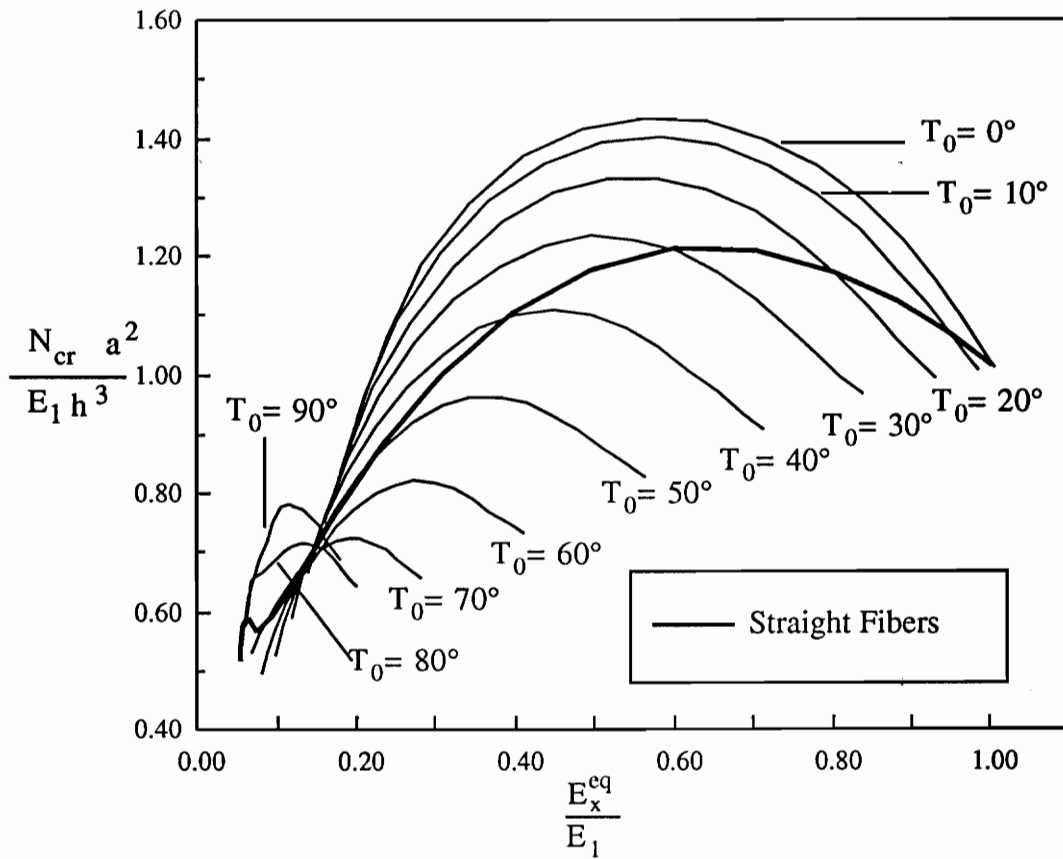


Figure 6.6 Critical Load as a Function of Stiffness for Case II ( $a/b = 1$ ).

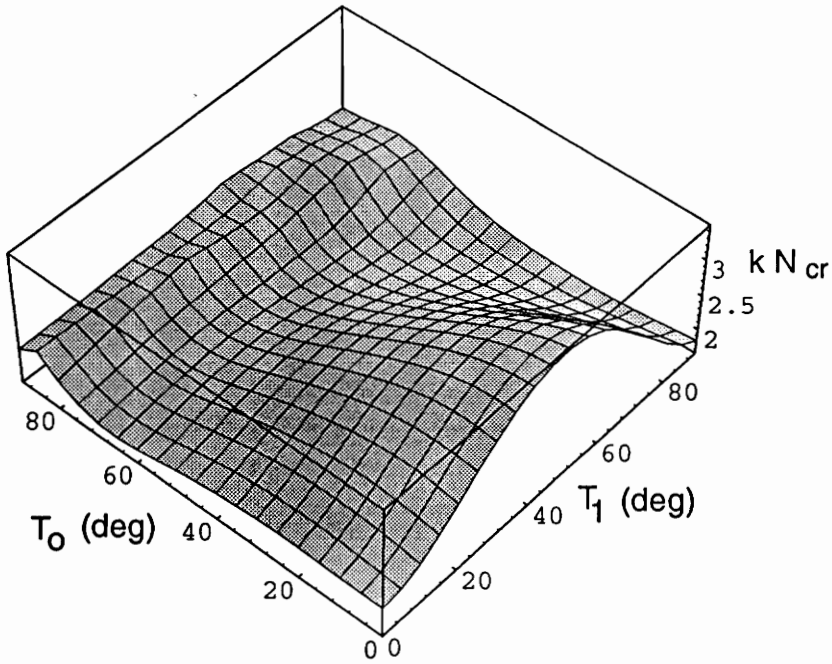
and less than  $65^\circ$ . In Figure 6.6 the curve for this configuration intersects with the straight fiber curve when  $T_1 = 30^\circ$ . The segment of the curve for which the buckling load is higher than the for straight fiber configurations, indeed corresponds to values of  $T_1$  between  $30^\circ$  and  $65^\circ$ .

Figure 2.5 also suggests that an alternative way of obtaining the  $N_y$  distribution that leads to improvements in the buckling load is to have values of  $T_o$  between  $65^\circ$  and  $90^\circ$  combined with  $T_1$  values that are smaller than  $T_1$  but greater than  $65^\circ$ . The curves for  $T_o = 80^\circ$  and  $T_o = 90^\circ$  reflect some of those configurations.

## 6.4.2 The Long Panel

The normalized buckling load for a panel with an aspect ratio of 2.0 is shown in Figure 6.7 as a function of the angles  $T_o$  and  $T_1$ . As was shown for the square panel, the maximum buckling load is obtained when  $T_o = 0^\circ$  and  $T_1 = 50^\circ$ . The normalized value of the buckling load for that configuration (3.45) is 25% higher than the maximum obtained with a straight fiber configuration (2.77). The effect of the load distribution is the same as was seen for the square panel, so a low transverse load is required at  $\bar{x} = a/2$  in order to achieve a high buckling load. Recall that when the aspect ratio is increased, the relative magnitude of the  $N_y$  term in the eigenvalue problem also increases, and the effect of the transverse load should be more pronounced for this case than for square panels.

The normalized buckling load for the long panel is shown in Figure 6.8 as a function of the equivalent panel stiffness. For some straight fiber configurations there can be up to three different straight fiber configurations that have the same buckling load. However, the buckling mode for these configurations will not be identical. The sudden drop in the load at  $E_x^{eq}/E_1 = 0.066$  marks the stiffness at which the buckling mode changes to two, three and four half-waves in the  $\bar{x}$  direction as the stiffness decreases; the buckling mode always has only one half-wave in the transverse direction. While for values of  $E_x^{eq}/E_1$  larger than 0.15, the buckling loads follow the patterns found for the square panels, at very low stiffnesses there is one peculiarity that needs to be addressed. The curves for  $T_o = 80^\circ$  and  $T_o = 90^\circ$  have higher buckling loads than the straight fiber configuration even for values of  $E_x^{eq}/E_1$  that correspond to  $T_1$  values smaller than  $65^\circ$ . This would seem to contradict the



**Figure 6.7** Critical Buckling Load as a Function of  $T_0$  and  $T_1$  for Case II ( $a/b = 2$ ).

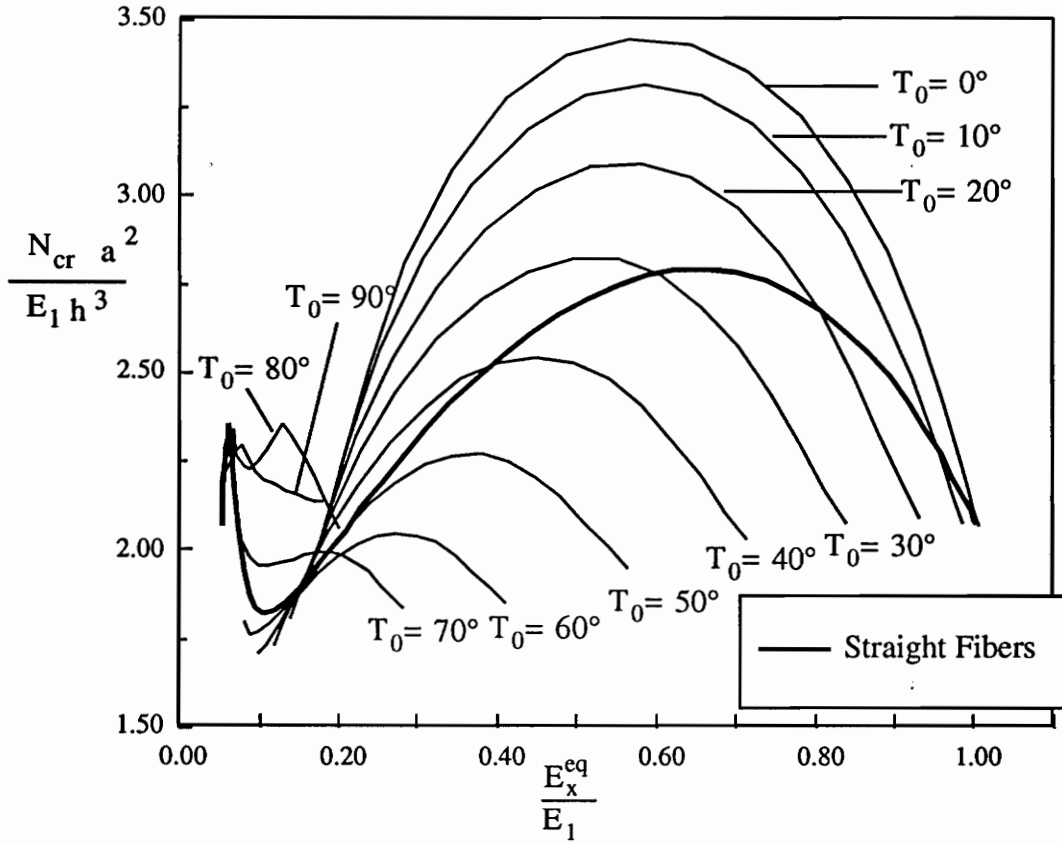


Figure 6.8 Critical Load as a Function of Stiffness for Case II ( $a/b = 2$ ).

conclusions about the transverse load distribution that were made earlier. However, the buckling modes for the panels with  $T_o = 80^\circ$  and  $T_o = 90^\circ$  for  $E_x^{eq}/E_1$  values that are between 0.09 and 0.13 are two half-waves in the  $\bar{x}$  direction and one half-wave in the  $\bar{y}$  direction. For the same range in the stiffness, the straight fiber panels buckle into only one half-wave in each direction. The buckling mode for the panel with  $T_1 = 80^\circ$  changes from two to one half-wave in the  $\bar{x}$  direction when  $E_x^{eq}/E_1$  is greater than 0.13; this change in the mode coincides with a peak in the load. The variable stiffness configuration, by buckling into a higher mode, yields a larger eigenvalue. Finally, the reason for the difference in the modes can be attributed to the fact that panel with  $T_o = 80^\circ$  or  $T_o = 90^\circ$  are very compliant in the center, so that the buckling modes for low stiffness straight fiber panels occur for these variable stiffness configurations also.

### 6.4.3 The Short Panel

The normalized buckling load for a panel with an aspect ratio of 0.5 is shown in Figure 6.9 as a function of the angles  $T_o$  and  $T_1$ . The maximum value for  $kN_{cr}$ , 0.90, occurs when  $T_o = 0^\circ$  and  $T_1 = 35^\circ$ . However, the value for this configuration is only 4.6% higher than what can be obtained with a straight fiber configuration with  $\theta = 0^\circ$ . By using a variable stiffness configuration, the increase in the buckling load is very slight because the aspect ratio is small and the  $N_x$  term dominates the eigenvalue problem. As seen in for the previous aspect ratios, the buckling load tends decrease as  $T_1$  increases. The lowest load occurs when the panel has a straight fiber configuration with  $\theta = 90^\circ$ .

The normalized load for this panel is shown in Figure 6.10 as a function the normalized equivalent stiffness. There are no mode changes with respect to the stiffness for either the straight fiber configuration or the variable stiffness configurations. All of the configurations that were modeled buckle into one half-wave in each direction as their dominant mode. For every value of  $E_x^{eq}/E_1$ , the configuration with  $T_o = 0^\circ$  has a buckling load which is higher than the values obtained with straight fibers. Although the buckling load obtained with the straight fiber configuration is not significantly higher than 0.86 (obtained when  $\theta = 0^\circ$ ), the stiffness values for which an equal or greater buckling can be obtained with a variable stiffness configuration range from 0.57 to 1.00.

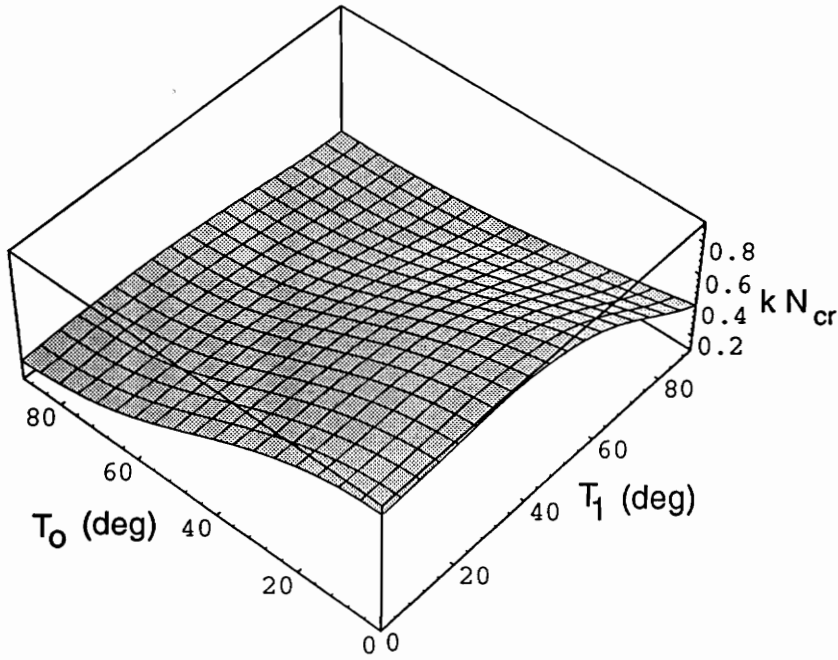


**Figure 6.9** Critical Buckling Load as a Function of  $T_0$  and  $T_1$  for Case II ( $a/b = 0.5$ ).

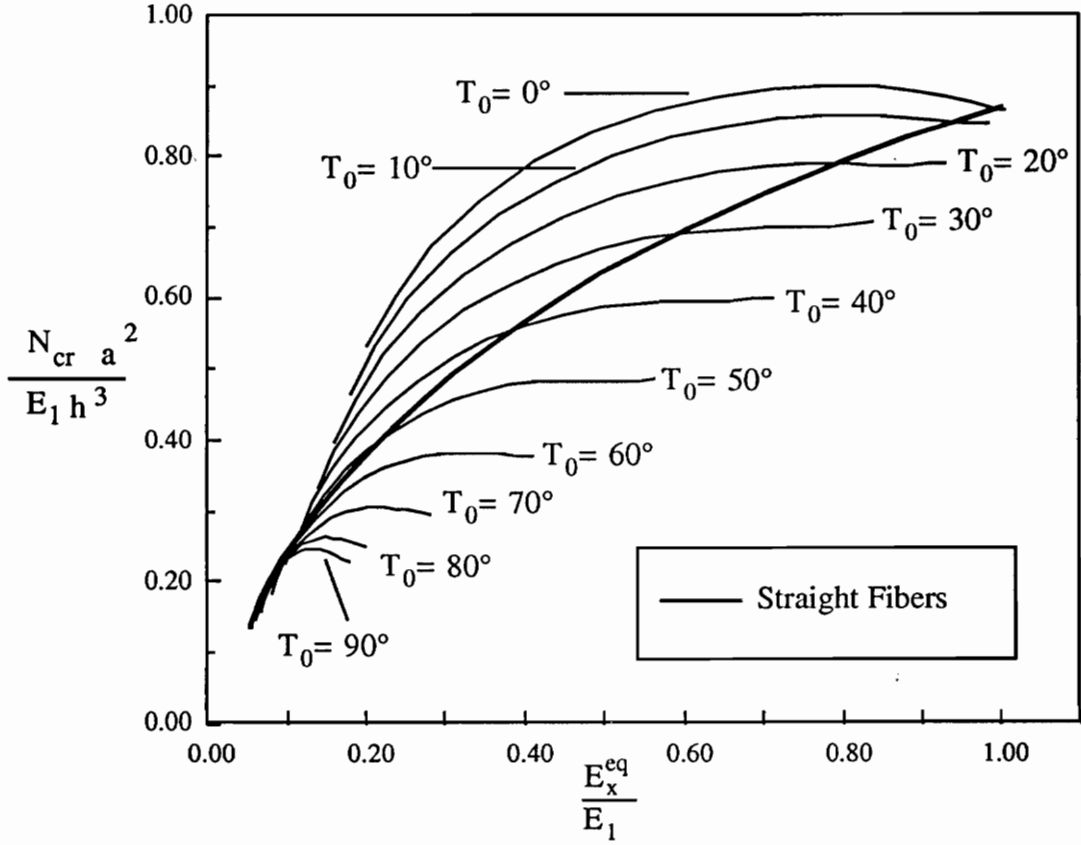


Figure 6.10 Critical Load as a Function of Stiffness for Case II ( $a/b = 0.5$ ).

## 6.5 Buckling for Case III

Case III is unique in that the loading of the panel is in the transverse direction only. For the sake of simplicity, the aspect ratio convention has not been changed. A panel with an aspect ratio of 0.5 is longer in the  $\bar{y}$  direction than in the  $\bar{x}$  direction. The stiffness used to compare the buckling behavior of panels for this case is the transverse equivalent stiffness,  $E_y^{eq}$ . Three aspect ratios have been modeled.

### 6.5.1 The Square Panel

The buckling load a square panel is shown in Figure 6.11 as a function of the angles  $T_0$  and  $T_1$ . The maximum value of  $kN_{\bar{y}cr}$ , 3.14, occurs when  $T_0 = 0^\circ$  and  $T_1 = 75^\circ$ . This value is 80% higher than 1.75, which is the maximum that can be obtained with a straight fiber configuration. In addition, the largest buckling loads are for similar configurations where the angle  $T_0$  is low and the angle  $T_1$  is large. This phenomenon can be explained by the distribution of the transverse load when the transverse displacement is applied.

Recall that the transverse load for this case is proportional to the effective transverse stiffness,  $E_y$ . As was shown in Figure 2.3, the transverse stiffness increases as the fiber angle increases. Since only the transverse load is acting on the panel, the buckling load is determined by the value of the integral in equation 6.4. If, instead of being a constant, the distribution of  $N_y$  is such that it is high along the edges of the panel and low at  $\bar{x} = a/2$ , the integral can lead to a low eigenvalue. Therefore, all variable stiffness configurations where the angle  $T_0$  is less than  $T_1$  should have a higher buckling load than straight fiber panels with the same equivalent stiffness. This is indeed true, and the results are shown in Figure 6.12, where the normalized buckling load is shown as a function of the normalized equivalent transverse stiffness,  $E_y^{eq}/E_1$ . The curve for panels with straight fibers divides the figure into two distinct spaces. Those variable stiffness configurations found under the straight fiber curve have values of  $T_0$  greater than  $T_1$ . All those variable stiffness configurations that have buckling loads higher than the straight fiber configurations have  $T_0$  less than  $T_1$ . Therefore, the curve for  $T_0 = 90^\circ$  does not have any variable stiffness configurations that offer a higher buckling load than  $T_0 = T_1 = 90^\circ$ . One drawback is that the normalized stiffness at which the maximum

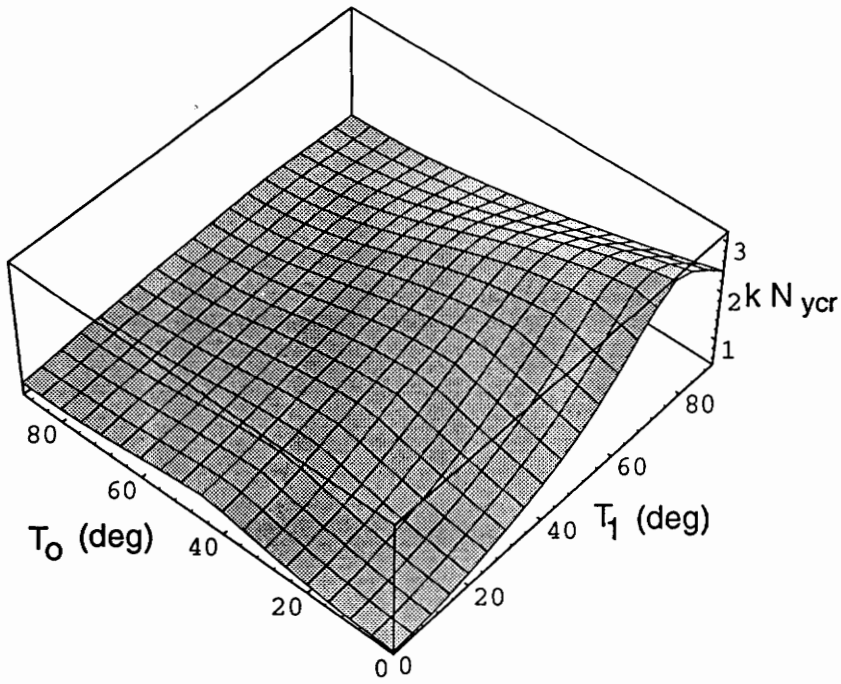


**Figure 6.11** Critical Buckling Load as a Function of  $T_0$  and  $T_1$  for Case III ( $a/b = 1$ ).

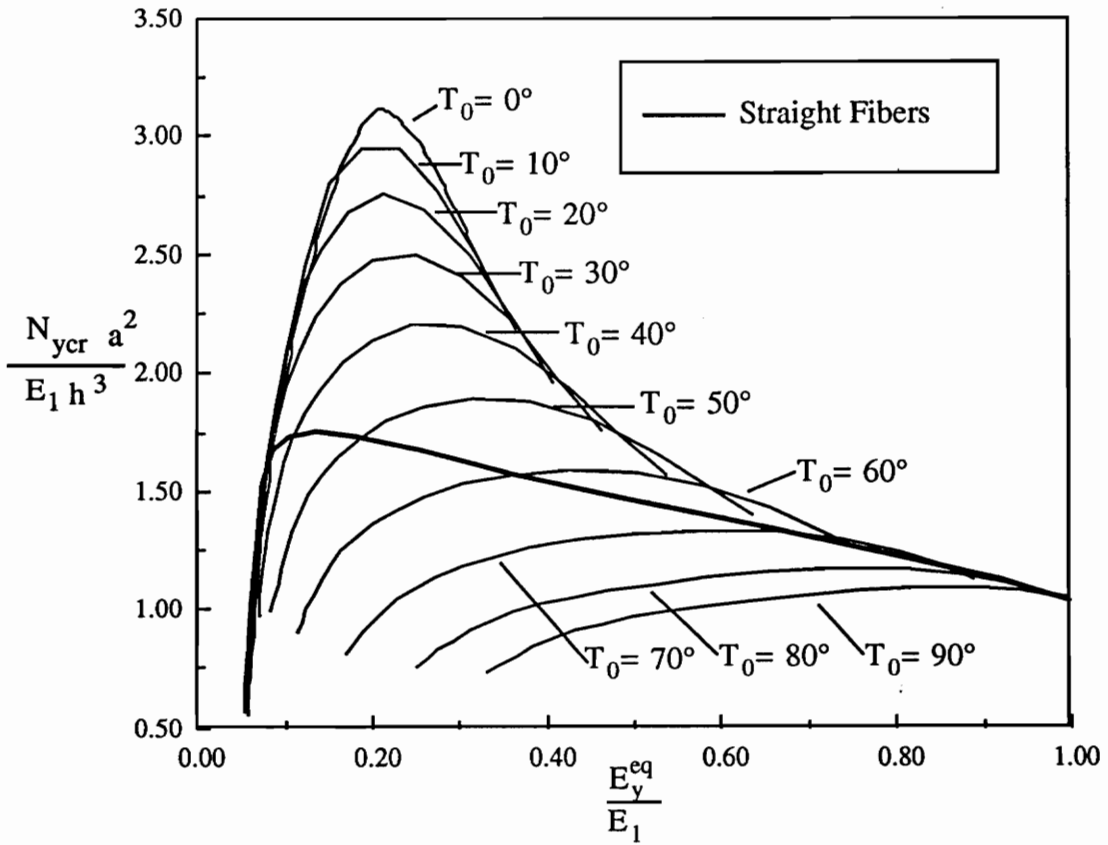


Figure 6.12 Critical Load as a Function of Stiffness for Case III ( $a/b = 1$ ).

buckling load occurs is only 0.21. If high stiffness is a priority, a straight fiber configuration can be used. All the curves for the variable stiffness configurations intersect the straight fiber curve when  $T_0 = T_1$ . In addition, as  $T_0$  increases, the maximum buckling load for each configuration decreases.

## 6.5.2 The Long Panel

The panel being analyzed here is long in the  $\bar{x}$  direction. Its shorter dimension is the width  $b$ . This should be kept in mind for the results presented below. The buckling load for a long panel ( $a/b = 2.0$ ) is shown in Figure 6.13 as a function of the angles  $T_0$  and  $T_1$ . The highest buckling load is found for a straight fiber configuration, where  $T_0 = T_1 = 90^\circ$ , which also has the highest transverse stiffness. The lowest buckling load occurs when  $T_0 = T_1 = 0^\circ$ . In addition, along the line for  $T_1 = 90^\circ$  there are many configurations with a high buckling load.

The buckling load as a function of stiffness is shown in Figure 6.14. Although the maximum load occurs for a straight fiber panel, loads within 10% of this value may be obtained for a normalized stiffness range between 0.18 and 1.00 by using a variable stiffness configuration. For a straight fiber configuration the range is between 0.48 and 1.00. Each  $T_0$  curve has a configuration that yields a maximum buckling load. The peaks in these curves do not reflect changes in the buckling mode, since the only buckling mode consists of one half-wave in each direction. No particular characteristics were found to explain these maxima, but they reflect angle combinations for which the stiffness matrix and the geometric stiffness matrix are such that a high eigenvalue results.

The fact that the highest load occurs for a straight fiber configuration for this aspect ratio might seem contradictory to the conclusions drawn for the same aspect ratio for Case II. However, the loading for Case II is in the axial direction, and the transverse load is induced (due to the Poisson's effect). The gains for that case reflect increases in the buckling load in the  $x$  direction. In this case the transverse load is *applied* so that a different view of the problem is necessary. For this aspect ratio the distribution of the transverse load has some significant effect on the buckling behavior, but Figure 6.14 suggests that the important parameter is the stiffness. By looking at equation 5.18, one can see that when the aspect ratio,  $a/b$ , is high, the term that contains  $D_{22}$  is larger in relation to the other terms in the equation. If the value of  $D_{22}$  is high, so will the value of

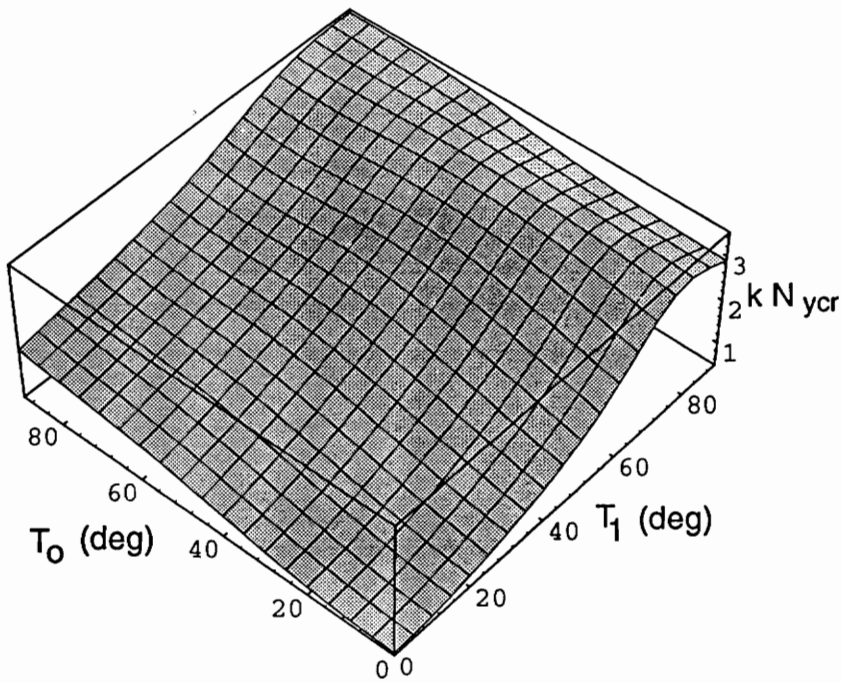


**Figure 6.13** Critical Buckling Load as a Function of  $T_0$  and  $T_1$  for Case III ( $a/b = 2$ ).

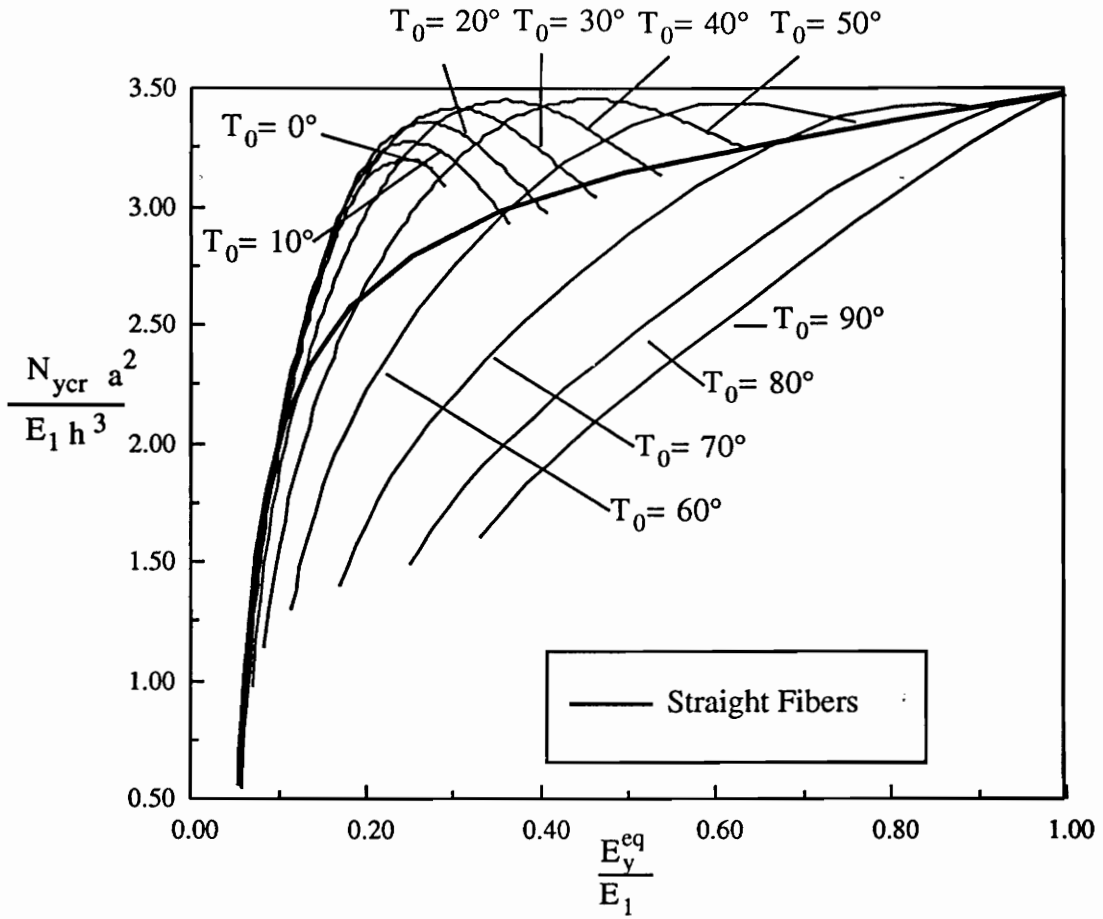


Figure 6.14 Critical Load as a Function of Stiffness for Case III ( $a/b = 2$ ).

the eigenvalue. Hence, the highest buckling load for this aspect ratio corresponds to a panel with all  $90^\circ$  plies.

### 6.5.3 The Short Panel

The buckling loads for a short transversely loaded panel is shown in Figure 6.15. The maximum buckling load occurs for a configuration with  $T_0 = 0^\circ$  and  $T_1 = 75^\circ$ , for which the value of  $kN_{y_{cr}}$  is 2.90; the maximum that can be obtained with straight fibers is 1.75. By using the variable stiffness configuration, the increase in the buckling load is 66%. The lowest buckling load corresponds to a straight fiber configuration with  $\theta = 0^\circ$ .

The buckling load is shown as a function of the normalized equivalent stiffness in Figure 6.16. For any value of  $E_y^{eq}/E_1$ , the critical load for variable stiffness panels that have  $T_1$  greater than  $T_0$  always exceeds the value that can be obtained with a straight fiber configuration. Hence, the buckling load is driven by the distribution of the transverse load, in the same fashion that it occurs for square panels. Since the value of  $E_y$  changes very little between  $0^\circ$  and  $10^\circ$  (see Figure 2.3), the curves for the configurations with  $T_0 = 0^\circ$  and  $T_0 = 10^\circ$  are almost identical. The flexibility of the variable stiffness configuration is also demonstrated by the fact that the buckling load of 1.75 can be obtained for a stiffness range of 0.09 to 0.50 by using a variable stiffness configuration. With straight fibers this value can only be obtained with a panel with a stiffness of 0.14.

## 6.6 Buckling for Case IV

The boundary conditions for Case IV are such that the axial stress resultant is constant with respect to  $\bar{x}$  and  $\bar{y}$ . Therefore, when considering buckling, comparisons may be made to straight fiber configurations by using the critical buckling load,  $N_{cr}$ , which is the  $\bar{x}$  direction stress resultant needed to obtain bifurcation.

### 6.6.1 The Square Panel

The normalized buckling load is shown in Figure 6.17 as a function of the angles  $T_0$  and  $T_1$  for a square panel configuration. The use of a variable stiffness configuration for this set of boundary conditions does indeed result in slight increases in the buckling load. The maximum value of the

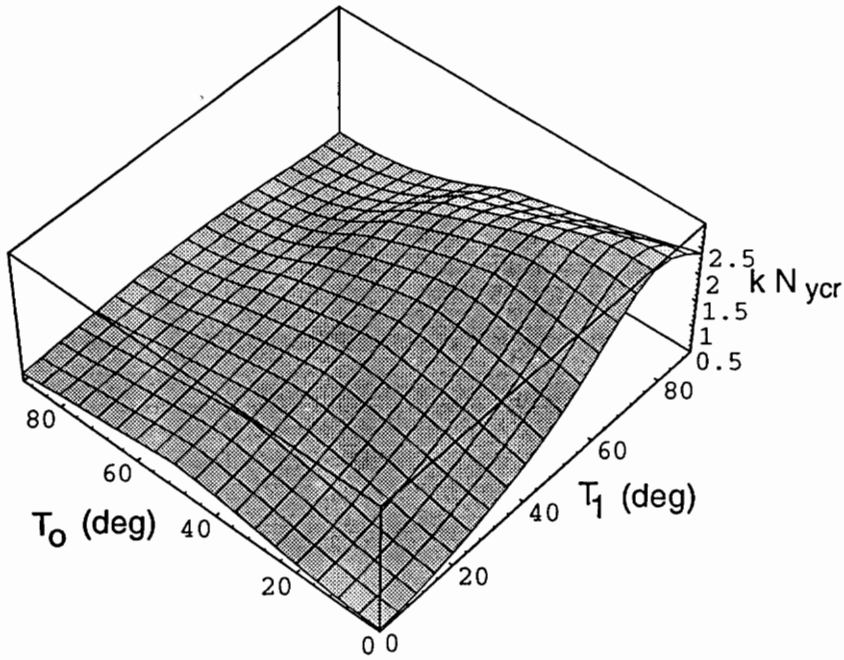


**Figure 6.15** Critical Buckling Load as a Function of  $T_0$  and  $T_1$  for Case III ( $a/b = 0.5$ ).

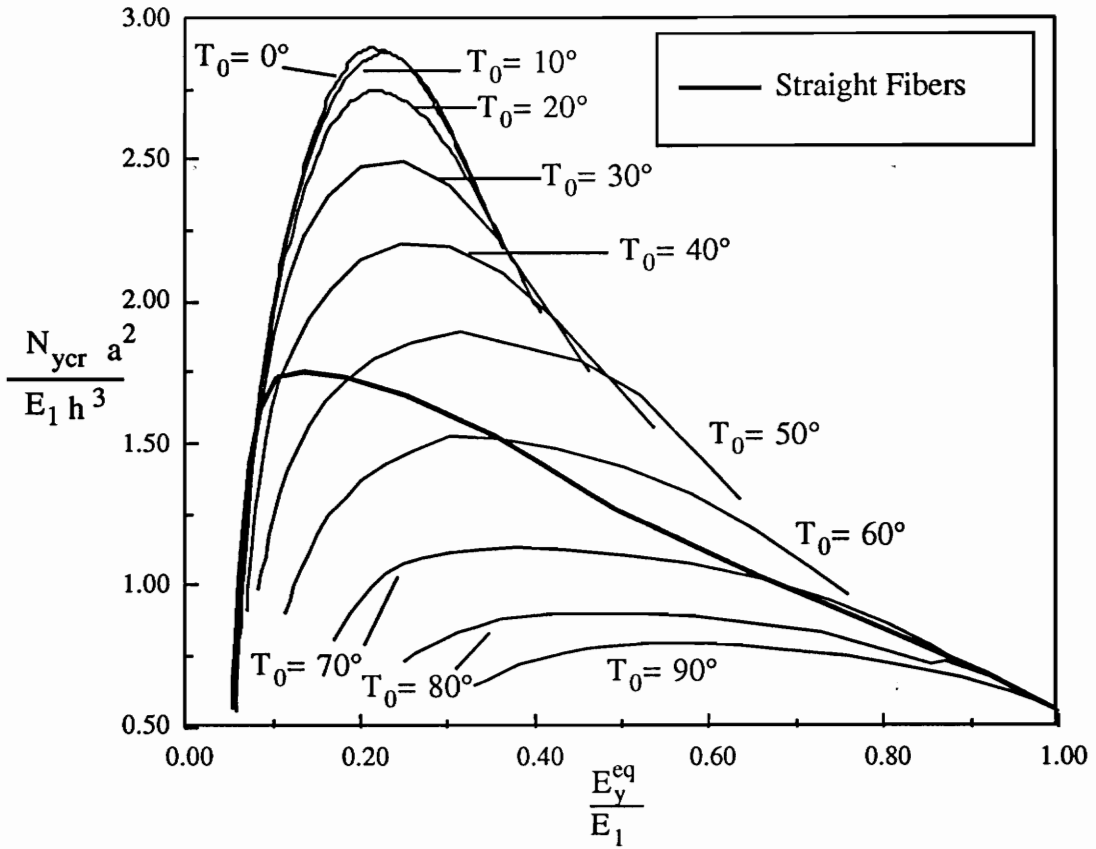


Figure 6.16 Critical Load as a Function of Stiffness for Case III ( $a/b = 0.5$ ).

normalized buckling load, 1.85, corresponds to a panel with  $T_0 = 60^\circ$  and  $T_1 = 45^\circ$ . However, this value is only 6% higher than the maximum load obtained using a straight fiber configuration, 1.74. The two ridges in the graph mark the configurations where the load is high. This occurs for most configurations where  $T_0$  is close to  $70^\circ$  and also in those configurations where  $T_1$  is close to  $70^\circ$ .

Many variable stiffness configurations exhibit a buckling load close to the maximum obtained using a straight fiber configuration, so this can be an advantage for the designer. The buckling load as a function of stiffness is shown in Figure 6.18 for straight fiber panels and variable stiffness panels. For panels with straight fibers, the range of values of  $E_x^{eq}/E_1$  for which the normalized buckling load is greater than 1.7 is only from 0.1 to 0.2. In addition, the normalized stiffness at which the maximum value of the buckling load occurs is low, only 0.14. By using the variable stiffness configuration, no large increases in the buckling load are obtained, but the configurations that have a buckling load greater than or equal to 1.7 have a stiffness that ranges from 0.1 to 0.44.

The loading conditions for this case are similar to the loading conditions for Case I. However, the buckling load for the variable stiffness configuration is lower for Case I panels than it is for Case IV panels. The reasoning behind this is that the Case IV panels lack shear, although the transverse load is non-zero for all values of  $\bar{x}$  and  $\bar{y}$ . By eliminating the shear stress resultant and having the center of some panels loaded under transverse tension, some gains are seen for Case IV.

## 6.6.2 The Long Panel

The buckling load distribution for a panel with  $a/b = 2.0$  is shown as a function of the angles  $T_0$  and  $T_1$  in Figure 6.19. Due to the domed shape of the surface, the maximum buckling load occurs for a panel with  $T_0 = T_1 = 45^\circ$ . There are some variable stiffness configurations that have values of  $kN_{cr}$  that are close to this maximum, but none surpass it. Since the loading in this problem is in the  $\bar{x}$  direction, the value of  $D_{22}$  cannot be as high as it was for the long panel under Case II boundary conditions. Instead, the resulting straight fiber configuration reflects a balance between the bending stiffness  $D_{22}$  and the term for the axial load,  $N_x$ .

The normalized critical load is shown in Figure 6.20 as a function of the equivalent stiffness. Note that there are a few designs in which the buckling load is higher than the buckling load that

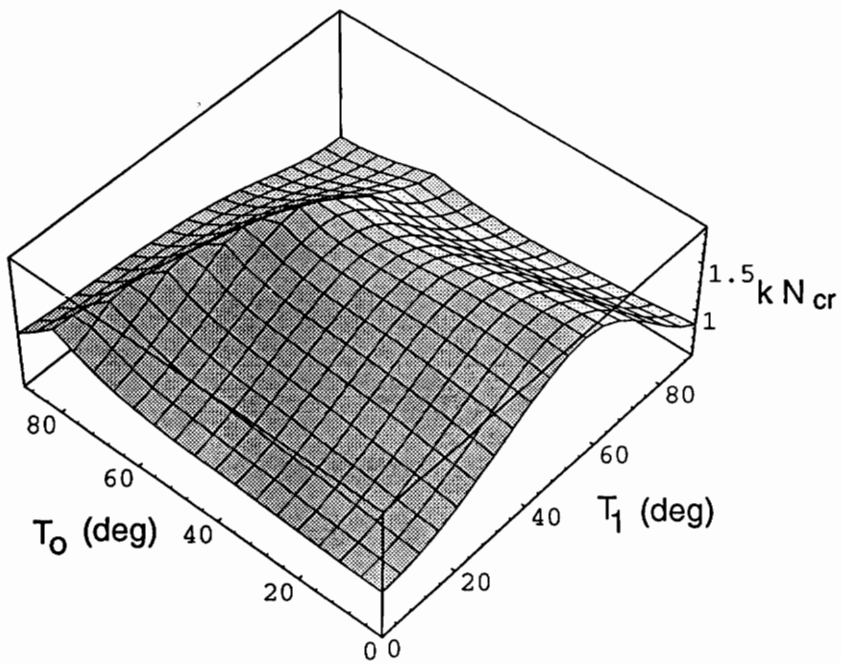


**Figure 6.17** Critical Buckling Load as a Function of  $T_0$  and  $T_1$  for Case IV ( $a/b = 1$ ).

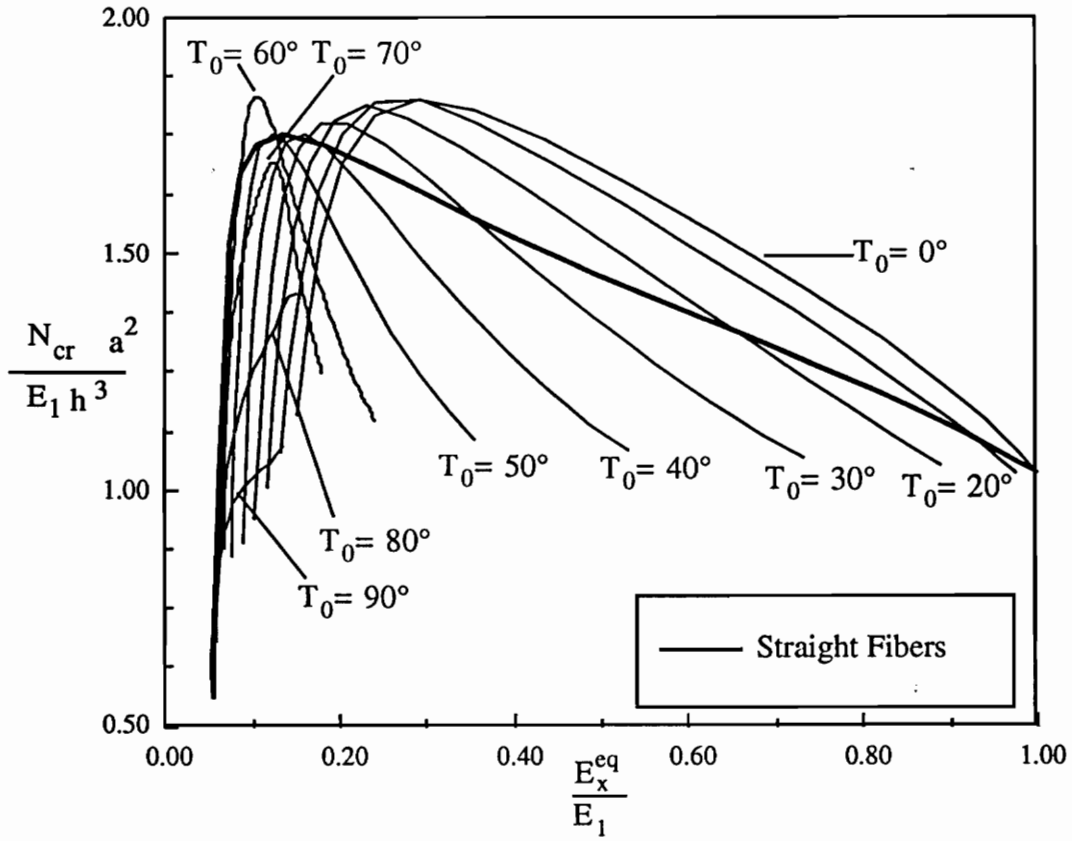


**Figure 6.18** Critical Load as a Function of Stiffness for Case IV ( $a/b = 1$ ).

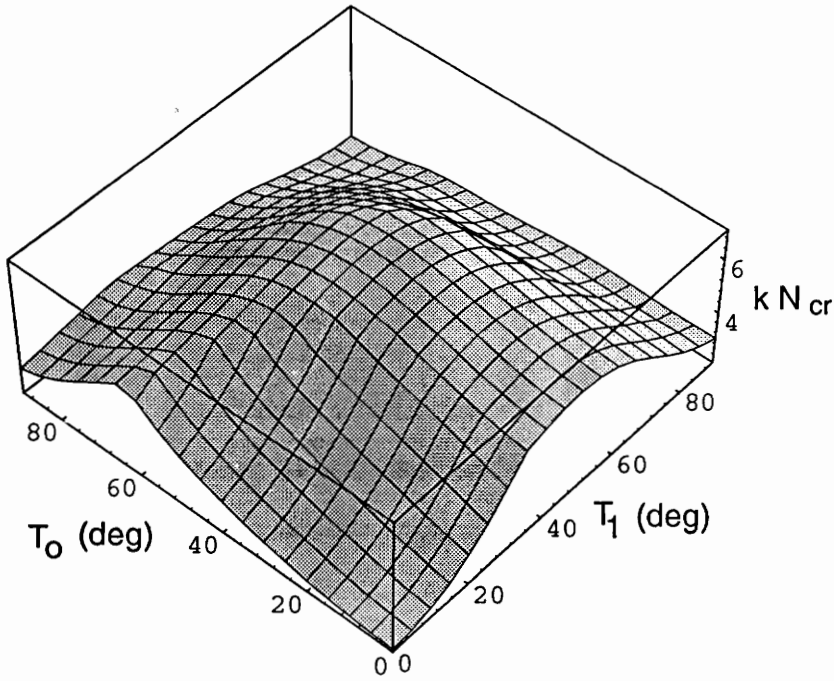


**Figure 6.19** Critical Buckling Load as a Function of  $T_0$  and  $T_1$  for Case IV ( $a/b = 2$ ).

can be obtained with a straight fiber panel. For a panel with  $E_x^{eq}/E_1$  value of 0.62 an increase in the buckling load over the straight fiber configuration of 30% is obtained by using a configuration with  $T_0 = 0^\circ$  and  $T_1 = 35^\circ$ . This panel has two important characteristics. Due to its configuration, the transverse load is tensile in the center of the panel and compressive close to the edges. This load distribution is the likely cause for a buckling mode that has two half-waves in the  $\bar{x}$  direction and one half-wave in the  $\bar{y}$  direction, whereas a straight fiber panel of equal stiffness buckles into one half-wave in each direction. Due to the tensile load in the middle of the panel and the higher mode shape, the variable stiffness configuration has a higher buckling load.

### 6.6.3 The Short Panel

For the short panel ( $a/b = 0.5$ ), there are only small gains in the buckling load when the variable stiffness configuration is used. This is shown in Figure 6.21, where the normalized buckling load is shown as a function of the angles  $T_0$  and  $T_1$ . The configuration with the highest load has  $T_0 = 0^\circ$  and  $T_1 = 40^\circ$ , and a normalized buckling load of 0.93. This value is only 7% higher than the buckling load obtained by using a straight fiber configuration. The buckling load for variable stiffness and straight fiber panels with an aspect ratio of 0.5 is shown in Figure 6.22 as a function of the panel stiffness. When  $T_0 = 0^\circ$  the buckling load remains nearly constant for values of  $T_1$  between  $0^\circ$  and  $50^\circ$ . These variable stiffness configurations have the same load, but a stiffness that ranges from 0.26 to 1.00. For any value of the normalized stiffness, there is always a variable stiffness configuration that has a buckling load higher than that obtained with straight fibers. The panel configurations with  $T_0 = 0^\circ, 10^\circ, 20^\circ, 30^\circ$ , and  $40^\circ$  all have tensile transverse loads in the middle of the panel when  $T_1$  is greater than  $T_0$ . These configurations all have a higher buckling load with respect to the stiffness when compared to straight fiber panels.

## 6.7 Buckling Modes

So far the buckled mode shapes of the variable stiffness panels have been described in terms of sine half-waves. This section seeks to justify this description while at the same time highlighting whatever differences are found between straight fiber panels and variable stiffness panels. In order

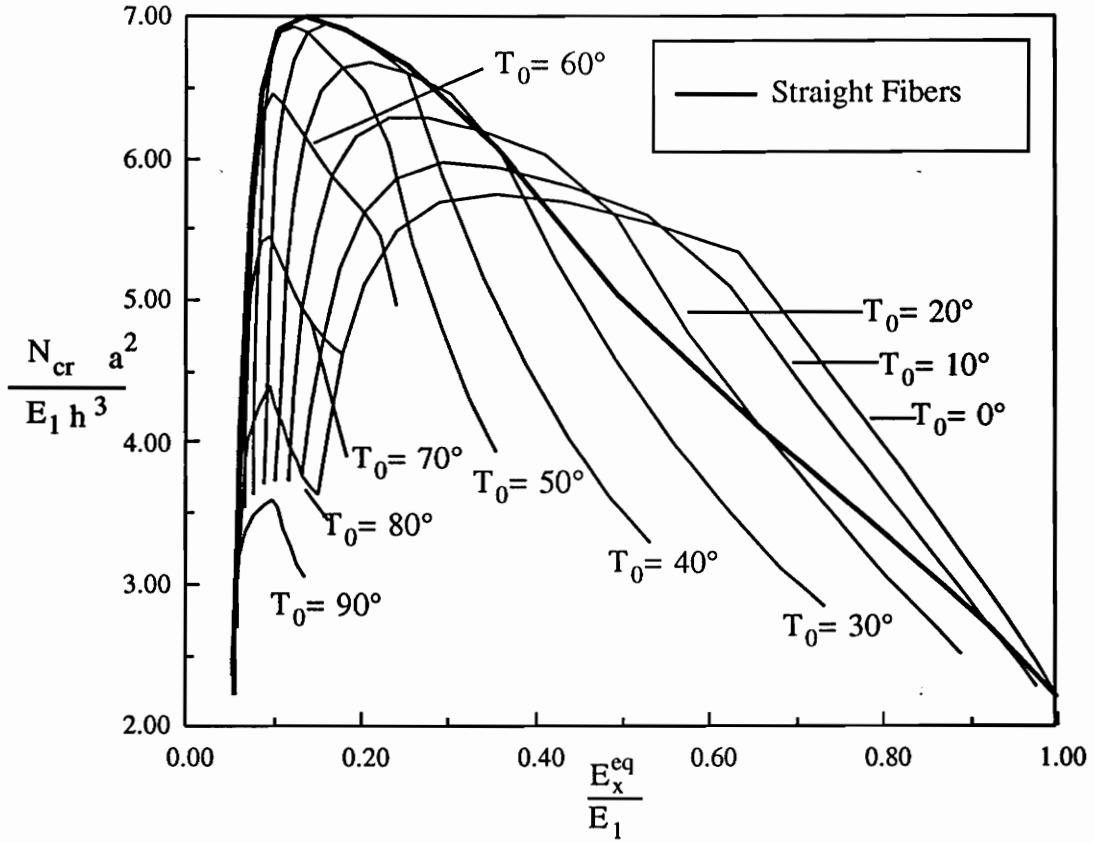
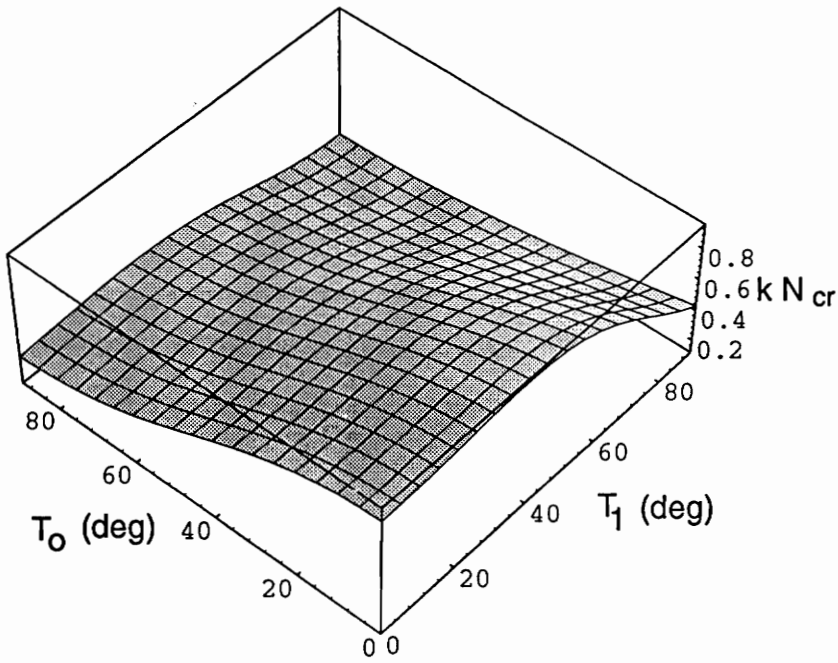


Figure 6.20 Critical Load as a Function of Stiffness for Case IV ( $a/b = 2$ ).



**Figure 6.21** Critical Buckling Load as a Function of  $T_0$  and  $T_1$  for Case IV ( $a/b = 0.5$ ).

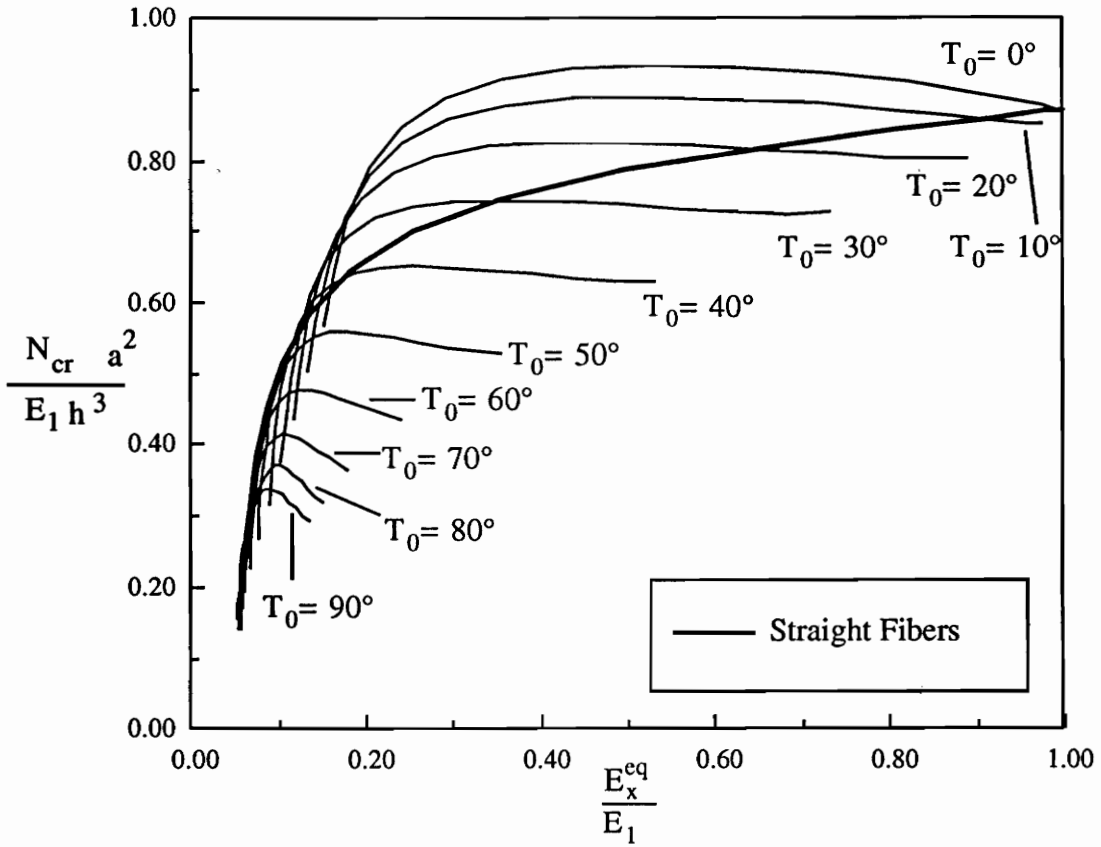
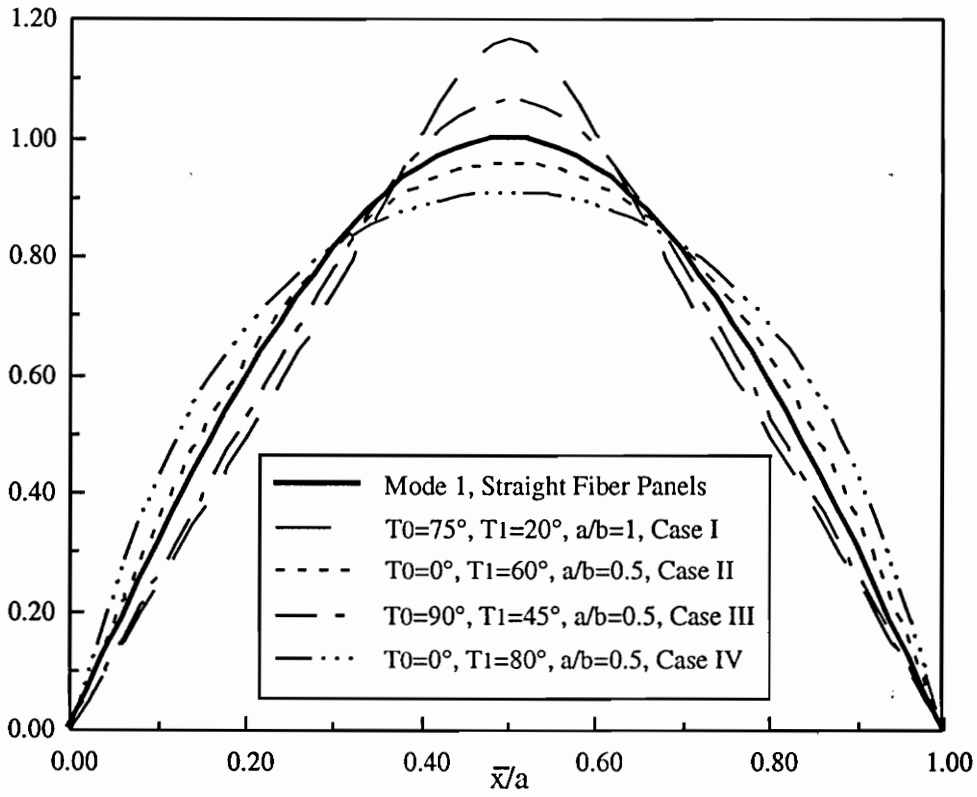


Figure 6.22 Critical Load as a Function of Stiffness for Case IV ( $a/b = 0.5$ ).

to highlight these differences an effort has been made to present modes that are extremes in terms of their deviation from true sine waves.

Several modes for panels whose dominant mode is one half-wave in the  $\bar{x}$  direction are shown in Figure 6.23. Also shown is the mode obtained when the buckling mode is a true half-wave. While the dominant mode is one half-wave, some differences that can be attributed to the changes in stiffness do occur. The panels shown for Cases I and III are more compliant in the middle than at the ends. The outward deflection will tend to be high in the compliant areas, so these curves are more sharp at  $\bar{x}/a = 0.5$  than the regular sine half-wave. Although the loading for Case III is in the transverse direction, buckling mode along the  $\bar{x}$  direction is shown, since this is the direction in which the bending stiffnesses change. For Case III the buckling mode in the transverse direction is perfect sine half-waves. Also shown in the figure are curves for Cases II and IV. For these cases the angle  $T_0$  in the middle of the panel is low, so the bending stiffness is high, while at the panel ends the bending stiffness is low. This change in stiffness is reflected in the modes. The curves are more blunt at  $\bar{x}/a = 0.5$  than a regular sine half-wave, but also have a higher slope at  $\bar{x}/a = 0$  and  $\bar{x}/a = 1.0$ .

Three modes that are dominated by two half-waves in the  $\bar{x}$  direction are shown in Figure 6.24. All three configurations are more compliant in the center of the panel, so the slope of the curves at  $\bar{x}/a = 0.5$  is higher than for a panel with two perfect half-waves. Since the panels are less compliant at the ends, the value of  $\frac{\partial w}{\partial \bar{x}}$  tends to be smaller at  $\bar{x} = 0$  and  $\bar{x} = a$  for the variable stiffness configuration than for the baseline case. A similar trend is seen in Figure 6.25, where a four half-wave buckled mode is shown. All of the configurations are more compliant in the middle of the panel than at the ends. Hence, the buckled mode shape for a configuration such as  $T_0 = 75^\circ$ ,  $T_1 = 50^\circ$  for Case I has a larger magnitude in the two inner half-waves than in the two outer ones. For this configuration the slope of the curve is almost zero at the panel ends. The reason why this buckled shape is so different from the regular four half-wave buckling mode can probably be attributed partly to the fact that the integral involving the shear stress resultant,  $N_{\bar{x}\bar{y}}$ , excites smaller modes that are not seen for the other boundary conditions. However, all the other configurations follow the same trend. Finally, note that the modes for the panel  $T_0 = 90^\circ$  and  $T_1 = 60^\circ$  is the same



**Figure 6.23 One Half-Wave Buckling Mode for Variable Stiffness Panels.**

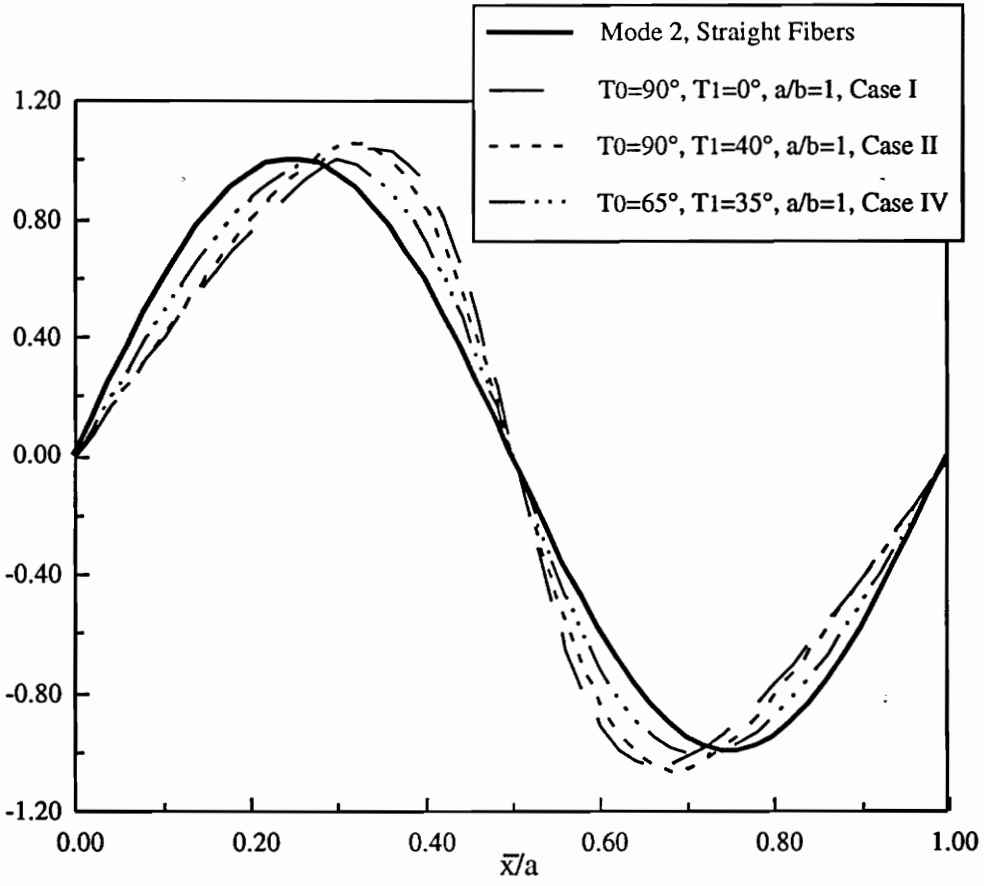
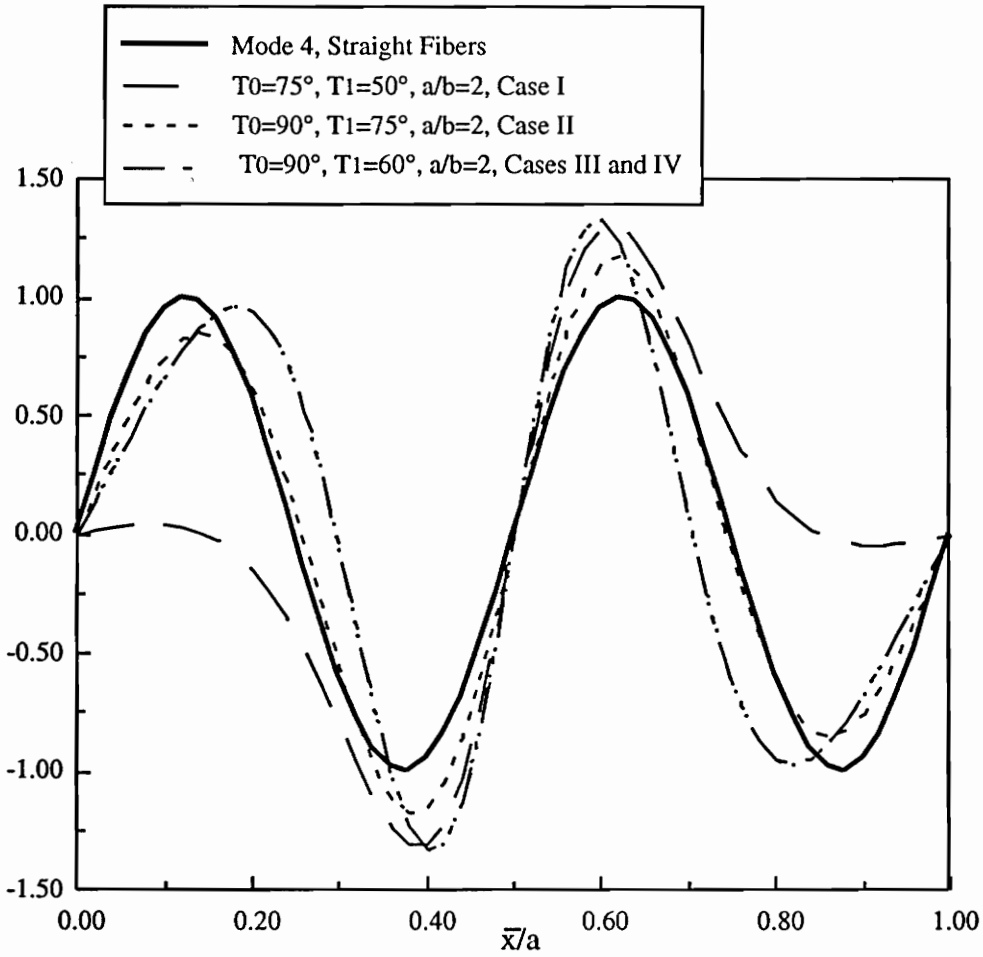


Figure 6.24 Two Half-Waves Buckling Mode for Variable Stiffness Panels.



**Figure 6.25 Four Half-Waves Buckling Mode for Variable Stiffness Panels.**

regardless of whether it is under Case III or Case IV boundary conditions. This suggests that in the absence of shear, for a given dominant mode, the buckled mode shape depends only on the stiffness distribution.

## 6.8 Failure

The improvements in the buckling load of the variable stiffness panels would be meaningless if the panel failed before it buckled. Although the failure mode of panels with curvilinear fibers has not been established experimentally, the analysis presented in section 3.7 can indicate whether the panel is likely to fail before it buckles or whether buckling occurs first. The low  $h/L$  ratio, where  $L$  is the smaller of the two panel dimensions,  $a$  and  $b$  was meant to produce a configuration where buckling would occur first, although this is not guaranteed.

The buckling and failure loads of various variable stiffness configurations are compared in Table 6.2 for all four cases and various aspect ratios. For cases I and III, the failure shown is an average load found in the same way as the average buckling load. Although somewhat awkward, the failure load has been normalized by using the factor  $k$  in order to provide a comparison to the critical load. The failure load has been calculated using the Maximum Strain Criterion on the in-plane pre-buckling problem; the cause and location of failure are also shown. For the configurations shown, the normalized failure load is anywhere from 3.5 times ( $T_0 = 0^\circ$ ,  $T_1 = 75^\circ$ , Case III,  $a/b = 0.50$ ) to 82.0 times ( $T_0 = 0^\circ$ ,  $T_1 = 15^\circ$ , Case I,  $a/b = 1.00$ ) greater than the normalized buckling load. It follows that the panel does not fail in the pre-buckling state. None of the panels that were modeled in this study failed by the Maximum Strain Criterion before buckling was induced. Therefore, in order to find the true failure load of the panels, a non-linear post-buckling analysis is necessary.

**Table 6.2 Buckling vs. Failure Load for Various Variable Stiffness Configurations.**

	$T_0$	$T_1$	$a/b$	$E_x/E_1$	Buckling Load <sup>†</sup>	Failure Load	Failure Mode	Location $x/a$ $y/b$	
Case I	0°	15°	1.00	0.94	1.31	107.34	2-dir tension	0.48	0.48
	30°	40°	2.00	0.25	6.63	101.40	Shear	0.50	0.00
Case II	0°	50°	1.00	0.57	1.44	63.46	Shear	0.50	—
	0°	50°	2.00	0.57	3.45	253.85	Shear	0.50	—
	0°	35°	0.50	0.78	0.90	35.06	Shear	0.50	—
Case III	0°	75°	1.00	0.21	3.14	20.48	2-dir tension	0.46	—
	30°	75°	2.00	0.30	3.43	59.98	2-dir tension	0.43	—
	0°	75°	0.50	0.21	2.90	10.24	2-dir tension	0.46	—
Case IV	60°	45°	1.00	0.10	1.85	16.15	Shear	0.00	—
	0°	35°	2.00	0.63	5.33	201.39	2-dir tension	0.00	—
	0°	40°	0.50	0.53	0.93	10.10	Shear	0.50	—

<sup>†</sup>For case I,  $kN_{xcr}$ ; for cases II and IV,  $kN_{cr}$ ; for case III,  $kN_{ygr}$ .

# CHAPTER 7

## Concluding Remarks

### 7.1 Conclusions

#### 7.1.1 In-Plane Response

The elastic behavior of variable stiffness panels has been shown to be governed by an elliptic boundary value problem. Due to the change in the stiffness along the  $x$  coordinate, the resulting displacement fields and stress resultants are seldom homogeneous. The solution of the in-plane problem for a panel with free transverse edges requires a numerical solution. The results of the numerical model show that, under uniaxial loading in the  $x$  direction, the changes in the elastic properties generate stress gradients that give rise to transverse stresses although the transverse edges are not loaded, and to shear even when no material shear-extension coupling is present. The distribution of the loads is found to depend not only on the stiffness distribution, but also on the aspect ratio of the panel.

The linear relationship between  $\theta$  and  $x/a$  proved useful in the development of closed form solutions for the in-plane response. The closed form solutions are found to be exact for the three sets of boundary conditions which have a forced boundary condition in  $v$  along the transverse edges. Through symbolic manipulation, closed form solutions for the displacements and stress resultants are easily obtainable. Under those conditions, there is no shear deformation under uniaxial loading, and the distribution of the transverse load depends directly on the distribution of the effective material properties,  $\nu_{yx}$  and  $E_y$ .

#### 7.1.2 Buckling

The Ritz method has been adapted to the variable stiffness configuration. The results that have been obtained indicate that when the transverse edges of the panel are free, no significant gains in the buckling load can be obtained. However, two of the other three boundary conditions exhibit significant gains in the buckling load when a variable stiffness configuration is used. A long panel with fixed transverse edges can have a buckling load as much as 25% higher than the maximum value

that can be obtained with a straight fiber  $[\pm\theta]_{ns}$  configuration. A square transversely loaded variable stiffness panel can have a buckling load which is 80% higher than the maximum load obtained using a straight fiber configuration. For panels with free but straight transverse edges, the gains in the buckling load are marginal, at most 6%. It has been shown that the buckling modes, while similar to those seen for straight fiber panels, do reflect the changes in stiffness along the length.

The variable stiffness concept also offers additional flexibility in the design process. As has been shown, the stiffness at which a certain buckling load can be obtained can be extended from one or two values (for straight fiber panels) to a wide range of values. Although the driving force behind the actual use of the variable stiffness concept in the design of aerospace structures is likely to be absolute structural gains, such as the 80% increase in the buckling load mentioned above, the added flexibility in the design process should not be overlooked. Coupled with optimization techniques, this concept has the potential to yield very efficient structures.

## 7.2 Suggestions for Future Work

There are several interesting problems that need to be addressed in order to gain a broader understanding of the variable stiffness concept. Significant gains in the buckling response have already been established. An important topic is to carry out the buckling analysis including the effects of anisotropy. In addition, a post-buckling analysis of these panels would confirm whether it is really an improvement over straight fiber panels in terms of stability and post-buckling load carrying capability.

Leissa and Martin have already shown increases in the natural frequency of composite sheets by using the variable stiffness concept. Similar results can probably be obtained using a curvilinear fiber format for laminates. The vibration analysis would simply be an extension of the buckling analysis that has already been developed. In addition, the bending response should also be analyzed. The stresses and deflections under pressure loads, for example, may be reduced by using the variable stiffness concept.

Other areas of suggested research involve more difficult topics. The large gradients in the in-plane stresses found for the variable stiffness configuration undoubtedly give rise to gradients in

the stresses,  $\sigma_z$ ,  $\tau_{xz}$  and  $\tau_{yz}$ , which so far have been assumed to be negligible. A more sophisticated analysis that confirms or contradicts this assumption is necessary. Furthermore, study of the damage tolerance of these panels might yield interesting results. Intuitively, it seems that the curvilinear fiber pattern of the fibers may be useful in retarding crack growth.

The fiber patterns and angle variations that can be used with this concept are so vast that in order to further investigate gains over straight fiber configurations, optimization studies must be carried out. After such an analysis, the comparisons between straight fiber and curvilinear fiber designs would be more fair, since the optima of both configurations would be compared. Upon confirming the advantages of this concept, the manufacture and testing of these panels could be undertaken.

# Appendix 1

## The Stiffness Matrix

As described in Chapter 5, the stiffness matrix in the buckling eigenvalue problem contains integrals that are products of the bending stiffnesses,  $D_{ij}$  and trigonometric terms. These integrals may be obtained by in a closed form by applying certain trigonometric identities to the integrand and then carrying out the integration. That procedure is presented here.

In Chapter 5 it was established that the terms of the stiffness matrix are given by

$$\begin{aligned}
 K[n + N(m - 1), q + N(p - 1)] = & \frac{\pi^4 b}{2a^4} m^2 p^2 \delta_{qn} \int_0^a D_{11} \sin\left(\frac{p\pi\bar{x}}{a}\right) \sin\left(\frac{m\pi\bar{x}}{a}\right) d\bar{x} \\
 & + \frac{\pi^4}{2a^2 b} (m^2 q^2 + n^2 p^2) \delta_{qn} \int_0^a D_{12} \sin\left(\frac{p\pi\bar{x}}{a}\right) \sin\left(\frac{m\pi\bar{x}}{a}\right) d\bar{x} \\
 & + \frac{\pi^4}{2b^3} n^2 q^2 \delta_{qn} \int_0^a D_{22} \sin\left(\frac{p\pi\bar{x}}{a}\right) \sin\left(\frac{m\pi\bar{x}}{a}\right) d\bar{x} \\
 & + \frac{2\pi^4}{a^2 b} mnpq \delta_{qn} \int_0^a D_{66} \cos\left(\frac{p\pi\bar{x}}{a}\right) \cos\left(\frac{m\pi\bar{x}}{a}\right) d\bar{x} \quad \begin{array}{l} m, p = 1, 2, \dots, M \\ n, q = 1, 2, \dots, N \end{array} \quad (A1.1)
 \end{aligned}$$

Note that there are to types of integrands. Three integrands, those that contain  $D_{11}$ ,  $D_{12}$ , and  $D_{22}$ , are products of a bending stiffness times two sine terms. One is the product of the  $D_{66}$  bending stiffness times two cosine terms. It is not necessary to carry out all four integrations. Instead a general form for the first three integrals will be found. The integral involving  $D_{66}$  must be found individually.

The integrals involving  $D_{11}$ ,  $D_{12}$ , and  $D_{22}$  may be written as,

$$\frac{h^3}{12} \int_0^a [K_1 + K_2 \cos(2\theta) + K_3 \cos(4\theta)] \sin\left(\frac{p\pi\bar{x}}{a}\right) \sin\left(\frac{m\pi\bar{x}}{a}\right) d\bar{x}, \quad (A1.2)$$

where the constants  $K_1$ ,  $K_2$  and  $K_3$  are the appropriate invariants given in Chapter 2 for each bending stiffness. Hence, if the above integral is obtained, then the first three integrals in equation A1.1 are easily found by substituting the appropriate values for  $K_1$ ,  $K_2$  and  $K_3$ . The term containing  $K_1$  is given by

$$\frac{h^3}{12} \int_0^a K_1 \sin\left(\frac{p\pi\bar{x}}{a}\right) \sin\left(\frac{m\pi\bar{x}}{a}\right) d\bar{x}, \quad (A1.3)$$

which by orthogonality of the sine terms simplifies to

$$\frac{ah^3}{24} \delta_{mp} K_1 \quad (\text{A1.4})$$

The second and third terms of the integrals in equation A1.2 contain  $\cos(2\theta)$  and  $\cos(4\theta)$ , respectively, in which  $\theta = \theta(\bar{x})$ . By using the identity,

$$\sin(\varphi) \sin(\psi) = \frac{1}{2} [\cos(\varphi - \psi) - \cos(\varphi + \psi)] \quad (\text{A1.5})$$

the second term in equation A1.2 becomes,

$$\frac{h^3 K_2}{24} \int_0^a \cos(2\theta) \left\{ \cos\left(\frac{(p-m)\pi\bar{x}}{a}\right) - \cos\left(\frac{(p+m)\pi\bar{x}}{a}\right) \right\} d\bar{x}. \quad (\text{A1.6})$$

It is now necessary to substitute for  $\theta$ , which in the  $\bar{x}$ - $\bar{y}$  coordinate system is given by equation 5.2. Since the expression for  $\theta$  is piecewise defined, depending on whether  $x$  is smaller or greater than  $a/2$ , it is necessary to split the integral into two different integrals, given by

$$\begin{aligned} & \frac{h^3 K_2}{24} \left[ \int_0^{a/2} \cos\left(\frac{4(T_o - T_1)\bar{x}}{a} + 2T_1\right) \left\{ \cos\left(\frac{(p-m)\pi\bar{x}}{a}\right) - \cos\left(\frac{(p+m)\pi\bar{x}}{a}\right) \right\} d\bar{x} \right. \\ & \left. + \int_{a/2}^a \cos\left(\frac{4(T_1 - T_o)\bar{x}}{a} + 4T_o - 2T_1\right) \left\{ \cos\left(\frac{(p-m)\pi\bar{x}}{a}\right) - \cos\left(\frac{(p+m)\pi\bar{x}}{a}\right) \right\} d\bar{x} \right]. \quad (\text{A1.7}) \end{aligned}$$

Each one of these integrals may be further simplified by the identity,

$$\cos(\varphi) \cos(\psi) = \frac{1}{2} [\cos(\varphi - \psi) + \cos(\varphi + \psi)] \quad (\text{A1.8})$$

After substituting, expression A1.7 is given by eight terms,

$$\begin{aligned} & \frac{h^3 K_2}{48} \left\{ \int_0^{a/2} \cos\left[(4T_o - 4T_1 - \pi p + \pi m)\frac{\bar{x}}{a} + 2T_1\right] + \cos\left[(4T_o - 4T_1 + \pi p - \pi m)\frac{\bar{x}}{a} + 2T_1\right] d\bar{x} \right. \\ & - \int_0^{a/2} \cos\left[(4T_o - 4T_1 - \pi p - \pi m)\frac{\bar{x}}{a} + 2T_1\right] + \cos\left[(4T_o - 4T_1 + \pi p + \pi m)\frac{\bar{x}}{a} + 2T_1\right] d\bar{x} \\ & + \int_{a/2}^a \cos\left[(4T_1 - 4T_o - \pi p + \pi m)\frac{\bar{x}}{a} + 4T_o - 2T_1\right] d\bar{x} \\ & \left. + \int_{a/2}^a \cos\left[(4T_1 - 4T_o + \pi p - \pi m)\frac{\bar{x}}{a} + 4T_o - 2T_1\right] d\bar{x} \right\} \end{aligned}$$

$$\begin{aligned}
& - \int_{a/2}^a \cos \left[ (4T_1 - 4T_o - \pi p - \pi m) \frac{\bar{x}}{a} + 4T_o - 2T_1 \right] d\bar{x} \\
& - \int_{a/2}^a \cos \left[ (4T_1 - 4T_o + \pi p + \pi m) \frac{\bar{x}}{a} + 4T_o - 2T_1 \right] d\bar{x} \Big\}. \tag{A1.9}
\end{aligned}$$

These terms are easily integrated, since they consist of only one cosine term. However, problems arise when the factor that multiplies the  $\bar{x}$  in each of the terms is identically zero. By using IF statements in the computer code, the value of each factor is checked, so that the integration is only carried out when the integrand is truly a function of  $\bar{x}$ . Once each term is integrated and evaluated, and like factors are grouped together, the following four terms result,

$$\begin{aligned}
& \frac{h^3 K_2}{48} \left\{ \frac{a}{4T_o - 4T_1 + p\pi - m\pi} \left[ \sin \left( 2T_o + \frac{\pi}{2}(p - m) \right) + \sin \left( 2T_o + \frac{\pi}{2}(m - p) \right) \right. \right. \\
& \quad \left. \left. - \sin(2T_1 + \pi(m - p)) - \sin(2T_1) \right] \right. \\
& + \frac{a}{4T_o - 4T_1 - p\pi + m\pi} \left[ \sin \left( 2T_o + \frac{\pi}{2}(p - m) \right) + \sin \left( 2T_o + \frac{\pi}{2}(m - p) \right) \right. \\
& \quad \left. - \sin(2T_1 + \pi(p - m)) - \sin(2T_1) \right] \\
& + \frac{a}{4T_o - 4T_1 + p\pi + m\pi} \left[ -\sin \left( 2T_o + \frac{\pi}{2}(p + m) \right) - \sin \left( 2T_o - \frac{\pi}{2}(m + p) \right) \right. \\
& \quad \left. + \sin(2T_1 - \pi(p + m)) + \sin(2T_1) \right] \\
& + \frac{a}{4T_o - 4T_1 - p\pi - m\pi} \left[ -\sin \left( 2T_o + \frac{\pi}{2}(p + m) \right) - \sin \left( 2T_o + \frac{\pi}{2}(m + p) \right) \right. \\
& \quad \left. + \sin(2T_1 + \pi(p + m)) + \sin(2T_1) \right] \Big\} = \frac{h^3 K_2}{48} (\varrho_1^1 + \varrho_2^1 + \varrho_3^1 + \varrho_4^1), \tag{A1.10}
\end{aligned}$$

where the terms on the left side of the equation are represented by the  $\varrho_i^1$  on the right side. The superscript simply indicates that the terms are for the first type of integral. Finally, the following conditional statements apply in case the denominator in any of the four terms is zero,

$$\text{if } 4T_o - 4T_1 + p\pi - m\pi = 0 \quad \text{then} \quad \varrho_1^1 = \frac{a}{2} \{ \cos(2T_1) + \cos(4T_o - 2T_1) \}, \tag{A1.11}$$

$$\text{if } 4T_o - 4T_1 - p\pi + m\pi = 0 \quad \text{then} \quad \varrho_2^1 = \frac{a}{2} \{ \cos(2T_1) + \cos(4T_o - 2T_1) \}, \tag{A1.12}$$

$$\text{if } 4T_o - 4T_1 + p\pi + m\pi = 0 \quad \text{then} \quad \varrho_3^1 = \frac{a}{2} \{ -\cos(2T_1) - \cos(4T_o - 2T_1) \}, \tag{A1.13}$$

$$\text{if } 4T_o - 4T_1 - p\pi - m\pi = 0 \text{ then } \varrho_4^1 = \frac{a}{2} \{-\cos(2T_1) - \cos(4T_o - 2T_1)\}. \quad (\text{A1.14})$$

The third term in equation A1.2 is found in exactly the same manner. Therefore, the integral term that contains  $K_3$  is given by,

$$\begin{aligned} \frac{h^3 K_3}{48} & \left\{ \frac{a}{8T_o - 8T_1 + p\pi - m\pi} \left[ \sin\left(4T_o + \frac{\pi}{2}(p - m)\right) + \sin\left(4T_o + \frac{\pi}{2}(m - p)\right) \right. \right. \\ & \quad \left. \left. - \sin(4T_1 + \pi(m - p)) - \sin(4T_1) \right] \right. \\ & + \frac{a}{8T_o - 8T_1 - p\pi + m\pi} \left[ \sin\left(4T_o + \frac{\pi}{2}(p - m)\right) + \sin\left(4T_o + \frac{\pi}{2}(m - p)\right) \right. \\ & \quad \left. - \sin(4T_1 + \pi(p - m)) - \sin(4T_1) \right] \\ & + \frac{a}{8T_o - 8T_1 + p\pi + m\pi} \left[ -\sin\left(4T_o + \frac{\pi}{2}(p + m)\right) - \sin\left(4T_o - \frac{\pi}{2}(m + p)\right) \right. \\ & \quad \left. + \sin(4T_1 - \pi(p + m)) + \sin(4T_1) \right] \\ & \left. + \frac{a}{8T_o - 8T_1 - p\pi - m\pi} \left[ -\sin\left(4T_o + \frac{\pi}{2}(p + m)\right) - \sin\left(4T_o + \frac{\pi}{2}(m + p)\right) \right. \right. \\ & \quad \left. \left. + \sin(4T_1 + \pi(p + m)) + \sin(4T_1) \right] \right\} = \frac{h^3 K_3}{48} (\varrho_5^1 + \varrho_6^1 + \varrho_7^1 + \varrho_8^1), \quad (\text{A1.15}) \end{aligned}$$

which is subject to,

$$\text{if } 8T_o - 8T_1 + p\pi - m\pi = 0 \text{ then } \varrho_5^1 = \frac{a}{2} \{\cos(4T_1) + \cos(8T_o - 4T_1)\}, \quad (\text{A1.16})$$

$$\text{if } 8T_o - 8T_1 - p\pi + m\pi = 0 \text{ then } \varrho_6^1 = \frac{a}{2} \{\cos(4T_1) + \cos(8T_o - 4T_1)\}, \quad (\text{A1.17})$$

$$\text{if } 8T_o - 8T_1 + p\pi + m\pi = 0 \text{ then } \varrho_7^1 = \frac{a}{2} \{-\cos(4T_1) - \cos(8T_o - 4T_1)\}, \quad (\text{A1.18})$$

$$\text{if } 8T_o - 8T_1 - p\pi - m\pi = 0 \text{ then } \varrho_8^1 = \frac{a}{2} \{-\cos(4T_1) - \cos(8T_o - 4T_1)\}. \quad (\text{A1.19})$$

The function  $\text{int}_1$ , as given in Chapter 5, is therefore defined as,

$$\begin{aligned} \text{int}_1(K_1, K_2, K_3, m, p) & = \frac{h^3}{12} \int_0^a (K_1 + K_2 \cos(2\theta) + K_3 \cos(4\theta)) \sin\left(\frac{p\pi\bar{x}}{a}\right) \sin\left(\frac{m\pi\bar{x}}{a}\right) d\bar{x} = \\ & \frac{h^3}{48} \{2a\delta_{mp}K_1 + K_2(\varrho_1^1 + \varrho_2^1 + \varrho_3^1 + \varrho_4^1) + K_3(\varrho_5^1 + \varrho_6^1 + \varrho_7^1 + \varrho_8^1)\}. \quad (\text{A1.20}) \end{aligned}$$

The function therefore defines the integrals for the terms containing  $D_{11}$ ,  $D_{12}$  and  $D_{22}$ .

For the term in the stiffness matrix that contains  $D_{66}$  a similar technique is used. The integral for that term is defined as,

$$\frac{h^3}{12} \int_0^a [K_1 + K_3 \cos(4\theta)] \cos\left(\frac{p\pi\bar{x}}{a}\right) \cos\left(\frac{m\pi\bar{x}}{a}\right) d\bar{x} \quad (\text{A1.21})$$

The first term simplifies by using the orthogonality condition for the double cosine series and becomes,

$$\frac{h^3}{12} \int_0^a K_1 \cos\left(\frac{p\pi\bar{x}}{a}\right) \cos\left(\frac{m\pi\bar{x}}{a}\right) d\bar{x} = \frac{h^3 K_1 a}{24} \delta_{mp}. \quad (\text{A1.22})$$

The second term is obtained by using the trigonometric identities. Once the integrals have been carried out and rearranged, the term containing  $K_3$  becomes,

$$\begin{aligned} & \frac{h^3 K_3}{12} \int_0^a \cos(4\theta) \cos\left(\frac{p\pi\bar{x}}{a}\right) \cos\left(\frac{m\pi\bar{x}}{a}\right) d\bar{x} = \\ & \frac{h^3 K_3}{48} \left\{ \frac{a}{8T_0 - T_1 - p\pi + m\pi} \left[ \sin\left(4T_0 + (m-p)\frac{\pi}{2}\right) - \sin\left(4T_1 - (m-p)\frac{\pi}{2}\right) \right. \right. \\ & \quad \left. \left. + \sin\left(4T_0 - (m-p)\frac{\pi}{2}\right) - \sin\left(4T_1\right) \right] \right. \\ & + \frac{a}{8T_0 - T_1 + p\pi - m\pi} \left[ \sin\left(4T_0 + (p-m)\frac{\pi}{2}\right) - \sin\left(4T_1 - (p-m)\frac{\pi}{2}\right) \right. \\ & \quad \left. + \sin\left(4T_0 - (p-m)\frac{\pi}{2}\right) - \sin\left(4T_1\right) \right] \\ & + \frac{a}{8T_0 - T_1 - p\pi - m\pi} \left[ \sin\left(4T_0 - (m+p)\frac{\pi}{2}\right) - \sin\left(4T_1 + (m+p)\frac{\pi}{2}\right) \right. \\ & \quad \left. + \sin\left(4T_0 + (m+p)\frac{\pi}{2}\right) - \sin\left(4T_1\right) \right] \\ & + \frac{a}{8T_0 - T_1 + p\pi + m\pi} \left[ \sin\left(4T_0 + (m+p)\frac{\pi}{2}\right) - \sin\left(4T_1 - (m+p)\frac{\pi}{2}\right) \right. \\ & \quad \left. + \sin\left(4T_0 - (m+p)\frac{\pi}{2}\right) - \sin\left(4T_1\right) \right] \left. \right\} = \frac{h^3 K_3}{48} (\varrho_1^2 + \varrho_2^2 + \varrho_3^2 + \varrho_4^2), \quad (\text{A1.23}) \end{aligned}$$

which is subject to the following conditions,

$$\text{if } 8T_0 - 8T_1 + p\pi - m\pi = 0 \quad \text{then } \varrho_1^2 = \frac{a}{2} \{ \cos(4T_1) + \cos(8T_0 - 4T_1) \}, \quad (\text{A1.24})$$

$$\text{if } 8T_0 - 8T_1 - p\pi + m\pi = 0 \quad \text{then } \varrho_2^2 = \frac{a}{2} \{ \cos(4T_1) + \cos(8T_0 - 4T_1) \}, \quad (\text{A1.25})$$

$$\text{if } 8T_0 - 8T_1 + p\pi + m\pi = 0 \quad \text{then } \varrho_3^2 = \frac{a}{2} \{ \cos(4T_1) + \cos(8T_0 - 4T_1) \}, \quad (\text{A1.26})$$

$$\text{if } 8T_0 - 8T_1 - p\pi - m\pi = 0 \quad \text{then } \varrho_4^2 = \frac{a}{2} \{ \cos(4T_1) + \cos(8T_0 - 4T_1) \}. \quad (\text{A1.27})$$

The function  $\text{int}_2$  is therefore defined by

$$\text{int}_2(K_1, K_2, m, p) = \frac{h^3}{48} [2K_1 a \delta_{pm} + K_3 (\varrho_1^2 + \varrho_2^2 + \varrho_3^2 + \varrho_4^2)]. \quad (\text{A1.28})$$

## REFERENCES

- [1] U.S. Congress, Office of Technology Assessment, *Advanced Materials by Design*, OTA-E-351. U.S. Government Printing Office, Washington, DC, 1988.
- [2] Suppliers of Advanced Composite Materials Association, *Personnel Needs in the Advanced Composite Materials Industry: An Assessment*, SACMA, Washington, DC, 1988.
- [3] Mishiku, M., and Teodosiu, K., "Solution of An Elastic Static Plane Problem for Nonhomogeneous Isotropic Bodies by Means of the Theory of Complex Variables," *Journal of Applied Mathematics and Mechanics*, 30:1, 1957, pp. 713-721.
- [4] Pao, Y. C., "Momentless Design of Composite Structures with Variable Elastic Constants," *J. of Composite Materials*, 3, 1969, pp. 605-615.
- [5] Ashton, J. E., "Analysis of Anisotropic Plates II," *Journal of Composite Materials*, 3, 1969, pp. 471-479.
- [6] Leissa, A. W., and Vagins, M., "The Design of Orthotropic Materials for Stress Optimization," *Int. J. Solids Structures*, 14, 1978, pp. 517-526.
- [7] Kemp, B, and Johnson, E. R., "Response and Failure Analysis of a Graphite-Epoxy Laminate Containing Terminating Internal Plies," *Proceedings of the 26<sup>th</sup> AIAA Structures, Structural Dynamics and Materials Conference*, AIAA, New York, NY, pp. 13-24.
- [8] DiNardo, M. T. and Lagace, P. A., "Buckling and Postbuckling of Laminated Composite Plates with Ply Dropoffs," *AIAA Journal*, 27, October 1989, pp. 1392-1398.
- [9] Martin, A. F., and Leissa, A. W., "Application of the Ritz Method to Plane Elasticity Problems for Composite Sheets with Variable Fiber Spacing," *International Journal of Numerical Methods in Engineering*, 28, 1989, pp. 1813-1825.
- [10] Kuo, C. M., Takahashi, H., and Chou, T. W., "Effect of Fiber Waviness on the Nonlinear Elastic Behavior of Flexible Composites," *J. of Composite Materials*, 22, November 1988, pp. 1004-1022.

- [11] Hyer, M. W., and Charette, R. F., "The Use of Curvilinear Fiber Format In Composite Structure Design," *Proceedings of the 30<sup>th</sup> AIAA Structures, Structural Dynamics and Materials Conference*, AIAA, New York, NY, pp. 2137-2145.
- [12] Jones, R. M., *Mechanics of Composite Materials*. Hemisphere Publishing Corp., New York, NY, 1975.
- [13] Whitney, J. M., *Structural Analysis of Laminated Anisotropic Plates*. Technomic Publishing Co., Lancaster, PA, 1987.
- [14] Tsai, S. W., and Pagano, N. J., "Invariant Properties of Composite Materials," *Composite Materials Workshop*, Technomic Publishing Co., Westport, Conn., 1968, pp. 233-253.
- [15] Wolfram, S., *Mathematica: A System for Doing Mathematics by Computer*. Addison-Wesley, New York, NY, 1992.
- [16] Sewell, G., *The Numerical Solution of Ordinary and Partial Differential Equations*. Academic Press, Inc., San Diego, CA, 1988.
- [17] Carnahan, B., *Applied Numerical Methods*. Wiley, New York, NY, 1987.
- [18] Rice, J. R. and Boisvert, R. F., *Solving Elliptic Problems Using ELLPACK*. Springer-Verlag, New York, NY, 1985.
- [19] Brush, D. O., and Almroth, B. O., *Buckling of Bars, Plates and Shells*. McGraw-Hill, New York, NY, 1975.
- [20] Nemeth, M. P., "Importance of Anisotropy on Buckling of Compression-Loaded Symmetric Composite Plates," *AIAA Journal*, 24:11, 1986, pp. 1831-1835.
- [21] IMSL Inc., *Math Library*. IMSL Inc., Houston, TX, 1987.

## Vita

Reynaldo Alberto Olmedo Marroquín was born in México City, México on August 11, 1968 to Juan C. Olmedo and Elsy Marroquín de Olmedo. In 1969 he moved with his parents to their native El Salvador. He lived in San Salvador, El Salvador until the fall of 1980, when he moved to Miami, Florida. In 1986 he graduated with Honors from Miami Coral Park Senior Highschool, and in the fall of the same year he entered Florida International University (FIU) as a Faculty Scholar. While pursuing a Mechanical Engineering degree, he served as a Student Government Senator for the College of Engineering and as Chairman of the Student Chapter of ASME. In the summer of 1990, he graduated from FIU with High Honors and received a Bachelor of Science Degree in Mechanical Engineering. He began his graduate studies at Virginia Tech in the fall of 1990 in the Engineering Science and Mechanics Department. He completed his Master's degree in Engineering Mechanics in the summer of 1992.

A handwritten signature in black ink that reads "Reynaldo Olmedo". The signature is written in a cursive style with a large initial 'R' and a long, sweeping tail on the 'o'.